

# HEAT TRANSFER AND FLOW VISUALIZATION OF FALLING FILM CONDENSATION ON TUBE ARRAYS WITH PLAIN AND ENHANCED SURFACES

THÈSE N° 3015 (2004)

PRÉSENTÉE À LA FACULTÉ SCIENCES ET TECHNIQUES DE L'INGÉNIEUR

Institut des sciences de l'énergie

SECTION DE GÉNIE MÉCANIQUE

ÉCOLE POLYTECHNIQUE FÉDÉRALE DE LAUSANNE

POUR L'OBTENTION DU GRADE DE DOCTEUR ÈS SCIENCES

PAR

**Daniel GSTÖHL**

ingénieur mécanicien diplômé EPF  
et de nationalité liechtensteinoise

acceptée sur proposition du jury:

Prof. J. Thome, directeur de thèse  
Prof. D. Favrat, rapporteur  
Prof. A. Jacobi, rapporteur  
Prof. J. Rose, rapporteur

Lausanne, EPFL  
2004



# Abstract

The tubes in shell-and-tube condensers, widely used in refrigeration and chemical process industries, are subjected to condensate inundation from the neighboring tubes. The aim of the present investigation is to study the effect of condensate inundation on the thermal performance of an vertical array of horizontal tubes with plain and enhanced surfaces. The experimental approach is split in two parts: measurement of the heat transfer coefficients and visualization of the flow patterns of the condensate falling between the tubes. Refrigerant R-134a was condensed at a saturation temperature of  $304K$  on tube arrays with up to ten tubes at pitches of 25.5, 28.6, and 44.5mm. Four commercially available copper tubes with a nominal diameter of 19.05mm and 544mm in length were tested: a plain tube, a 26 fpi / 1024 fpm low finned tube (Turbo-Chil) and two tubes with three-dimensional enhanced surface structures (Turbo-CSL and Gewa-C). Measurements were performed at three nominal heat flux levels up to  $60kW/m^2$  with liquid overfeed corresponding to film Reynolds numbers up to 3000. The test section offers full visual access to study the flow patterns of the condensate. Furthermore, the large experimental database is unique in that true local heat transfer coefficients were measured as opposed to tube length averaged values in previous studies. With little liquid inundation the tubes with 3D enhanced surface structures outperform the low finned tube. Increasing liquid inundation deteriorates the thermal performance of the 3D enhanced tubes, while it has nearly no affect on the low finned tube, resulting in a higher heat transfer coefficient for the low finned tube at high film Reynolds numbers. Large differences in condensate flow patterns were observed. For the 3D enhanced tubes the ideal flow modes (droplet, column and sheet mode) were observed, while the flow was very unstable for the other two types of tubes. For the 3D enhanced tubes oscillations occurred in the sheet mode at film Reynolds numbers such that liquid left the array of tubes sideways. A heat transfer model for an array of 3D enhanced tubes based on these visual observations was proposed, including the effects of liquid lost by the sideways slinging phenomenon. The measurements were predicted within a mean error of 3% and a standard deviation of 13% by this model.



# Résumé

Les tubes dans les condenseurs à tubes, largement utilisés dans le domaine de la réfrigération et lors de processus chimiques industriels, sont inondés par le liquide provenant de la condensation sur les tubes environnants. Le travail concerne l'étude de l'influence de cette inondation sur les performances thermiques d'un arrangement vertical de tubes horizontaux à surfaces lisses ou améliorées. L'approche expérimentale a été divisée en deux parties: d'une part, la mesure des coefficients de transfert de chaleur et, d'autre part, la visualisation des modes d'écoulement du condensat entre les tubes. Le réfrigérant R-134a a été condensé à la température de saturation de  $304K$  sur un arrangement de dix tubes, pour des distances inter-axes de  $25.5$ ,  $28.6$  et  $44.5mm$ . Quatre tubes commerciaux en cuivre, ayant un diamètre nominal de  $19.05mm$  et une longueur de  $544mm$ , ont été testés: un tube lisse, un tube à ailettes à  $26\text{ fpi} / 1024\text{ fpm}$  (Turbo-Chil) et deux tubes à surfaces améliorées par des structures tridimensionnelles (Turbo-CSL and Gewa-C). Les mesures ont été réalisées pour trois valeurs nominales de densité de flux de chaleur allant jusqu'à  $60kW/m^2$  et pour des débits de réfrigérant liquide, correspondant à des nombres de Reynolds de film allant jusqu'à 3000. La conception de la section d'essai permet l'observation complète des modes d'écoulement du condensat entre les tubes. Par ailleurs, la base de données expérimentales ainsi constituée est unique dans le sens où ce sont des valeurs locales du coefficient de transfert de chaleur qui ont été mesurées et non des valeurs moyennées sur la longueur des tubes, comme c'était le cas dans les études menées jusqu'ici. Pour les configurations à faible inondation, les tubes à structures tridimensionnelles surclassent le tube à ailettes. L'accroissement du débit de condensat détériore les performances des tubes à structures tridimensionnelles alors qu'il n'affecte que marginalement celles du tube à ailettes. De ce fait, ce dernier permet d'obtenir de plus grandes valeurs du coefficient de transfert de chaleur pour des nombres de Reynolds de film importants. Une grande diversité de modes d'écoulement de condensat a été observée. Pour les tubes à structures tridimensionnelles, les modes d'écoulement typiques (mode gouttes, colonnes et film) ont été rencontrés, tandis que, pour les deux autres types de tubes, l'écoulement s'est révélé très instable. Pour les tubes à surfaces améliorées 3D, des oscillations sont apparues lors du mode d'écoulement en film, pour des nombres de Reynolds de

film élevés, permettant au liquide de quitter latéralement l'arrangement de tubes. Basé sur ces observations visuelles, un modèle physique de transfert de chaleur a été proposé pour les tubes à surfaces améliorées 3D, incluant ces effets de pertes latérales de condensat. L'écart entre valeurs calculées par ce modèle et les valeurs mesurées expérimentalement est de 3% pour un écart type de 13%.

# Acknowledgements

First of all I would like to thank Prof. John R. Thome who gave me the opportunity to perform this investigation at the EPFL. His confidence, motivation, optimism and good humor guided me smoothly over the past several years.

I would like to express my gratitude to my thesis committee, Prof. Daniel Favrat, EPFL, Prof. Anthony M. Jacobi, University of Illinois, and Prof. John W. Rose, University of London, for their support and suggestions.

I must also acknowledge the EPFL/LTCM Falling Film Research Club members, Axima Refrigeration AG, Dunham-Bush Inc., UOP Inc., Wieland-Werke AG and Wolverine Tube Inc. for their financial support, in particular Wieland-Werke AG and Wolverine Tube Inc. for providing the tube samples.

Special thanks to our technicians Laurent Chevalley and Fredy Thomas for building the test facility, for their help with any technical problem and the tedious tube replacing, as well as Monique Barraud Plummer for taking care of the administrative work, creating a pleasant work environment and being a walking guide book.

I am also grateful to the past and present members of the Laboratory of Heat and Mass Transfer, Jean El Hajal, Patrice de Gol, Leszek Wojtan, Douglas Robinson, Thierry Ursenbacher, Vincent Dupont, Jesus Moreno Quiben, Rémi Revellin, Gherhardt Ribatski and Lorenzo Consolini for their help and the friendly scientific and social environment.

In particular I would like to thank Jean-François Roques for sharing a good time in developing and constructing the test facility, for all the fruitful discussions and for being a good friend.

A very special thankyou to Karin Zürcher for her continuous support and for reminding me that there is life beyond the tubes.

Finally, all my gratitude goes to my family, in particular to my parents, Christl and Hugo Gstöhl for their love and encouragement.





# Contents

<b>Acknowledgements</b>	<b>V</b>
<b>List of Figures</b>	<b>XI</b>
<b>List of Tables</b>	<b>XVII</b>
<b>Nomenclature</b>	<b>1</b>
<b>1 Introduction</b>	<b>3</b>
<b>2 State of the Art Review</b>	<b>7</b>
2.1 Condensation on single tubes . . . . .	7
2.2 Condensation on tube rows and bundles . . . . .	13
2.3 Conclusion . . . . .	24
<b>3 Experimental Setup</b>	<b>27</b>
3.1 Overview . . . . .	27
3.2 Refrigerant circuit . . . . .	28
3.2.1 Vapor refrigerant circuit . . . . .	29
3.2.2 Liquid refrigerant circuit . . . . .	31
3.3 Water circuit . . . . .	32
3.4 Glycol circuit . . . . .	33
3.5 Test section . . . . .	35
3.5.1 Liquid distributor . . . . .	36
3.5.2 Tube arrangements . . . . .	37
3.5.3 Copper tubes tested . . . . .	38
3.5.4 Tube instrumentation . . . . .	41
3.5.5 Instrumentation of the test section . . . . .	42
3.6 Data acquisition and control . . . . .	42
3.6.1 Data acquisition system . . . . .	42
3.6.2 Control system . . . . .	43
3.7 Operating procedure . . . . .	44
3.8 Instrumentation accuracy . . . . .	45
3.8.1 Thermocouples . . . . .	46

3.8.2	Pressure transducers . . . . .	47
3.8.3	Mass flow meters . . . . .	48
3.9	Conclusion . . . . .	49
<b>4</b>	<b>Modified Wilson Plot Technique</b>	<b>51</b>
4.1	Heat transfer calculation principle . . . . .	51
4.2	Modified Wilson plot method . . . . .	53
4.2.1	Internal heat transfer coefficient . . . . .	53
4.2.2	External heat transfer coefficient . . . . .	55
4.2.3	Overall heat transfer coefficient . . . . .	56
4.2.4	Measurement procedure . . . . .	56
4.3	Physical properties evaluation . . . . .	57
4.4	Results and accuracy . . . . .	57
4.5	Influence of external heat transfer coefficient . . . . .	60
4.6	Independent cross checks . . . . .	61
4.7	Conclusion . . . . .	62
<b>5</b>	<b>Heat Transfer Measurements</b>	<b>63</b>
5.1	Data reduction . . . . .	63
5.2	Measurement accuracies . . . . .	65
5.3	Test conditions . . . . .	69
5.4	Single tube data . . . . .	71
5.4.1	Reproducibility . . . . .	71
5.4.2	Comparison with other investigations . . . . .	74
5.4.3	Comparison with single tube correlations . . . . .	76
5.4.4	Single tube correlations . . . . .	80
5.5	Measurements with liquid inundation . . . . .	83
5.5.1	Tube Behavior . . . . .	83
5.5.2	Tube Pitch Influence . . . . .	91
5.5.3	Heat Flux Influence . . . . .	95
5.6	Conclusion . . . . .	98
<b>6</b>	<b>Flow Visualization</b>	<b>99</b>
6.1	Flow pattern map and flow modes . . . . .	99
6.2	Observed flow modes . . . . .	102
6.2.1	Droplet mode . . . . .	102
6.2.2	Column mode . . . . .	103
6.2.3	Sheet mode . . . . .	104
6.2.4	Droplet-Column mode . . . . .	104
6.2.5	Column-Sheet mode . . . . .	104
6.3	Adiabatic flow pattern observations . . . . .	105
6.4	Flow pattern observations with heat transfer . . . . .	112
6.4.1	Without liquid overfeed . . . . .	112
6.4.2	With liquid overfeed . . . . .	121

6.5	Conclusion . . . . .	129
<b>7</b>	<b>Heat Transfer Models</b>	<b>131</b>
7.1	3D enhanced tubes . . . . .	131
7.1.1	Without liquid leaving sideways . . . . .	131
7.1.2	With liquid leaving sideways . . . . .	138
7.2	Plain tube . . . . .	144
7.2.1	Comparison with Nusselt's theory . . . . .	144
7.2.2	Tube row effect . . . . .	146
7.2.3	Waves and turbulent film condensation . . . . .	148
7.2.4	With liquid leaving sideways . . . . .	154
7.3	Low finned tube . . . . .	156
7.4	Conclusion . . . . .	160
<b>8</b>	<b>Conclusions</b>	<b>163</b>
<b>A</b>	<b>Integral Analysis of Nusselt</b>	<b>169</b>
A.1	Laminar film condensation on a vertical plate . . . . .	169
A.2	Laminar film condensation on a horizontal tube . . . . .	174
A.3	Condensation on horizontal tube bundles . . . . .	176
A.3.1	Tube row effect for non-uniform surface temperature . . . . .	176
	<b>Bibliography</b>	<b>179</b>
	<b>Curriculum Vitae</b>	<b>187</b>



# List of Figures

1.1	Influence of condensate inundation on the average heat transfer coefficient from Marto for steam [4] . . . . .	4
2.1	Heat transfer coefficient and film thickness ( $y_o$ ) on the first (left) and second tube (right) according to Nusselt [1]. . . . .	8
2.2	Surface tension drainage on a fin having small tip radius with increasing radius from fin tip [11] . . . . .	9
2.3	Condensate retention on integral-fin tubes [11] . . . . .	11
3.1	Overall view of the falling film test facility. Main unit on the right and auxiliary unit on the left. . . . .	28
3.2	Detailed schematic of the refrigerant circuit with all piping. . . . .	29
3.3	Simplified schematic of the refrigerant circuit showing only the tubing used in present study. . . . .	30
3.4	Schematic of the forced circulation loop for the cooling water. . . . .	32
3.5	Schematic of the circulation loop of glycol as cold source for the auxiliary condenser. . . . .	34
3.6	Test section. . . . .	35
3.7	Schematic of the liquid distributor for condensate inundation. . . . .	37
3.8	Schematic of the three tested arrangements of tubes in the test section. . . . .	38
3.9	Close-up pictures of the surface of the four types of tubes: Plain tube (on the top left), Turbo-Chil (on the top right), Turbo-CSL (on bottom left), and Gewa-C (on the bottom right). . . . .	39
3.10	Photomicrographs of an axial cut of the tubes tested: Plain tube (on the top left), Turbo-Chil (on the top right), Turbo-CSL (on bottom left), and Gewa-C (on the bottom right). . . . .	40
3.11	Schematic of a trapezoidal-fin tube. . . . .	40
3.12	Schematic of the instrumentation setup of the tubes to measure the temperature profile of the water flowing inside. . . . .	42
3.13	Calibration of one stainless steel tube insert instrumented with six thermocouples for increasing and decreasing calibration temperature. . . . .	47

3.14	Isothermal temperature check of the sixteen thermocouples in one two-pass circuit connected to a thermal bath (left) and installed in the test section (right). . . . .	48
4.1	Modified Wilson plots for all types of tubes in pool boiling. . .	58
4.2	Modified Wilson plots using the condensation data (without inundation) for the plain and low finned tubes. . . . .	62
5.1	Reproducibility tests for top tube row without overfeed for all four types of tubes at a tube pitch of $28.6mm$ . . . . .	71
5.2	Top tube without liquid overfeed for all three tube pitches for all four types of tubes. . . . .	72
5.3	Top tube without liquid overfeed for all three tube pitches for all four types of tubes. . . . .	73
5.4	First tube without liquid overfeed. . . . .	74
5.5	Comparison of single plain tube data with Nusselt's theory. . .	77
5.6	Comparison of single low finned tube data with different correlations. . . . .	78
5.7	Curve fit of single tube data without liquid overfeed for all four types of tubes. . . . .	81
5.8	Comparison of single tube performance without liquid overfeed. .	82
5.9	Measurements with liquid inundation of the Turbo-CSL tube with tube pitch of $25.5mm$ at a nominal row heat flux of $40kW/m^2$ . . . . .	84
5.10	Measurements with liquid inundation of the Gewa-C tube with tube pitch of $25.5mm$ at a nominal row heat flux of $40kW/m^2$ . . . . .	86
5.11	Limited heat flux range of measurements of the Turbo-CSL tube and Gewa-C tube with tube pitch of $25.5mm$ at a nominal bundle heat flux of $40kW/m^2$ . . . . .	87
5.12	Comparison of the Turbo-CSL tube and Gewa-C tube at the tube pitch of $25.5mm$ with limited heat flux range. . . . .	88
5.13	Measurements with liquid inundation of the Turbo-Chil tube with tube pitch of $25.5mm$ at a nominal row heat flux of $40kW/m^2$ . . . . .	89
5.14	Measurements with liquid inundation of the plain tube with tube pitch of $25.5mm$ at a nominal row heat flux of $12kW/m^2$ . . .	90
5.15	Comparison of the four types of tubes with tube pitch of $25.5mm$ at a nominal row heat flux of $40kW/m^2$ (respective to $12kW/m^2$ for the plain tube). . . . .	90
5.16	Tube spacing influence of Turbo-CSL tube at a nominal bundle heat flux of $40kW/m^2$ with limited heat flux range. . . .	91
5.17	Tube spacing influence of Gewa-C tube at a nominal bundle heat flux of $40kW/m^2$ with limited heat flux range. . . . .	92

5.18	Tube spacing influence of Turbo-Chil tube at a nominal bundle heat flux of $40kW/m^2$ with limited heat flux range. . . . .	93
5.19	Tube spacing influence of plain tube at a nominal bundle heat flux of $12kW/m^2$ on the top three tubes in the array. . . . .	94
5.20	Heat flux influence of Turbo-CSL tube at tube pitch of $28.6mm$ . . . . .	95
5.21	Heat flux influence of Gewa-C tube at tube pitch of $28.6mm$ . . . . .	96
5.22	Heat flux influence of Turbo-Chil tube at tube pitch of $25.5mm$ . . . . .	97
5.23	Heat flux influence of plain tube at tube pitch of $25.5mm$ . . . . .	97
6.1	Schematic of the three main flow modes: a) Droplet mode, b) Column mode and c) Sheet mode from Mitrovic [72] . . . . .	100
6.2	Intertube flow modes observed for R-134a under adiabatic conditions on the Turbo-CSL tube with a tube pitch of $28.6mm$ : Droplet (D), Droplet-Column (DC), Column (C), Column-Sheet (CS), and Sheet (S). . . . .	103
6.3	Intertube flow modes observed for R-134a under adiabatic conditions at a tube pitch of $28.6mm$ : Gewa-C (left), Turbo-Chil (middle), and plain tubes (right). . . . .	107
6.4	Observed transition film Reynolds numbers on Turbo-CSL (top) and Gewa-C tubes (bottom) for tube pitch $25.5mm$ (1), $28.6mm$ (2), and $44.5mm$ (3) with increasing mass flow rate ( $\Delta$ ) and decreasing mass flow rate ( $\blacktriangledown$ ). . . . .	110
6.5	Observed transition film Reynolds numbers on Turbo-Chil (top) and plain tubes tubes (bottom) for tube pitch $25.5mm$ (1), $28.6mm$ (2), and $44.5mm$ (3) with increasing mass flow rate ( $\Delta$ ) and decreasing mass flow rate ( $\blacktriangledown$ ). . . . .	111
6.6	Intertube flow patterns observed on the second tube in the array (without overfeed) at a tube pitch of $28.6mm$ for R-134a condensing at a nominal heat flux of $20kW/m^2$ (top), $40kW/m^2$ (middle), and $60kW/m^2$ (bottom): Turbo-CSL (left), Gewa-C (middle), and Turbo-Chil (right). . . . .	113
6.7	Condensate flow on the second tube in the array of low finned tubes (without overfeed) at a tube pitch of $28.6mm$ for R-134a condensing at a nominal heat flux of $40kW/m^2$ . . . . .	114
6.8	Intertube flow patterns observed on the second tube in the array (without overfeed) for R-134a condensing at a nominal heat flux of $60kW/m^2$ : Turbo-CSL (top row), Gewa-C (middle row), and Turbo-Chil (bottom row). . . . .	116
6.9	Heat transfer and flow pattern observations during the measurements without overfeed at a tube pitch of $28.6mm$ : Turbo-CSL (top) and Gewa-C (bottom). . . . .	119
6.10	Heat transfer and flow pattern observations during the measurements without overfeed at a tube pitch of $28.6mm$ : Turbo-Chil (top) and plain tube (bottom). . . . .	120

6.11	Intertube flow patterns observed on the second tube in the array for R-134a condensing at a nominal heat flux of $20kW/m^2$ with liquid overfeed ( $Re \approx 500$ ): Tube pitch $28.6mm$ (top), Tube pitch $44.5mm$ (bottom). . . . .	121
6.12	Intertube flow patterns observed on the second tube in the array (with overfeed) at a tube pitch of $28.6mm$ for R-134a condensing at a nominal heat flux of $40kW/m^2$ : Turbo-CSL (left), Gewa-C (middle), and Turbo-Chil (right). . . . .	122
6.13	Intertube flow patterns observed on the second tube in the array (with overfeed) at a tube pitch of $28.6mm$ for R-134a condensing at a nominal heat flux of $40kW/m^2$ : Turbo-CSL (left), Gewa-C (middle), and Turbo-Chil (right). . . . .	123
6.14	Intertube flow patterns observed for the plain tube on the second tube in the array (with overfeed) at a tube pitch of $28.6mm$ for R-134a condensing at a nominal heat flux of $6kW/m^2$ . . . . .	125
6.15	Heat transfer and flow pattern observations during the measurements with overfeed at a tube pitch of $28.6mm$ at a nominal heat flux of $40kW/m^2$ : Turbo-CSL (top) and Gewa-C (bottom). . . . .	127
6.16	Heat transfer and flow pattern observations during the measurements with overfeed at a tube pitch of $28.6mm$ : Turbo-Chil (top) and plain tube (bottom) at a nominal heat flux of $40kW/m^2$ and $6kW/m^2$ , respectively. . . . .	128
7.1	Limited heat flux range of measurements of the Turbo-CSL at the tube pitch $25.5mm$ . . . . .	132
7.2	Prediction relative error of data at the tube pitch $25.5mm$ (first method). . . . .	135
7.3	Prediction relative error of data at the tube pitch $25.5mm$ (second method). . . . .	135
7.4	Prediction of heat transfer coefficient of the 3D enhanced tubes at a tube pitch of $25.5mm$ (first method). . . . .	136
7.5	Prediction of heat transfer coefficient of the 3D enhanced tubes at a tube pitch of $25.5mm$ (second method). . . . .	137
7.6	Schematic of liquid leaving the tube sideways. . . . .	139
7.7	Prediction of heat transfer coefficients of the 3D enhanced tubes. . . . .	142
7.8	Relative errors of predictions. . . . .	143
7.9	Distribution of the relative errors. . . . .	143
7.10	Comparison with Nusselt Theory for top two tubes (left) and top three tubes (right) with a tube pitch of $28.6mm$ . . . . .	145
7.11	Measurements without liquid overfeed on the plain tube. . . . .	145



7.12	Tube row effect for the plain tube at a tube pitch of $25.5mm$ at a nominal heat flux of $6kW/m^2$ (left) and $20kW/m^2$ (right).	147
7.13	Local heat transfer coefficients on the top three plain tubes in the array. Comparison with correlations for the wavy and turbulent flow regimes on a vertical plate. . . . .	152
7.14	Prediction of heat transfer coefficients of the plain tubes (note that the vertical axis has been truncated to begin at 1000). . . . .	153
7.15	Distribution of the relative errors. . . . .	154
7.16	Comparison of all data of the measurements without overfeed with a selection of existing models for the low finned tube. . . . .	157
7.17	Relative errors compared to the model of Sreepahti (1996) for the measurements without overfeed. . . . .	158
7.18	All data of the measurements without overfeed for the Turbo-Chil tube. . . . .	159
7.19	Relative errors of the curve fit for the measurements without overfeed. . . . .	159
A.1	Film condensation on a vertical plate. . . . .	170
A.2	Integral representation of falling laminar film condensation on a vertical plate. . . . .	171



# List of Tables

3.1	Geometrical specifications of the tubes tested. All dimensions are in <i>mm</i> . . . . .	39
4.1	Measurements of the corrective multiplier of the water side coefficient for the plain tube. . . . .	59
4.2	Measurements of the corrective multiplier of the water side coefficient for the Turbo-Chil tube. . . . .	59
4.3	Measurements of the corrective multiplier of the water side coefficient for the Turbo-CSL tube. . . . .	59
4.4	Measurements of the corrective multiplier of the water side coefficient for the Gewa-C tube. . . . .	60
4.5	Corrective multipliers for internal heat transfer coefficient ( $\alpha_i = C_i \alpha_{gni}$ ). . . . .	62
5.1	Corrective multipliers for internal heat transfer coefficient $\alpha_i$ with absolute and relative uncertainty. . . . .	67
5.2	Mean relative errors in local heat flux at the three nominal heat flux levels. . . . .	68
5.3	Mean relative errors in local heat transfer coefficient at the three nominal heat flux levels. . . . .	68
5.4	Test matrix for the measurements with liquid overfeed. . . . .	69
5.5	Experimental database for refrigerant R-134a at a saturation temperature of $304K$ : ranges of the main variables and maximum values of the vapor velocity in the test section, superheating of the vapor, subcooling of the overfeed liquid and film Reynolds number. . . . .	70
5.6	Deviation of different applications of Nusselt's theory to the measured values for a single plain tube. . . . .	77
5.7	Deviation of different correlations to the measured values for the single low finned tube data. . . . .	78
5.8	Coefficients in equation 5.15 for condensation on a single tube without liquid overfeed for all four types of tested tubes. . . . .	80
5.9	Coefficients in equation 5.16 for the heat flux on a single tube without liquid overfeed for all four types of tested tubes. . . . .	82

6.1	Coefficients for transition relations (equation 6.8) without spacing effect from Roques et al. [75] and Roques (unpublished work). . . . .	102
6.2	Transitions film Reynolds numbers for refrigerant R-134a measured at room temperature ( $Ga^{1/4} \approx 453$ ). . . . .	109
7.1	Coefficients in equation 7.2 for condensation on the tube array with a tube pitch of $25.5mm$ with no liquid leaving sideways. . . . .	133
7.2	Coefficients in equation 7.11. . . . .	140
7.3	Coefficients in equations 7.10 and 7.11 and relative errors of the prediction methods. . . . .	141
7.4	Tube row effect for the plain tube without surface temperature correction (exponents in equation 7.15) for all tubes in the array and on the first six tubes (values in brackets). . . . .	148
7.5	Tube row effect for the plain tube with surface temperature correction (exponents in equation 7.17) for all tubes in the array and on the first six tubes (values in brackets). . . . .	148
7.6	Tube row effect for the low finned tube (exponent $m$ in equation 7.27) for all tubes in the array. . . . .	156

# Nomenclature

Symbol	Description	SI units
<b>Roman letters</b>		
$A$	area	$[m^2]$
$c_p$	specific heat at constant pressure	$[J/kgK]$
$D$	diameter of the tubes	$[m]$
$e$	fin height	$[m]$
$g$	acceleration due to gravity (9.81)	$[m^2/s]$
$h$	vaporization latent heat	$[J/kg]$
$N$	tube row number	$[-]$
$\dot{m}$	mass flow	$[kg/s]$
$P$	pressure	$[kPa]$
$p$	tube pitch	$[m]$
$pf$	fin pitch	$[m]$
$q$	local heat flux relative to a surface	$[W/m^2]$
$r$	radius of the tubes	$[m]$
$r_w$	thermal resistance of the tube	$[m^2K/W]$
$s$	spacing	$[m]$
$T$	temperature	$[K]$
$t$	thickness	$[m]$
$U$	overall heat transfer coefficient	$[W/m^2K]$
$u$	velocity	$[m/s]$
$x$	coordinate in axial direction	$[m]$
$z$	coordinate in vertical direction	$[m]$
<b>Greek letters</b>		
$\alpha$	heat transfer coefficient	$[W/m^2K]$
$\beta$	retention angle	$[rad]$
$\delta$	falling film thickness	$[m]$
$\eta$	fin efficiency	$[-]$
$\theta$	deflection angle	$[rad]$
$\lambda$	thermal conductivity	$[W/mK]$

$\Gamma$	liquid flow rate on one side of the tube per unit length	$[kg/ms]$
$\mu$	dynamic viscosity	$[kg/ms], [Pa\ s]$
$\nu$	kinematic viscosity ( $\mu/\rho$ )	$[m^2/s]$
$\phi$	fin half tip angle	$[rad]$
$\rho$	density	$[kg/m^3]$
$\sigma$	surface tension	$[N/m]$

### Subscript

$b$	fin base
$cop$	copper
$crit$	critical
$f$	fin
$gni$	Gnielinski
$h$	hydraulic (diameter)
$i$	internal side
$L$	saturated liquid
$mean$	mean value
$o$	external side
$r$	fin root
$ref$	refrigerant
$sat$	saturation conditions
$t$	fin tip
$V$	saturated vapor
$wat$	water
$w$	wall

### Dimensionless numbers

$Ga$	Modified Galileo number $\rho_L \sigma^3 / \mu_L^4 g$
$Nu$	Nusselt number $\alpha D / \lambda$
$Nu^*$	Condensation number $\alpha_o / \lambda_L \cdot [\mu_L^2 / (\rho_L (\rho_L - \rho_V) g)]^{1/3}$
$Pr$	Prandtl number $\mu c_p / \lambda$
$Re_L$	refrigerant film Reynolds number $4\Gamma / \mu_{ref}$
$Re_{wat}$	water Reynolds number $\rho_{wat} u D_h / \mu_{wat} = 4\dot{m} / \pi (D_i + D_{stainless}) \mu_{wat}$

# Chapter 1

## Introduction

Shell and tube condensers are widely used in large refrigeration systems, heat pumps, and the chemical process industry. In this type of condenser, the refrigerant is flowing on the outside of the tubes and typically water is flowing inside the tubes. Horizontal tubes are arranged in a bundle located within a shell. The refrigerant enters the shell as vapor typically close to its saturation condition at the top and condenses on the external surface of the tubes. The condensed liquid leaves the heat exchanger at the bottom by gravity. Thus, the latent heat of the refrigerant is transferred to the cooling water.

Condensation on single tubes has been widely studied analytically on plain and low finned tubes (but not 3D enhanced surface tubes) and in numerous experimental investigations. Laminar film condensation has first been successfully treated by Nusselt [1] in 1916, who provided an analysis for laminar film condensation on an isothermal vertical plate and applied it also to horizontal plain tubes. Since the early 1940s finned tubes have been used widely in heat exchangers. Originally, these tubes were introduced to increase the surface area. The fin geometry and fin spacings were limited by manufacturing techniques and the flow of the condensate was assumed to be governed by gravitational and viscous forces. In 1954, Gregorig [2] showed that surface tension is of importance on enhanced surface structures. This work stimulated research to use the surface tension mechanism to improve the heat transfer performance of condensing surfaces. Complex surface structures with three-dimensional fins were made by notching of conventional two-dimensional low fins to form saw-toothed fins, or by cross cutting the fins. While for the plain tubes and two-dimensional finned tubes analytical models and empirical correlations have been developed, no general models have been established for the three-dimensional finned tubes. The few existing prediction methods are always for one specific surface structure and fluid and thus lack generality. In order to judge the thermal performance of the three-dimensional finned tubes, industry depends

on experimental investigations. Condensation in actual condensers may be very different from condensation on a single tube, as the tubes are affected by inundation of condensate from the neighboring tubes above. In general, the top tube without condensate inundation in a vertical array of horizontal tubes has the highest heat transfer performance. The condensate of this tube falls on the tube below and thus, with increasing row number starting from the top, the amount of condensate increases and thermal performance decreases. Numerous studies have been performed in order to quantify the effect of condensate inundation on the thermal performance, mainly concerning plain tubes. In Nusselt's theory the mean heat transfer coefficient  $\bar{\alpha}_N$  of a vertical array of horizontal tubes compared to the heat transfer coefficient of the top tube  $\alpha_1$  in the array is given by

$$\frac{\bar{\alpha}_N}{\alpha_1} = N^{-1/4} \quad (1.1)$$

where  $N$  is the row number counting from the top. In thermal design, this equation was found to be too conservative resulting in condensers that were consistently over-surfaced. Kern [3] suggested the use of a less conservative relationship by replacing the exponent of  $-1/4$  by the value of  $-1/6$ . Figure 1.1 depicts an example of the influence of condensate inundation on the mean heat transfer coefficient in experimental investigations given by Marto for steam [4], which illustrates the large difference in tube row effect of a plain tube compared to two types of enhancements.

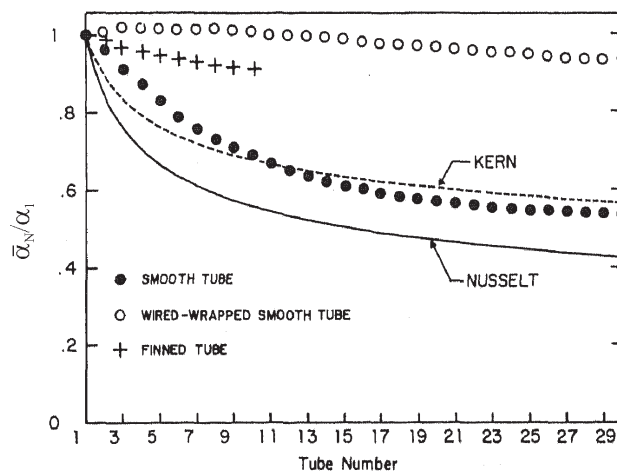


Figure 1.1: Influence of condensate inundation on the average heat transfer coefficient from Marto for steam [4] .



In the literature, the effect on condensate inundation has mainly been investigated experimentally. Large differences in the effect of inundation were found for different types of tubes and test conditions. Very often these differences were attributed to different flow patterns of the condensate on the array of tubes, but in many studies there was little or no visual access to observe the condensation process itself.

The aim of the current investigation is to study the effect of condensate inundation on plain and enhanced tubes. The experimental approach is split in two parts: measurement of the local condensing heat transfer coefficients and visualization of the flow patterns of the condensate on the tubes over a wide range of test conditions. Heat transfer measurements are performed on a vertical array of horizontal tubes. A novel measurement approach is applied in order to get local heat transfer coefficients at the mid point of every tube in the array of tubes as opposed to tube length averaged values measured in previous studies. A test facility capable to recreate various operating conditions in a large condenser has been constructed especially for this investigation. The test section offers full visual access to study the flow pattern of condensate on the tubes. These results will then be compared against existing methods and new/improved methods will be proposed based on the current experimental findings.

In the next chapters, a state of the art review is given first. Then the test facility is described, followed by a discussion of the measurement technique and data reduction, involving a modified Wilson plot approach. The experimental results of the heat transfer measurements are presented and visual observations of the intertube flow patterns are discussed. Finally, comparisons are made with existing models and new models are proposed.



## Chapter 2

# State of the Art Review

The objective of this chapter is to review the literature on film condensation on horizontal tubes. Primary emphasis is given in enhanced surface geometries. For stagnant vapor, film condensation on a single tube is governed by gravity and surface tension forces. On tube arrays, in addition, the inundation by condensate from the tube above has to be considered (apart from vapor shear effects which are not considered in the current investigation). First, the two mechanisms of condensate drainage and the condensate retention are illustrated by a chronological description of the development of analytical models on single tubes. Next, recent experimental investigations of condensation on arrays of horizontal tubes and tube bundles are reviewed focusing on studies using R-134a.

### 2.1 Condensation on single tubes

Important steps on the understanding of film condensation on enhanced surfaces are shown and some recommended models for condensation on low finned tubes are mentioned. This review does not claim to be exhaustive but gives a basic overview; for more details refer to following reviews. Marto [5] provided a extensive review of condensation on horizontal integral-fin tubes. More general, Webb [6] reviewed fundamental theories and experimental studies. Thome [7] reviewed experimental tests and analytical studies of condensation of pure refrigerants and mixtures on single tubes and tube bundles, including vapor shear effects, during the nineties. Shah [8] focused on the role of surface tension and gives a description of recent models for low finned tubes.

Laminar film condensation of pure single-component vapor was first analyzed by Nusselt [1] in 1916 that has been widely described in numerous books since (see appendix A). He formulated the problem in terms of simple force and energy balances within the condensate film. The original analysis applied specifically to laminar flow of a condensing film on a vertical surface,



the following expression:

$$\alpha_o = 0.689 \left[ \frac{\rho_L(\rho_L - \rho_V)gh_{LV}\lambda_L^3}{\mu_L(T_{sat} - T_w)} \right]^{1/4} \left( \frac{1}{D_{eq}} \right)^{1/4} \quad (2.2)$$

where

$$\left( \frac{1}{D_{eq}} \right)^{1/4} = \frac{0.943}{0.725} \eta \frac{A_f}{A_{ef}} \cdot \frac{1}{\bar{L}^{1/4}} + \frac{A_f}{A_{ef}} \cdot \frac{1}{D_{or}^{1/4}} \quad (2.3)$$

and

$$\bar{L} = \pi \frac{D_o^2 - D_{or}^2}{4D_o} \quad (2.4)$$

In these equations,  $D_{eq}$  is the equivalent diameter of the finned tube,  $\eta$  is the fin efficiency,  $A_f$  is the actual fin area,  $A_t$  is the horizontal tube area,  $D_{or}$  is the root diameter, and  $D_o$  is the fin tip diameter. In their model the condensate flow is only driven by gravity, neglecting surface tension. Although Katz and Geist [10] reported data of liquid retention between the fins at the bottom of a horizontal tube under static conditions (without heat transfer), they concluded erroneously that this was not a good criterion for judging performance under condensing conditions.

Later studies recognized the importance of the effect of surface tension on condensation on enhanced surface tubes. Gregorig [2] was the first investigator who introduced the concept of surface tension drained condensate to enhance film condensation. His work addressed condensation on vertical fluted tubes. This surface tension drainage mechanism is basically the same as that for the fin profile illustrated in figure 2.2.

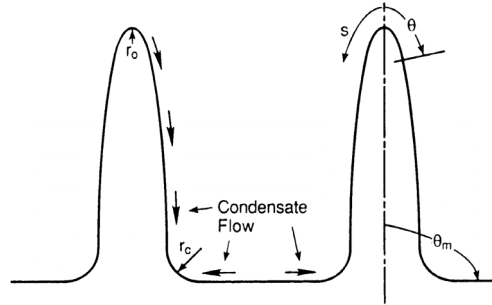


Figure 2.2: Surface tension drainage on a fin having small tip radius with increasing radius from fin tip [11] .

This profile has a small radius at the fin tip, and the local radius increases with increasing distance from the tip. For a constant vapor pressure, the pressure gradient in the liquid with a convex interface is

$$\text{convex interface: } \frac{dP}{ds} = \sigma \frac{d(1/r)}{ds} \quad (2.5)$$

where  $s$  is the distance coordinate along the liquid vapor-interface and  $r$  is its radius of curvature. According to equation 2.5, the liquid pressure will decrease with increasing distance from the fin tip because the local radius of the condensate increases. This means, the condensate formed on the fin is drained from the fin tip towards the fin base. The pressure gradient for a two-dimensional concave liquid film is

$$\text{concave interface: } \frac{dP}{ds} = -\sigma \frac{d(1/r)}{ds} \quad (2.6)$$

For a concave interface shape, the liquid pressure decreases in the direction of decreasing radius. The condensate in the interfin space ( $r = \infty$ ) is thus pulled into the corner. Similarly, condensate is pulled from the region near the fin base into the corner. The thermal resistance in film condensation is that of conduction across the condensate film and the local film thickness is determined by the force that drains the condensate. Thus, the local thinning of the film by surface tension on the sides of the fin can be used to increase the heat transfer performance.

Gregorig [2] described a profile shape that gives a constant film thickness. Zener and Lavi [12] defined a profile shape that gives constant pressure gradient. Adamek [13] defined a family of convex interface profiles that support surface tension drainage. The family includes both the Gregorig and the Zener and Lavi profile shapes.

After the Gregorig publication, one of the first analyses that recognized the importance of surface tension was made by Karkhu and Borovkov [14], who investigated theoretically and experimentally film condensation on trapezoidal shaped finned tubes.

Low integral fin tubes were introduced initially to increase surface area and as shown above it took a long time to understand the mechanism of surface tension drainage which enhances the heat transfer by reducing the film thickness much more than the simple increase in surface area. An adverse effect of surface tension is the condensate retention by capillary forces between the fin on the lower part of the tube as illustrated in figure 2.3.

Rudy and Webb [15] [16] developed an equation to predict the condensate retention angle on integral fin tubes based on their observations. Honda et al. [17] derived a similar expression for the retention angle  $\beta$ :

$$\beta = \pi c_b = \arccos \left( 1 - \frac{4\sigma \cos \phi}{\rho_L g s_t D_o} \right) \quad (2.7)$$

where  $\phi$  is the fin half tip angle and  $s_t$  is the fin spacing at the fin tip. This approximate expression is valid for cases with relatively small fin

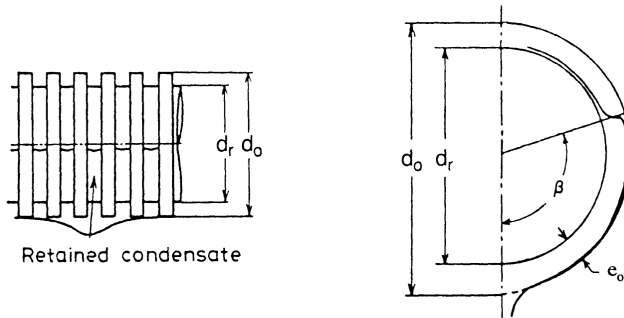


Figure 2.3: Condensate retention on integral-fin tubes [11] .

spacings, where the fin height is greater than  $s_t/2$ . For rectangular fins,  $\phi = 0$  the expressions of Honda et al. and Rudy and Webb give the same retention angle. In the flooded region, the thermal resistance is very high due to large thickness of the retained condensate; thus this region does little to contribute to heat transfer. Masuda and Rose [18] analysed in detail the liquid film retained by surface tension on horizontal low finned tubes.

From the above considerations, it is obvious that an accurate design method for condensation on a horizontal tube with an enhanced surface has to consider the effects of surface tension besides gravity force.

An early model including surface tension drainage and condensate retention was proposed by Webb et al. [19]. They divided the tube into an unflooded and a flooded zone; the unflooded zone was divided further into the fin area and the root area. The heat transfer was calculated in each zone and combined to give:

$$\alpha = (1 - c_b) \left( \alpha_h \frac{A_r}{A} + \alpha_f \eta_f \frac{A_f}{A} \right) + c_b \alpha_b \quad (2.8)$$

where  $c_b$  is the fraction of the tube circumference that is condensate flooded,  $A_r$  is the fin root area,  $A_f$  the fin surface area, and  $A$  the total area. The heat transfer on the fin root  $\alpha_h$  is calculated from the Nusselt equation. In order to determine the heat transfer coefficient on the fin  $\alpha_f$ , they approximated their fin geometry by an Adamek fin profile [13], involving an iterative determination of the fin shape parameter  $\zeta$ . They found, the second term in equation 2.8 to be negligible for most practical cases of interest. The predicted condensation coefficients using their model were within  $\pm 20\%$  for R-11 condensing on tubes having 748 to 1378 fpm.

Honda and Nozu [20] and Honda et al. [21] made a similar approach dividing the fin in several zones for which the heat transfer coefficient is determined. The latter of these two models is the most advanced analysis of condensation on a horizontal low-finned tube. They included the effects

of condensate flow and heat transfer on the fin root tube surface in the unflooded region of the tube, and the wall temperature variation between the fin root and the fin root tube surface. They also extended the expression for the flooding angle to include the case of relatively large fin spacings. Their model was in an agreement within  $\pm 20\%$  for experimental data covering 12 fluids and 31 tubes. This elaborate model of Honda and co-workers involves numerical calculations and is thus of little applicability potential in practical heat exchanger design.

Rose [22] proposed an equation for the heat transfer on low finned tubes based on simplified approximations and a dimensional analysis. He provided an expression for the enhancement ratio, defined as the ratio of the heat transfer coefficient for a finned tube to that for a plain tube, both based on the area at the fin root diameter and the same condensation temperature difference. The model combined the Nusselt approach for gravity drained condensation on a vertical plate and horizontal tube and included the effect of surface tension. Two constants of this semi-empirical model were determined by a comparison to measurements. The model is applicable to trapezoidal fins. A comparison to independent data gave an agreement of about  $\pm 20\%$ . For tubes where fin efficiency effects become significant, Briggs and Rose [23] developed an iterative calculation scheme.

Sreepathi et al. [24] proposed a generalized correlation to determine the heat transfer performance of horizontal integral-fin tubes. They also divided the fin tube into flooded and unflooded regions. The fin surface was further divided in three sub-regions. The effect of fin efficiency was taken into account by two temperature correction factors for the fin tip region and the fin flank region (the latter contains an error in their equation in [24]). They used 583 data points covering various fluids and fin geometries to determine nine constants in their correlation. The accuracy of their method is about  $\pm 20\%$ .

Besides the low finned tubes with a two-dimensional fin shapes, complex three dimensional ones are used to improve condensation heat transfer. Compared to the two-dimensional fin shapes, little work was done to model condensation on 3D enhanced surface geometries. These models were always adapted for one specific type of surface and lack of general applicability. For example, Belgahzi et al. [25] proposed a prediction method for the Gewa C+ tube, with notches on the fin flank. The heat transfer performance of the 3D enhanced surface structures has mainly been investigated experimentally without prediction methods proposed. In the literature, these are mostly performed as single tube tests, as a setup of a vertical array of tubes, or as bundles. For the current investigation, the experimental tests with multiple tubes are of major interest and will be discussed below.



## 2.2 Condensation on tube rows and bundles

Katz and Geist [10] were among the first to measure the row effect of integral fin tubes. Their work was done by condensing R-12 (Freon-12), n-butane, acetone and water on a vertical row of six horizontal tubes. The tubes were  $18.95\text{mm}$  in diameter and had 15 fpi (591 fpm) and a fin height of  $1.59\text{mm}$ . They observed that some of the condensate did not fall on the tubes below but splashed to the sides, owing to the motions imparted in draining from the fins. At low rates of condensation, the condensate fell from the tubes in drops, at high rates of condensation, continuous streams flowed from the tubes. Their experiments indicated that the decrease in condensing film coefficients with the number of tubes in a vertical row is much less for finned tubes than would be predicted by the application of Nusselt's theory. They found a row effect exponent  $m = -0.04$  for 16 fpi (630 fpm) integral fin tubes as opposed to  $m = -0.25$  by Nusselt from his plain tube theory. They also investigated the retention of liquids under static conditions and showed it to be a function of the ratio of the surface tension to the density of the liquid. Surprisingly, their conclusion was that the static liquid retention did not decrease the condensing coefficients under dynamic heat transfer conditions.

Between 1948 and 1980, little work was done to quantify and predict the row effect of enhanced tubes. Smirnov and Lukanov [26] studied condensation of R-11 on a bundle of finned tubes and Gogonin, Kabov, and Sosunov [27] condensed R-12 vapor on bundles of finned tubes. Regarding plain tubes, the following two articles are of interest for the current investigation.

Kutateladze, Gogonin and Sosunov [28] presented results of experiments on heat transfer in film condensation of R-12 and R-21 on a bank of horizontal plain tubes. They tested different arrangements of tubes with up to ten tubes in a vertical array. The tubes were 3, 6, 10, 16, and  $45\text{mm}$  in diameter. They found three distinct types of condensation by visual observation: drops, stream filaments and a continuous sheet with increasing heat flux. The influence of free-fall on heat transfer was studied on the banks of 6 and  $16\text{mm}$  tubes using different tube pitches ( $p/D = 2$  and  $p/D = 5$ ). An increase in condensate free-fall speed ( $\sqrt{2gz}$ ) by more than a factor of 2 resulted in an insignificant increase of heat transfer (only up to 20%). Interestingly, they placed thermocouples at various points below the tubes to determine the temperature of the condensate. They found that the subcooled condensate becomes quickly warmed up and arrived at the lower tube with a temperature close to the saturation temperature, testifying to intertube condensation on the falling liquid. Their measurements of heat transfer on different tube diameters showed that data for the 10, 16 and  $45\text{mm}$  tubes were nearly the same. On the 3 and  $6\text{mm}$  diameter tubes a pronounced intensification was observed. In their analysis, the heat transfer on the tube was split in a starting length with convective heat transfer

on the top where the condensate impinges at saturation temperature and a region where condensation occurs.

Honda, Uchima, Nozu, Nakata and Fujii [29] investigated experimentally film condensation of R-113 on in-line and staggered bundles of smooth tubes. The test sections were  $15 \times 3$  tube bundles. For the in-line tube arrangement,  $10 \times 3$  and  $20 \times 3$  bundles were also used to study the effect of bundle depth. They used inundation tubes to distribute liquid refrigerant on the bundle. The tubes were  $15.9\text{mm}$  in diameter and had a length of  $100\text{mm}$  (three pass,  $3 \times 100\text{mm}$ ). Both the horizontal and the vertical tube pitch were  $22\text{mm}$ . The wall temperature of the tubes was measured by resistance thermometry. The inlet vapor velocity was varied from  $2.1$  to  $20\text{m/s}$ , while the condensation temperature difference was varied from  $3$  to  $30\text{K}$ . At low vapor velocity, the condensate left the tube bottom in the form of droplets or condensate columns and impinged on the top of the lower tube. The sheet mode was not observed in this study. At high vapor velocity, the condensate leaving the tube disintegrated into small droplets and was distributed in the open space between the tubes as a mist. The condensate subcooling just after leaving the tube bottom was  $20$  to  $23\%$  of the condensation temperature difference. Empirical equations were derived for both the in-line and staggered tube bundles. These equations combined the effects of downward vapor velocity and condensate inundation and were found to correlate well most of the available experimental data for refrigerants and steam.

In the last twenty years, Honda and co-workers have published many studies about condensation of refrigerants on enhanced tube bundles. An overview of Honda and his co-worker's work in this field is given below followed by an review of other studies.

Honda, Nozu and Takeda [30] extended their theoretical model of film condensation on a single horizontal low finned tube to include the effect of condensate inundation. Based on the flow characteristics of condensate on a vertical column of horizontal low finned tubes, two major flow modes, the column mode and the sheet mode, were considered. In the column mode, the surface of the lower tubes was divided into the portion under the condensate column where the condensate flow is affected by the impinging condensate from the upper tubes, and the portion between the condensate columns where the condensate flow is not affected by the impinging condensate. In the sheet mode, the whole tube surface was assumed to be affected by the impinging condensate. For given conditions of vapor, tube bundle, and coolant, the heat transfer for each tube row was obtained by solving a set of simultaneous nonlinear equations describing the vapor to coolant heat transfer. Sample calculations for a set of practical conditions were made to study the effects of fin spacing and the number of vertical tube rows. In the case of R-12, the heat transfer coefficient was strongly influenced by the fin spacing and decreased sharply with increasing row number at small fin spacing. The optimum fin spacing increased with bundle depth. In their

example, the optimum fin spacing for the top tube was  $0.2\text{mm}$  whereas it was near  $0.3\text{mm}$  for a column of 15 tubes. In their calculations, they found a small increase in the heat transfer coefficient at the column mode to sheet mode transition. Their predicted value of the heat transfer coefficient for each tube row compared well with their experimental data, including four fluids and five tube bundles.

Honda, Uchima, Nakata, Nozu, and Torigoe [31] investigated experimentally film condensation of R-113 on in-line bundles of horizontal finned tubes with vapor downflow. The test sections were  $15 \times 3$  tube bundles with and without two rows of inundation at the top. Both the horizontal and vertical tube pitch were  $22\text{mm}$ . Six different tubes with diameter of  $15.6$  to  $16.1\text{mm}$  were tested. Tube A and tube B were low finned tubes with 26 fpi (1042 fpm) and 51 fpi (2000 fpm). The fin heights were  $1.43\text{mm}$  and  $1.3\text{mm}$ . Tube B was machined from a smooth tube. This tube had dimensions that were close to the optimum values obtained from their previous theoretical model [30]. The procedure for optimizing the fin dimensions was described in detail by Honda and Nozu [32]. Their optimum fin dimensions depended on the bundle depth, tube material, and conditions of vapor and coolant. Tubes C to F had three-dimensional fins with fin heights of  $0.99\text{mm}$ ,  $1.28\text{mm}$ ,  $1.01\text{mm}$ , and  $1.14\text{mm}$ . The wall temperatures of the tubes were measured by resistance thermometry. The experiments were performed at a saturation temperature of about  $50^\circ\text{C}$ . The vapor velocity at the tube bundle inlet was varied from  $3.3$  to  $18.9\text{m/s}$ . The condensate flow rate on the duct wall was collected and measured by using a measuring glass tube and a stop watch. The measured condensate retention angle for tube A and B was independent of the vapor velocity and agreed well with the theoretical predictions for a stagnant vapor (Honda et al. [17]). The flow modes of condensate for all tubes were basically the same at small condensate Reynolds numbers, but were considerably different at high Reynolds numbers. On the three-dimensional tubes, the condensate fell in a sheet in contrast to two-dimensional tubes where a complete sheet mode was not observed. This was also in contrast to a previous study for stagnant vapor (Honda et al. [33]) where condensate formed a complete sheet. Generation of small droplets due to vapor shear were more marked for the three-dimensional fin tubes. At low vapor velocity the measured values of the heat transfer coefficient for the two-dimensional fin tubes agreed well with their previous model for stagnant vapor. The heat transfer enhancement due to vapor shear for their finned tube bundle was much less than for a smooth bundle. The decrease in heat transfer coefficient due to condensate inundation was more marked for the three-dimensional fin tubes. Among the six tubes tested, the highest heat transfer performance was provided by tube B, with fin dimensions close to the theoretical values.

Honda, Uchima, Nozu, Torigoe, and Imai [34] continued this study using a staggered tube arrangement instead of the in-line arrangement. The

test conditions, the tubes, and the setup were the same as in the previous measurements, including the tube pitches, which were both  $22\text{mm}$ . The flooding level of the 2D-finned tubes agreed again well with their theoretical predictions for stagnant vapor. The observed flow patterns are basically the same as those for the in-line bundle mentioned above. However, at a low vapor velocity and a high condensate Reynolds numbers for the tubes with 3D-fins, the condensate flow pattern was the column mode. This is in contrast to the case of the in-line tube bundles where the observed flow pattern was the sheet mode. They ascribed this to the large difference in vertical tube spacing between the two tube bundles ( $6.2$  and  $28.2\text{mm}$  for the in-line and staggered tube bundles, respectively). The 2D-fin tubes showed a very slow decrease in the heat transfer coefficient with increasing condensate inundation rate. The heat transfer performance of the in-line and staggered tube bundles were virtually the same at a low vapor velocity, but the latter showed a higher performance at high vapor velocity. The 3D-fin tubes showed a faster decrease in the heat transfer coefficient with increasing condensate inundation rate. The decrease was more marked for the in-line tube bundles and for a lower vapor velocity. The measured heat transfer coefficient for the 2D-fin tubes agreed well with their theoretical prediction at low values of vapor velocity and condensate inundation rate. Among the in-line and staggered bundles of the six tubes tested, the highest performance was provided by the staggered bundle of the 2D-fin tube with fin dimensions close to the theoretically determined optimum values.

Honda, Takamatsu and Kim [35] next carried out theoretical and experimental studies on the effect of fin geometry on four different two-dimensional low finned tubes for condensing of R-11 and R-123 on tube bundles using their 3-tube wide by 15-tube row deep in-line bundle. All tubes had a nominal diameter of  $15.9\text{mm}$  and were installed at the same time at different locations in the bundle. Tubes A and B were commercial trapezoidal-shape fin tubes of 26.5 and 48.8fpi (1042 and 1923 fpm) with fin heights of 1.43 and 1.09mm. Tubes C and D, which were produced by an electric discharge machining process, had fin shapes close to the best performing profile in their theoretical analysis [35]. These tubes had 50.8 fpi (2000 fpm) fins of 1.41 and 1.39mm height with thinner average thicknesses and small tip radii. The saturation temperature was maintained within the range of 47.1 to 52.2°C. The vapor inlet velocities were varied from 0.9 to 9.8m/s. For all tubes, the measured flooding level between the fins agreed well with the theoretical prediction of stagnant vapor [17]. For R-123 condensation on the conventional 26 fpi tube, the heat transfer coefficient was about 10% lower than that for R-11. Heat transfer enhancement due to vapor shear was much less for the finned tube than for a smooth tube. The enhancement was most significant for the top row and it decreased sharply with increasing the row number. For both the conventional and newly developed 2D-finned tubes, the theoretical predictions agreed well with the experimental data at low

vapor velocity and low to medium condensate inundation. Among the four kinds of tubes tested, the highest heat transfer performance (about 85% higher than that for the 26 fpi tube at a low vapor velocity) was obtained with tube C. This newly proposed fin shape had a monotonically increasing radius of curvature near the fin tip and a constant thickness near the fin root. The performance of this tube was also higher than the the best performing tube of the previous study having rectangular fins and dimensions close to tube C [31].

Honda and Kim [36] extended their previous theoretical analysis fin geometry effect on condensation performance of R-123 condensing on in-line tube bundles of two-dimensional low finned tubes. They performed a parametric study of the effects of fin shape, fin dimensions and bundle depth on the overall heat transfer coefficient. The results showed that their newly proposed finned tube provided a considerably higher performance than the rectangular fin tube. The difference between the two tubes was more significant when coolant side heat transfer was enhanced, showing that the condensation side enhancement must be accompanied by the coolant side enhancement to obtain a high overall heat transfer coefficient. For the newly proposed finned tube, the effect of fin thickness was relatively small. Both the optimum fin height and optimum fin spacing increased with increasing the vertical bundle depth. For their operating conditions and a bundle depth of 30, the newly proposed finned tube with optimized fin geometry provided an enhancement in the mean overall heat transfer coefficient of a factor 5.8 over the smooth tube.

Honda, Takamatsu, Takada, and Yamasaki [37] presented heat transfer data of R-134a condensing in a staggered bundle of low-finned tubes. The test tube was the standard 26 fpi tube which they had used in earlier studies. The refrigerant vapor inlet velocity ranged from 0.6 to 3.3m/s (mass velocity 8.7 to 44kg/m<sup>2</sup>s). A comparison was made with the previous results of R-123 (mass velocity 9.5 to 33kg/m<sup>2</sup>s)[38]. The effect of mass velocity for R-134a was less significant than in the case of R-123, mainly due to the large difference in the vapor density, which results in a higher vapor shear effect for R-123. There was a minor falloff with tube row at the lowest inlet velocity, which was more pronounced at high vapor velocities. The effect of the vapor velocity was less evident on the lower tubes; in fact, most of vapor effect was felt only by the first tube row. The heat transfer enhancement as compared to the smooth tube bundle decreased with increasing vapor velocity. At a low vapor velocity, the heat transfer coefficient for R-134a was about 17% higher than for R-123, and the experimental data compared well with the theoretical prediction for a stagnant vapor.

Honda, Takamatsu and Takada [39] measured heat transfer data during condensation of R-123 in staggered bundles of two-dimensional fins. Following their previous study for in-line tube bundles [35], they tested their four kinds of two-dimensional fins and compared them with the previous results.

The inlet vapor velocity was varied in the range of 1.9 to 7.6m/s. No difference in condensate flow patterns was observed for the four tubes. The falling modes of condensate were also basically the same for the staggered and the in-line bundle. However, at a high condensate inundation rate the width of condensate column impinging on the lower tube was smaller for the staggered bundle due the larger distance in the staggered tube arrangement. The effect of vapor velocity was most significant for tube A (commonly used 26 fpi tube). It was somewhat higher for the staggered tube bundle. The effect of condensate inundation on the heat transfer coefficient was more significant for the in-line tube bundles than for the staggered tube bundle. The highest heat transfer performance was provided by the staggered bundle of tube C (one of the newly developed finned tubes). They thus found more of an adverse effect of the in-line arrangement than on the staggered arrangement since some condensate in the staggered skips the two out of line tubes below it and goes directly to the next tube below, and the condensate flows with a higher velocity and smaller column diameter because of the larger intertube spacing.

Honda, Takata, Takamatsu, Kim and Usami [40] presented results showing the effect of fin geometry on condensation of R-134a in a staggered bundle of finned tubes. Two types of conventional low-fin tubes (A,B) and three types of three-dimensional fin tubes were tested (C,D,E). All tubes were commercially available. The test section was like in the previous studies a  $15 \times 3$  staggered bundle. But the tubes had diameters of about 19mm (3/4 in.) and were larger than their previous tubes with diameters of 15.9mm (5/8 in.). The horizontal and vertical tube pitches were increased to 26 and 25mm, respectively. The experimental apparatus and procedures were the same as before. Tubes A and B had 26.5 fpi (1042 fpm) and 19.5 fpi (769 fpm) with fin heights of 1.38 and 1.29mm, respectively. Tube C had pyramid shape fins (1409 fpm). Tube D had saw-tooth shape fins. Tube E had a three-dimensional structure at the fin tip that was produced by secondary machining of low-fins. The fin heights of the three-dimensional finned tubes were 0.87, 0.95, and 1.11mm. Experiments were conducted by using two kind of test sections. One test section consisted of all types of test tubes and the other of tube A only. The vapor temperature was about 40°C. The refrigerant mass velocity  $G$  was changed in three steps (8,18 and 23kg/m<sup>2</sup>s). The condensation temperature difference was changed in five steps (1.5, 3, 5, 8 and 12K.) The effect of condensate inundation rate on the heat transfer performance of the test tubes was studied by changing the number of upper tube rows through which the cooling water was passed. The three-dimensional fin tubes showed a higher heat transfer coefficient than the low-fin tubes when the condensate inundation was small. However, the three-dimensional fin tubes were subjected to a higher adverse effect of condensate inundation. The decrease was most significant for tube C with pyramid-shape fins. On the other hand, the low-fin tubes were not

affected so much by the condensate inundation. The effect of the mass velocity  $G$  was generally small. For the low-fin tubes, the heat transfer coefficient increased slightly as  $G$  increased. For the three-dimensional fin tubes, the heat transfer coefficient decreased as  $G$  increased. For all tubes the heat transfer coefficient decreased as the condensation temperature difference increased as would be expected from the thicker condensate film. At low  $G$  and small condensate Reynolds numbers, tube E with three-dimensional structure showed the highest performance. For large  $G$  and condensate Reynolds numbers, the low-fin tube A showed the highest performance.

Webb and Murawski [11] studied the row effect on enhanced tubes on a vertical bank of five tubes using R-11. They tested five tube geometries: a low finned tube, a Y-finned tube (Gewa-SC), two tubes with saw-tooth fin shape (Turbo-C and Tred-D), and a modified Turbo-C with a nylon cord wrapped in every third groove. All tubes had 26 fpi (1024 fpm), except the Turbo C, which had 40 fpi (1575 fpm). The tubes were 18.9mm in diameter with fin heights of 1.3mm, 1.1mm, 1.25mm, and 1.3mm. The length of the tubes was 305mm. Thermocouples were installed on the external surface of tubes at the top, side, and bottom of the tubes in rows 1, 3, and 5 to obtain the average wall temperature. The in-line tubes had a relatively large tube pitch of 44.5mm (1.75 in.). The tests were run at a saturation temperature of 37.8°C. The highest single-tube performance was provided by Turbo-C, followed by the Gewa-SC and the Tred-D. The standard 26 fpi tube had the lowest performance which was 60% of the Turbo-C. Plotting their data for all tube rows versus the film Reynolds number they found that the average heat transfer coefficients fell on a single curve, because it depended only on  $Re$ , and not on tube rows. They proposed curve fits in the form of  $\alpha_{mean} = a Re^{-n}$ . The 26 fpi tube showed no row effect ( $n = 0.00$ ). The greatest row effect was displayed by the Tred-D ( $n = 0.58$ ), followed by the Turbo-C ( $n=0.51$ ), and the Gewa-SC ( $n = 0.22$ ). Their attempt to improve the row effect of the Turbo-C tube using a nylon wrap decreased the row effect relative to the original Turbo-C only 10%, and the single-tube performance also dropped. They gave a detailed description of the observed condensate drainage pattern including a map for the flow mode transitions for all tubes. They speculated that the absence of a row effect for the 26 fpi tube resulted because the continuous fins acted as dams, which prevented axial spreading of the condensate. The authors also concluded that the Turbo-C showed a high row effect because of the flow pattern of condensate on the tube. The geometry impeded circumferential condensate flow, allowed spreading, and did not establish any axial regions that were clear of condensate.

Memory, Mazzone, and Marto [41] performed measurements using R-113 on a vertical in-line column of four tubes with a centreline to centreline spacing of 36mm. The tubes had nominal diameter of 15.9mm and a condensing length of 1220mm. Plain tubes, single roped tubes and wire-wrapped roped

tubes with three different wire diameters were tested. A single roped tube gave an enhancement in the heat transfer coefficient of 25%. This decreased to 20% for a bundle of four tubes due to condensate inundation. Wrapping a wire in the grooves of the roped tubes significantly reduced inundation effects. A wire diameter of  $1.24\text{mm}$  gave the maximum enhancement of 60% for a single wire-wrapped tube, rising to 68% for the bundle of four tubes. The smooth and roped bundle data lie between the equations of Kern and Eissenberg [42], the former lying above the latter, indicating that the inundation affected the roped bundle more than the smooth bundle. The wire-wrapped roped tube bundle showed less effect of inundation. The data for these tubes were close to the equation of Eissenberg.

Chu and McNaught [43] measured condensate heat transfer coefficients during down flow over a test section consisting of a  $12 \times 5$  staggered tube bundle. The length of the tubes was  $330\text{mm}$ ; the tube pitches were  $24\text{mm}$  horizontal and  $21\text{mm}$  vertical. Only a horizontal row of five tubes in the lower part of the bundle was active (9th row). The test series covered three tube types: a plain tube with a diameter of  $19.05\text{mm}$  and low finned tubes with 748 fpm (19 fpi) and 1406 fpm (36 fpi). The finned tubes were  $19.0\text{mm}$  and  $18.9\text{mm}$  in diameter with a fin height of  $1.6\text{mm}$  and  $0.95\text{mm}$  respectively. Data were collected for R-113 condensing at 74 to  $235\text{kPa}$  (40 to  $75^\circ\text{C}$ ) with liquid overfeed from 0.08 to  $0.96\text{kg/s}$  and vapor velocities up to  $11\text{m/s}$ . Condensate inundation on low finned tube bundles produced a steady and moderate reduction in the condensation heat transfer coefficient. With plain tubes, there was initially a greater reduction in coefficient, but subsequently the coefficient began to increase with increasing inundation as the film became turbulent. The vapor shear effect on low finned tube heat transfer appeared moderate compared to that of plain tubes. They found a heat transfer enhancement for the low finned tubes of 2 to 12 times, decreasing with increasing vapor velocities, as the performance of the plain tube bundle increased with increasing vapor velocity.

McNaught and Chu [44] ran more experiments with two more fin densities. They tested 448 fpm (11 fpi) tubes and 1058 fpm (27 fpi) tubes from Wieland. The diameters of these two tubes were  $19.14$  and  $18.90\text{mm}$  and the fin heights  $1.57$  and  $1.45\text{mm}$ . The experimental setup and test conditions were the same as in previous tests (Chu and McNaught [43]) except for the tube layout for the 27 fpi tubes. These tubes were tested in an in-line bundle with a horizontal and vertical tube pitch of  $24\text{mm}$ . They confirmed the previous results that the effect of vapor velocities on condensation heat transfer on low-finned tube bundles were weak for all fin geometries. The condensate inundation on their low-finned tube bundles produced a steady and moderate reduction in the condensate heat transfer coefficient. They did not find a particular trend of the inundation effect with fin geometry.

Chu and McNaught [45] compared their database of the four low-finned tubes with the method developed by Rose [22] for a single tube. They found



good agreement at low vapor velocity with no inundation. They extended this method for the single tube heat transfer coefficient on low finned to tube bundles adding the effect of condensate inundation and vapor shear. Their model correlates their measurements of the heat transfer coefficient for three of the finned tube bundles (11 fpi, 19 fpi, 27 fpi) within a standard deviation of 10% and underpredicted the 36 fpi tube by 30%.

Huber, Rewerts, and Pate [46], [47], and [48] presented data for condensation of refrigerant R-134a on a small tube bundle in a three part publication. The bundles tested are five rows wide by five rows deep and have a staggered arrangement with a horizontal pitch of  $22.2\text{mm}$  (7/8 in.) and a vertical pitch of  $19.1\text{mm}$  (3/4 in.). The tubes had a nominal diameter of  $19.1\text{mm}$  and a length of  $603\text{mm}$ . Tests were conducted at a saturation temperature of  $35^\circ\text{C}$  over a bundle heat flux range from  $18\text{kW}/\text{m}^2$  to  $40\text{kW}/\text{m}^2$ . A modified Wilson plot approach was used and the measurements were accurately made, including degassing of the refrigerant. Average condensing heat transfer coefficients for the bundle as well as average condensing heat transfer coefficients for the middle tube of each row were calculated. Data were given in tabular form.

In the first part, 26 fpi (1024 fpm) and 40 fpi (1575 fpm) tubes were tested. The 40 fpi had a fin height of  $0.86\text{mm}$  versus the  $1.45\text{mm}$  fin height of the 26 fpi. They measured a 15% increase in the average bundle heat transfer coefficient for the 40 fpi over the 26 fpi. In their opinion, the improved performance may be due to the shorter fins, which allowed the condensate droplets to move axially along the tube. The shorter fins may also have less capillary action than the high fins of the 26 fpi, thus allowing the 40 fpi to drain better. The row-to-row heat transfer coefficient behaviors of the 26 fpi and 40 fpi bundles were significantly different.

In the second part, two different enhanced tube geometries were tested: Turbo-CII tubes from Wolverine and Gewa-SC tubes from Wieland. The Turbo-CII had short fins that have been roughened by mechanical working, while the Gewa-SC was characterized by long, Y-shaped fins (26 fpi). The fin heights were  $0.91\text{mm}$  and  $1.06\text{mm}$ , respectively. The Turbo-CII performed significantly better than the Gewa-SC. The row-to-row heat transfer coefficient behavior also differed between the two tube bundles. The decrease of the average bundle heat transfer coefficient was significantly more pronounced for the Turbo-CII. For this tube, the average bundle heat transfer coefficients of almost  $60\text{kW}/\text{m}^2\text{K}$  were reported at low heat flux with an uncertainty over 30%. The Turbo C-II also performed better than the 40 fpi and the 26 fpi tubes, while the Gewa-SC only performed better than the 26 fpi tube.

In part III, a comparison was made with condensation of R-12. The data showed that R-134a performed better than R-12 on all four tube geometries.

Rewerts, Huber and Pate [49] studied the effect of R-134a inundation on enhanced tube geometries. The test bundle consisted of five instrumented

tubes in a five-row test bundle surrounded by inactive tubes in the staggered tube arrangement mentioned above. They simulated the effect of condensate inundation up to a depth of 30 rows by introducing a two-phase refrigerant mixture into the test section. The four tubes tested were the same as in the previous study. The Turbo-CII enhanced geometry performed more than twice as well as the other geometries at low inundation levels. At high inundation rates its performance fell to be within 10% of the other geometries. In terms of row effect behavior, the 26 fpi tube showed the best performance with negligible inundation effects through the full range of condensate flow rates tested. The Turbo-CII and the 40 fpi tube were characterized by a change in heat transfer above a certain film Reynolds number. Because the condensation took place on the center of each row, it was not possible to observe the flow patterns. Judging from the flow patterns leaving the bottom row of tubes, they believed that the change in heat transfer behavior corresponds to the point where the shorter fins of these tubes become completely flooded along the bottom surface of the tubes and the liquid begins to move axially. They supposed this to be the transition between column and sheet mode of condensate flow. They correlated each range using an equation of the form  $\alpha_o = a Re^{-n}$ . The ranges were separated by a unique critical Reynolds number for each tube.

Rewerts, Huber and Pate [50] continued the study above testing the effect of R-123 condensate inundation and vapor shear with the same experimental setup. Simulations of the effect of inundation up to a depth of 25 rows were presented at three different vapor velocities. The effect of inundation was found to dominate over the effect of vapor shear for all geometries over the ranges of inundation rate and vapor velocity. The results with R-123 were similar to one of the tests with R-134a, except that the 26 fpi tube showed an additional change in heat transfer behavior above a critical film Reynolds number, like the 40 fpi tube and the Turbo-CII tube. They attributed this fact of this two-region behavior not being observed with the 26 fpi tube when inundating with R-134a to the higher viscosity and surface tension of R-123, which tends to hold the liquid in the fins longer and allows the condensate film to build up to the point that axial movement becomes possible. The transition between the two regions occurred at much lower condensate Reynolds numbers for the 40 fpi tube than it does for the 26 fpi tube. They assumed that this was due to the 40 fpi tube's shorter fins and tighter fin spacing, which allows flooding of the fins to occur sooner than with the 26 fpi tube. The data were quantified like in the previous study.

Rewerts, Huber and Pate [51] investigated the effect of noncondensing gas on the condensation of R-123 for bundles of four enhanced tube geometries: a 26 fpi tube, a 40 fpi tube, and two enhanced tubes the Turbo-CII and the Gewa-SC, all with a nominal diameter of  $19.1\text{mm}$ . The test bundles were five columns wide by five rows deep in a staggered tube arrangement with a  $22.2\text{mm}$  horizontal and a  $19.1\text{mm}$  vertical pitch, and a tube length of

603mm. The data were obtained at a saturation temperature of  $35^{\circ}C$  with concentrations of 0.5%, 1.0%, 2.0%, and 5.0% nitrogen by volume. Four heat fluxes were tested between  $18kW/m^2$  to  $34kW/m^2$ . A modified Wilson plot approach was used to reduce the data. The Turbo-CII performed best at noncondensing gas concentrations up to 5%, followed by the 40 fpi tube, the Gewa-SC, and the 26 fpi tube. The Turbo-CII was also found to be the most susceptible to small gas concentrations (0.5%), with decreases in average bundle heat transfer coefficients of 50% at the lowest heat flux and 35% at the highest heat flux. The drop in performance for the 26 fpi tube was much smaller, suggesting that the relatively large fin spaces and large fin heights prevented the noncondensing gas layer from completely covering the condensation surface of the tube and allowed shearing effects to keep the gas layer around each tube relatively small. Row-by-row data showed that noncondensing gases work to smooth out individual row performance. High concentrations brought also the performances of all bundles to be within 13% of each other (while they did not note why, this is because the mass transfer resistance in the vapor becomes dominant).

Nguyen and Orozco [52] investigated the effect of row spacing between horizontal tubes on the average condensation heat transfer coefficient. They performed tests with R-123 condensing on two plain tubes and three enhanced tubes (Gewa-SC, Gewa-TW, and Gewa-TWX of Wieland) The tubes ranged from 12.6 to 15.9mm in diameter and had a length of 88.9mm. Four tubes of every type were arranged in a vertical row in a clear acrylic test section. The wall temperatures of the tubes were measured with thermocouples installed on the internal surface of each tube. Increasing the water flow rate in the tubes with constant temperature increased the heat transfer coefficient. At a high water flow rate, the condensate drained as liquid columns from the lower tubes. They explained that a continuous stream of condensate, instead of drops, makes it easy for gravitational effects to overcome surface tension effects. A faster removal of the condensate liquid from the tube made the thickness of condensate thinner and thus increased the heat transfer process. For lower water inlet temperatures they observed a lower heat transfer coefficient, as condensate film is thicker. Their experimental data for the plain tubes were lower than Nusselt's theoretical prediction. For smaller tube spacings the coefficient increased and was in good agreement with Nusselt's theory as for this case the condensate flow pattern consisted of a continuous layer of condensate which matches Nusselt's assumption. The analysis by Rudy and Webb adequately predicted (within 30%) their experimental data, while the formulation of Beatty and Katz grossly underpredicted by a factor 2.

Cheng and Wang [53] conducted experiments on six tubes arranged in two rows, located side-by-side with three tubes one above the other in each row, set in stationary vapor. Seven kinds of tubes were tested including three low finned tubes (26 fpi, 32 fpi, and 41 fpi), three 3D-fin tubes, and a plain

tube. For the low finned tubes, the fin heights were 1.3, 1.01 and 1.42 $mm$ . The tube were 18.26 to 20.75 $mm$  in diameter with a vertical tube pitch of 30 $mm$  and horizontal pitch of 50 $mm$ . The length of the tubes was 1220 $mm$ . R-134a was used as working fluid at 963 $kPa$ . Average condensing heat transfer coefficients were obtained from the modified Wilson plot technique. The Beatty and Katz model underpredicted the data by as much as 54%. As this model was based on experimental data for low surface tension fluids with tubes of low fin density, the application to high fin densities was questionable in their opinion. The row effect penalty for the plain tube was lower than Nusselt's prediction and higher than Kern's. The row effect on heat transfer coefficient was negligible for integral fin tubes in the range of this study. The row effect was more pronounced for 3D-fin tubes than for low fin tubes. Neither the heat flux nor the temperature difference was cited for these results.

Kulis, Compingt, Mercier, and Rivier [54] presented experimental data for R-134a and R-12 condensing on a staggered bundle of 19 finned tubes with 3 columns and 13 rows, of which 12 tubes were active. The length of the tubes was 300 $mm$ . No specific information about the two tube geometries, a trapezoidal and a Y finned tube, nor the saturation temperature were given. The tests were conducted over temperature differences of 1 to 10 $K$  resulting in heat fluxes from 20 to 100 $kW/m^2$ . The Beatty and Katz model was very close to the data for the trapezoidal finned tube (within  $\pm 7\%$ ). For the Y finned tubes, this model underpredicted, the data by about 10%. A tube row effect depending on tube geometry an heat flux was observed. The higher the heat flux, the smaller was the adverse tube row effect. The Eissenberg tube row effect matched best their data. For both types of tubes, the condensing performance of R-134a was 10% lower than these of R-22. A design method based on a finite volume method was described roughly.

## 2.3 Conclusion

Three principal mechanisms governing condensation on a single enhanced horizontal tube are: gravity driven condensate flow in the root area between fins, surface tension controlled condensation drainage on the sides of the fins and condensate retention on the lower part of the tube by capillary forces. Condensation on a single low finned tube has been treated in the literature by analytical and semi-empirical approaches and experimental tests, while comparably little work has been done for modelling condensation on 3D enhanced surfaces.

On an array of horizontal tubes or a tube bundle, additionally, the effect of condensate inundation from upper tubes has to be taken into account (apart from vapor shear effects which are not considered in the present investigation). The effect of condensate inundation is not only determined

by the amount of liquid falling from the tube above, but also by flow pattern, how the liquid falls onto the tube and how it spreads on the tube. Heat transfer on arrays of low-finned and 3D enhanced tubes has mainly been investigated experimentally. In experimental studies without condensate inundation, the tubes with 3D enhanced surface structures outperformed the low finned tubes, while the deterioration in heat transfer with inundation was found to be less pronounced for the low finned tubes. This difference in behavior was often attributed to differences in flow pattern on the low finned and 3D enhanced tubes. However, in many investigations, there was little visual access to observe the condensate flow, especially during bundle tests.

For this reason, the aim of the current investigation is to study condensation on an array of horizontal tubes in a test facility offering complete visual access to observe the condensation process. Tests will be performed with refrigerant R-134a, for which little data is available in literature, as it is a relatively new refrigerant but widely used. Secondly, modern heat exchanger design software uses a completely incremental design approach, dividing the heat exchanger up into a multitude of small zones and calculating local heat transfer performance in each of these zones. In contrast, up until now, all condensation data have been obtained as mean values along the tube length (not withstanding the varying axial conditions), which are not optimal for developing local design methods. Hence, since local data are really needed to progress further in this research area, here a temperature profile approach already used successfully for intube boiling and bundle boiling in the LTCM laboratory will be applied for the first time to shell-side condensation (to our knowledge) to obtain true local heat transfer coefficients. These results will then be used to compare to the prior methods and to propose new ones.



## Chapter 3

# Experimental Setup

In this chapter, the falling film heat transfer test facility built specifically for this project is described. An overview is first given, then the three different liquid circuits (refrigerant, water and ethylene-glycol) are detailed with their components. A focus on the test section follows. The operational control of the test facility by computer is then described with a special focus on the instrumentation accuracy. Finally, the operating procedures are discussed. The conception, design and supervision of the construction has been made in collaboration with Jean-François Roques (of the LTCM laboratory at the EPFL), who is working on falling film evaporation using the same test facility.

### 3.1 Overview

The aim of this study is to measure local external heat transfer coefficients during condensation on a vertical array of horizontal tubes. The test facility recreates various operating conditions of a falling film condenser but without the effect of vapor shear nor neighboring rows of tubes. This test facility is completely new, designed especially for this study. Its capabilities are: one vertical array of horizontal tubes of  $19.05\text{mm}$  ( $3/4$  in.) outer diameter. Depending on the tube spacing, six to ten tubes can be tested simultaneously. The length of the tubes tested is  $554\text{mm}$ . The heat flux on the surface of the tubes can be varied from  $10$  to  $100\text{kW}/\text{m}^2$  by adjusting the temperature difference between the refrigerant vapor on the outside of the tubes and temperature of the water flowing inside the tubes. The test section is equipped with a liquid overfeed system to investigate the effect of condensate inundation. The test section has six large windows ( $120 \times 250\text{mm}$ ) for visualization during falling film condensation. The falling film test facility can be operated in condensation or evaporation test mode. In the following, a description of the condensation test mode is given; for the evaporation test mode, refer to Roques [55]. The test facility consists basically of nat-

ural circulation loop for refrigerant R-134a and a forced circulation loop for the cooling water. The complete test facility is depicted in figure 3.1. In order to avoid pump vibrations and simplify the construction, the test facility is divided in two units: The main unit with the refrigerant circuit including the evaporator, the test section, and the auxiliary condenser and the auxiliary unit with the pumps and heat exchangers for conditioning the water for the test section and the glycol for the auxiliary condenser.

In the following subsections, detailed descriptions of the refrigerant circuit, the cooling water circuit, and the glycol circuit of the auxiliary condenser are given.

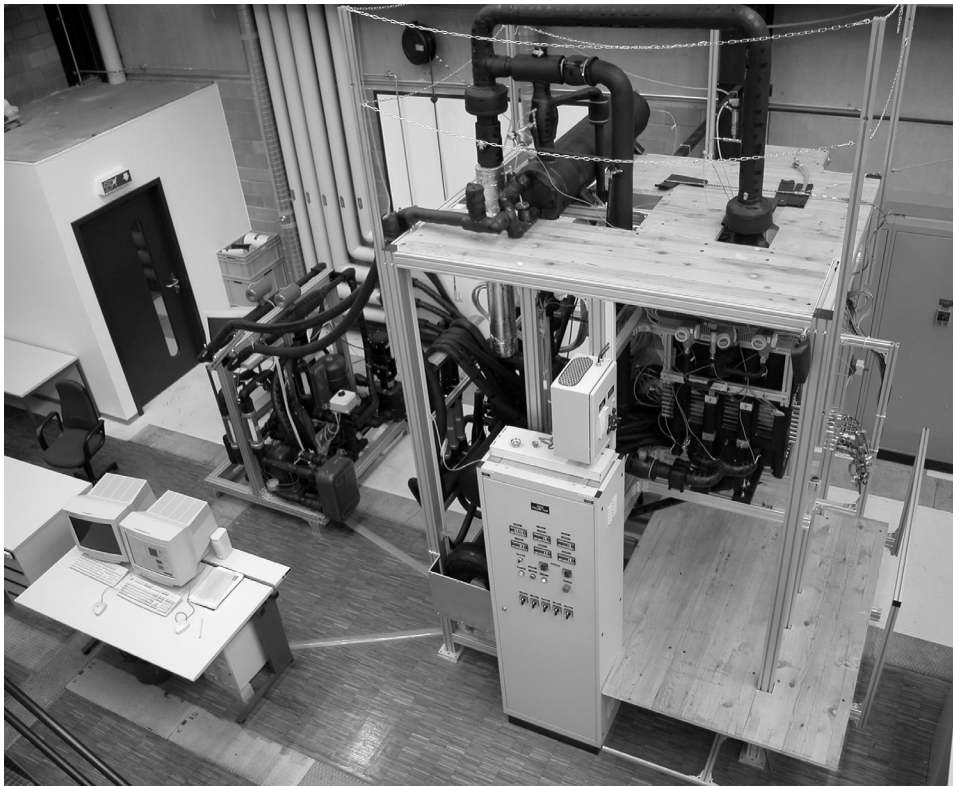


Figure 3.1: Overall view of the falling film test facility. Main unit on the right and auxiliary unit on the left.

## 3.2 Refrigerant circuit

The refrigerant circuit is the main circuit of the test facility. It basically comprises an electrically heated evaporator to maintain the desired saturation condition, an auxiliary condenser to create a vapor flow in the test



section and the test section itself. As the test facility is designed for multiple purposes, various pipe connections were made between these three basic elements. The operating mode can be chosen by opening and closing the valves in the circuit to set the path for the vapor and liquid flows. A detailed schematic diagram containing all piping in the refrigerant circuit is shown in figure 3.2.

In the present investigation, the capability of the test facility was only partially used. How the vapor and liquid refrigerant loop were used in the present study is described below.

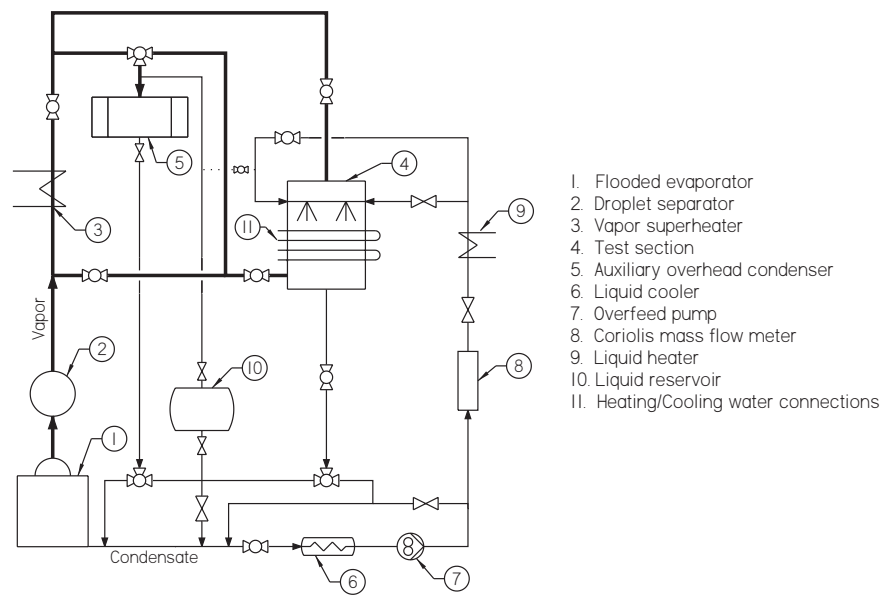


Figure 3.2: Detailed schematic of the refrigerant circuit with all piping.

### 3.2.1 Vapor refrigerant circuit

The circuit of the vapor refrigerant is a natural circulation loop. The refrigerant is evaporated in the lower part of the loop and condensate is formed in the upper parts. The liquid flows back from the test section and the auxiliary condenser to the evaporator by gravity. A height of  $2m$  between the auxiliary condenser and the evaporator insures a maximum driving pressure difference of about  $23kPa$  with refrigerant R-134a at  $304K$ .

The vapor refrigerant circuit as it was used in the present study is illustrated in the simplified schematic in figure 3.3. Refrigerant vapor is gen-

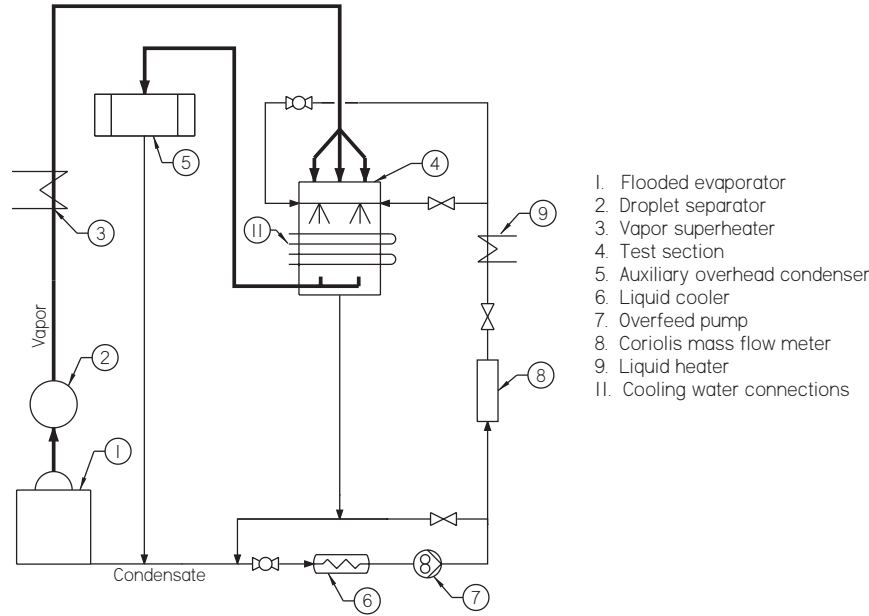


Figure 3.3: Simplified schematic of the refrigerant circuit showing only the tubing used in present study.

erated in the flooded evaporator with immersion heating elements that can provide a heating capacity of  $60kW$  (1). The saturated vapor leaving the evaporator passes through the droplet separator (2). This is large volume vessel slows down the vapor flow such that the low velocity allows droplets entrained from the evaporator to settle out and return back to the evaporator. This ensures that the vapor does not contain droplets. After leaving the droplet separator, the vapor passes into the superheater, which is a  $1.1m$  long section copper pipe wrapped with electrical heat tape (3). The heating capacity of the vapor superheater is  $1kW$ . It was only used at low power to compensate for heat losses to the environment and it was adjusted so that the vapor arrives a little superheated at the test section. The vapor enters the test section through three large inlets at the top in order to distribute it evenly within the test section (4). In the test section, the vapor is partially condensed on the tubes. The excess vapor leaves the test section in the lower part through four outlets (two on the front side and two at the back side). Then the vapor goes to the auxiliary condenser, where it is condensed completely (5). The condensate formed in the test section and in the auxiliary condenser drains back to the evaporator by gravity.

In this configuration, the vapor flows downward in the test section which is the typical situation encountered in a condenser. The test facility also offers the possibility to study the effect of upward vapor flow in the test section. By changing the vapor valve positions, the above described situation can be inverted: The three upper vapor pipes of the test section are connected to the auxiliary condenser and the four lower ones to the evaporator (figure 3.2). However, this capability was not used in the present investigation. The vapor flow was always directed downward in the test section and minimized to reduce the vapor flow rate to levels that do not induce shear effects on the condensate.

### 3.2.2 Liquid refrigerant circuit

In order to study the effect of liquid inundation on the performance of the tubes, the test section is equipped with a liquid overfeed capability. In this way not only the behavior of the top ten tube rows in a condenser can be investigated, but also the situation on lower tube rows in large condensers can be simulated.

The liquid refrigerant loop is depicted in figure 3.3 (thin lines). During operating, most of the liquid is in the evaporator which acts as a liquid reserve in the circuit (1). All liquid tends to drain to the evaporator. Starting the description from the evaporator, the refrigerant flows through the filter and the subcooler (6) to the magnetically driven gear pump (7). The filter removes eventual particles from the liquid refrigerant and contains also a refrigerant drying cartridge. The subcooler is a heat exchanger connected to an external thermal temperature controlled bath. It is thus possible to control the subcooling of the liquid refrigerant before the pump to avoid cavitation. However, as during condensation measurements the saturation temperature was above room temperature, the heat loss to environment and the static head of liquid in front of the pump were sufficient to avoid cavitation. Therefore the liquid subcooler was not used during the measurements. Parallel to the pump, bypass piping together with a frequency controller are also installed to achieve the desired liquid flow rate. For very low flow rates, the bypass is opened rather than going to very small frequencies with the gear pump, which would give an oscillating flow rate. After the pump a vibration absorber is installed, to reduce propagation of vibrations from the pump. The liquid refrigerant then passes through a Coriolis mass flow meter (8) to the liquid heater (9). The liquid heater consists of two electric heating elements in series wrapped tightly around the copper pipe with a heating capacity of 500W each. The liquid heater is used to bring the refrigerant close to the saturation conditions. The liquid refrigerant enters the test section through one inlet on the left and one inlet on the right. Both inlets are equipped with valves to control the distribution in the test section. Special care has been taken to achieve uniform distribution of the

liquid onto the test tubes. The liquid distributor designed for this purpose is detailed below in section 3.5. Once the liquid leaves the distributor, it falls on the top of the cooled tubes. Including the condensate formed on the tubes, all liquid refrigerant leaves the test section by gravity and flows back to the evaporator.

### 3.3 Water circuit

The cooling water flowing inside the test tubes is heated up in the test section and cooled back down in the auxiliary unit. This forced-circulation loop for the cooling water is illustrated in figure 3.4.

The circuit is equipped with a centrifugal pump (1). An electronic speed controller together with a bypass and a valve affords a good precision in the mass flow adjustment. After the pump, the water goes into the first liquid-liquid heat exchanger (2). In this heat exchanger, the test section water exchanges heat with industrial water (9). This is water from Lake Geneva, available in the laboratory at a very constant temperature of about  $280K$  ( $7^\circ C$ ). The cooling capacity of the exchanger is set by adjusting the mass

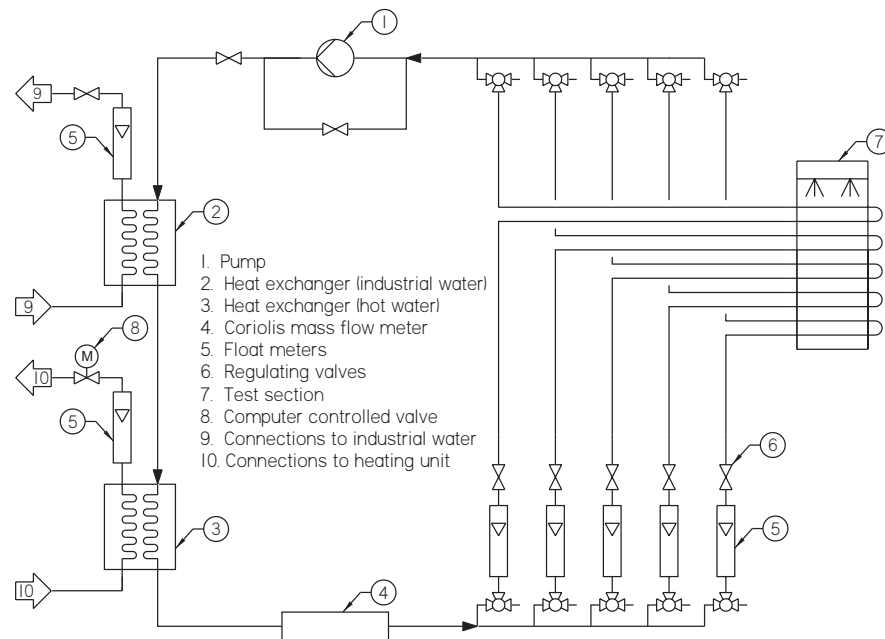


Figure 3.4: Schematic of the forced circulation loop for the cooling water.

flow rate of industrial water. The test section water flows then through a second liquid-liquid heat exchanger (3) where it can be heated with hot water from a heating unit (10). This heating unit available at the laboratory, is gas fired and can provide hot water with adjustable temperature from  $313K$  ( $40^{\circ}C$ ) to  $363K$  ( $90^{\circ}C$ ) with a maximum capacity of  $160kW$ . The heat exchanged in this heat exchanger is linked to the flow rate of the hot water. A motorized and computer-controlled valve sets this flow rate, based on the test section water temperature at the outlet of the heat exchanger (8). The water temperature at the test section inlet is thus automatically maintained constant when the flow rate is changed or if there are any temperature variations in the water provided by the heating unit. At this point, the water for the test section is well conditioned in terms of stability of its temperature and flow rate. The total mass flow rate is then measured with a Coriolis mass flow meter (4).

The main flow of water is then split to the sub-circuits of the test section. Each sub-circuit has its own float flow meter (5) and valve (6) to control its flow rate and thus set the water distribution uniformly between the sub-circuits. The goal is to have the same flow rate in all sub-circuits. There are five sub-circuits and each one can be included in the main circuit (or not) with two three-way valves for each. A sub-circuit usually has two tube passes, i.e. water goes in a copper tube in one direction (right to left) and comes back through the copper tube just above in the opposite direction within the test section (7). With this setup, the water temperature profiles in the two tubes are opposed. The quantity of liquid refrigerant condensed after each two tubes in the test array is thus nearly uniform along the tube length. Tests in other published projects often use only one water pass, which creates an imbalance in the condensate distribution and hence data dependent on the test setup, which is to be avoided. After the test section, the sub-circuits merge and the water flows back to the pump.

During the condensation measurements, most of the time the first heat exchanger with the industrial water was sufficient and the second one was not used.

### 3.4 Glycol circuit

Glycol is used as a cold source for the auxiliary condenser of the test facility. The glycol is heated up when it passes through the auxiliary condenser and has to be cooled in the auxiliary unit. The circulation loop of glycol is depicted in figure 3.5.

The circuit is equipped with a centrifugal pump (1). An electronic speed controller together with a bypass and a valve are used for the glycol mass flow adjustment. After the pump a part of the glycol passes through a float meter (2) to a liquid-liquid heat exchanger (3). In this heat exchanger

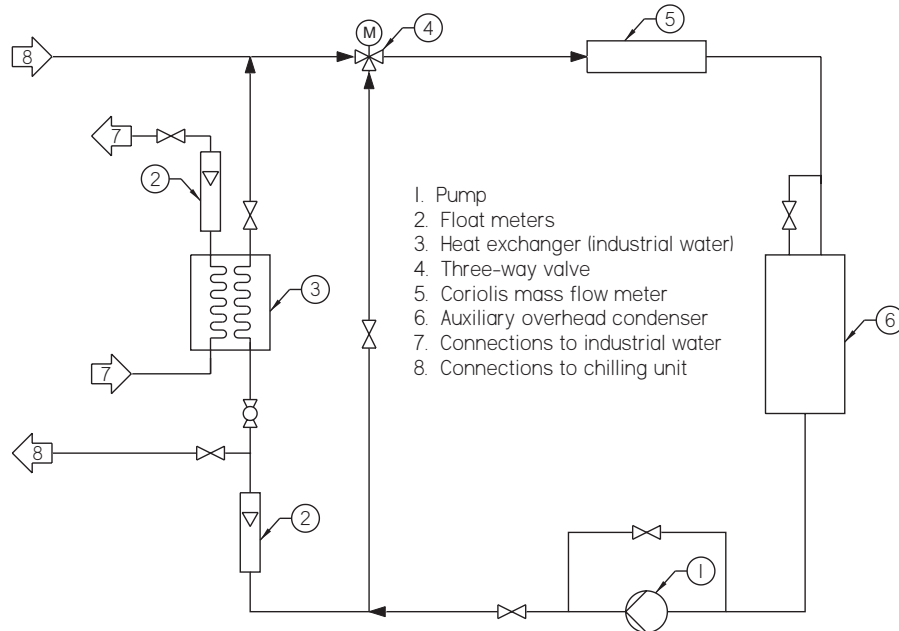


Figure 3.5: Schematic of the circulation loop of glycol as cold source for the auxiliary condenser.

the glycol is cooled by industrial water (7). As the industrial water is at constant temperature, the cooling capacity of the heat exchanger is set by adjusting the mass flow of industrial water by a hand valve. The cooled glycol leaving the heat exchanger flows to the motorized three-way valve (4). In this valve the cold glycol is mixed with the other part of glycol that did not pass through the heat exchanger to obtain the desired temperature. This recirculation allows a fine adjustment of glycol temperature. The glycol mass flow is then measured by a Coriolis flow meter (5). The conditioned glycol goes then to the auxiliary condenser, which is a three-pass condenser with a design capacity of  $50kW$ . It is possible to use only one half of the tubes in the condenser to have a good power adjustment accuracy over a wide operating range.

For very low glycol temperatures and very high thermal capacity of the auxiliary condenser, the glycol loop has the capability to use a chilling unit as a cold source. In this case, the valve at the inlet to the heat exchanger (3) is closed and the glycol passes to the chilling unit (8). In this configuration the recirculation can also be used for fine adjustment of the temperature. The

chilling unit available in the laboratory can provide glycol at  $253K$  ( $-20^{\circ}C$ ) and has a maximum continuous cooling capacity of  $80kW$ . However, during the present investigation the use of the heat exchanger with the industrial water as a cold source was sufficient.

### 3.5 Test section

The test section is a rectangular stainless steel vessel illustrated in figure 3.6. Its internal dimensions are  $554 \times 650 \times 69mm$  ( $W \times H \times D$ ). In the present investigation the heat transfer coefficient during condensation on the outside of horizontal tubes is measured. The tubes tested have a nominal outer diameter of  $19.05mm$  ( $3/4$  in.) and are arranged in a vertical array. The end plates which hold the tubes on the left and on the right are removable. This allows the set of end plates to be changed to obtain different distances between the tubes. Depending on the tube pitch, six to ten tubes can be tested (and a half tube liquid distributor as shown on the right diagram of figure 3.6). The length of the tubes tested is  $554mm$ . In order to have full visual access to observe the condensate flow on the tubes, the test section is equipped with six large windows. Three windows are situated on the front of the test section and three opposed on the rear. The windows measure

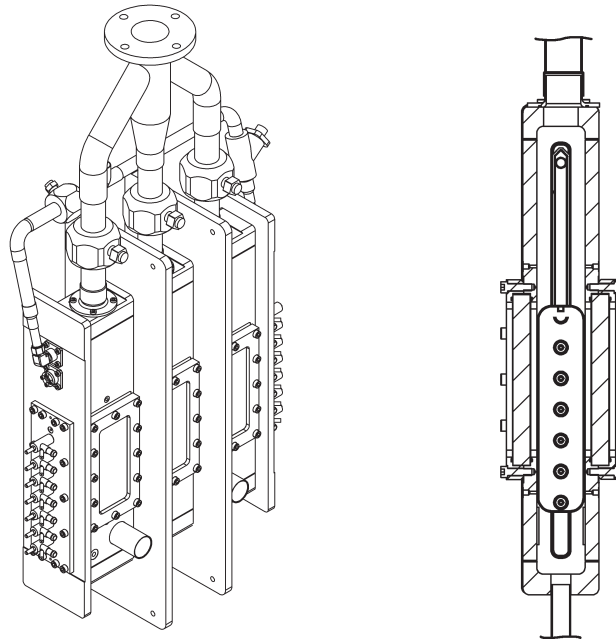


Figure 3.6: Test section.

120mm in width and 250mm in height. The vapor enters the test section through three inlets at the top. It condenses partially on the tubes and the excess vapor leaves the test section by four outlets in the lower part of the test section. Two outlets are located on the front and two on the rear of the test section. The vapor velocity in the test section is always below 0.2m/s. In order to investigate the effect of condensate inundation on the heat transfer coefficient, the test section is equipped with a system to distribute liquid refrigerant onto the top tube. The liquid refrigerant enters the test section by two inlets; one inlet is located on the left and one on the right. Both inlets are equipped with hand valves to adjust the distribution between left and right. The liquid refrigerant from the distributor and the condensate generated on the tubes leaves the test section by an outlet on the bottom. The liquid distributor located inside the test section, the arrangements of the test tubes, and the tested tubes are described in more detail below.

### 3.5.1 Liquid distributor

Special care has been taken to achieve uniform distribution of liquid refrigerant along the top tube in the array. The distributor designed for this purpose is a rectangular box inserted in the test section above the tube array. Its external dimensions are  $554 \times 200 \times 20\text{mm}$  ( $W \times H \times D$ ). A cross sectional schematic of the distributor is given in figure 3.7. The purpose of the liquid distribution system is (i) to distribute the nearly saturated liquid uniformly along the top of the array and (ii) to mimic the flow of an upper tube onto the first test tube.

The liquid refrigerant enters on both sides at the top and is pre-distributed with an stainless steel pipe (13mm I.D.) in which there are holes oriented upwards (1). The holes are 3mm in diameter and spaced 5mm center to center. Then the liquid flows through two layers of foam material compatible with R-134a. The first is a 150mm high layer of soft foam material (2). This is a polyurethane foam with a pore diameter of  $200\mu\text{m}$  and 60 pores per inch. The second is a 10mm high layer of a filter plate (3), which is a polyethylene foam material with a pore diameter of  $35\mu\text{m}$  and a porosity of 37%. This second layer is more compact and creates a larger pressure drop to force a good lateral liquid repartition in the distributor. After this porous section, the liquid reaches the bottom of the distributor, which is a removable machined brass piece with 268 holes along its centerline (4). The diameter of these holes is 1.5mm and the distance center to center is 2mm. The liquid distributor width is 550mm. At high liquid flow rates a continuous sheet leaves the distributor, but at low flow rates the distribution of the droplets is not uniform. For this reason a half-tube was added just below the distributor (5). It was machined from a plain stainless steel tube 20mm in diameter. The bottom of the half tube was machined to form a sharp edge. The liquid falls locally along in the half-tube and overflows on



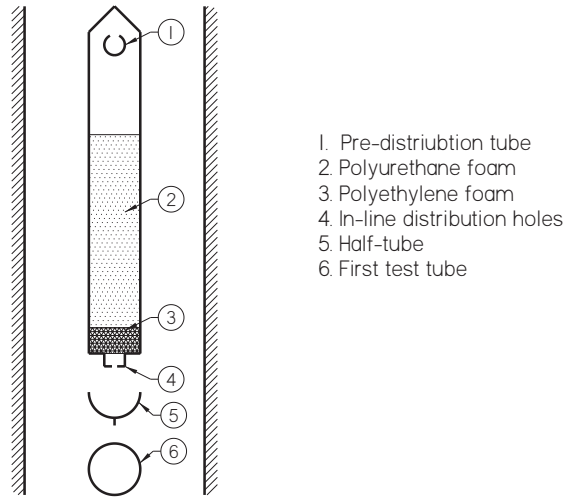


Figure 3.7: Schematic of the liquid distributor for condensate inundation.

both sides. The sharp edge forces the liquid to leave at the bottom of the half tube. By rotating the half tube the direction of the liquid leaving the tube at the edge can be adjusted to ensure that the liquid falls exactly on the top of the first test tube (6). The temperature of the overfeed liquid is controlled by a heater to maintain its subcooling to less than  $0.8K$ .

### 3.5.2 Tube arrangements

In order to study the effect of the distance between the tubes, three different tube arrangements have been tested. The arrangements are depicted in figure 3.8. The tube pitches center-to-center were  $25.45$ ,  $28.6$ , and  $44.5mm$ . With the nominal tube diameter of  $19.05mm$ , intertube spacings of  $6.4$ ,  $9.5$ , and  $25.5mm$  are obtained.

The distance between the distribution half tube and the top tube was equal to the distance between the tubes to reproduce the same falling effect. At the smallest tube pitch of  $25.5mm$ , ten tubes were installed. At the tube pitch of  $28.6mm$ , nine tubes were installed. At the largest tube pitch of  $44.5mm$ , only six tubes could be mounted.

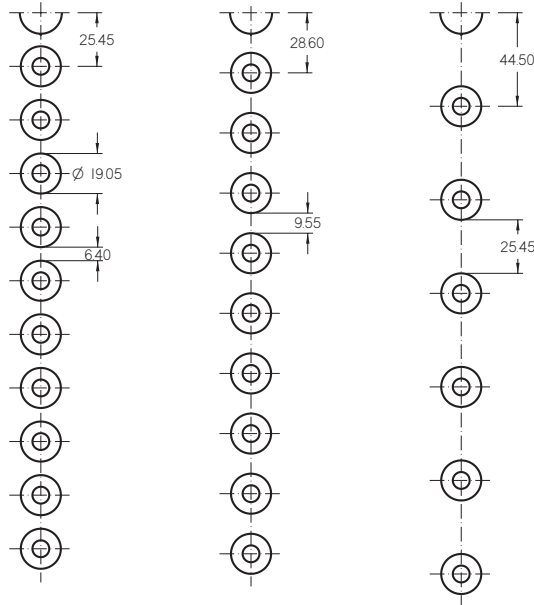


Figure 3.8: Schematic of the three tested arrangements of tubes in the test section.

### 3.5.3 Copper tubes tested

Four commercially available tubes were tested: a plain tube, a standard 26 fpi / 1024 fpm low finned tube (the Turbo-Chil) and two condensation tubes with 3D enhanced surfaces (the Turbo-CSL and the Gewa-C). The Gewa-C tube was provided by Wieland-Werke AG and all the others by Wolverine Tube Inc. All tubes were made from copper. Close-up pictures of the external tube surfaces are given in figure 3.9.

The two 3D enhanced condensation tubes are low finned tubes that were oblique cut through the upper part of the fins. The Turbo-Chil, the Turbo-CSL, and the Gewa-C tube have helical ribs on the inside to increase the water side heat transfer coefficient. Photomicrographs of an axial cut of the tested tubes are shown in figure 3.10. On the pictures of the 3D enhanced tubes, deformed fins and non-deformed fins can be seen as the fins are cut helically.

As seen on the photomicrographs, the profile of the fins of the low finned Turbo-Chil tube can be approximated by a trapezoidal-fin tube. A schematic of trapezoidal-fin tube is depicted in figure 3.11. The tube diameter at the

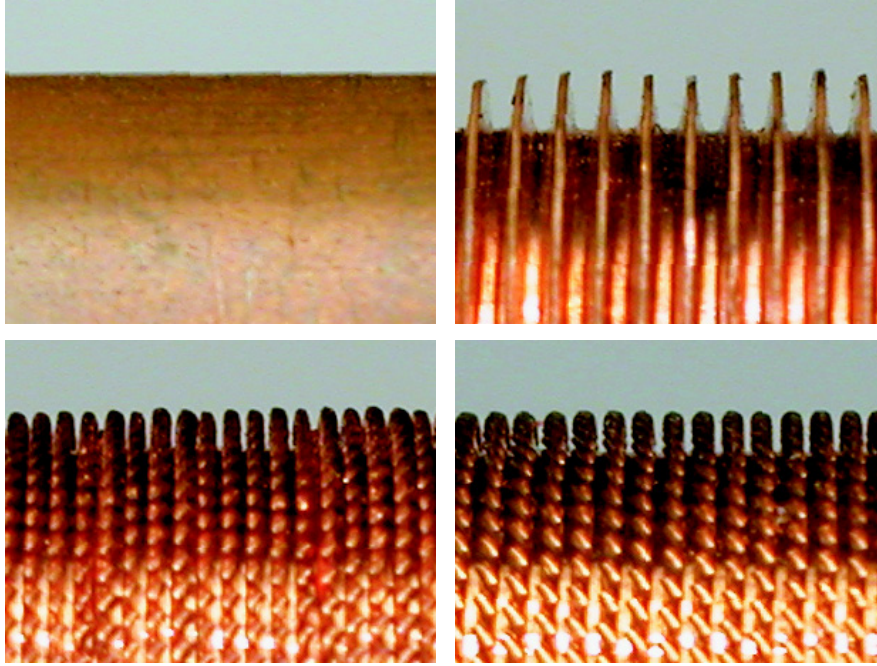


Figure 3.9: Close-up pictures of the surface of the four types of tubes: Plain tube (on the top left), Turbo-Chil (on the top right), Turbo-CSL (on bottom left), and Gewa-C (on the bottom right).

fin tip  $D_o$  was measured with a micrometer. The root diameter of the tube was determined by a measurement with a micrometer after machining off the fins. The internal diameter, which is actually the internal root diameter, was determined in the same way than external root diameter. The fin pitch  $p_f$ , fin height  $e$ , fin thickness at the tip  $t_t$  and the fin thickness at the base  $t_b$  were measured on several photomicrographs. The results of these measurements are given in table 3.1.

Tube	$D_o$	$D_{or}$	$D_i$	$p_f$	$e$	$t_t$	$t_b$
Plain Tube	18.91	-	16.22	-	-	-	-
Turbo-Chil	18.94	15.99	14.65	0.94	1.36 <sup>†</sup>	0.18	0.51
Turbo-CSL	18.90	17.15	15.94	0.53	(0.87)	(0.11)	(0.22)
Gewa-C	18.88	17.06	15.54	0.65	(0.91)	(0.18)	(0.33)

Table 3.1: Geometrical specifications of the tubes tested. All dimensions are in  $mm$ .

<sup>†</sup>Mean value of fin height

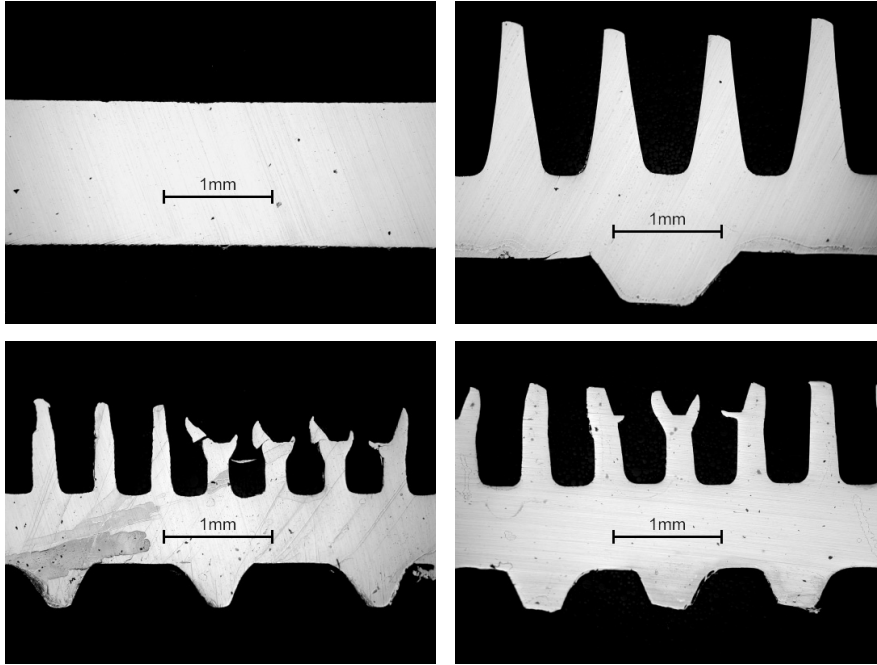


Figure 3.10: Photomicrographs of an axial cut of the tubes tested: Plain tube (on the top left), Turbo-Chil (on the top right), Turbo-CSL (on bottom left), and Gewa-C (on the bottom right).

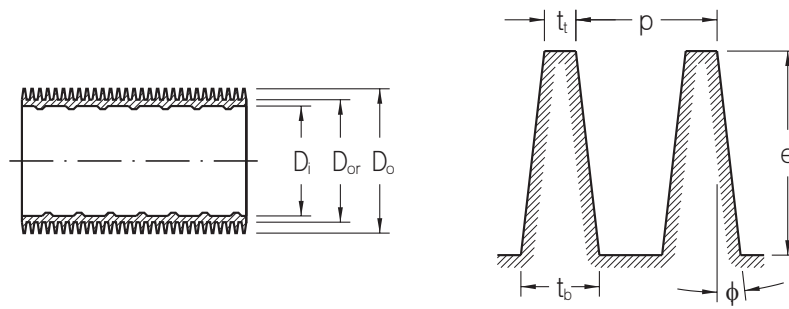


Figure 3.11: Schematic of a trapezoidal-fin tube.

The fin pitch of the Turbo-Chil tube determined on the photomicrographs corresponds to a fin density of 27.2 fpi, which is a little higher than the nominal of 26 fpi. However, in the further discussion only the nominal nomination is used for the Turbo-Chil tube. As seen on the photomicrograph of the Turbo-Chil tube, the heights of the fins are not equal due to the manufacturing procedure of the tube. The values of the fin height measured on the photomicrographs ranged from 1.24 to 1.47mm. The value of 1.36mm given in table 3.1 is the mean value of 16 fins that have been measured. This mean value of the fin height will be used in further calculations.

The geometrical specifications of the 3D enhanced tubes were determined in a similar way. For these tubes the non-deformed fins were approximated by a trapezoidal fin shape. The values of the non-deformed fins are put in brackets in table 3.1. The fin pitches of the Turbo-CSL and Gewa-C tube correspond to a fin density of 48.3 fpi and 38.9 fpi, respectively. For the Turbo-CSL and the Gewa-C tube, the values for the fin heights given in table 3.1 are the values determined by the difference of the measured fin tip diameter and fin root diameter  $e = (D_o - D_{or})/2$ . The values of the fin heights measured on the photomicrographs were very close to these values (0.84 and 0.92mm). However, for all calculations the geometrical specifications given in table 3.1 were used.

### 3.5.4 Tube instrumentation

A new type of heat transfer measurement strategy has been developed in order to obtain local values of the heat transfer coefficient on each tube in the array. In previous published studies, only the inlet and outlet temperatures of the water have been measured. With that type of measurement, only a mean heat transfer coefficient for each tube can be obtained. In this study, a stainless steel tube with an external diameter of  $D_{stainless} = 8mm$  is inserted inside each copper tube. This tube is instrumented with six thermocouples. A schematic of this instrumentation setup is depicted in figure 3.12. The thermocouples are located at three positions in axial direction of the tube. At every location, one thermocouple is facing upwards and one is facing downwards to measure the temperature of the water flowing in the annulus between the stainless steel tube and the tested tubes. The thermocouple leads are all brought out at one end on the inside of the tube. The distance between the thermocouples is 185mm and the distance to the wall approximately 92mm. The distance to the wall assures that no entrance effects are measured. The thermocouples are 0.5mm in diameter and have a length of 400 to 750mm.

In addition, the stainless tube helps to increase the water side coefficient as flow area for the water is reduced. For an accurate measurement of the water temperature, a copper wire with a rectangular cross section ( $0.9 \times 2.8mm$ ) has been wound helically (12mm pitch) around the stainless steel

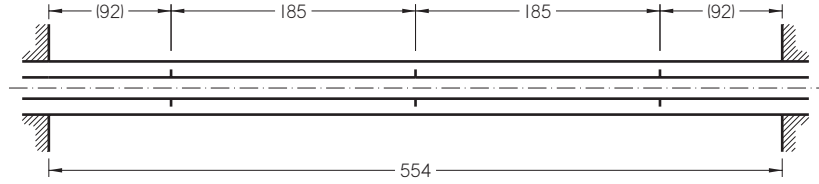


Figure 3.12: Schematic of the instrumentation setup of the tubes to measure the temperature profile of the water flowing inside.

tube (not shown). This promotes mixing, minimizes any entrance effect and further increases the water side heat transfer coefficient.

### 3.5.5 Instrumentation of the test section

The vapor pressure in the test section is measured with two absolute pressure transducers. One is connected to the test section above the array of tubes and one below. The vapor temperature above the tubes is measured with six thermocouples. Three are situated on the front and three on the rear of the test section. They are  $1\text{mm}$  in diameter and the junction is located in the middle between the test section wall and the distributor. The temperature of the liquid entering the test section is measured with one thermocouple inserted in each inlet. Below the array of tubes, three thermocouples  $2\text{mm}$  in diameter are installed on the front of the test section. The junctions of these thermocouples are situated in the middle between the front and rear side. The temperature of the vapor leaving the test section is measured with one thermocouple in the vapor pipe on the front after the two vapor outlets on the front joined and one at the same position on the rear. The temperature of the liquid leaving the test section is measured with a thermocouple inserted in the liquid outlet. The wall temperature of the test section is measured with one thermocouple attached on the outside.

## 3.6 Data acquisition and control

### 3.6.1 Data acquisition system

All the measurements are made with the separate data acquisition computer. The acquisition system is a National Instruments SCXI. The acquisition card is a PCI MIO 16XE 50 installed in the PC. The resolution of this card is 16 bits and the maximum acquisition frequency on a single channel is

10kHz. A SCXI 1000 module with four bays is connected to this card. For the acquisition computer, each of the four bays has a 32 channel voltage measurement card (type 1102). The total number of acquisition channels is thus 128. Each channel of this system has a computer programmable gain: 1 for 0 to 10V signal (pressure transducer and mass flow meter) and 100 for low voltage signals (thermocouples). The signals can be adjusted to the 0 to 10V range of the acquisition card in the computer. A 2Hz low pass frequency filter is also included in the card for each channel. This helps to diminish the measurement noise and does not affect the steady-state measurements of this study. At the end of the acquisition chain, a terminal block with 32 sockets is connected to the 1102 card. Each card has its own terminal block. The cold junction for every thermocouple is made in this terminal block at the socket. The material of this socket is copper for both poles (+ and -), the continuity of the two different specific materials of the thermocouple is so broken at this point located inside the terminal block. The temperature of the 32 cold junctions is maintained uniform with a metallic plate and is measured by the system via a RTD installed in the middle. Additionally, all the terminal blocks are placed in a closed cupboard away from external thermal influences.

In order to measure a test parameter in a channel, 100 acquisitions are made in 0.02s – the 50Hz electric network period – and the average of these 100 values is calculated during the acquisition. The result is the measured value of this channel. By this way, the noise from alternating current on the measured signal is removed. This value is stored and the system goes to the next channel. With this measurement method, the theoretical channel measurement frequency is 50 channels per second, but due to the switching time between channels, the actual frequency is 30 channels per second. In total, it takes thus 4.3s to measure all the channels of the acquisition computer once. To obtain one data point, 30 such acquisition cycles are recorded and averaged.

### 3.6.2 Control system

A second computer is used to control the test facility. It has the same SCXI system as the data acquisition computer. The four bays of the SCXI 1000 module contain two cards for voltage measurement, one card for current measurement and one card with eight output channels. These outputs are used to control the three-way valve for the glycol, the valve for hot water, the two electric heaters in the evaporator, the heater for the liquid refrigerant and the heater for the vapor refrigerant. Two PID controllers are programmed on this computer: one for the electric heater of the evaporator, (the saturation pressure in the test facility is maintained automatically constant) and one for the hot water valve (the flow rate of hot water in the heat exchanger is controlled based on the temperature of the water entering

the copper tubes). All the parameters are displayed online on the screens of the two computers and experimental parameters are calculated, for example: water temperature profile in the copper tubes, heat transfer coefficient on the measurement computer or PID status, various heating and cooling capacities on the control computer, etc.

### 3.7 Operating procedure

The operating procedure determines the way the test facility is utilized to get the measurements of all the desired parameters (pressure, temperature, flow rate etc.) for every point of the test matrix. As steady state values are measured, care has to be taken to obtain stable conditions during the data acquisition period.

Once the particular tubes are mounted with the desired tube pitch (one variable of the test matrix) and the air was removed by a vacuum pump out of the test section for at least one night, the tests section is connected to the refrigerant loop and the measurements can be started.

First of all, the test facility has to be brought to the desired saturation condition. The electric heaters in the evaporator are started with the controller based on the pressure. The set point of the controller is set to  $800kPa$  in the current investigation which corresponds to a saturation temperature of  $304K$  ( $31^{\circ}C$ ) for refrigerant R-134a. While the test facility is heating up, the auxiliary condenser is already started. On one hand, this slows down the heating up, but on the other hand, a vapor circulation from the evaporator to the condenser passing through the test section is generated. This vapor flow purges the test section and, if there are any noncondensing gases, then they are trapped in the auxiliary condenser away from the test section. The saturation conditions are automatically attained and maintained constant at the desired value by the controller on the evaporator. This regulation mode has been chosen because it is easier and faster to change electric power in the evaporator than the glycol flow rate or temperature in the condenser. By using a solid state relay (Triac) for the electric command, the response between the command voltage and output power is approximately linear over the complete range.

The test facility is run in this mode about half an hour at the saturation condition. Then the pump in the water loop is started and the mass flow of water is set by adjusting the speed controller of the pump and the by-pass valve. The circulating water is cooled in the plate heat exchanger with the industrial water, which is at a constant temperature of about  $280K$  ( $7^{\circ}C$ ). As the water flow inside the tested tubes is cooled, the refrigerant vapor starts to condensate on the tubes. The controller increases automatically the capacity of the electrical evaporator to compensate for the heat load of the test section to maintain the saturation condition. The desired heat flux



in the test section is set by changing the temperature of the water circulating in the tested tubes. This is done by adjusting the mass flow of industrial water in the plate heat exchanger by a hand valve. The water flow rate in the tested tubes determines the water Reynolds number and thus the value of the internal heat transfer coefficient  $\alpha_i$ . It is best to keep the internal heat transfer coefficient (or the water flow rate) as high as possible. The overall heat transfer is mainly driven by the external heat transfer coefficient so the uncertainty in the determination of this external heat transfer coefficient is smaller with a higher value of  $\alpha_i$ . On the other hand, a higher water flow rate means, for a given thermal duty, a smaller temperature difference between inlet and outlet. This creates a larger uncertainty on the energy balance. For every case, a compromise between these two opposite tendencies is necessary. The data acquisition subroutine performs a propagation of error analysis for each test condition (online) so an optimum can be achieved.

After running the test facility at least for another half hour with the test section at the desired operating condition, the acquisition of the first data point can be made. At every operating condition, three data points are taken.

Depending on the experiments to be performed, the temperature of the water is changed to make one series of measurements without liquid overfeed or the heat flux is kept constant and the the refrigerant pump is started and the liquid flow rate is increased stepwise to make a series of measurements at constant heat flux with increasing inundation rate. When the operating condition is attained, an acquisition is made after a stabilization period. It takes 20 to 30 minutes for changing the operating condition and for stabilization.

For shutting down the test facility, first the condensation in the test section is stopped and the vapor flow from evaporator to auxiliary condenser is maintained for a while to assure that noncondensing gas does not flow to the test section. Afterwards the evaporator and the auxiliary condenser are shut down and the test facility cools slowly down to room temperature.

### 3.8 Instrumentation accuracy

Uncertainties in measurements have mainly two origins. Errors directly from the measurement devices: error of a pressure transducer, thermocouple deviation, etc. and uncertainties due to oscillations of the measurement conditions, such as variation of the water temperature during an acquisition. These two points are discussed below. Another aspect with respect to errors is the statistical propagation in the calculations of the desired variables such as the heat transfer coefficient. This will be treated later in chapter 5 where the complete analysis of errors is estimated.

### 3.8.1 Thermocouples

The measured temperatures are around  $304K$  ( $31^\circ C$ ) for the refrigerant and between  $280K$  ( $7^\circ C$ ) and  $303K$  ( $30^\circ C$ ) for the water in the copper tubes. Type K thermocouples (NiCr/NiAl) are used because they offer a good precision in this range. The working principle of a thermocouple is based on the Seebeck effect. When two wires made of two different metallic materials are welded together at each end, a voltage appears if the two welded ends (or junctions) are at different temperatures. This voltage can be correlated to the temperature difference between the two ends. Measuring the temperature with a thermocouple consists of measuring the temperature of one junction (called cold junction) and the voltage that appears. With these two values, the temperature of the other junction (measurement point of the thermocouple) can be calculated.

In our case, the system measures the temperature of the cold junction and the voltage. It calculates the temperature of the thermocouple with standard polynomials of the type K thermocouples. This is the default function of the system.

In order to improve accuracy, a calibration is made. The calibration procedure consists of immersing the thermocouples in a thermal bath at one temperature and measuring the temperature of this thermal bath with a reference thermometer, changing the temperature step by step to cover the desired range. The results are compiled to find an individual correlation between the temperatures measured by the specific thermocouple and the reference thermometer. In most of the cases, a third order polynomial is used for correction. The typical calibration range is  $276K$  ( $3^\circ C$ ) to  $306K$  ( $33^\circ C$ ) for water temperature and  $263K$  ( $-10^\circ C$ ) to  $323K$  ( $50^\circ C$ ) for refrigerant temperature. The temperature step is  $3K$  and the calibration is made with increasing and decreasing temperature to average hysteresis effects. Between calibration and measurement, all the acquisition system is maintained turned on all the time and the connections are never unplugged. The most important thermocouples are the ones inside the copper tubes for measuring the water temperature. These ones are calibrated after their mounting on the stainless steel internal pipe where they are tin soldered. They protrude out through holes into the water flow. A new calibration is also made while changing the type of tube to be tested or the tube pitch. These thermocouples are thus calibrated once every month to obtain optimum accuracy. Little variation in their calibrations was typically noted.

The result of this careful calibration is a maximum deviation of  $0.03K$  between the reference and the temperature from the thermocouple. Figure 3.13 illustrates the calibration of one tube insert with six thermocouples. On the left, the difference between the measurement of the six thermocouples and the reference temperature is given over the whole calibration range with increasing and decreasing temperature. Without calibration (circles)

the differences between the six thermocouples are about  $0.4K$  and the difference compared to the reference temperature range from about  $0.6K$  at a calibration temperature of  $276K$  to  $0.8K$  at a calibration temperature of  $306K$ . With the polynomial corrections of the measured temperatures (x), the differences compared to the reference temperature become very small, as also illustrated on the right. With the calibration, the deviations compared to the reference temperature are here for all six thermocouples over the whole calibration range smaller than  $0.02K$ .

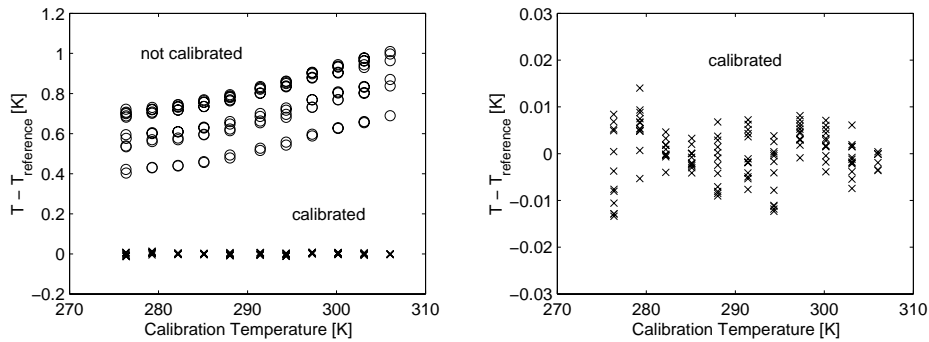


Figure 3.13: Calibration of one stainless steel tube insert instrumented with six thermocouples for increasing and decreasing calibration temperature.

After a calibration, the readings from thermocouples were also double-checked at some isothermal conditions in the thermal bath as illustrated on the left in figure 3.14, which depicts the measured temperatures in one circuit (2 passes) and the reference temperature. The deviations for all 16 thermocouples compared to the reference temperature are smaller than  $0.03K$ .

The readings from the thermocouples were also verified by checking for deviations between the thermocouples at isothermal conditions in the test facility with water circulation at room temperature. The typical deviations of a single thermocouple compared to the mean value were again  $\pm 0.03K$  as illustrated on the right in figure 3.14.

### 3.8.2 Pressure transducers

All the pressure transducers used are electronic and based on membrane deformation measurement. The operating range of the transducers is 0 to  $1000kPa$ , except for the transducer at the outlet of the evaporator, which is also used for security purposes that has a range of 0 to  $2000kPa$ . They are class 1, 2, and 4 devices. The most critical for the measurements are the two transducers connected to the test section, which are class 1 devices. They

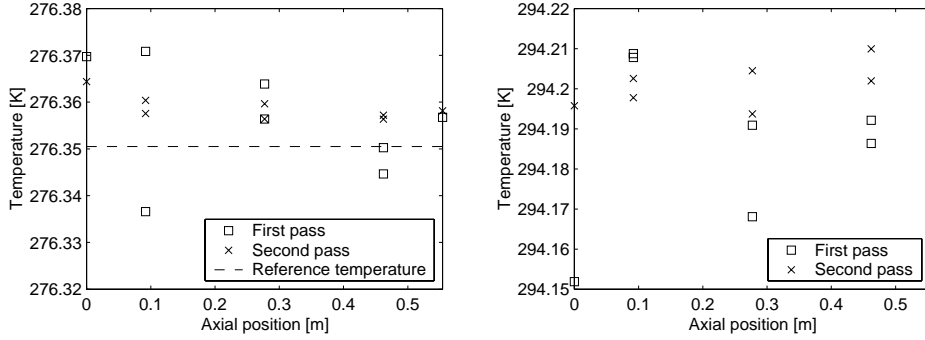


Figure 3.14: Isothermal temperature check of the sixteen thermocouples in one two-pass circuit connected to a thermal bath (left) and installed in the test section (right).

have an accuracy of 0.1% of full scale, which corresponds to an absolute error of  $1kPa$ . Once again, the transducers are calibrated in the laboratory for a better accuracy. The reference (known) pressure was made by a calibrator balance. The calibration ranges are 100 to  $1000kPa$  and 100 to  $1600kPa$ , respectively, with a step of  $100kPa$ . The deviation after calibration is always smaller than the specified absolute error.

In addition to the transducers mentioned above, there is one pressure transducer connected to the test section with a small operating range from 0 to  $10kPa$ . This transducer is used only when the air is pumped out of the test section to measure the pressure of the remaining gas.

### 3.8.3 Mass flow meters

There are three mass flow meters on the test facility, two with an operating range from 0 to  $1.666kg/s$  in the water and glycol circuits and one with range 0 to  $0.166kg/s$  in the refrigerant circuit. They are all Coriolis type and measure directly the mass flow rate in  $kg/s$ . The uncertainty of their measured mass flow rate is given by the following equation:

$$\Delta\dot{m}/\dot{m} \leq \pm(0.15 + S/\dot{m})\% \quad (3.1)$$

where  $\dot{m}$  is the measured mass flow rate and  $S$  is a constant that depends on the mass flow meter. The values are  $S = 8.3 \cdot 10^{-3}kg/s$  for the large mass flow meters (water/glycol) and  $S = 8.3 \cdot 10^{-4}kg/s$  for the small one (refrigerant).

### 3.9 Conclusion

The test facility constructed specifically for the current investigation was described. The test facility consists basically of a natural circulation loop for refrigerant R-134a and a forced convection loop for the cooling water. Vapor is generated in an electrically heated evaporator and condensed in the test section and in an auxiliary condenser. The saturation pressure of  $800kPa$  ( $T_{sat} = 31^{\circ}C$ ) is maintained by an automatic controller on the evaporator. The mass flow of refrigerant vapor in the loop is set by adjusting the cooling capacity of the test section and the auxiliary condenser. The cooling water of the test section is cooled by an heat exchanger with industrial water at a temperature of approximately  $7^{\circ}C$ . The cooling capacity of the auxiliary condenser is accurately adjusted by a forced circulation loop of ethylene glycol, which is also cooled by industrial water.

An vertical array of horizontal tubes is installed in the test section. The tubes are  $554mm$  in length and  $19.05mm$  ( $3/4$  in.) in diameter. The test section is equipped with an elaborated distribution system of liquid refrigerant onto the top of the array of tested tubes to study the effect of condensate inundation. The test section is equipped with six large windows to have full visual access to the tubes. Depending on the tube pitch, 6 to 10 tubes can be installed in the test section in the array at one time. All the tubes are instrumented to measure the temperature profile of the water flowing inside. This temperature profile approach, importantly, allows local heat transfer coefficients to be measured at the center of each tube in the test array, rather than tube length averaged values available in the past in literature. Local heat transfer coefficients are more valuable for developing local predicting methods required for incremental design of heat exchangers. The two-tube pass design ensures nearly uniform condensate flow along the test section after each two tube passes, which is a point overlooked in most other studies that typically use only one tube pass.



## Chapter 4

# Modified Wilson Plot Technique

In this chapter, the procedure to determine the external heat transfer coefficient between the outside surface of the copper tubes and the refrigerant from the measurements is described. This procedure requires knowledge of the internal heat transfer coefficient  $\alpha_i$  between the water and internal tube surface. The Wilson plot technique to find this internal heat transfer coefficient is described and the results of this method applied to each type of tube tested. The Wilson plot procedure was implemented using nucleate pool boiling on the outside of the tubes.

### 4.1 Heat transfer calculation principle

The heat transfer coefficient during condensation on the outside of a tube is given by Newton's law of cooling to be the ratio of the heat flux to the temperature difference across the condensate layer:

$$\alpha_o = \frac{q_o}{T_{sat} - T_{wall,o}} \quad (4.1)$$

where  $T_{sat}$  is the saturation temperature of the vapor and  $T_{wall,o}$  the temperature of the tube surface. The surface temperature of the tube is not measured in this study. The external heat transfer coefficient is derived from a temperature measurement of the water flowing inside the tube.

The internally mounted thermocouples measuring the water temperature within the tubes in the axial flow direction permit the water temperature profile to be determined as a function the distance  $x$  along the tubes:

$$T_{wat} = f(x) \quad (4.2)$$

With the assumption that axial conduction along the tubes is negligible, an energy balance on a differential element of water inside the tube gives

$$dq = \dot{m}c_{p,wat}dT_{wat} \quad (4.3)$$

where  $\dot{m}$  is the mass flow rate and  $c_{p,wat}$  is the specific heat of water. The local heat flux on the outside of the tube may be expressed as

$$q_o = \frac{dq}{dA_o} = \frac{dq}{\pi D_o dx} \quad (4.4)$$

Substituting from equation 4.3, it follows that

$$q_o = \frac{\dot{m}c_{p,wat}}{\pi D_o} \frac{dT_{wat}}{dx} \quad (4.5)$$

The thermal resistance of a differential element of the tube is the sum of the thermal resistance for condensation on the outside of the tube, the thermal resistance for convection inside, and the thermal resistance for conduction through the wall:

$$R_{tot} = R_o + R_i + R_w \quad (4.6)$$

In terms of heat transfer coefficients, this equation gives locally

$$\frac{1}{U_o dA_o} = \frac{1}{\alpha_o dA_o} + \frac{1}{\alpha_i dA_i} + R_w \quad (4.7)$$

where  $U_o$  is the overall heat transfer coefficient and  $\alpha_o$  and  $\alpha_i$  are the outside and the inside heat transfer coefficients, respectively. Multiplying equation 4.7 by the outer surface of the differential element  $dA_o = \pi D_o dx$  results in

$$\frac{1}{U_o} = \frac{1}{\alpha_o} + \frac{1}{\alpha_i} \left( \frac{D_o}{D_i} \right) + r_w \quad (4.8)$$

where

$$r_w = \pi D_o dx R_w = \frac{D_o}{2\lambda_{cop}} \ln \left( \frac{D_{or}}{D_i} \right) \quad (4.9)$$

$D_i$  is the inside diameter of the tube and  $D_{or}$  the outside root diameter of the enhanced tubes. For the plain tube,  $D_{or}$  is the outer diameter  $D_o$ . This means that the fins on the outside and the ribs on the inside of the tube are not considered. They are encompassed in the external and internal heat transfer coefficients.

Using the local overall heat transfer coefficient  $U_o$ , the heat flux can be written alternatively to equation 4.5 as

$$q_o = U_o(T_{sat} - T_{wat}) \quad (4.10)$$

The goal of this study is to determine the heat transfer on the outside of the tube. With the help of equations 4.5, 4.8, 4.9, and 4.10, the external



heat transfer can be calculated only if the internal heat transfer coefficient is known. In order to determine the experimental condensing heat transfer coefficient with a minimum of uncertainty, it is necessary to characterize the water side heat transfer coefficient as accurately as possible. The technique used to determine the water side coefficient is described in the following section.

## 4.2 Modified Wilson plot method

Wilson [56] noted that for a small range of cooling-water temperature rise, the inside heat transfer coefficient is proportional to velocity of the cooling-water to the power of 0.82. He proposed to plot the overall resistance ( $1/U_o$ ) versus the inverse of the velocity to the power of 0.82 (that is,  $1/u^{0.82}$ ) to obtain a straight line. The intercept of the Y-axis of this straight line corresponds to the overall resistance at infinite cooling-water velocity. At this point the internal heat transfer coefficient is zero and external heat transfer coefficient can be determined from the overall heat transfer coefficient. This traditional Wilson plot method is based on the assumption, that the external thermal resistance remains constant as the cooling-water velocity is changed. During condensation the wall temperature of the tube and consequently the external heat transfer coefficient change when only the cooling-water velocity is varied. Under these conditions saturation temperature or the cooling-water temperature have to be adjusted to maintain a constant external thermal resistance.

To cope with this difficulty, Briggs and Young [57] recommended an extensive modification of this technique proposing the modified Wilson plot method. The essence of this technique is that the form of the relationships for the heat transfer on the internal and external side of the tube are known apart of certain constants. The modified Wilson plot technique consists of measuring the overall heat transfer for several conditions (at different water Reynolds number covering the expected range in the experiments) and correlating all the results to find the unknown constants.

Kumar et al. [58] provided a comprehensive study of the modified Wilson technique to determine the heat transfer coefficient during condensation over single and horizontal plain and finned tubes. More in general, Rose [59] discussed the accuracy of the Wilson plot technique. However, the method used in the present study is based on the modified Wilson plot as proposed by Briggs and Young [57] with the goal to find an accurate predictive relation for the internal heat transfer in the tube between the water and the copper.

### 4.2.1 Internal heat transfer coefficient

Typically, the modified Wilson plot method is used to determine a leading empirical constant in the Sieder and Tate correlation for single phase

internal flow [60]. One disadvantage of this is that the Sieder and Tate equation is only suitable for fully turbulent flows ( $Re_{Dh} > 10000$ ). For this reason, in the present study the Gnielinski correlation [61] for single phase internal flow is used for the internal heat transfer coefficient. This correlation is suitable for Reynolds numbers corresponding to the transition region ( $2300 \lesssim Re_{Dh} \lesssim 10000$ ) as well as the fully turbulent regime up to  $Re_{Dh} = 10^6$ :

$$\alpha_{gni} = \frac{Nu_{gni}\lambda_{wat}}{D_h} = \frac{(f/8)(Re_{Dh} - 1000)Pr_{wat}}{1 + 12.7(f/8)^{1/2}(Pr_{wat}^{2/3} - 1)} \frac{\lambda_{wat}}{D_h} \quad (4.11)$$

$Nu_{wat}$  is the Nusselt number

$$Nu_{wat} = \frac{\alpha D_h}{\lambda_{wat}} \quad (4.12)$$

$Pr_{wat}$  is the Prandtl number

$$Pr_{wat} = \frac{\mu_{wat}c_{p,wat}}{\lambda_{wat}} \quad (4.13)$$

$Re_{wat}$  is the water Reynolds number

$$Re_{wat} = \frac{\rho_{wat}uD_h}{\mu_{wat}} = \frac{4\dot{m}}{\pi(D_i + D_{stainless})\mu_{wat}} \quad (4.14)$$

where  $u$  is the mean velocity of the water and  $D_h$  is the hydraulic diameter inside the tube for the annulus section (there is an  $D_{stainless} = 8.0mm$  stainless steel tube centered inside the tubes with the water side thermocouples that measure the water temperature profile):

$$D_h = \frac{4 \times \text{cross section}}{\text{wetted perimeter}} = \frac{4\pi(D_i^2 - D_{stainless}^2)}{4\pi(D_i + D_{stainless})} = D_i - D_{stainless} \quad (4.15)$$

The definition of the hydraulic diameter is different in the case of heat transfer. The considered wetted perimeter is only the part through which there is heat transfer, which is the nominal perimeter of the internal diameter of the copper tube in our case. However, this definition leads to two different Reynolds numbers: one with heat transfer and one without. Despite the fact that the flow rate at the transition is the same (for the same temperature), there will be two ranges of Reynolds numbers for the transition from laminar to turbulent flow and physically this transition does not depend on the presence of heat transfer. For this reason, the definition used here is the classical one, i.e. equation 4.15. It is also compatible with the Reynolds number used in the following friction factor definition. A correlation for the friction factor  $f$  for a smooth surface has been developed by Petukhov [62]:

$$f = (0.79 \ln Re_{Dh} - 1.64)^{-2} \quad 3000 \lesssim Re_{Dh} \lesssim 5 \times 10^6 \quad (4.16)$$

The low fin and 3D enhanced tested tubes have an enhancement of their internal surface so that the benefit of the improvement of the external heat transfer is not cancelled by poor internal heat transfer. The Petukhov relation for the friction factor is strictly only valid for a smooth internal tube surface. However, this correlation was used for all measurements. The effect of all internal enhancement is taken into account in the leading constant  $C_i$  (see equation 4.17).

In the Wilson plot technique, one assumes that the internal heat transfer coefficient  $\alpha_i$  is the one given by the Gnielinski correlation multiplied by a constant  $C_i$  to be determined experimentally:

$$\alpha_i = C_i \alpha_{gni} \quad (4.17)$$

The leading constant  $C_i$  characterizes the influence of the inside surface enhancement on the heat transfer. It also includes the influence of the copper wire wound around the inner stainless steel tube to increase mixing and improve the accuracy and uniformity of water temperature measurements.

#### 4.2.2 External heat transfer coefficient

In condensation studies, typically the external heat transfer coefficient is chosen in the form of the Nusselt theory as the Wilson plot technique is performed with condensation on the outside of the tubes. A disadvantage of this method is that for externally enhanced tubes surface tension is important and a Nusselt type equation may not be adequate as noted by Rose [59]. Even for the plain tube this method may lead to unsatisfactory results. In the current study, pretests showed that for the plain tube the overall thermal resistance is dominated by the thermal resistance of the condensing side. This means the observed variations in the overall heat transfer coefficients are small when the velocity of the cooling water is changed to vary the internal heat transfer coefficient. Thus, the determination of the straight line in the modified Wilson plot becomes difficult. For this reasons in the present investigation the modified Wilson plot technique is performed using nucleate pool boiling on the outside of the tube. The reasons of this choice can be summarized as follows:

- It is easy to recreate and maintain the external conditions. The tube being evaluated is immersed in a refrigerant liquid pool within the test section while an upper tube condenses the vapor formed.
- The external coefficient is quite large compared to the that of the water side. Its influence on the measured overall  $U_o$  is thus small, which is desirable for measuring  $C_i$  accurately.

- The external boiling heat transfer coefficient is easily represented by a proportional correlation, similar to the assumption of the Wilson plot technique.

During modified Wilson plot tests, it is not possible to maintain the heat flux fixed, and there is a maximum variation of about  $\pm 4\%$ . To account for this for nucleate pool boiling, a common relation for the heat transfer coefficient is:

$$\alpha \sim q_o^{0.7} \quad (4.18)$$

Which became in our case:

$$\alpha_o = C_o q_o^{0.7} \quad (4.19)$$

The value 0.7 of the exponent in equation 4.19 is strictly only applicable for plain tubes. As in the present study the Wilson plots were performed at a fixed heat duty, the influence of the exponent was expected to be negligible and thus the value 0.7 was used for all types of tubes as a first estimate. The influence of this exponent on the determined values of  $C_i$  will be discussed in detail in section 4.5.

### 4.2.3 Overall heat transfer coefficient

The overall heat transfer coefficient  $U_o$  is given by equation 4.8. Substitution of equations 4.17 and 4.19 in this equation and rearranging leads to

$$\left(\frac{1}{U_o} - r_w\right) q_o^{0.7} = \frac{1}{C_i} \left(\frac{q_o^{0.7}}{\alpha_{gni}}\right) \left(\frac{D_o}{D_i}\right) + \frac{1}{C_o} \quad (4.20)$$

This equation has a simple linear form of

$$Y = \frac{1}{C_i} X + \frac{1}{C_o} \quad (4.21)$$

With a change of the water velocity, the values of  $X$  and  $Y$  are altered. The modified Wilson plot technique consists of measuring several points of this linear relation and performing a linear regression on these points. The inverse slope of this fit gives the value of  $C_i$  and the inverse of the Y-axis intercept yields  $C_o$ . Our interest is the value of  $C_i$ , as in combination with the Gnielinski correlation the water side coefficient can be determined according to 4.17.

### 4.2.4 Measurement procedure

The experimental procedure for the Wilson plot technique on a single tube is the following:

1. The tube to be tested is connected to the water loop in a one water pass configuration. The top two tubes are connected in a two pass configuration to a thermal bath which provides cold glycol. Condensation takes place on these two tubes to compensate for the evaporation on the tested tube. All the other tubes are inactive.
2. The outlet of the test section is closed and test section is filled with refrigerant by the pump. The liquid level is adjusted to be just above the tested tube and then the test section is isolated from the rest of the refrigerant circuit.
3. The temperature and the flow rate of the water are adjusted to reach the desired heat flux on the tube while the temperature of the glycol is chosen to maintain the saturation conditions. When everything is stable, an acquisition of the key parameters is made.
4. Water flow rate and water temperature are then changed so that the heat flux (and thus the external heat transfer coefficient of equation 4.19) remains constant. For example, the inlet temperature is decreased and the flow rate is increased.

This last operation is repeated for each measurement point. The conditions of the water in terms of temperature and flow rate in this Wilson plot technique are chosen to cover the planned experimental conditions so that the relation for the water side heat transfer will be applicable.

### 4.3 Physical properties evaluation

All the physical properties of water were determined with the software EES. For the physical properties of the refrigerant, the software REFPROP was used. The values have been exported from these programs as a function of temperature into a look up table with a step size of  $0.1K$ . Every time a physical property is necessary, our calculation program goes into this table and makes a linear interpolation of the value based on the current temperature and the two closest ones in the table. The linear interpolation is usually based on the temperature but could also be any other property. For example, the properties of the refrigerant at saturation are often determined based on the pressure. By this procedure, accurate values of the physical properties are used all the time in the calculations.

### 4.4 Results and accuracy

Modified Wilson plots for each type of tube are shown in figure 4.1. The slope of the linear regression in these plots corresponds to the inverse of the corrective multiplier,  $C_i$ , for the internal heat transfer coefficient.

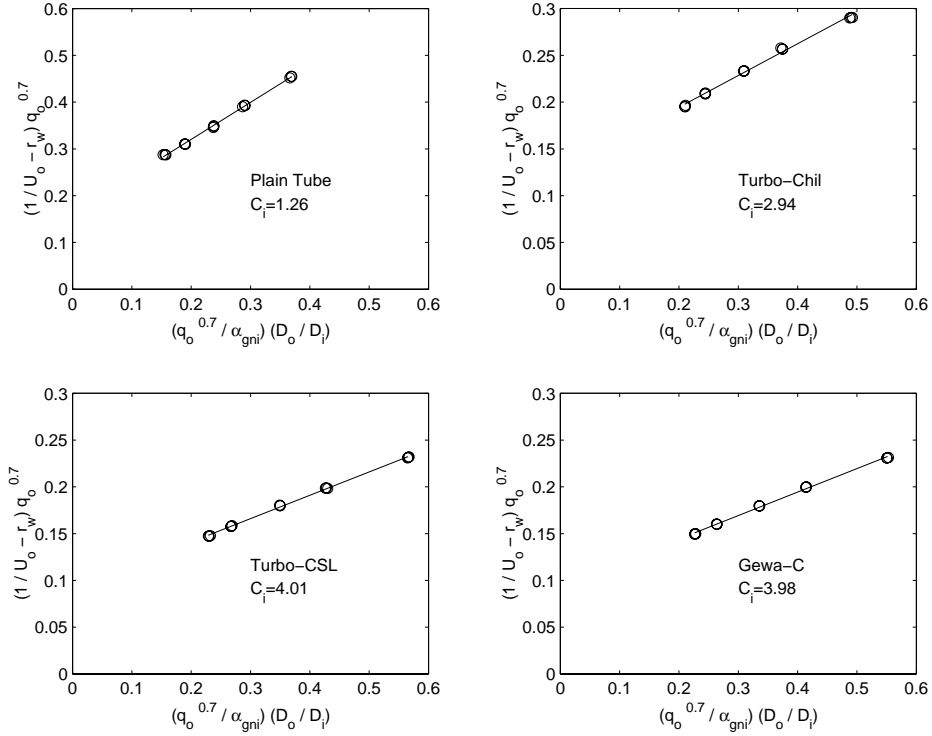


Figure 4.1: Modified Wilson plots for all types of tubes in pool boiling.

The modified Wilson tests were conducted over a water side Reynolds number range from 6000 to 16000 that will be used in the condensation experiments. For the plain tube, different instrumented stainless steel tubes inside different plain tubes were tested to verify the reproducibility of the measurements. To check the reliability of the method, tests were performed also at different heat fluxes and different saturation temperatures, implying different water temperatures.

The results of all modified Wilson plots for the plain tube are summarized in table 4.1. The measured value  $C_i$  does not show a distinct dependence of heat flux or temperature. For this reason, the average value of 1.27 obtained from all eight Wilson plots is used for the plain tubes. The uncertainty of this value is estimated to be within  $\pm 0.1$ . The value of  $C_i$  includes the effect of the inserted stainless steel tube with a spiral wire wound on it and so it is expected to be larger than the normal value of 1.0.

For each type of enhanced tube, three modified Wilson plots tests were conducted: Two measurements of different instrumented stainless steel tubes under identical conditions and one test at a different heat flux. All tests were performed at a saturation temperature close to room temperature. The

instrumented tube	$T_{sat}$ [K]	$q_o$ [kW/m <sup>2</sup> ]	$C_i$ [-]
5	283	24 to 27	1.30
6	283	25 to 27	1.18
3	283	23 to 24	1.27
4	283	25 to 28	1.26
2	283	24 to 28	1.19
4	283	24 to 26	1.40
4	293	32 to 35	1.26
4	300	33 to 35	1.30
average value for plain tube			1.27

Table 4.1: Measurements of the corrective multiplier of the water side coefficient for the plain tube.

results of these tests are given in tables 4.2 to 4.4.

instrumented tube	$T_{sat}$ [K]	$q_o$ [kW/m <sup>2</sup> ]	$C_i$ [-]
10	294	38 to 43	2.94
4	294	38 to 40	3.25
10	291	73 to 77	2.93
average value for Turbo-Chil			3.04

Table 4.2: Measurements of the corrective multiplier of the water side coefficient for the Turbo-Chil tube.

instrumented tube	$T_{sat}$ [K]	$q_o$ [kW/m <sup>2</sup> ]	$C_i$ [-]
10	298	39 to 41	4.01
3	297	37 to 39	3.73
10	297	79 to 82	3.76
average value for Turbo-CSL			3.83

Table 4.3: Measurements of the corrective multiplier of the water side coefficient for the Turbo-CSL tube.

The average values of  $C_i$  are: for Turbo-Chil 3.04, for Turbo CSL 3.83, and for Gewa-C 3.99. The uncertainty for these values is estimated to be within  $\pm 0.2$ .

The internal enhancements and the stainless steel tube with the spiral wound wire help also to reduce entrance effects of the cooling water which are expected to be negligible. However, to verify this assumption the  $C_i$  values were additionally determined at several axial locations and found to

instrumented tube	$T_{sat}$ [K]	$q_o$ [kW/m <sup>2</sup> ]	$C_i$ [-]
10	296	41 to 44	3.99
3	296	39 to 40	4.14
10	296	78 to 79	3.86
average value for Gewa-C			3.99

Table 4.4: Measurements of the corrective multiplier of the water side coefficient for the Gewa-C tube.

be consistent with the values mentioned above.

## 4.5 Influence of external heat transfer coefficient

In order to determine the values of  $C_i$ , a value of 0.7 of the exponent was assumed in equation 4.19. Roques [55] determined in pool boiling measurements (using  $C_i = 1.27$ ) a value of the exponent of 0.4 for the plain tube also used in the present study. Reevaluation of all eight Wilson plots for the plain tube with this exponent of 0.4 instead of 0.7 in equation 4.19 lead to a small decrease of the average value from  $C_i = 1.27$  to  $C_i = 1.26$ , showing that Wilson plots involving nucleate pool boiling performed in the current investigation are not sensitive to the value of the exponent used in equation 4.19. As this influence is negligible, the value of  $C_i = 1.27$  was kept for further processing of the data for the plain tube.

For the low finned tube, it was also assumed above that the heat transfer during pool boiling can be described by 4.19. With the assumed value of 0.7 for the exponent, a value of  $C_i = 3.04$  was obtained. As the Wilson plots were performed at different heat flux levels, the data of all three Wilson plots for the Turbo-Chil tube could also be treated as pool boiling data (using the first guess  $C_i = 3.04$ ) to determine a new value of the exponent. By this procedure, the new value of the exponent was found to be 0.28. Reevaluating the three Wilson plots for the Turbo-Chil tube with this experimentally determined exponent gave a new mean value of  $C_i = 2.93$ . The data of all three Wilson plots was then processed again (using  $C_i = 2.93$ ) to redetermine the value of the exponent. In this second iteration, the value of the exponent increased slightly to 0.29, which leads after reevaluation of the Wilson plots to a mean value of  $C_i = 2.94$  for the Turbo-Chil tube. The values obtained in the second iteration step were close to the values obtained in the first iteration step. For this reason no further iterations were made and the value of  $C_i = 2.94$  was used for the further data reduction for the Turbo-Chil tube.

For the 3D enhanced tubes, the Turbo-CSL and the Gewa-C tube, the first estimates obtained from the Wilson plots using  $\alpha_o = C_o q_o^{0.7}$  were  $C_i = 3.83$  and  $C_i = 3.99$ , respectively. Applying the same iterative procedure as



for the low finned tube described above, the values of the exponents of the heat flux were determined to be 0.47 for the Turbo-CSL tube and 0.49 for the Gewa-C tube in the first iteration. Using of these exponents instead of the value 0.7 in evaluating the Wilson plots had no effect on the mean value of  $C_i$  for both 3D enhanced tubes.

This iterative procedure allowed the values of  $C_i$  to be determined from the Wilson plots for the enhanced tubes without making an assumption of the exponent of the heat flux to describe the nucleate pool boiling heat transfer on the outside of the tube.

## 4.6 Independent cross checks

An alternative approach is to determine the coolant side multiplier  $C_i$  using condensation data (without inundation). For the plain tubes and low finned tubes, it is very well established that for condensation on a single tube the  $q_o$ - $\Delta T$  relationship is very closely represented by

$$q_o = C_o \Delta T^{3/4} \quad (4.22)$$

This corresponds to the Nusselt theory for plain tubes and it has also been established in many measurements with different fluids and where wall temperatures have been measured directly. Based on this assumption, all the condensation data measured on the top tube in the array without inundation can be used to perform a Wilson plot. The evaluation is the same as mentioned above for the Wilson plot involving pool boiling, except that equation 4.19 becomes:

$$\alpha_o = C_o q_o^{-1/3} \quad (4.23)$$

The results of this approach of a Wilson plot using the condensation data (without inundation) are depicted in figure 4.2. For the plain tube a value  $C_i = 1.25$  is obtained and for the low finned tube  $C_i = 2.82$ . These values are within the estimated uncertainty of the ones determined in the Wilson plots involving nucleate pool boiling ( $1.27 \pm 0.1$  and  $2.94 \pm 0.2$ ).

The values of the water side multiplier obtained by the pool boiling Wilson plots are expected to be the more accurate ones, as no assumption describing the heat transfer on the outside of the tube (as  $q_o = C \Delta T^{3/4}$ ) has to be made. In addition during nucleate pool boiling, the external heat transfer coefficient is larger than during condensation, resulting in smaller uncertainty in determining  $C_i$ . Nucleate boiling coefficients around the perimeter of a tube are close to uniform at high heat fluxes while those for condensation are not. As mean perimeter-averaged values are measured, it is favorable to minimize stratification effects on the water temperature and have a uniform heat transfer coefficient around the external perimeter of the tube.

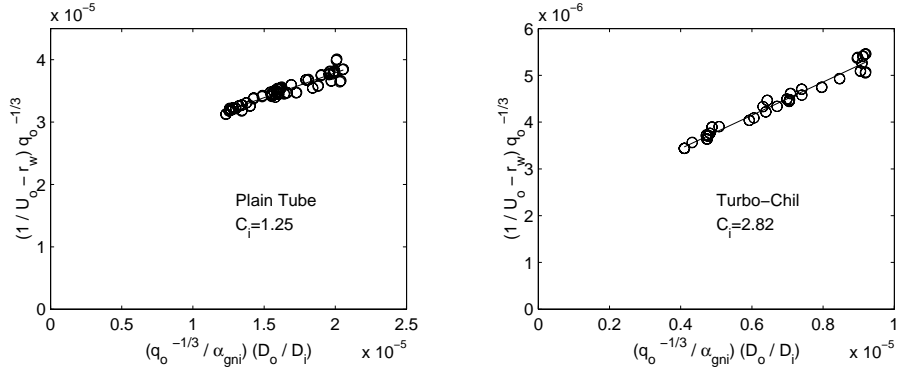


Figure 4.2: Modified Wilson plots using the condensation data (without inundation) for the plain and low finned tubes.

## 4.7 Conclusion

The water side heat transfer coefficients were determined experimentally for all tubes using a modified Wilson plot technique. The Wilson plot procedure was implemented using nucleate pool boiling on the outside of a tube for each type of tubes, while the tube was installed identically in the test section as for the condensation tests. The multipliers  $C_i$  for the four types of tubes to be experimentally tested were accurately obtained, which include the characteristics of the experimental setup. This means mainly the influence of the instrumented stainless steel tube with the spiral wound wire and also the internal enhancement of the copper tubes. With these corrective multipliers and the Gnielinski correlation, the water side coefficient can be calculated. A known water side coefficient allows the determination of the external heat transfer coefficient during condensation based on measurement of the water temperature inside the tube and its profile to get the local heat flux. The values of the multipliers for all types of tubes are listed in table 4.5.

Tube	$C_i$ [-]
Plain Tube	$1.27 \pm 0.1$
Turbo-Chil	$2.94 \pm 0.2$
Turbo-CSL	$3.83 \pm 0.2$
Gewa-C	$3.99 \pm 0.2$

Table 4.5: Corrective multipliers for internal heat transfer coefficient ( $\alpha_i = C_i \alpha_{gni}$ ).

## Chapter 5

# Heat Transfer Measurements

In this chapter, first the method used to determine the heat transfer coefficient locally on the outside of the tubes during condensation is described and then a propagation of error analysis is performed. Next, the test conditions are given and finally the results of the heat transfer measurements are presented.

### 5.1 Data reduction

Using water flowing through the tubes to condense the refrigerant on the outside of the tubes, the water undergoes a temperature change while the phase changing refrigerant stays at the same saturation temperature. This produces a change in local heat flux as the temperature difference between the water and the refrigerant decreases along the length of the tubes. In previous published studies, only the inlet and outlet temperature of the water have been measured. This means they have all assumed a linear water temperature profile as function of tube length, subsequently implying a constant heat flux, to obtain a mean heat transfer coefficient for each tube rather than local values

In this study, the internally mounted thermocouples measuring the water temperature within the tubes in the axial direction permit the determination of the water temperature profile as a function of the distance along the tubes:

$$T_{wat} = f(x) \quad (5.1)$$

As shown in chapter 4, the local heat flux on the outside of the tube can be derived from the water temperature profile as

$$q_o = \frac{\dot{m}c_{p,wat}}{\pi D_o} \frac{dT_{wat}}{dx} \quad (5.2)$$

where  $\dot{m}$  is the mass flow rate and  $c_{p,wat}$  the specific heat of water. The local overall heat transfer coefficient  $U_o$  can be calculated from the heat flux

as

$$U_o = \frac{q_o}{T_{sat} - T_{wat}} \quad (5.3)$$

with the saturation temperature of the refrigerant  $T_{sat}$  and the bulk temperature of the water  $T_{wat}$ . The condensing side heat transfer coefficient  $\alpha_o$  is obtained from:

$$\alpha_o = \left[ \frac{1}{U_o} - \frac{1}{\alpha_i} \left( \frac{D_o}{D_i} \right) - r_w \right]^{-1} \quad (5.4)$$

where  $\alpha_i$  is the water side heat transfer coefficient and  $r_w$  the thermal resistance of the copper tube given by

$$r_w = \frac{D_o}{2\lambda_{cop}} \ln \left( \frac{D_{or}}{D_i} \right) \quad (5.5)$$

$D_i$  is the inside diameter of the tube,  $D_{or}$  the outside root diameter, and  $\lambda_{cop}$  the thermal conductivity of the tube material.

The inside heat transfer coefficient  $\alpha_i$  is obtained from the Gnielinski correlation with a corrective multiplier:

$$\alpha_i = C_i \alpha_{gni} \quad (5.6)$$

The determination of this corrective multiplier  $C_i$ , which includes influences of the experimental setup, was described earlier in chapter 4.

With the help of equations 5.2 to 5.6, the heat transfer on the outside of the tube can be calculated from a measured water temperature profile, the water mass flow rate, and the saturation temperature of the refrigerant. For a given water temperature profile, the outside heat transfer coefficient can be calculated at any location along the axis of the tube. However, in this study the coefficient  $\alpha_o$  is only evaluated at the midpoint of every tube, where the most accurate measurement can be made.

The amount of condensate created on the outside of one tube is derived from the local heat flux given by equation 5.2 and the latent heat  $h_{LV}$  of the refrigerant. With the assumption that the liquid on the tube is at its saturation condition, the mass flow of refrigerant condensing on one tube locally is calculated by an energy balance on a differential element

$$(2\Gamma_{bottom} - 2\Gamma_{top})h_{LV}dx = q_o\pi D_o dx \quad (5.7)$$

where  $2\Gamma$  is the total mass flow rate on the tube per unit width and  $\Gamma$  is the flow rate on one side of the tube per unit length of tube falling on top of the tube or leaving at the bottom, respectively. With this definition, the film Reynolds number on the tube is

$$Re = \frac{4\Gamma}{\mu_L} \quad (5.8)$$

and is equivalent to that on a vertical plate in the Nusselt theory. For the measurements with liquid overfeed, the film Reynolds number of the liquid arriving on the first tube is obtained from the measured mass flow rate (Coriolis mass flow meter) and the tube length, assuming that the refrigerant is at saturation conditions (it is subcooled less than  $0.8K$ ). The amount of the additional liquid condensate formed on the first tube calculated with 5.7 is added to obtain the film Reynolds number at the bottom of the first tube. The film Reynolds number of the liquid falling on the second tube is set to the value leaving the first and so on. This means an ideal one-dimension downward flow is assumed on the tube rows. All the liquid flows from one tube to the next without leaving the tube row. Thus, the mass flow rate per unit width of the liquid falling onto the  $N$ th tube in the array one side of the tube is obtained by

$$\Gamma_{top,N} = \Gamma_{overfeed} + \sum_{n=1}^{N-1} \frac{q_{o,n} \pi D_o}{2h_{LV}} \quad (5.9)$$

where  $\Gamma_{overfeed}$  is the amount of liquid from the liquid distributor per unit width of tube and on one side of the tube.

## 5.2 Measurement accuracies

As shown in the previous section, the experimentally obtained external heat transfer coefficient  $\alpha_o$  is mainly a function of the saturation temperature  $T_{sat}$ , the water temperature  $T_{wat}$ , the heat flux  $q_o$  and the internal heat transfer coefficient  $\alpha_i$ . The influence of parameters like the tube dimensions and geometrical properties of the experimental setup have been found to be of minor importance and are not considered in this error analysis. Thus:

$$\alpha_o = f(T_{sat}, T_{wat}, q_o, \alpha_i) \quad (5.10)$$

The *saturation temperature* is calculated from the pressure measured by one pressure transducer above the tube row and one below the tube row with the assumption that the vapor is at saturation. The absolute error of both pressure transducers is  $1kPa$ . The measured variation in pressure during the data acquisition is always smaller than the absolute error of the transducers. The measured pressure difference of the two transducers is in most of the measurements also smaller than  $1kPa$ . With refrigerant R-134a, a change in saturation pressure of  $1kPa$  corresponds to a change in saturation temperature of  $0.05K$ . To cover this temperature range, the error on the saturation temperature is estimated to be within  $\Delta T_{sat} = \pm 0.03K$  since it is based on two measurement sensors, i.e.  $0.05/\sqrt{2}$ .

The *water temperature* in the middle of the tube is evaluated from the polynomial fit of the water temperature profile. As a second order poly-

mial is used for the fit of the six thermocouples at three axial locations, the fit is exactly the mean value of the two thermocouples at every location. In other words, the water temperature calculated with the polynomial in the middle of the tube is the same as the mean value of the two thermocouples at this position. The uncertainty of a single thermocouple after calibration is  $\pm 0.03K$ . Consequently, the error of the water temperature measured by two sensors is estimated to be within  $\Delta T_{wat} = \pm 0.03/\sqrt{2}K = \pm 0.02K$ , as it is measured by two thermocouples at the same location, i.e. the mean temperature at each location is taken from two independent measurements and hence the error of the mean value is  $1/\sqrt{n}$  where  $n$  is the number of independent measurements.

According to equation 5.2, the *heat flux* is calculated from the derivative of the water temperature profile. Alternatively, it can be shown that for the specific case of a second order polynomial fit through the thermocouples at three equidistant locations, the heat flux in the middle of the tube can also be calculated by

$$q_o = \frac{\dot{m}c_{p,wat}}{\pi D_o L}(T_{wat,out} - T_{wat,in}) \quad (5.11)$$

where  $T_{wat,in}$  is the mean value of the two thermocouples at the inlet,  $T_{wat,out}$  is the mean value of the two thermocouples at the outlet, and  $L$  is the distance between these two locations. This means that the local heat flux in the middle of the tube (equation 5.2) is exactly the mean value over the tube length (equation 5.11).

The uncertainty of the local heat flux  $\Delta q_o$  can now be estimated for this case as follows

$$\Delta q_o = \sqrt{\left(\frac{\partial q_o}{\partial \dot{m}} \cdot \Delta \dot{m}\right)^2 + \left(\frac{\partial q_o}{\partial T_{wat,out}} \cdot \Delta T_{wat,out}\right)^2 + \left(\frac{\partial q_o}{\partial T_{wat,in}} \cdot \Delta T_{wat,in}\right)^2} \quad (5.12)$$

Evaluation of the partial derivatives and substitution of the temperature uncertainties by  $\Delta T_{wat} = \Delta T_{wat,out} = \Delta T_{wat,in}$  leads to

$$\Delta q_o = \sqrt{\left(\frac{c_{p,wat}}{\pi D_o L}(T_{wat,out} - T_{wat,in}) \cdot \Delta \dot{m}\right)^2 + 2\left(\frac{\dot{m}c_{p,wat}}{\pi D_o L} \cdot \Delta T_{wat}\right)^2} \quad (5.13)$$

The uncertainty of the total water mass flow is given by equation 3.1, which gives a relative value smaller than 0.18% for all measurements. During the measurements, the total water mass flow is split into five parallel circuits going to the test section as mentioned before. To assure a uniform distribution to the sub-circuits, all five are equipped with a rotameter. With an ideal distribution, the absolute error of the total mass flow can be divided

by the number of circuits, each with its own valve and float meter ( $\pm 1\%$  accuracy). To account for any maldistribution, the absolute uncertainty of the water flowing in one tube is assumed to be the same as the one of the total mass flow, which is for all measurements smaller than  $0.002\text{kg/s}$  (equivalent to increasing the uncertainty by a factor of 5). With these assumptions, the uncertainty of the heat flux is mainly determined by the second summand in equation 5.13 by the uncertainty of temperature measurement. During the heat transfer measurements, the error in the measurement of the mass flow was found to be almost negligible compared to the error in the temperature measurements.

According to equation 5.6, the *internal heat transfer coefficient*  $\alpha_i$  is calculated from the Gnielinski correlation and a corrective multiplier  $C_i$ . The accuracy of the internal heat transfer coefficient is mainly determined by the accuracy of this corrective multiplier. The relative uncertainty in the value of  $C_i$  corresponds approximately to the relative uncertainty of the internal heat transfer coefficient. The values of  $C_i$ , the absolute error and the relative error determined in chapter 4 for the four tested tubes are summarized in table 5.1.

Tube	$C_i$ [-]	$\Delta C_i$ [-]	$\Delta C_i/C_i$ [%]
Turbo-CSL	3.83	0.2	5.2
Gewa-C	3.99	0.2	5.0
Turbo-Chil	2.94	0.2	6.8
Plain Tube	1.27	0.1	7.8

Table 5.1: Corrective multipliers for internal heat transfer coefficient  $\alpha_i$  with absolute and relative uncertainty.

Finally, the accuracy of the external heat transfer coefficient  $\Delta\alpha_o$  is estimated based on equation 5.10 by

$$\Delta\alpha_o = \left[ \left( \frac{\partial\alpha_o}{\partial T_{wat}} \cdot \Delta T_{wat} \right)^2 + \left( \frac{\partial\alpha_o}{\partial T_{sat}} \cdot \Delta T_{sat} \right)^2 + \left( \frac{\partial\alpha_o}{\partial q_o} \cdot \Delta q_o \right)^2 + \left( \frac{\partial\alpha_o}{\partial \dot{m}} \cdot \Delta \dot{m} \right)^2 + \left( \frac{\partial\alpha_o}{\partial C_i} \cdot \Delta C_i \right)^2 \right]^{1/2} \quad (5.14)$$

The values of the mean relative errors in local heat flux for all principal tests at three different nominal heat fluxes are presented in table 5.2. The mean relative errors in local heat transfer coefficient are given in table 5.3.

The uncertainty in local heat flux and local heat transfer coefficient decreases with increasing heat flux. For a higher heat flux, the temperature differences become larger which means that the relative error of a temperature difference decreases for a constant absolute error in the temperature

Tube	$\Delta q_o/q_o$		
	$q_o = 20kW/m^2$	$q_o = 40kW/m^2$	$q_o = 60kW/m^2$
Turbo-CSL	3.7%	2.1%	1.9%
Gewa-C	3.6%	2.0%	1.8%
Turbo-Chil	3.5%	2.0%	1.8%
<hr/>			
Plain Tube	$q_o = 6kW/m^2$	$q_o = 12kW/m^2$	$q_o = 20kW/m^2$
	8.1%	4.7%	3.6%

Table 5.2: Mean relative errors in local heat flux at the three nominal heat flux levels.

Tube	$\Delta\alpha_o/\alpha_o$		
	$q_o = 20kW/m^2$	$q_o = 40kW/m^2$	$q_o = 60kW/m^2$
Turbo-CSL	10.6%	6.1%	4.4%
Gewa-C	10.7%	6.3%	4.3%
Turbo-Chil	13.0%	8.8%	6.1%
<hr/>			
Plain Tube	$q_o = 6kW/m^2$	$q_o = 12kW/m^2$	$q_o = 20kW/m^2$
	12.0%	7.4%	5.7%

Table 5.3: Mean relative errors in local heat transfer coefficient at the three nominal heat flux levels.

measurement. In laminar film condensation the external heat transfer coefficient is determined by the thickness of the condensate film. A low heat flux creates a thin condensate film and hence a high heat transfer coefficient. In this case, the error in the measurement of the external heat transfer coefficient caused by the uncertainty of the internal heat transfer coefficient increases as the heat flux decreases.

The above propagation of error analysis has been applied to each experimental data point. For all measurements, the experimental uncertainty of the heat transfer coefficient  $\alpha_o$  is on average  $\pm 8.3\%$ , with 90% of points having an uncertainty less than  $\pm 12.8\%$ , and all points less than  $\pm 20.5\%$ .

The dominating parameters in the propagation of error analysis were found to be the measurements of the water temperatures and the internal heat transfer coefficient (due to the error on  $C_i$ ). In order to minimize the experimental errors during the experiments, this propagation of error analysis was also implemented on the data acquisition computer. This allowed the mass flow rate to be adjusted (to adjust  $\alpha_i$ ) during the measurements to obtain minimum experimental errors depending on the measured heat fluxes.



### 5.3 Test conditions

Four commercially available tubes were tested at three different intertube spacings: two condensation tubes with 3D enhanced surfaces (the Turbo-CSL and the Gewa-C), a low finned tube with 26 fpi / 1024 fpm (the Turbo-Chil), and a plain tube were used. The Gewa-C tube was provided by Wieland-Werke AG, all the others by Wolverine Tube Inc. Tube pitches tested were  $25.5mm$ ,  $28.6mm$ , and  $44.5mm$  resulting in intertube spacings between the tube rows of approximately  $6.4mm$ ,  $9.5mm$ , and  $25.5mm$ . During the measurements, the heat flux was kept constant and liquid overfeed rate was increased stepwise. Measurements with increasing overfeed rate were performed at three heat flux levels. The nominal heat fluxes were 20, 40, and  $60kW/m^2$  for the three enhanced tubes. For the plain tube lower heat fluxes of 6, 12, and  $20kW/m^2$  were tested because of its lower thermal performance. The matrix of the principal tests is given in table 5.4.

Tube pitch	Turbo-CSL $q_o [kW/m^2]$	Gewa-C $q_o [kW/m^2]$	Turbo-Chil $q_o [kW/m^2]$	Plain Tube $q_o [kW/m^2]$
$25.5mm$	20/40/60	20/40/60	20/40/60	6/12/20
$28.6mm$	20/40/60	20/40/60	20/40/60	6/12/20
$44.5mm$	20/40/60	20/40/60	20/40/60	6/12/20

Table 5.4: Test matrix for the measurements with liquid overfeed.

In addition, measurements without liquid overfeed were taken over the same heat flux range mentioned above. Due to of the current two-pass setup, the heat fluxes achieved on the odd and even tubes at one nominal heat flux varied substantially. An overview of the complete database established in the current investigation is given in table 5.5. The ranges of the main variables are listed for all types of tubes. The maximum values of vapor velocity, the superheating of the vapor and the subcooling of the liquid overfeed and the liquid inundation film Reynolds number in the test section are also given.

Tube	$q_o$ [kW/m <sup>2</sup> ]	$\Delta T_{wat}$ [K]	$T_{sat} - T_{wat}$ [K]	$T_{sat} - T_w$ [K]	$Re_{wat}$ [-]
Turbo-CSL (3384 points)	11.6 to 99.8	0.37 to 2.94	1.18 to 15.6	0.44 to 12.8	5780 to 12630
Gewa-C (3675 points)	12.9 to 95.0	0.47 to 3.00	1.34 to 13.8	0.43 to 10.9	7120 to 12810
Turbo-Chil (3921 points)	12.7 to 72.9	0.45 to 2.69	1.94 to 10.7	0.66 to 5.83	7820 to 12750
Plain Tube (4245 points)	3.6 to 22.9	0.20 to 0.97	4.49 to 21.7	2.50 to 16.3	4590 to 5580

Tube	$\alpha_i$ [kW/m <sup>2</sup> K]	$\alpha_o$ [kW/m <sup>2</sup> K]	$\alpha_i/\alpha_o$ [-]	$\Delta\alpha_o/\alpha_o$ [%]
Turbo-CSL (3384 points)	13.1 to 27.3	4.1 to 32.1	0.5 to 5.8	2.8 to 20.5
Gewa-C (3675 points)	18.2 to 30.8	5.0 to 33.8	0.6 to 5.6	2.8 to 19.8
Turbo-Chil (3921 points)	16.1 to 24.9	10.2 to 24.0	0.7 to 2.4	5.0 to 18.2
Plain Tube (4245 points)	3.5 to 4.4	0.9 to 2.6	1.5 to 4.1	5.5 to 17.5

Tube	Max. $u_V$ [m/s]	Max. $T_{super,V}$ [K]	Max. $T_{sub,L}$ [K]	Max. $Re_{ref,top}$ [-]
Turbo-CSL	0.14	0.21	0.49	4720
Gewa-C	0.16	0.21	0.72	4740
Turbo-Chil	0.16	0.24	0.62	4910
Plain Tube	0.08	0.16	0.65	2710

Table 5.5: Experimental database for refrigerant R-134a at a saturation temperature of 304K: ranges of the main variables and maximum values of the vapor velocity in the test section, superheating of the vapor, subcooling of the overfeed liquid and film Reynolds number.

## 5.4 Single tube data

### 5.4.1 Reproducibility

As mentioned above, at every specific tube pitch four series of measurements were performed. One series were the measurements without liquid overfeed on the top of the array of tubes where the heat flux was varied. During the other three series, the heat flux was held constant and the liquid overfeed rate was varied. These three series were always started without liquid overfeed before increasing the liquid overfeed rate. This means that the first measurement of the tests with liquid overfeed are in common with the series of measurements without overfeed. As the different test series were most of the time performed on different days, the comparison of the measurements without liquid overfeed can be used to check the reproducibility of the measurements. Figure 5.1 shows the data for the repeatability of the runs for all four types of tubes for the measurements at a tube pitch of  $28.6\text{mm}$ .

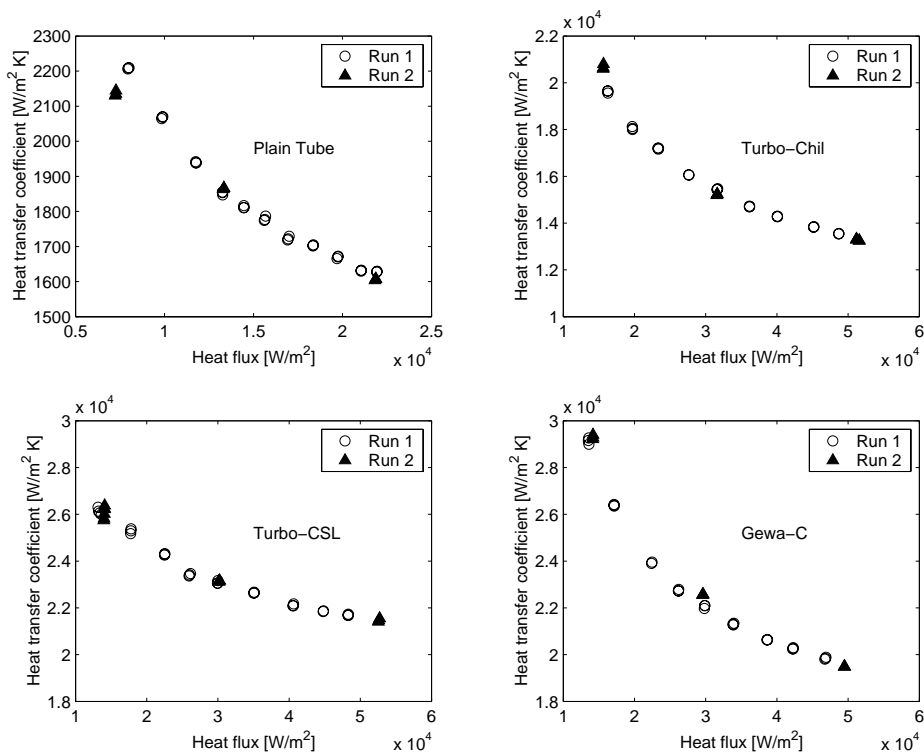


Figure 5.1: Reproducibility tests for top tube row without overfeed for all four types of tubes at a tube pitch of  $28.6\text{mm}$ .

The reproducibility of the experiments can be seen by comparing the data points of the measurements with varying heat flux (Run 1) and the

measurements at constant heat flux (Run 2). These figures (note the truncated vertical axis) indicate that the data for the top tube without liquid overfeed can be repeated over the entire range of heat fluxes. Comparisons were made for the measurements for the other two tube pitches showing that the measurements were repeatable for every experimental setup.

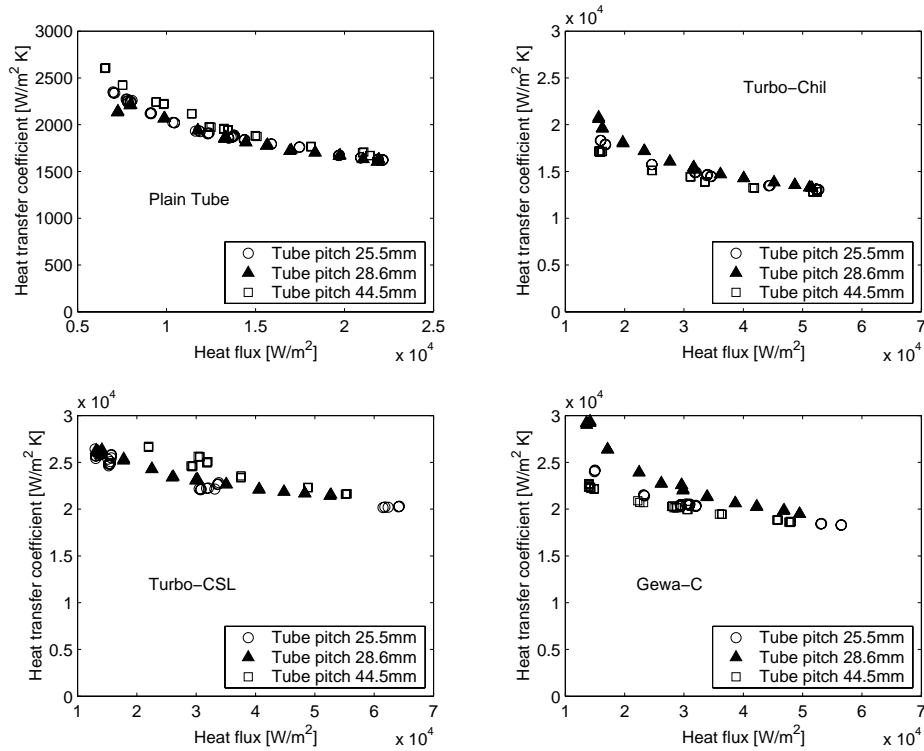


Figure 5.2: Top tube without liquid overfeed for all three tube pitches for all four types of tubes.

In figure 5.2, all the heat transfer coefficients measured on the top tube without liquid overfeed for all four types of tubes are plotted for all the three different tube pitches. The data obtained over the whole measurement period of six months are in good agreement for all types of tubes and all pitches, except the measured heat transfer coefficients for the Gewa-C at the tube pitch of 28.6mm are higher than for the other two tube pitches. The difference increases with decreasing heat flux. No effect of tube pitch is expected on the heat transfer performance of the top tube. The condensate flow pattern off the bottom of the top tube may change with increasing distance between the tube but this might only have an effect at high heat fluxes and not at low heat fluxes where the condensate drains in the form of droplets from the top tube. The observed deviations are probably due to

the increased uncertainty in the measurements at low heat flux. In order to change the tube pitch, the end plates of the test section had to be changed. This means that also the test tubes and the instrumentation of the tubes were dismantled. The tubes and instrumentation were not always mounted at exactly the same position. This might explain the observed differences at the different tube spacings.

In figure 5.3, the same data as in figure 5.2 is plotted as a function of the condensation temperature difference across the liquid film ( $T_{sat} - T_{wall,o}$ ) on a logarithmic scale.

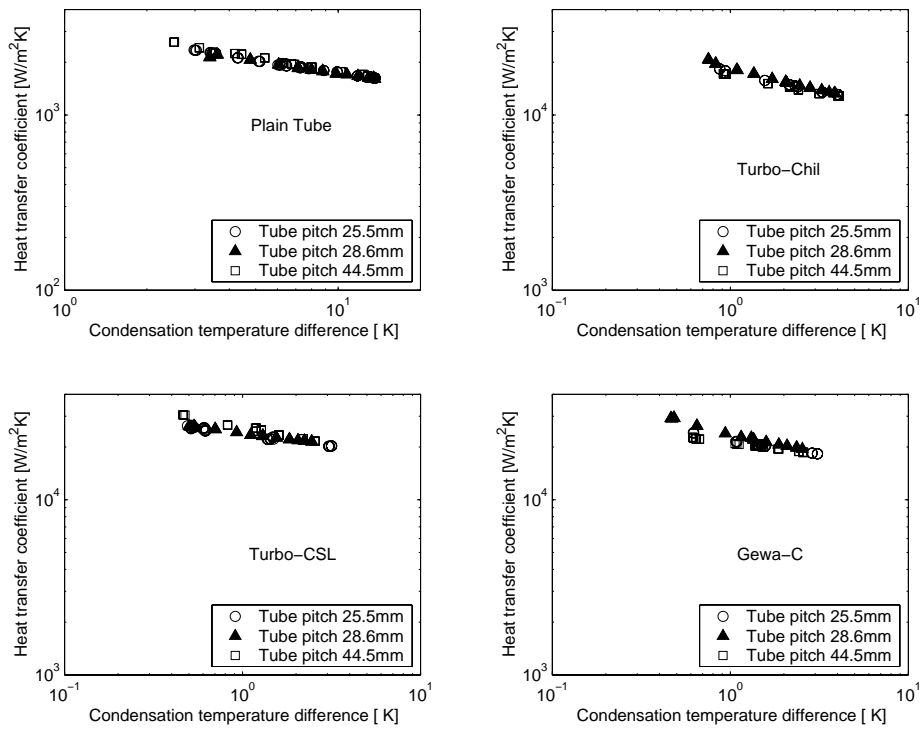


Figure 5.3: Top tube without liquid overfeed for all three tube pitches for all four types of tubes.

The measurements were performed at three heat flux levels with water cooling. For the enhanced tubes, the row average heat flux ranged from  $20kW/m^2$  to  $60kW/m^2$  and for the plain tube from  $6kW/m^2$  to  $20kW/m^2$ , respectively, which resulted in local heat fluxes on the top tube of approximately 15 to  $60kW/m^2$  for the enhanced tubes and 6 to  $22kW/m^2$  for the plain tube in the whole series of tests. As the tubes differ in heat transfer coefficients, the condensation temperature difference to achieve the desired heat flux is different for the tested tubes. The condensation temperature

difference ranged from 2.5 to 14K for the plain tube, from 0.8 to 4.2K for the Turbo-Chil, from 0.5 to 3.2K for the Turbo-CSL, and from 0.5 to 3.1K for the Gewa-C.

### 5.4.2 Comparison with other investigations

As R-134a is a new refrigerant, only a few data are available in literature for direct comparison with the tubes tested here. A comparison of the present experimental data with experimental data of R-134a of other investigations is made in figure 5.4. The data points of these investigations were digitized from the publications.

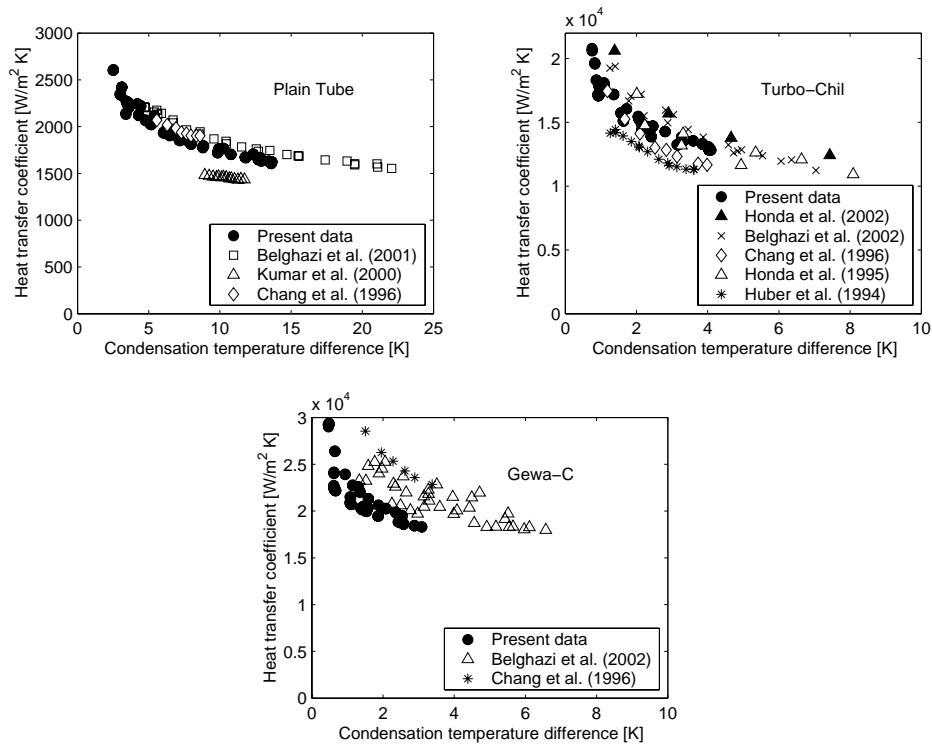


Figure 5.4: First tube without liquid overfeed.

For plain tubes in figure 5.4, Belghazi et al. [63] performed measurements on a 13x3 bundle of smooth horizontal tubes. They report data of the heat transfer coefficient on the first row for condensation of R-134a at a saturation temperature of 40°C. Their values are slightly higher than values for the plain tube in the present study. This might be due to the fact that the tubes they tested were 16.8mm in diameter as opposed to 18.99mm used in the present investigation. Smaller tubes tend to have a higher heat transfer coefficient as the condensing length is shorter (i.e. as per Nusselt's theory).

Kumar et al. [64] performed single tube tests with R-134a condensing on a plain tube which was  $21.35\text{mm}$  in diameter. The data they obtained at a saturation temperature of  $39^\circ\text{C}$  are lower than in the present study, again as would be expected. Chang et al. [65] conducted experiments to study the condensation heat transfer characteristics of horizontal enhanced tubes. He tested a plain tube and different enhanced tubes including a 26 fpi low fin tube and a Gewa-C tube. Their experimental points for the plain tube with a diameter of  $19.03\text{mm}$  are close to those of the current investigation.

A comparison for the Turbo-Chil tube is given in figure 5.4 on the right. More data are available in the literature for condensation of R-134a on 26 fpi low fin tubes than for plain tubes. Honda et al. [40] studied the condensation of R-134a on a staggered bundle of finned tubes. In their publication the effect of vapor shear was investigated. For the comparison here, only their data at the lowest vapor velocity were taken. The geometrical specification of their tube is close to the Turbo-Chil tested in the present investigation, but their measured values of the heat transfer coefficient are a little higher which might be due to vapor shear or the small dimensional differences. Belghazi et al.[66] gave data for the heat transfer coefficient on the top row in their bundle of K26 tubes, 26 fpi low fin tubes from Wieland. The same data are apparently also reported in [25]. Their experimental data for their low finned tube are a little higher than the present data. This might be due to the larger fin height of their tubes, which is  $1.5\text{mm}$  as opposed to  $1.36\text{mm}$  of the tubes used in the present study. Chang et al. [65] tested a 26 fpi low finned tube with a fin height of  $1.16\text{mm}$ . Their experimental data are a little lower than the present data at higher condensate temperature differences. Honda et al. [37] tested a bundle of smaller diameter low finned tubes. Their tubes were  $15.6\text{mm}$  in diameter, but had approximately the same fin height of  $1.43\text{mm}$ . Their data is a little higher than the present data, but lower than their data for the larger tubes. Condensation on low finned tubes is controlled by surface tension with the fin height as the characteristic length and not the tube diameter which is the characteristic length for the gravity controlled condensation on the plain tube. Huber et al. [46] studied condensation of R-134a on a 5x5 staggered bundle of 26 fpi low fin tubes. Their tubes were  $18.8\text{mm}$  in diameter and had a fin height of  $1.45\text{mm}$ . They provided the experimental data in a tabular format. The heat transfer coefficients for the first row are listed in their publication, but only the average bundle heat flux is mentioned. For the comparison here, the condensation temperature difference was calculated based on the average bundle heat flux. Their data were a little lower than the present data.

A comparison of the heat transfer performance of the 3D enhanced tubes Turbo-CSL and Gewa-C is difficult. These geometries are only produced by Wolverine Tube and Wieland-Werke, respectively, and few data are available. No published data are currently obtainable for the Turbo-CSL to our

knowledge. A comparison of the heat transfer performance for the Gewa-C is also given in figure 5.4. Belghazi et al. [66] tested a Gewa C+ tube. Chang et al. [65] tested a Gewa-C tube. The geometric specifications (tube diameter, fin pitch, fin height) are very close to the ones of the Gewa-C tube used in the present investigations, but the fins were notched. However, the heat transfer coefficients measured in these studies are higher than the present data. In both studies, the external heat transfer was determined using a modified Wilson plot approach. In this technique the external heat transfer coefficient is derived from a measurement of the overall heat transfer coefficient. This means difficulties occur when the external heat transfer coefficient is high compared to the internal heat transfer coefficient. Another explanation for differences may be the fact that they measured mean values for the whole length of tube with a non-linear axial variation in the condensing temperature difference, as opposed to local values obtained in the present study.

### 5.4.3 Comparison with single tube correlations

For the plain tube, a comparison with Nusselt's well known equation for condensation (equation 2.1) on a single tube has been made. This equation is derived from his theory for laminar film condensation on a vertical plate given in appendix A. The Nusselt theory on a vertical plate has been extended to take into account the subcooling of the condensate. Rohsenow [67] suggested the use of an effective latent heat of evaporation  $h'_{LV}$  (equation A.18). Regarding other physical properties, Drew [68] proposed to evaluate the physical properties at an effective film temperature, which he gave as  $T_w + 0.25(T_{sat} - T_w)$ .

The effects of these two modifications for condensation predictions on a horizontal tube are illustrated in figure 5.5 in comparison to the plain tube data. Equation 2.1 was evaluated using both the effective latent heat of evaporation  $h'_{LV}$  and the latent heat of evaporation  $h_{LV}$ . The other physical properties were evaluated at the effective film temperature or at the saturation temperature. The use of the effective latent heat of vaporization and the effective film temperature gives the highest predictions for the heat transfer coefficient on the tube. Neglecting the effect of condensate subcooling and evaluation of the physical properties at the saturation temperature leads to the lowest prediction. The difference of these two methods is about 1% at a condensation temperature difference of  $2K$  and 6% at a condensation temperature difference of  $14K$ . The mean relative errors  $\epsilon$  of all four methods compared to the measured values are listed in table 5.6.

The deviations of the four methods are in the range of the scatter of the measured values and are smaller than the uncertainty in the measurement of the heat transfer coefficients. For this reason, the Nusselt theory without including the effect of subcooling and evaluation of the physical properties



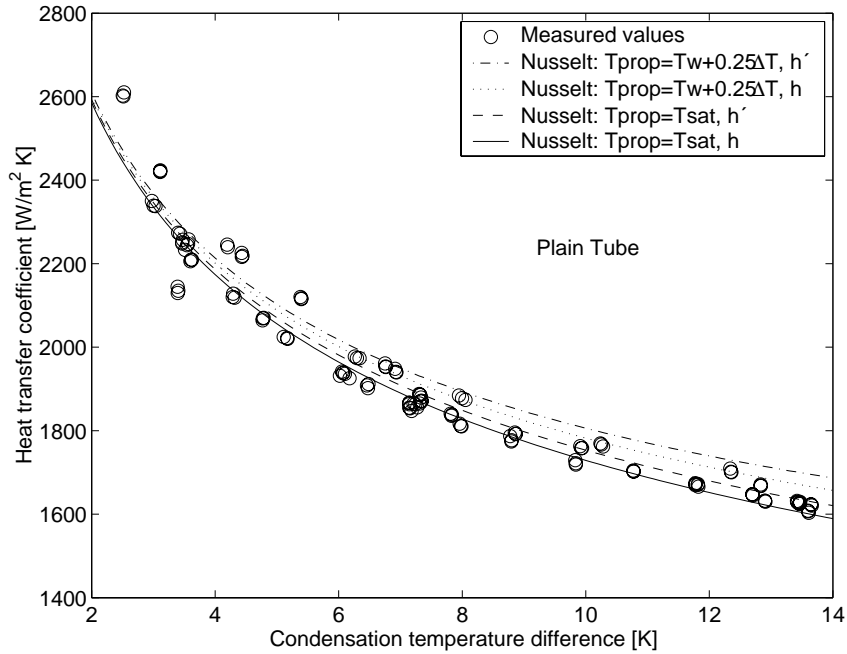


Figure 5.5: Comparison of single plain tube data with Nusselt's theory.

Method	$\epsilon$ [%]
$T_{prop} = T_w + 0.25(T_{sat} - T_w), h'_{LV}$	2.2
$T_{prop} = T_w + 0.25(T_{sat} - T_w), h_{LV}$	1.2
$T_{prop} = T_{sat}, h'_{LV}$	0.0
$T_{prop} = T_{sat}, h_{LV}$	-1.0

Table 5.6: Deviation of different applications of Nusselt's theory to the measured values for a single plain tube.

at saturation temperature, which is the easiest to implement, will be used for further comparisons.

Different correlations are available in the literature for condensation on a horizontal low finned tube. A comparison for the Turbo-Chil tube and a selection of correlations is shown in figure 5.6.

For the calculation of heat transfer coefficient of the Turbo-Chil tube, the actual fin pitch, the diameter at the fin root and mean value of the fin height given in table 3.1 were used in the correlations. The heat transfer coefficient was then related to the nominal area of the low finned tube using the diameter at the fin tip  $D_o$ . For all calculations, the physical properties of the refrigerant have been evaluated at saturation temperature, except

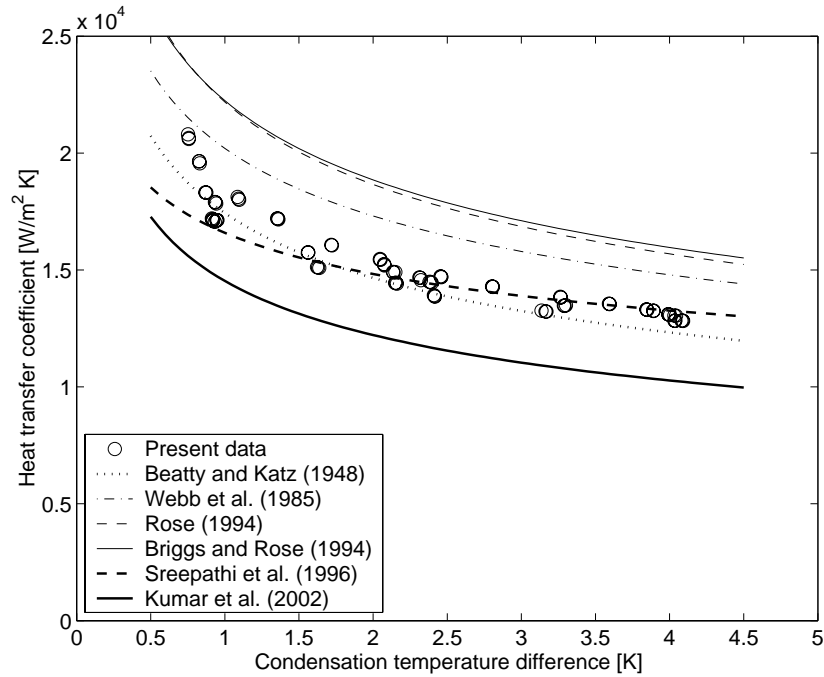


Figure 5.6: Comparison of single low finned tube data with different correlations.

for the model of Sreepathi et al. [24], who mentioned that they evaluated the physical properties at  $T_w + 0.5(T_{sat} - T_w)$ . The mean relative errors compared to the measured data for the low finned tube are listed in table 5.7.

Correlation	$\epsilon$ [%]
Beatty and Katz (1948)	-3.4
Webb et al. (1985)	14.0
Rose (1994)	22.9
Briggs and Rose (1994)	24.2
Sreepathi et al. (1996)	-2.2
Kumar et al. (2002)	-19.5

Table 5.7: Deviation of different correlations to the measured values for the single low finned tube data.

Surprisingly, the model of Beatty and Katz [9] is very close to the measured data, even though this model does not take into account the effects of surface tension. They assumed that the entire tube surface was active for

condensation as no condensate retention occurred, while they neglected the surface tension drainage from the fin to the fin root. In the present situation, the overestimation of active surface area seems to compensate for the underestimation of the increase in heat transfer on the fins due to thinning of the liquid film by surface tension. The fin efficiency, following the recommendation of Beatty and Katz, was set to one, which gives higher values for the heat transfer coefficient than when using the actual fin efficiency.

An early model for condensation on horizontal integral-fin tubes including the effect of surface tension was proposed Webb et al. [19]. In this method, they use an Adamek fin profile to predict the heat transfer coefficient on the fins involving the determination of the fin shape parameter  $\zeta$ . In the present evaluation of their model, the condensation on the fins was predicted using their earlier simplified linear pressure gradient model described in [69] as suggested by Thome [70] in order to avoid the determination of the shape parameter. However, Rudy and Webb [69] showed that this linear pressure gradient model lacks general validity and they do not recommend to use it. Evaluating their model in this way overestimates the measured heat transfer coefficient by 14%.

More recently, Rose [22] proposed a semi-empirical model for condensation on a low finned tube with a trapezoidal fin shape. This model overestimates the measured heat transfer coefficient by approximately 23%. This might be partially explained by the fact that this model neglects the temperature variation of the fin. Briggs and Rose [23] extended the model by adding the fin efficiency, but they assumed rectangular fin profiles only. For the evaluation of this model, a rectangular fin shape with average fin thickness  $t = (t_t + t_b)/2$  was used. The values obtained from this model are very close to the previous values of the model of Rose.

Sreepathi et al. [24] developed a correlation for a trapezoidal fin shape including fin efficiency effects. As seen on figure 5.6, this model underpredicts slightly the present data at low condensate temperature differences and overpredicts slightly the data at high condensate temperature differences. The mean deviation with respect to all measured data is only  $-2\%$ . By the way, neglecting the effect of fin efficiency, this model would overestimate the measured data by approximately 9%.

Kumar et al. [71] presented a very easy to use correlation. This correlation underestimates the present data by approximately 20%, which is smaller than the deviation of 35% they observed in a comparison with thirteen other investigators. Considering that all these methods typically claim to be accurate to about  $\pm 20\%$ , the deviations are within expectations.

Due to the complex surface structure of the 3D enhanced tubes, no analytical models and only few semi-empirical correlations exist for these types of types of tubes. Kumar et al. [71] also used data of spine shaped integral fin tubes for development of their correlation used for the comparison with the finned tube above. They manufactured these tubes by cutting axial slots

on the surface of a finned tube. Belghazi et al. [66] proposed a model for their 3D enhanced Gewa C+ tube data, which is a notched fin tube provided by Wieland-Werke AG. However, those methods are for their specific geometries and not for general application.

#### 5.4.4 Single tube correlations

No attempt has been made to provide a new analytical model for condensation on a single tube here. The previous section showed that the existing correlations for the plain tube and the low finned tube are in good agreement with the existing correlations. Instead, the experimental data are used to provide empirical correlations for all four types of tubes. Based on the Nusselt theory, an equation of following form is used:

$$\frac{\alpha_o}{\lambda_L} \left[ \frac{\mu_L^2}{\rho_L(\rho_L - \rho_V)g} \right]^{1/3} = a Re^b \quad (5.15)$$

The bracketed term together with its exponent is a characteristic length and the complete term to the left of the equal sign corresponds to the Nusselt number  $Nu^*$  with this characteristic length. The data for the top tube for all measurements without overfeed and for all four types of tubes are fit by equation 5.15 and the comparisons are given in figure 5.7. The term on the left of the equal sign, also denoted as condensation number, is plotted versus the film Reynolds number of the condensate leaving at the bottom of the tube.

As seen on figure 5.7, where best fit of the data is also depicted, the data can be well described with equation 5.15. Except for the data of the 3D enhanced tubes at low film Reynolds numbers, where some data are at higher values, which may be explained by the higher uncertainty in the measurement in this region. As a reference, the theoretical curve obtained from the Nusselt theory for a plain tube is also given. The values of the multiplier  $a$  and the exponent  $b$  in equation 5.15 for all types of tubes are listed in table 5.8. The values  $a$  and  $b$  obtained from the fit for the plain tube are very close to the theoretical values of the Nusselt theory which are 1.21 and  $-1/3$  respectively.

Tube	a	b
Plain Tube	1.20	-0.33
Turbo-Chil	10.32	-0.29
Turbo-CSL	8.50	-0.16
Gewa-C	9.99	-0.21

Table 5.8: Coefficients in equation 5.15 for condensation on a single tube without liquid overfeed for all four types of tested tubes.

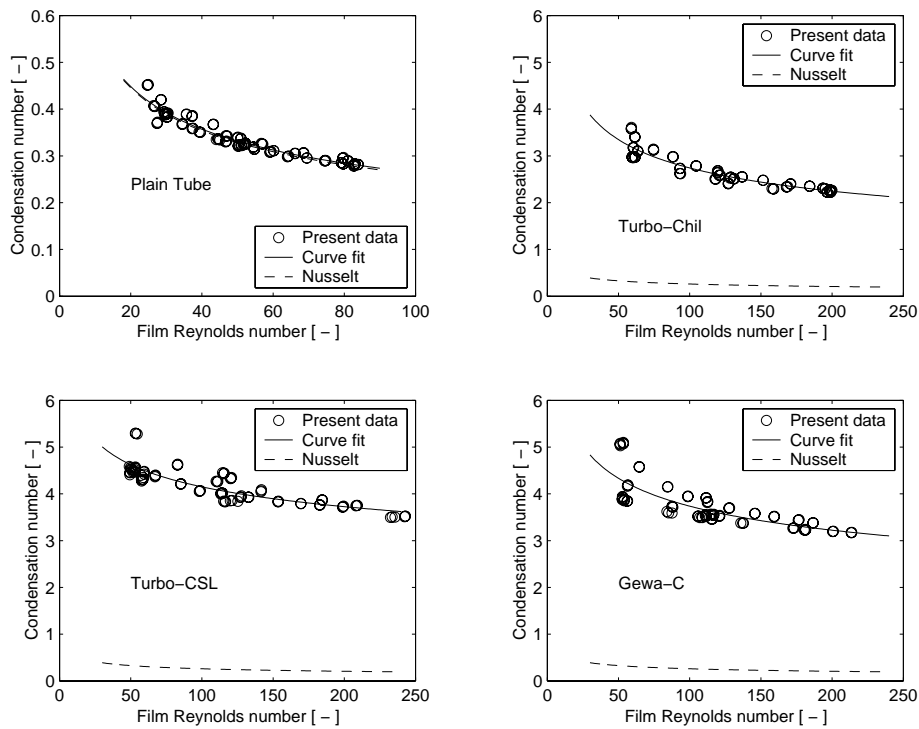


Figure 5.7: Curve fit of single tube data without liquid overfeed for all four types of tubes.

A comparison of the present empirical correlations for the single tube performance of all four types of tubes is given in figure 5.8. The ranges of the film Reynolds numbers correspond approximately to the measured ones. For the plain tube the film Reynolds numbers are smaller as the measured heat fluxes for this tube were smaller. The Turbo-CSL tube shows the highest single tube performance followed by the Gewa-C and low-finned tube.

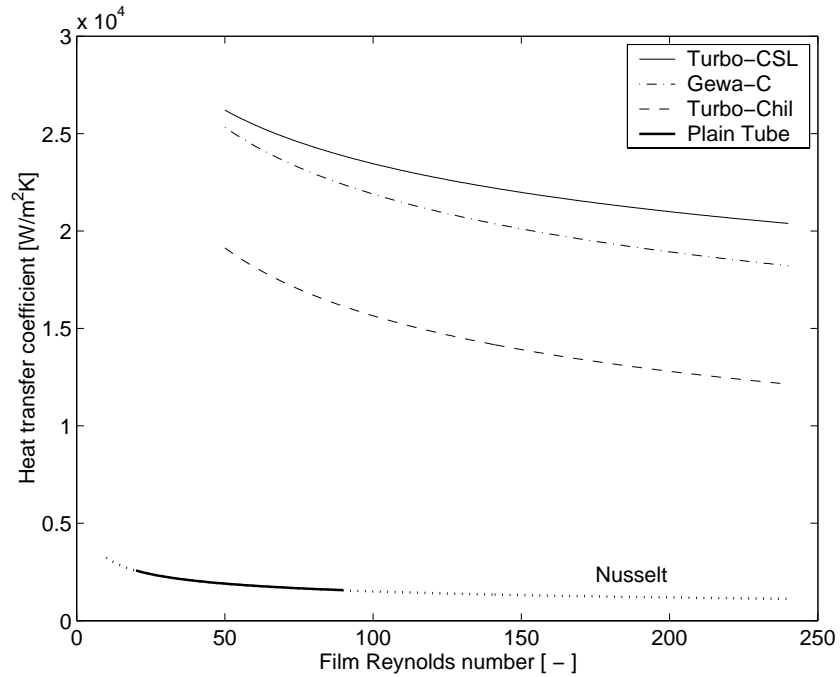


Figure 5.8: Comparison of single tube performance without liquid overfeed.

Alternatively to the correlations given above, the heat flux on the top tube without inundation can be correlated by an equation of the following form

$$q_o = C \cdot \Delta T^b \quad (5.16)$$

The values of the coefficients  $C$  and  $b$  for all types of tubes are listed in table 5.9. This approach is less general, as the coefficients  $C$  also include geometrical specifications and the physical properties of R-134a condensing at a saturation temperature of 304K.

Tube	C [W/m <sup>2</sup> ]	b [-]
Plain Tube	3100	0.75
Turbo-Chil	17780	0.77
Turbo-CSL	24270	0.86
Gewa-C	22420	0.81

Table 5.9: Coefficients in equation 5.16 for the heat flux on a single tube without liquid overfeed for all four types of tested tubes.

## 5.5 Measurements with liquid inundation

In order to characterize the heat transfer performance of the four types of tubes over a large operating range, measurements have been performed with liquid overfeed on the top of the array of tubes. The measurements were conducted with four different types on three arrays with different tube pitches at three nominal heat fluxes. The effect of these three main parameters, the general behavior of the four types of tubes, the influence of the tube pitch and heat flux are illustrated in the following subsections

### 5.5.1 Tube Behavior

Measurements were performed at three tube pitches and and three heat fluxes for each type of tubes. The nominal heat fluxes were 20, 40, and  $60kW/m^2$  for the enhanced tubes and 6, 12 and  $20kW/m^2$  for the plain tube. The differences in tube behavior for four types of tubes are illustrated by a comparison at heat flux of 40 and  $12kW/m^2$ , respectively, at the smallest tube pitch of  $25.5mm$ .

As shown in the preceding section, the tubes with a 3D enhanced surface structure, the Turbo-CSL and Gewa-C tubes, have the highest single tube heat transfer performance. The result of one series of measurements with liquid overfeed of the Turbo-CSL tube is given in figure 5.9. The heat transfer coefficient is plotted versus the film Reynolds number of the condensate leaving the bottom of each tube in analogy to the single tube tests. These measurements were performed with the smallest tube pitch of  $25.5mm$  at a mean heat flux of  $40kW/m^2$ . Starting with no liquid overfeed, the mass flow rate was increased stepwise to a maximum mass flow rate of  $0.135kg/ms$ , with a smaller step width at low mass flow rates.

The upper plot in figure 5.9 depicts the measured local heat transfer coefficient of each of the ten tubes for every overfeed rate  $\Gamma$  fed onto the top tube of the array. The bullets are the measured values for the ten tubes without liquid overfeed ( $\Gamma = 0kg/ms$ ). The film Reynolds number leaving the top tube in this measurement is about 150 and 1500 leaving the bottom of the tenth tube, respectively. These film Reynolds numbers are determined from an energy balance with the assumption that all the liquid condensed on a tube flows onto the tube below. Without overfeed, the heat transfer coefficient decreases from a value of about  $23kW/m^2K$  on the first tube to a value  $13kW/m^2K$  on the tenth tube in the array. The smallest liquid overfeed rate ( $\Gamma = 0.009kg/ms$ ) corresponds approximately to the amount of liquid leaving the top tube without liquid overfeed. The data obtained from this measurement as well as the measurements with higher overfeed rate follow the data without overfeed proving the consistency of the experimental setup with overfeed to simulate a large number of tube rows.

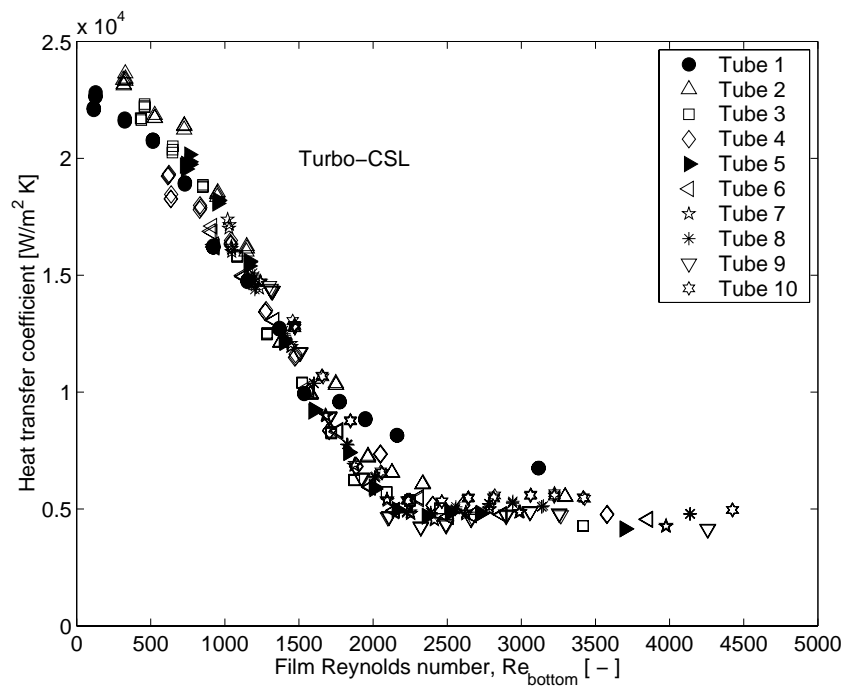
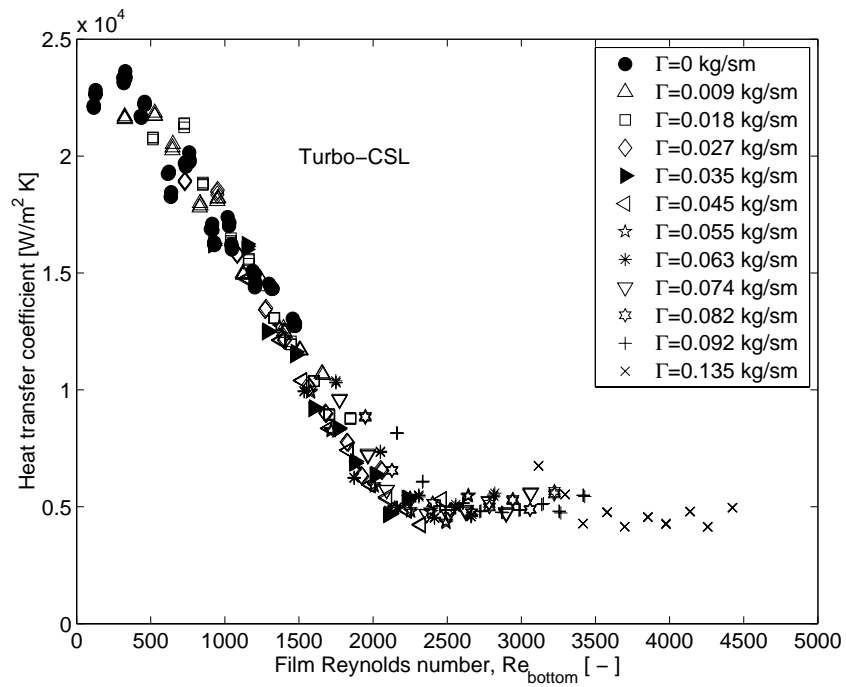


Figure 5.9: Measurements with liquid inundation of the Turbo-CSL tube with tube pitch of  $25.5mm$  at a nominal row heat flux of  $40kW/m^2$ .



The amount of liquid leaving the tenth tube during the measurement without overfeed corresponds approximately to the inundation rate of the measurement with  $\Gamma = 0.055\text{kg/ms}$ , thus the second tube of this measurement would correspond to the eleventh tube in a setup without liquid overfeed. Subsequently, the second tube of this measurement would correspond to the twelfth etc. Continuing to count the number of tube rows in this way, the film Reynolds number leaving the tenth tube during the measurement with the highest inundation rate would correspond approximately to the 30th row in a heat exchanger at this specific heat flux. In general, the heat transfer coefficient is high at low film Reynolds numbers and it decreases with increasing film Reynolds number. Above a certain film Reynolds number, the heat transfer coefficient reaches a plateau and flattens out.

The lower plot in figure 5.9 shows the same data as in the upper graph, but different symbols are used for the ten tubes in the array to illustrate the evolution of heat transfer performance of every tube during one series of measurements when the liquid inundation rate is increased. The top tube deviates from the others. At low film Reynolds numbers, its heat transfer coefficients are a little below the other tubes and at high film Reynolds numbers its values are higher than the other tubes. This might be explained by the fact that the liquid flow leaving the distribution half tube differs from the liquid flow leaving the enhanced tube (see figure 3.7).

Figure 5.10 depicts the corresponding plots for the Gewa-C tube: one series of measurements at a nominal heat flux of  $40\text{kW/m}^2$  at the tube pitch of  $25.5\text{mm}$ . Basically the same behavior as for the Turbo-CSL is observed. The heat transfer coefficients starts at a high level at low film Reynolds numbers and decreases with increasing film Reynolds numbers, reaching also a plateau.

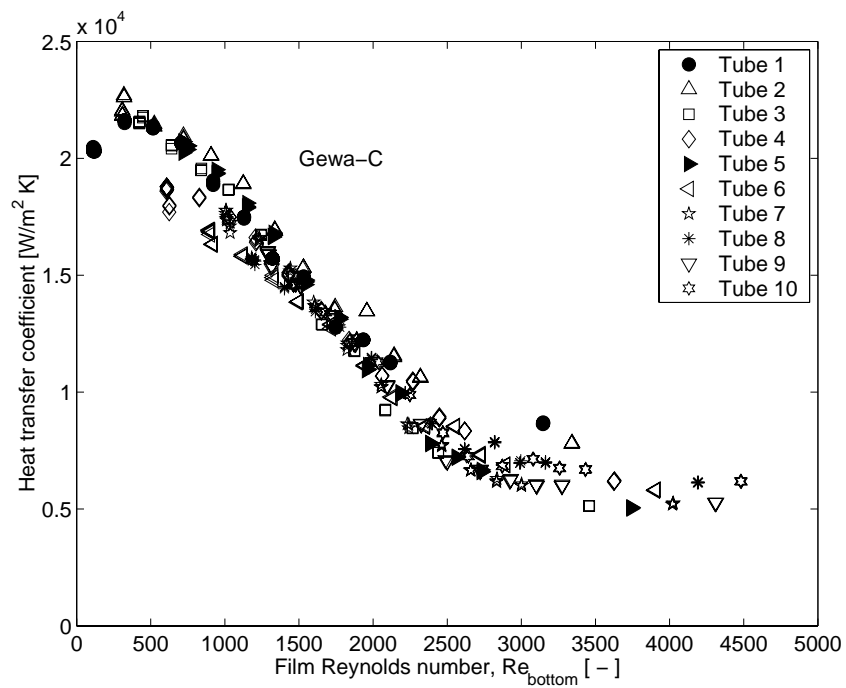
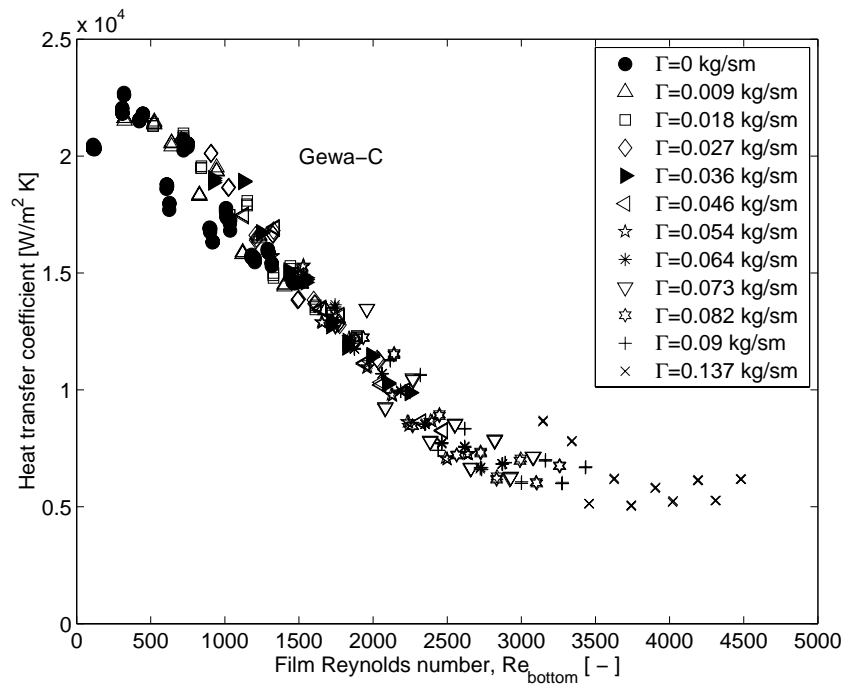


Figure 5.10: Measurements with liquid inundation of the Gewa-C tube with tube pitch of  $25.5mm$  at a nominal row heat flux of  $40kW/m^2$ .

During each series of measurements, the nominal row heat flux was held constant, but as mentioned above, the experimental setup has two tube passes. Thus, heat flux varied substantially between the even and the odd rows in the bundle. In addition, as seen in figures 5.9 and 5.10, the external heat transfer coefficient is higher on the upper tubes in the array as the inundation is less resulting in a higher heat flux on the upper tubes for the same condensation temperature difference. These two effects lead to a wide range of heat flux on the tubes in the array at the imposed nominal row heat flux. For example, for the measurements shown in figure 5.9 at a nominal heat flux of  $40kW/m^2$  with an overfeed rate of  $\Gamma = 0.027kg/ms$ , the heat flux varied in the row starting on the top tube to tenth tube as follows: 36, 57, 35, 49, 33, 44, 30, 38, 26,  $36kW/m^2$ .

In order to illustrate this variation in heat flux on the tubes at a nominal row heat flux, only the data points in the heat flux range from 25 to  $35kW/m^2$  are plotted in figure 5.11; on the left the data for the Turbo-CSL tube are depicted and on the right the data for the Gewa-C tube. With this limited range of heat flux, the width of the curves is reduced, showing that the scatter of the points in figures 5.9 and 5.10 is in part due the difference in heat flux. The influence of the heat flux on the measured heat transfer coefficient will be discussed in detail in subsection 5.5.3. Thus, these graphs attest to the high quality of the data and the reproducibility from tube to tube.

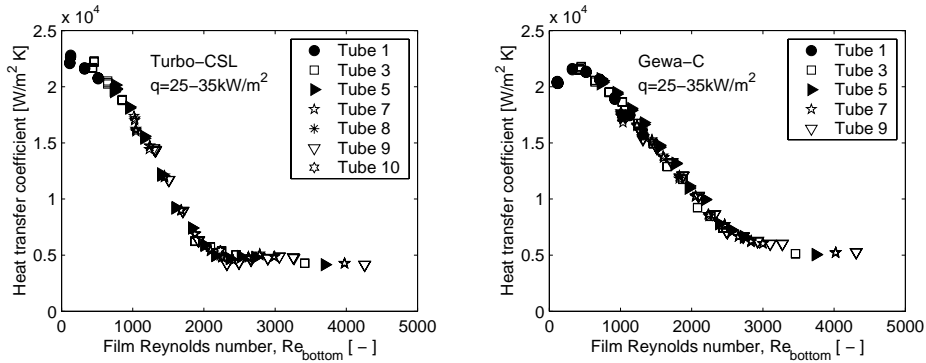


Figure 5.11: Limited heat flux range of measurements of the Turbo-CSL tube and Gewa-C tube with tube pitch of  $25.5mm$  at a nominal bundle heat flux of  $40kW/m^2$ .

A comparison of the Turbo-CSL and Gewa-C tubes is given in figure 5.12. At low film Reynolds numbers the heat transfer coefficient is slightly higher for the Turbo-CSL tube. With increasing film Reynolds number the heat transfer coefficient of Turbo-CSL decreases faster than the one of the Gewa-C. The heat transfer coefficient of the Gewa-C tube flattens out at a higher film Reynolds compared to the Turbo-CSL and the value of this plateau is slightly above the value of the Turbo-CSL.

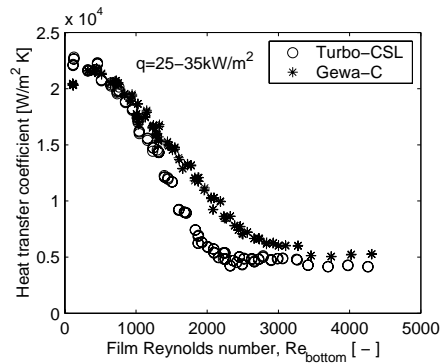


Figure 5.12: Comparison of the Turbo-CSL tube and Gewa-C tube at the tube pitch of  $25.5\text{mm}$  with limited heat flux range.

Figure 5.13 depicts the measured heat transfer coefficients for Turbo-Chil, a low finned tube with 26 fpi. The nominal tube row heat flux is  $40\text{kW}/\text{m}^2$  and the tube pitch  $25.5\text{mm}$ . The observed behavior of this tube is very different compared to the 3D enhanced tubes discussed before. Roughly speaking, the observed heat transfer coefficient does not change over the whole range of Reynolds numbers. There is a small increase in heat transfer coefficient with increasing film Reynolds numbers for film Reynolds number below 1000 approximately (note that the axis ranges from 10000 to  $21000\text{W}/\text{m}^2\text{K}$ ). Above this value, the heat transfer coefficient on the upper tubes in the array tends to decrease. These variations are smaller than differences between the ten tubes.

For the plain tube, the measurements were performed at lower heat fluxes. The measured heat transfer coefficients at a nominal row heat flux of  $12\text{kW}/\text{m}^2$  are given in figure 5.14 (note that the axis ranges from 1000 to  $2000\text{W}/\text{m}^2\text{K}$ ). At low film Reynolds numbers the heat transfer coefficient decreases sharply with increasing film Reynolds. At a film Reynolds number of approximately 500 the coefficient starts to increase with increasing film Reynolds number. The differences in heat transfer coefficient observed for the ten tubes are a little larger than the uncertainty in the measurements. The rise in the heat transfer coefficient with increasing Reynolds numbers above 500 is the result of liquid "slinging" off the tubes from the unstable

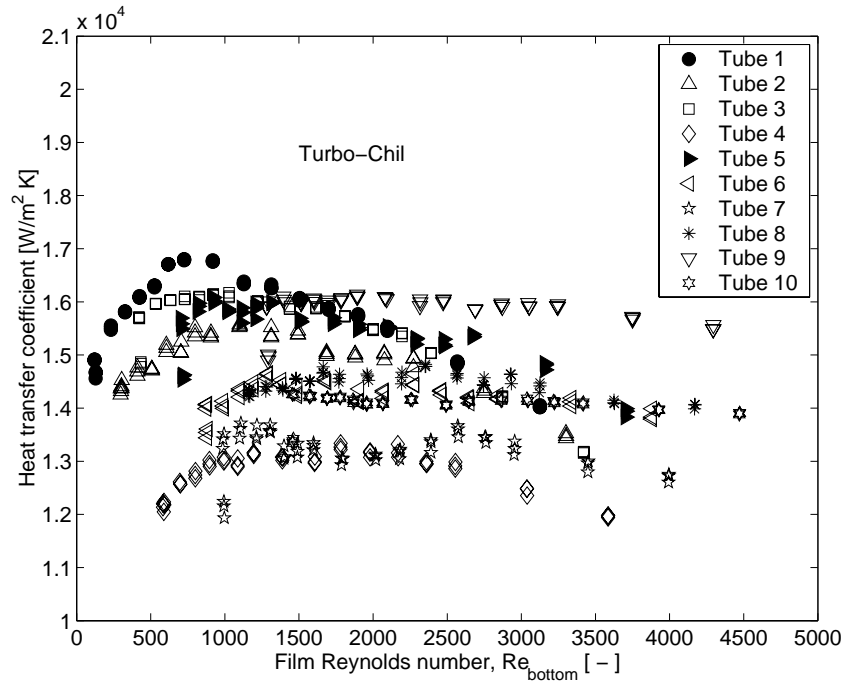


Figure 5.13: Measurements with liquid inundation of the Turbo-Chil tube with tube pitch of  $25.5\text{mm}$  at a nominal row heat flux of  $40\text{kW/m}^2$ .

column flow between the tubes.

In order to summarize the differences in the heat transfer coefficient for the four types of tubes, the measured values at one nominal heat flux at smallest tube pitch are plotted in figure 5.15. For small inundation rates the heat transfer coefficients for the 3D enhanced tubes are high compared to the finned tube. Increasing the inundation rates deteriorates the performance the 3D enhanced tubes. The heat transfer coefficient flattens out above a certain film Reynolds number for the 3D enhanced tubes. The heat transfer coefficient of the Turbo-CSL is slightly higher than the one of the Gewa-C for small inundation, but the decrease with increasing inundation rate is less pronounced for the Gewa-C compared to the Turbo-CSL. The heat transfer coefficient of the finned tube varies little with the inundation rate. The cross over in performance with the low finned tube suggests that in large bundles it may be judicious to use low finned tubes in the lower rows when the Reynolds number is larger 1250.

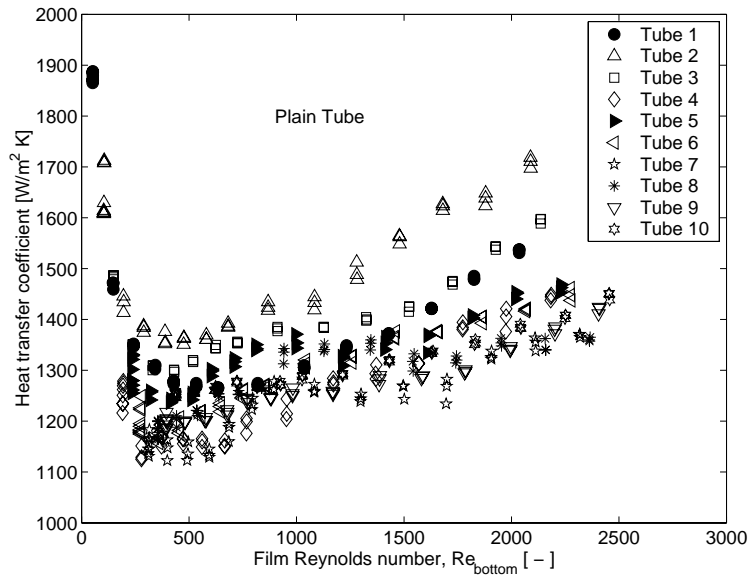


Figure 5.14: Measurements with liquid inundation of the plain tube with tube pitch of  $25.5\text{mm}$  at a nominal row heat flux of  $12\text{kW}/\text{m}^2$ .

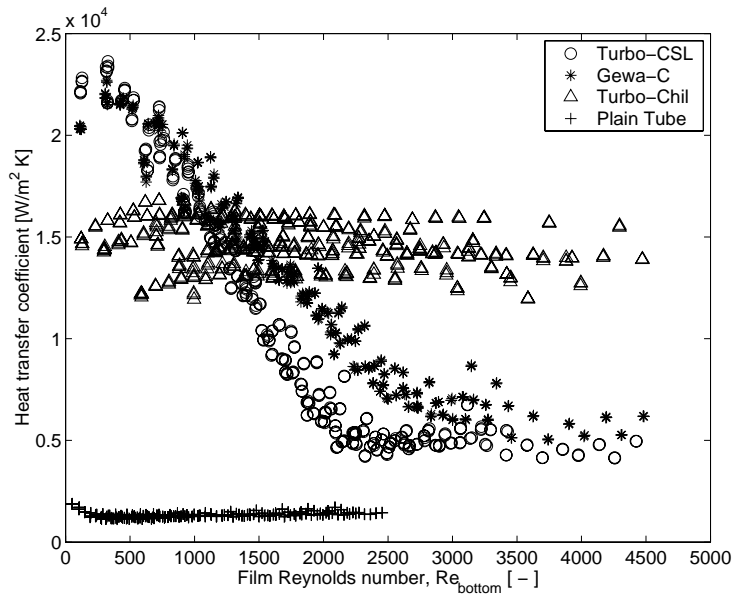


Figure 5.15: Comparison of the four types of tubes with tube pitch of  $25.5\text{mm}$  at a nominal row heat flux of  $40\text{kW}/\text{m}^2$  (respective to  $12\text{kW}/\text{m}^2$  for the plain tube).

### 5.5.2 Tube Pitch Influence

The effect of the tube pitch in the vertical array on performance is illustrated by the measurements at the nominal row heat flux of  $40\text{kW}/\text{m}^2$  and  $12\text{kW}/\text{m}^2$  for the enhanced tubes and the plain tube, respectively. Figure 5.16 depicts the measured heat transfer coefficient of the Turbo-CSL tube as a function of the film Reynolds number for all three tube pitches. For clearness, only the data in the heat flux range from 25 to  $35\text{kW}/\text{m}^2$  are shown. Although the scatter in the data for the tube pitch of 28.6 and  $44.5\text{mm}$  is larger than for the smallest tube pitch, it can be seen that for all three tube pitches the heat transfer coefficient decreases with increasing film Reynolds number and flattens out at a certain film Reynolds number. The larger the tube pitch the earlier this happens, and thus the higher the value of the plateau in the heat transfer coefficient. At low film Reynolds numbers (below 1000) the heat transfer coefficient increases with increasing tube pitch, apparently due to the higher velocity of the impinging liquid and the larger fraction of condensate between adjacent tubes.

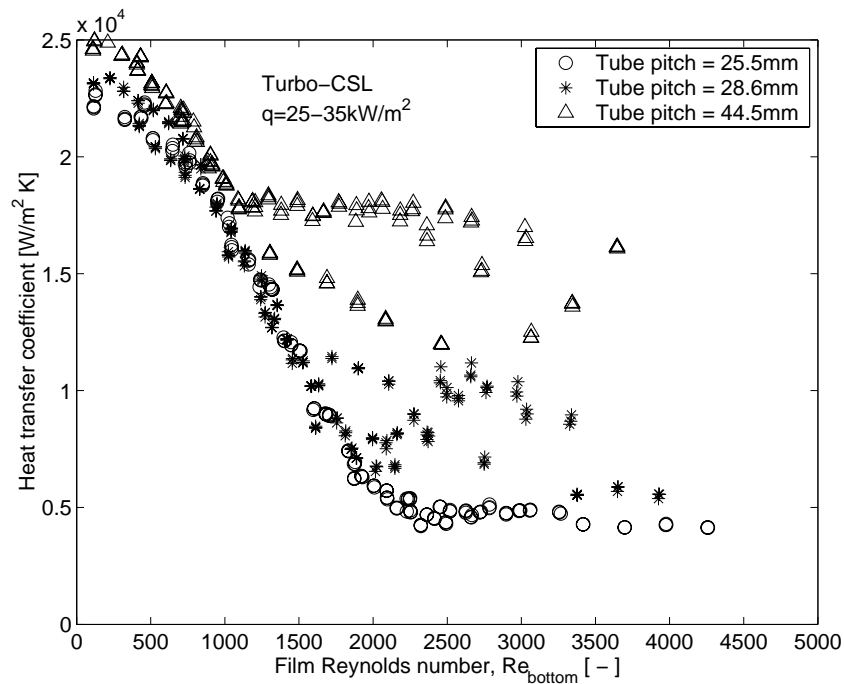


Figure 5.16: Tube spacing influence of Turbo-CSL tube at a nominal bundle heat flux of  $40\text{kW}/\text{m}^2$  with limited heat flux range.

The influence of the tube pitch for the Gewa-C tube is illustrated in figure 5.17. A similar behavior as observed for the Turbo-CSL can be seen.

The heat transfer coefficient deteriorates less with increasing tube pitch at high Reynolds numbers. At low film Reynolds numbers the behavior differs, however, as the heat transfer coefficients for all tube pitches are close together apart from some values of the middle tube pitch which lie above.

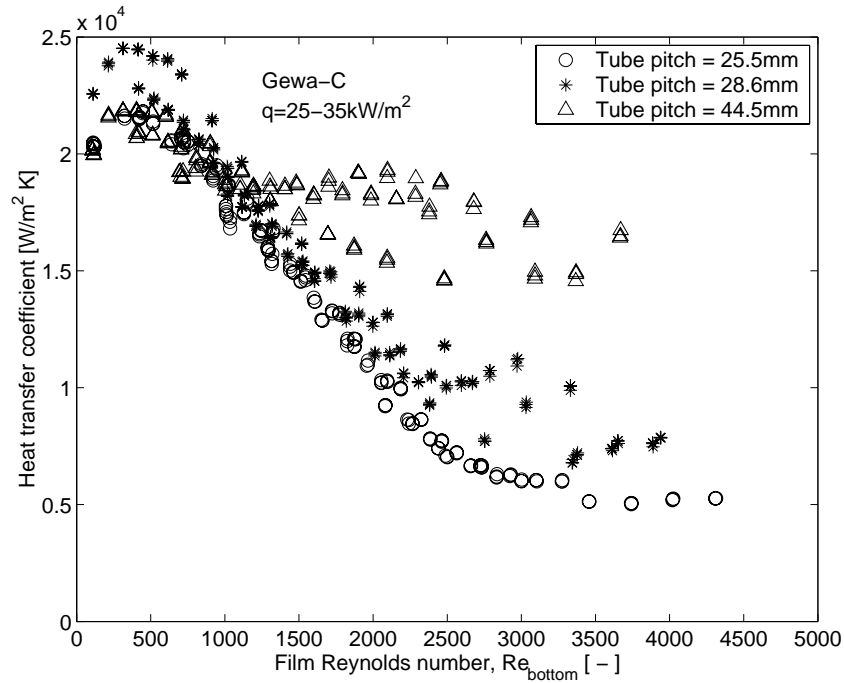


Figure 5.17: Tube spacing influence of Gewa-C tube at a nominal bundle heat flux of  $40\text{kW}/\text{m}^2$  with limited heat flux range.

For the low finned tube, the heat transfer coefficient stays approximately fixed over the whole film Reynolds number range for all three tube pitches as depicted in figure 5.18. No trend in the heat transfer coefficient as a function the tube pitch was observed for this tube.

In figure 5.19 the heat transfer coefficient for the plain tube for all three tube pitches is given. For the plain tube the temperature difference between the water inside the tubes and the saturation temperature is larger to obtain these heat fluxes as the heat transfer coefficients are small on this tube. Thus the temperature difference between the odd and even tubes in the array are small, and subsequently the differences in heat flux are smaller than for the enhanced tubes. The heat fluxes for all ten tubes are close together. This makes it difficult to select a range of heat flux for a clear representation of the effect of tube pitch. Instead, for the plain tube, only



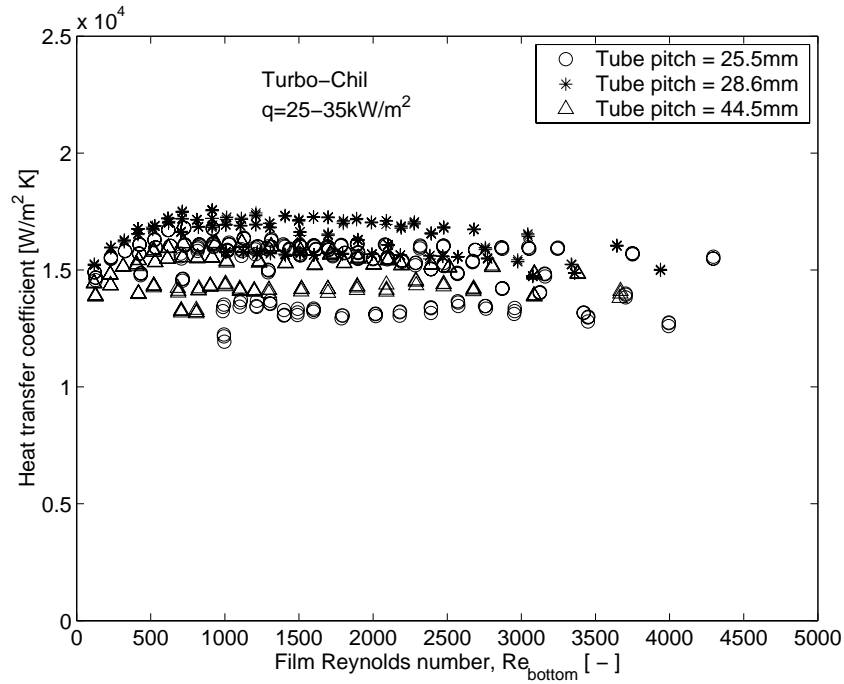


Figure 5.18: Tube spacing influence of Turbo-Chil tube at a nominal bundle heat flux of  $40\text{kW}/\text{m}^2$  with limited heat flux range.

the heat transfer coefficients for the top three tubes are shown. At low film Reynolds numbers the heat transfer coefficients are similar for all three tube pitches. At high Reynolds numbers the heat transfer coefficient is highest for the largest tube spacing due to increased liquid "slinging" off the tubes, which results in a lower effective liquid Reynolds number on the tubes compared to the plotted Reynolds numbers that assume all the liquid remains on the tubes. The difference for the tube pitch of 25.5 and 28.6mm are within the experimental uncertainty.

The effect of the tube pitch on the heat transfer coefficient on the array of tubes can be summarized as follows: For low inundation rates the heat transfer coefficients are similar for the three tube pitches. For the 3D enhanced tubes, the heat transfer coefficient achieves a constant level at a lower film Reynolds number for the larger tube pitch. This level is higher for the larger tube pitch. The heat transfer coefficient of the finned tube varies little with the tube pitch. For the plain tube an increase in heat transfer coefficient is observed for the largest tube pitch.

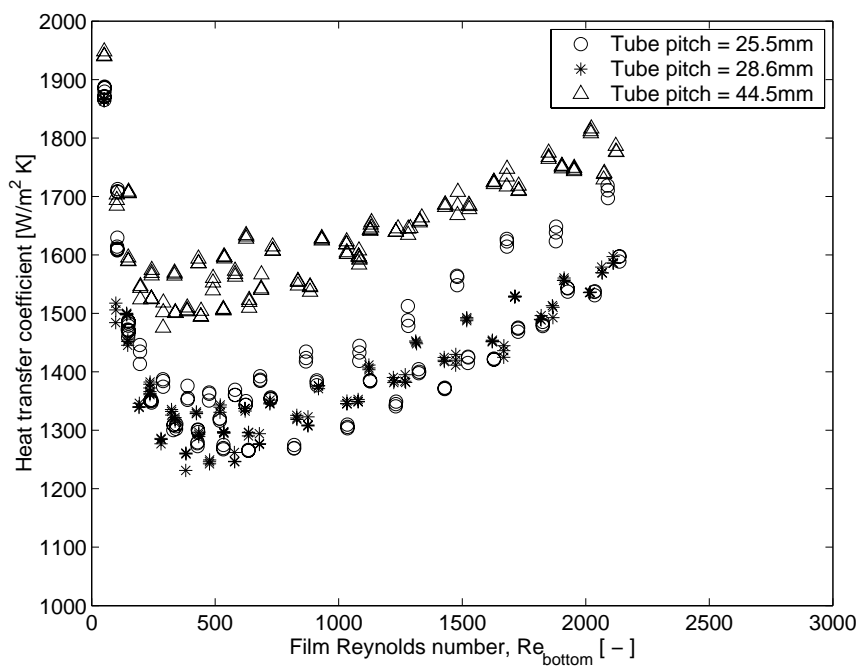


Figure 5.19: Tube spacing influence of plain tube at a nominal bundle heat flux of  $12kW/m^2$  on the top three tubes in the array.

### 5.5.3 Heat Flux Influence

For every type of tube and tube pitch, measurements have been performed at three nominal heat fluxes. The effect of heat flux for the 3D enhanced tubes is illustrated for a tube pitch of  $28.6\text{mm}$ . Figures 5.20 and 5.21 depict the heat transfer coefficient at the three different nominal row fluxes for the Turbo-CSL and the Gewa-C, respectively. For clearness only the data for the top tube tube (plain symbols) and the second tube (empty symbols) are given. For the three nominal heat fluxes, different symbols were used. The actual mean value of the local heat flux on each tube is given in brackets in the legend. Considering only the data of the top tube (plain symbols), it can be seen that the heat transfer coefficient decreases with increasing heat flux. This decrease is more pronounced for low film Reynolds numbers and is larger for the Gewa-C tube compared to the Turbo-CSL tube. For the second tube in the array (empty symbols) the same trend is observed.

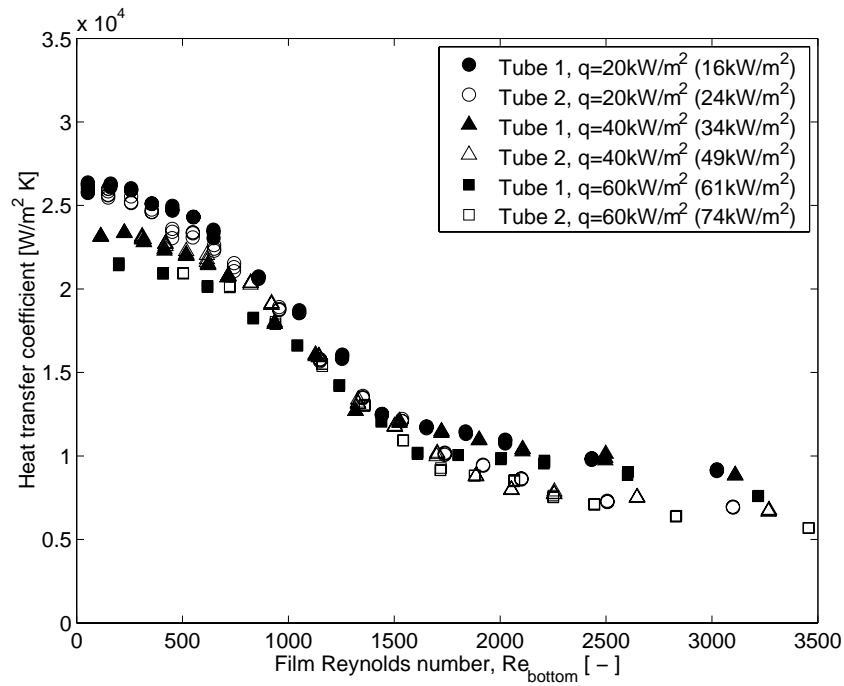


Figure 5.20: Heat flux influence of Turbo-CSL tube at tube pitch of  $28.6\text{mm}$ .

The measured heat transfer coefficients on the top two tubes for the low finned tube at the tube pitch of  $25.5\text{mm}$  are shown in figure 5.22. In general, the heat transfer coefficient decreases with increasing heat flux. The points of the second tube lie below the points of the first tube at the same nominal row heat flux and above the values of the first tube at the higher

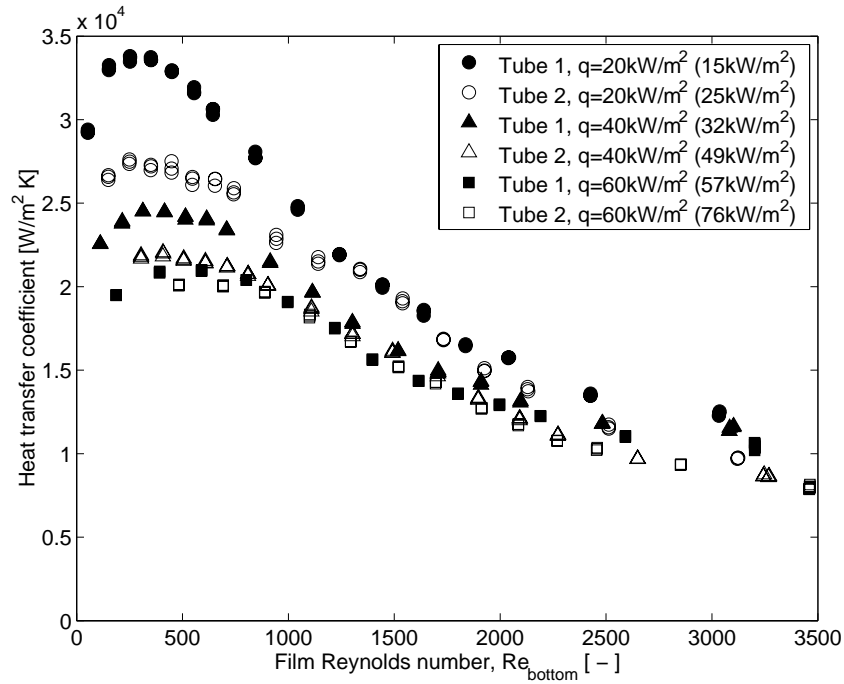


Figure 5.21: Heat flux influence of Gewa-C tube at tube pitch of  $28.6\text{mm}$ .

nominal bundle heat flux, corresponding to the local heat flux of the tubes. At the lowest local heat flux of  $16\text{kW/m}^2$ , a maximum in the heat transfer coefficient can be seen at a Film Reynolds number of 700. A similar behavior is observed for the other heat fluxes, but the maximum is less marked for higher heat fluxes and shifts to higher film Reynolds numbers. The same trend could also be observed for Turbo-Chil tube for the other tube pitches.

Figure 5.23 illustrates the influence of heat flux on the heat transfer coefficient on the plain tube. For the top tube and the second tube in the array the heat transfer coefficient decreases with increasing heat flux. This decrease is more pronounced on the second tube. However, the difference between the first and the second tube are more than influence of the heat flux.

The heat transfer coefficient decreases with increasing heat flux for the four different tubes. This decrease is less pronounced for increasing inundation rates for the enhanced tubes.

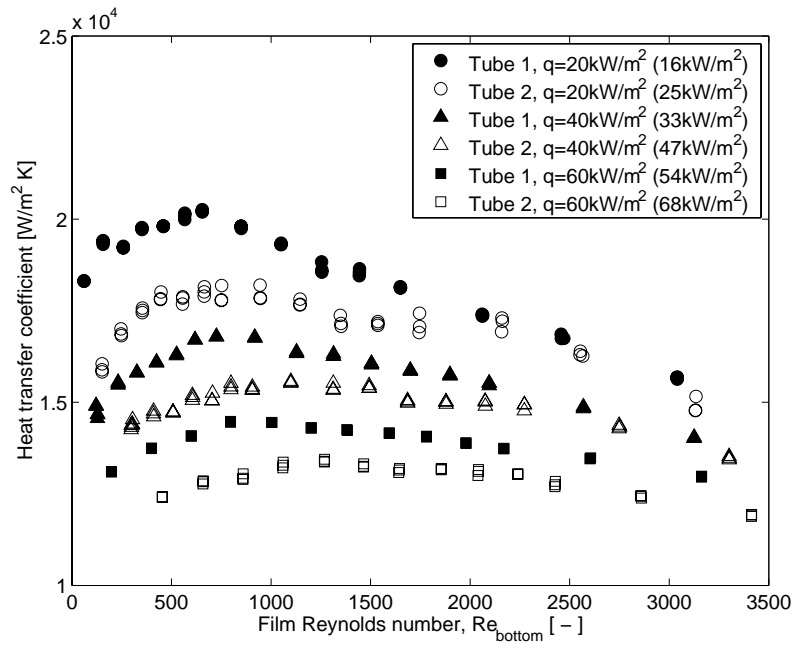


Figure 5.22: Heat flux influence of Turbo-Chil tube at tube pitch of 25.5mm.

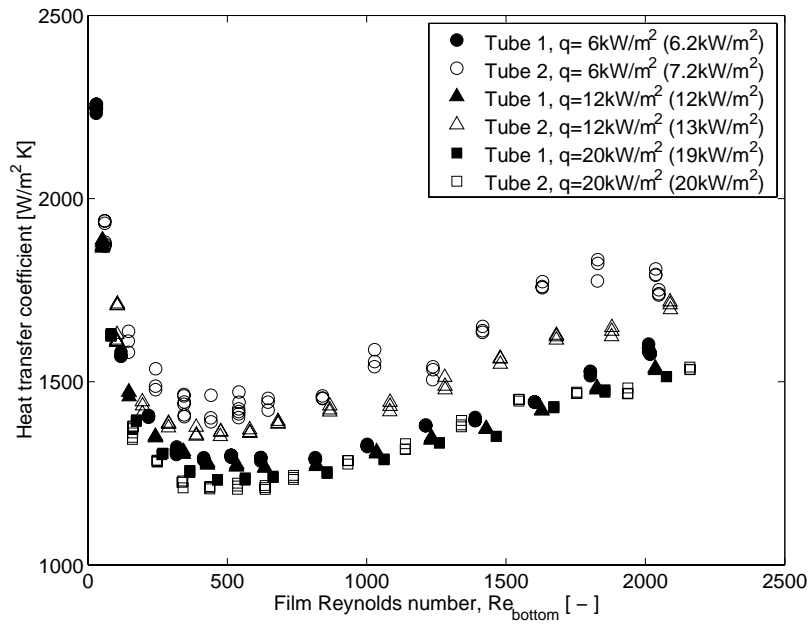


Figure 5.23: Heat flux influence of plain tube at tube pitch of 25.5mm.

## 5.6 Conclusion

The data reduction methods to determine the local external heat transfer coefficient at the midpoint of each of the tubes in the array was shown and a propagation of error analysis was performed to estimate the uncertainty of the measurement. Four types of tubes, a plain tube, a 26 fpi / 1024 fpm low finned tube (Turbo-Chil), and two tubes with 3D enhanced surface structures (Turbo-CSL and Gewa-C), were tested at the tube pitches of 25.5, 28.6 and 44.5mm. Measurements with liquid overfed onto the top of the array were performed for each type of tube at three different heat flux levels. Additionally, measurements without liquid overfed were made by varying the heat flux.

The measured heat transfer coefficients on the plain tube without liquid inundation were in good agreement with the Nusselt theory. For the low finned tube without liquid inundation, good agreements with the prediction methods of Sreepathi et al. [24] and Beatty and Katz [9] were found.

For small inundation rates, the heat transfer coefficients for the 3D enhanced tubes were high compared to the finned tube. Increasing the inundation rates deteriorated the performance the 3D enhanced tubes. The heat transfer coefficient flattened out at a certain film Reynolds number for the 3D enhanced tubes. The heat transfer coefficients of the Turbo-CSL were slightly higher than those of the Gewa-C for small inundations, but the decrease with increasing inundation rate was less pronounced for the Gewa-C compared to the Turbo-CSL. The heat transfer coefficient of the finned tube varied little with the inundation rate. The heat transfer performance of the plain tube decreased first sharply and then increased again slowly with increasing inundation rates.

For low inundation rates, the heat transfer coefficients were similar for the three tube pitches. For the 3D enhanced tubes, the heat transfer coefficient achieved a constant level at a lower film Reynolds number for the larger tube pitch. This level was higher for the larger tube pitch. The heat transfer coefficient of the finned tube varied little with the tube pitch. For the plain tube, an increase in heat transfer coefficient was observed for the largest tube pitch.

The heat transfer coefficients decreased with increasing heat flux for the four type of tubes. This decrease was less pronounced for increasing inundation rates, apart from the plain tube.

In summary, a new accurate, local heat transfer database has been obtained that includes approximately 15000 data points covering a wide range of liquid film Reynolds numbers (up to  $\sim 5000$ ), tube pitches (25.5 to 44.5mm) and heat fluxes (5 to  $100kW/m^2$ ) for four types of tubes for R-134a condensing at a saturation temperature of  $31^\circ C$ .

## Chapter 6

# Flow Visualization

Besides heat transfer considerations in the falling film condensers, the inter-tube flow patterns are investigated and compared to existing flow pattern maps as part of this study. A flow pattern map is basically a diagram or a predictive method from which it is possible to determine, at given conditions, the particular flow mode of the liquid falling between the tubes. Additionally, it could also be used to investigate any influence of flow mode on heat transfer. This chapter starts with an introduction to the flow patterns with the definition of the flow modes. Next, the flow mode observations under adiabatic test conditions are described and the determined transitions are compared to existing flow pattern maps. The last part is dedicated to the flow pattern observations with heat transfer and the effect on the heat transfer coefficient.

### 6.1 Flow pattern map and flow modes

In two phase heat transfer, the liquid flows are complex. In falling film condensation, the liquid is usually flowing on enhanced surfaces on which it is extremely difficult to study in details the liquid flow. There are heat transfer models for low Reynolds number films on simple geometries (i.e. condensation on low fin tubes) but for 3D enhanced surface geometries and higher liquid flow rates like on the lower rows in a large condenser, liquid flow is more complex. However, there are observable characteristics. These characteristics are classified and make up the flow modes. The parameters influencing these flow modes are: liquid physical properties, the liquid flow rate on the tube, the tube itself, the distance in-between the tubes and the tube diameter.

There are three principal flow modes when a liquid is flowing from tube to tube on a vertical array of horizontal tubes: droplet mode, column mode and sheet mode. These three principal flow modes are depicted in figure 6.1. Transition regimes of droplet-column mode and column-sheet mode (when

two types of modes are observed) are also sometimes defined.

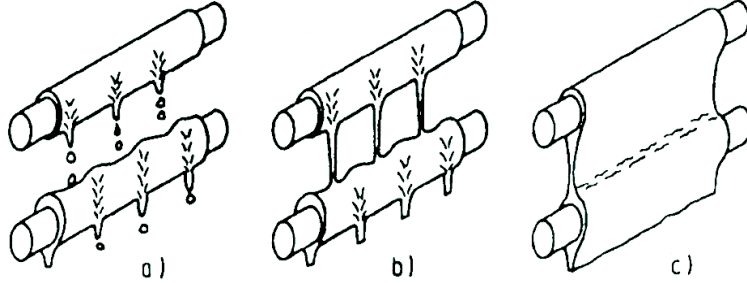


Figure 6.1: Schematic of the three main flow modes: a) Droplet mode, b) Column mode and c) Sheet mode from Mitrovic [72]

Despite numerous observations of condensation on rows of tubes, apparently no generalized flow mode map is currently available for either plain or enhanced types of tubes, although Honda et al. [33] have presented several transition expressions for R-113, methanol and propanol condensing on low finned tubes (27 fpi and 15.8mm diameter). They used the following dimensionless group to define the transitions between the different flow modes of the condensate:

$$K = \frac{\Gamma}{\sigma^{3/4}} \left( \frac{g}{\rho_L} \right)^{1/4} \quad (6.1)$$

where  $\Gamma$  is the liquid film flow rate per unit length for one side of a tube,  $\sigma$  is the surface tension,  $g$  is the acceleration due to gravity, and  $\rho_L$  is the density of the liquid. They observed a  $K$  value at the droplet mode to column mode transition ranging from 0.06 to 0.13. The value at the column mode to the column-sheet mode transition was 0.32 and it ranged at the column-sheet mode to sheet mode transition from 0.37 to 0.47.

These condensation processes however are similar to that of an adiabatic falling film of liquid fed onto the top of a tube array, which has been studied extensively by Hu and Jacobi [73] on plain tubes for a variety of fluids, tube diameters, tube pitches and flow rates and with/without cocurrent gas flow. Based on their observations, they proposed a flow mode transition map with coordinates of film Reynolds number ( $Re$ ) versus the Galileo number ( $Ga$ ). The map delineates the transitions between the three dominant modes (sheet, column and droplet) with two mixed mode zones (column-sheet and droplet-column) in which both modes are present. Their corresponding four flow transition expressions between these five zones are given below for plain tubes (valid for passing through the transitions in either direction and hence the symbol  $\Leftrightarrow$ ):



$$\text{Droplet} \Leftrightarrow \text{Droplet} - \text{Column} : Re = 0.074 Ga^{0.302} \quad (6.2)$$

$$\text{Droplet} - \text{Column} \Leftrightarrow \text{Column} : Re = 0.096 Ga^{0.301} \quad (6.3)$$

$$\text{Column} \Leftrightarrow \text{Column} - \text{Sheet} : Re = 1.414 Ga^{0.233} \quad (6.4)$$

$$\text{Column} - \text{Sheet} \Leftrightarrow \text{Sheet} : Re = 1.448 Ga^{0.236} \quad (6.5)$$

where the modified Galileo number of the liquid, which is the ratio between the gravity and the viscous force based on the capillary length scale, is defined as

$$Ga = \frac{\rho_L \sigma^3}{\mu_L^4 g} \quad (6.6)$$

and the liquid film Reynolds number is defined as

$$Re = \frac{4\Gamma}{\mu} \quad (6.7)$$

where  $\Gamma$  is the flow rate on one side and  $2\Gamma$  is the total flow rate on both sides of the tube,  $\rho_L$  is the density of the liquid,  $\mu_L$  is liquid dynamic viscosity,  $\sigma$  is the surface tension, and  $g$  is the acceleration due to gravity. This map is applicable to plain tubes for cocurrent, i.e., downflow, air velocities less than  $15m/s$ . Hu and Jacobi [74] reported additional data on tube spacing effects on column and droplet departure wavelengths.

More recently, Roques, Dupont and Thome [75] reported transition curves similar to those above for plain and enhanced tubes. The plain tube and the 26 fpi low finned tube (Turbo-Chil) they tested, are exactly the tubes used in the present investigation. They determined the transitions between the flow modes on an adiabatic test facility using water, glycol and a glycol-water mixture (50%/50% weight) as working fluids in order to cover a wide range of physical properties. Measurements were taken at ambient temperature. Their intertube spacings were 3.2, 4.8, 6.4, 9.5, 19.4, and 24.9mm. Roques and Thome reported additional observations for an enhanced condensation tube (Thermoexcel-C), two low finned tubes (19 and 40 fpi), enhanced boiling tubes (Turbo-BII HP and Gewa-B) in [76] [77] and [78].

Neglecting the effect of tube spacing, they analyzed the results using two dimensionless groups like Hu and Jacobi [73]. The fluid type is characterized by the modified Galileo number  $Ga$ . The mass flow rate is included in the film Reynolds number  $Re$ . They correlated the film Reynolds number at transition as a function of the Galileo number as:

$$Re = a Ga^b \quad (6.8)$$

where a transition is the change from one flow mode to another one. As there are five modes, there are four transitions (or eight if one takes into account

Tube	Transition	a	b
Plain Tube	Droplet to/from Droplet-Column	0.042	0.328
	Droplet-Column to/from Column	0.068	0.320
	Column to/from Column-Sheet	0.855	0.248
	Column-Sheet to/from Sheet	1.068	0.256
Turbo-Chil	Droplet to/from Droplet-Column	0.074	0.300
	Droplet-Column to/from Column	0.126	0.303
	Column to/from Column-Sheet	0.617	0.278
	Column-Sheet to/from Sheet	1.202	0.266
Turbo-CSL	Droplet to/from Droplet-Column	0.069	0.301
	Droplet-Column to/from Column	0.238	0.279
	Column to/from Column-Sheet	0.669	0.264
	Column-Sheet to/from Sheet	1.131	0.262
Gewa-C	Droplet to/from Droplet-Column	0.075	0.306
	Droplet-Column to/from Column	0.148	0.296
	Column to/from Column-Sheet	0.505	0.272
	Column-Sheet to/from Sheet	0.799	0.269

Table 6.1: Coefficients for transition relations (equation 6.8) without spacing effect from Roques et al. [75] and Roques (unpublished work).

the hysteresis effect for increasing or decreasing flow conditions). Since they observed only a small degree of hysteresis, the observations of these two cases were put together to determine the transitions. The numerical values of the coefficients  $a$  and  $b$  in relation 6.8 for each tube used in the present investigation and transition are presented in table 6.1.

## 6.2 Observed flow modes

In the present investigation the three principal and two intermediate transition modes have been observed. Photographs of these flow modes under adiabatic conditions are depicted in 6.2. The principal flow modes are described below together with the two intermediate modes.

### 6.2.1 Droplet mode

When a small amount of liquid is flowing on a tube, the flow off the bottom of the tube is intermittent and occurs only as droplets. There are no continuous liquid links between the bottom of one tube and the top of the next tube below. The frequency of these droplets increases with flow rate while the distance between the droplet departure sites remain the same. This distance is defined by the Taylor instability.

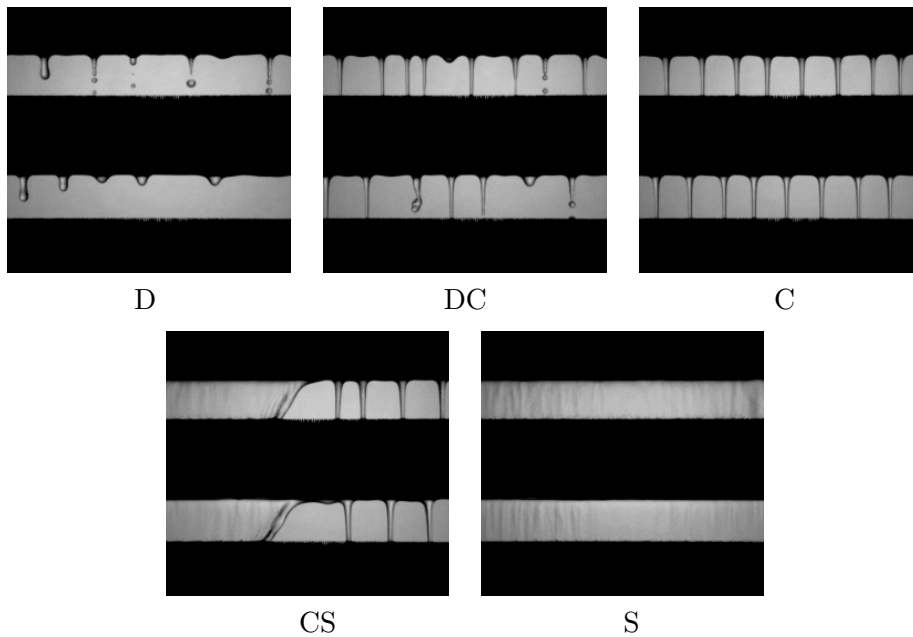


Figure 6.2: Intertube flow modes observed for R-134a under adiabatic conditions on the Turbo-CSL tube with a tube pitch of  $28.6\text{mm}$ : Droplet (D), Droplet-Column (DC), Column (C), Column-Sheet (CS), and Sheet (S).

### 6.2.2 Column mode

When the flow rate is increased further, there is a point when there is enough liquid to make the droplets merge vertically together and form continuous liquid columns between the tubes. If the liquid is flowing only in this form from the bottom of one tube to the top of the one below, the mode in this intertube is: Column mode. The diameter of the columns width increases with the flow rate while the distance between columns remains constant and close to the droplet departure site distance and the wavelength of the Taylor instability.

A distinction is made in this mode regarding the relative position between the columns of one inter-tube space and the columns of the following inter-tube space:

**In-line column.** At the beginning of the column mode (in terms of increasing flow rate), the liquid does not spread enough when it impinges on the top of a tube to encounter that of the neighboring columns and the next column at the bottom of this tube is formed exactly at the same position. The columns are thus vertically aligned. This in-line column position does not exist for all the liquid/tube combinations. It is more likely observed with viscous fluids and with low fin tubes. These two factors limit the

lateral spreading of liquid and make the in-line column mode possible.

**Staggered column.** When the flow rate is high enough (remaining in the column mode), the liquid spreads evermore laterally on the tube surface. On both sides of the impingement region, the liquid flows horizontally on the surface. The flows from two neighboring columns encounter each other and create a crest in the liquid layer. This crest forms a ring all around the tube. At the bottom of the tube, this ring is the departure site for a column in the next intertube space. The column positions are consequently shifted from one intertube to the following one by one half the length of the inter-column distance. This staggered column mode is that most typically observed.

### 6.2.3 Sheet mode

At even higher flow rate, the diameters of the columns increase and they become non cylindrical. The liquid columns spreads in the lateral direction along the tubes and form a liquid sheet. At the beginning, this sheet is not continuous but forms several unstable triangular small sheets (see Column-Sheet description below) from two neighboring columns. With increasing flow rate, those small sheets merge together and form a complete sheet along the entire tube length. The sheet mode is reached when there is one single wide sheet between the two tubes.

These three modes are the principal ones, but in between, there are two intermediate modes. These intermediate modes help in the description of the transition between one principal mode to the following one and correspond in fact to the coexistence of the two principal modes.

### 6.2.4 Droplet-Column mode

Between the stable droplet and column modes, there is an intermediate mode where droplets and columns coexist. In this mode, the liquid falls at the bottom of the tube from the departure sites (identical for droplet or column). Between these departure sites, the distance is most of time the wavelength of the Taylor instability and the liquid falls from these sites as a column or droplet. The droplet-column mode starts when there is at least one stable column and finishes when the last droplet site is replaced with a column site.

### 6.2.5 Column-Sheet mode

Between the column and sheet mode, there is an intermediate mode in which there are both columns and small sheets coexisting. This mode is the column-sheet mode. It starts when the two first columns merge and form a small sheet and finishes when a complete single sheet is formed.

### 6.3 Adiabatic flow pattern observations

The first objective was to observe the intertube flow modes and determine what transition takes place as the flow rate is varied for the present test fluid R-134a. Secondly, the flow rate was measured in order to determine the flow rate at which the various transitions take place. These measurements were made on all four types of tubes at each tube pitch under adiabatic conditions. For this purpose the test facility was at room temperature, all heating and cooling elements were switched off, and the water was not circulating inside the tubes. Only the refrigerant pump was used to distribute the liquid onto the top of the array. Room temperature was chosen, as the effect on the flow modes transitions due to changes in the physical properties is expected to be small as the Galileo number of R-134a at room temperature  $Ga^{1/4} \approx 453$  is close to that at  $31^\circ C$  (the condensation temperature) where  $Ga^{1/4} \approx 450$ . The measurements were started with increasing mass flow rate. This means, the mass flow rate was increased stepwise and at each transition the mass flow rate of refrigerant was noted and the viscosity (to determine the film Reynolds number) was derived from a measurement of the saturation pressure in the test section. The transitions were determined with help of a high speed camera. Short sequences were taken to determine the flow pattern when liquid was moving fast. The same procedure was done with decreasing mass flow rate to obtain the eight transitions between the five modes with the effect of hysteresis. Two complete runs like this were performed for all types of tubes and tube pitches.

The flow patterns were observed below the first and second tube in the array. Pictures of the five flow modes taken at the tube pitch of  $28.6mm$  for the Turbo-CSL tube were shown above in figure 6.2. For the other three types of tubes, the observed flow patterns are depicted in figure 6.3. On the left, the flow patterns for the Gewa-C tube are given, in the middle the flow pattern for the low finned tube and on the right the flow pattern for the plain tube. The five pictures for each type of tubes correspond to the five flow modes. The flow patterns on the Gewa-C tube are similar to the flow patterns on the Turbo-CSL tube. The flow patterns on these 3D enhanced tubes correspond to the ideal cases of the five flow modes. For the low finned tube and plain tube, there is no difference in flow pattern in the droplet mode compared to the 3D enhanced tubes (first row of pictures). The flow pattern of the Turbo-CSL tube and the plain tube are very different at higher film Reynolds numbers, where the liquid flow on these two tubes is unstable. Comparing the second row of pictures (DC) in figure 6.3, it was seen that the liquid columns are moving back and forth along the tubes for the plain and the finned tubes, while they were very stable and did not move for the 3D enhanced Gewa-C tubes. The same behavior of unstable liquid flow was seen for the higher flow rates as seen on the lower pictures. For the plain tube and the low finned tube no stable columns, small sheets

or the formation of a complete sheet were observed, even not for the smaller tube pitch of  $25.5\text{mm}$ . Nevertheless, an attempt was made to classify the flow patterns on these two tubes also in the ideal categories of the five flow modes and to compare them with existing flow pattern maps.

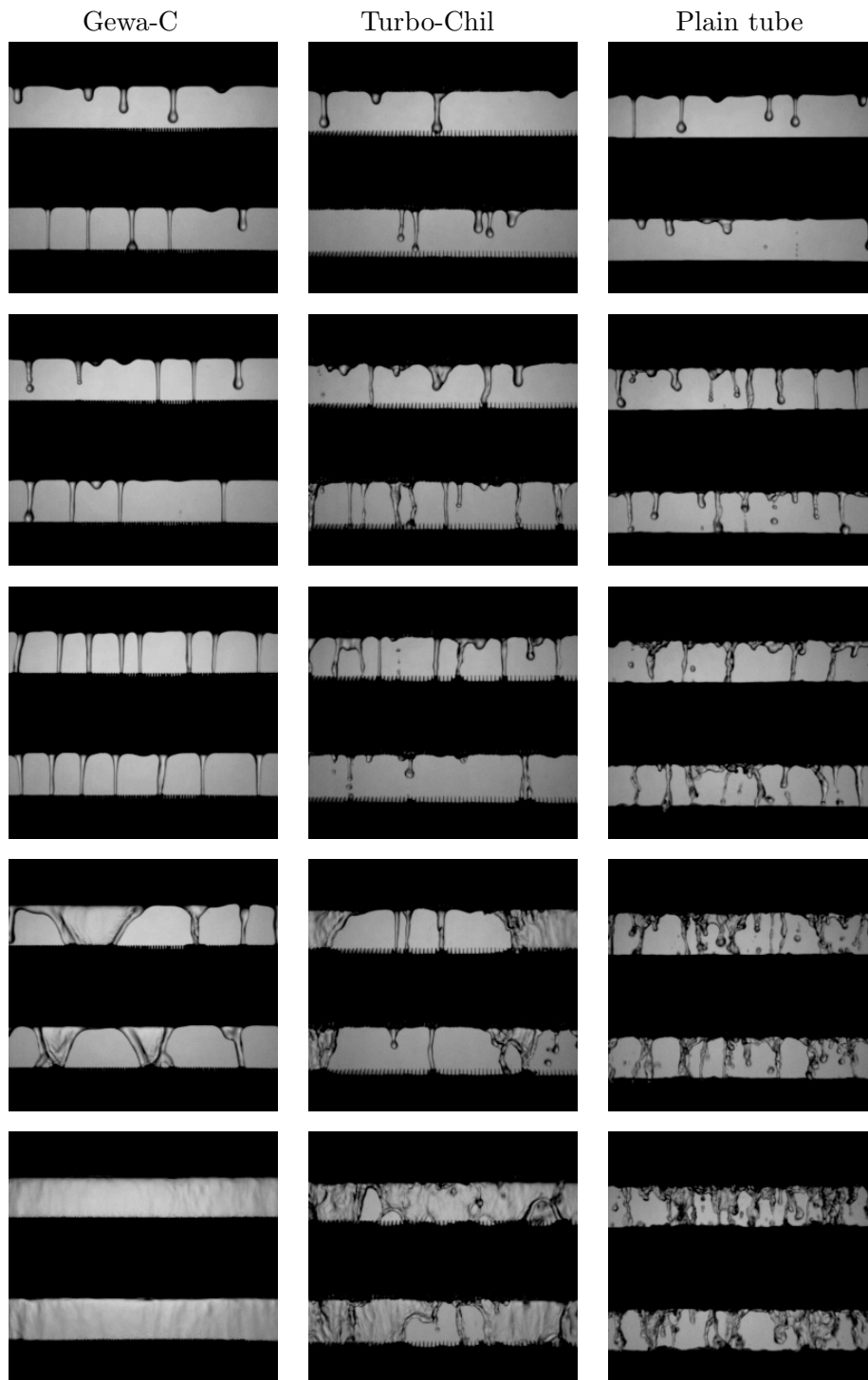


Figure 6.3: Intertube flow modes observed for R-134a under adiabatic conditions at a tube pitch of  $28.6\text{mm}$ : Gewa-C (left), Turbo-Chil (middle), and plain tubes (right).

Figure 6.4 depicts the observed flow mode transitions for the two 3D enhanced tubes for all three tube pitches: the upper and the lower four plots show the transitions for the Turbo-CSL tube and the Gewa-C tube, respectively. The observed transitions film Reynolds numbers with increasing mass flow rate ( $\Delta$ ) and decreasing mass flow rate ( $\blacktriangledown$ ) are plotted versus the three tube pitches:  $25.5\text{mm}$  (1),  $28.6\text{mm}$  (2), and  $44.5\text{mm}$  (3) corresponding to intertube distances of approximately  $6.4\text{mm}$ ,  $9.5\text{mm}$ , and  $25.5\text{mm}$ . For comparison, the transitions from the flow pattern map of Roques (unpublished work based on adiabatic observations with water, glycol and 50/50 water glycol mixture) neglecting the effect of intertube spacing are plotted as horizontal solid lines. The Galileo number of R134-a at room temperature ( $Ga^{1/4} \approx 453$ ) lies within the range of Galileo numbers he studied. In addition, his transition film Reynolds numbers determined at the intertube distances of  $6.4\text{mm}$ ,  $9.5\text{mm}$ , and  $24.9\text{mm}$  are given as dashed lines at the corresponding tube pitch when available (unpublished work). For both enhanced tubes, only a small hysteresis is observed for the first transition ( $D \Leftrightarrow DC$ ) and the second transition ( $DC \Leftrightarrow C$ ). For these two transitions, the observed transition film Reynolds numbers for refrigerant R-134a are in fairly good agreement with values of the flow pattern map of Roques. For the third transition ( $C \Leftrightarrow CS$ ) and the fourth transition ( $CS \Leftrightarrow S$ ), the hysteresis increases and also the difference compared to the flow pattern map of Roques, especially for the transition to the sheet mode. In most cases the observed transition film Reynolds numbers increase with increasing tube pitch. The same behavior can be seen for transitions by the flow map taking into account the tube spacings (dashed lines). However, this increase is small compared to the effect of hysteresis and difference of the two measurements of each point. In general, the transitions observed for the Turbo-CSL tube occur at slightly lower film Reynolds numbers compared to the Gewa-C tube. This behavior is opposed to the predictions of the flow pattern map of Roques, where the transitions for the Turbo-CSL tube occur at higher film Reynolds numbers.

Figure 6.5 depicts the observed transitions film Reynolds numbers for the Turbo-Chil and the plain tube. In addition to the predictions of the flow map mentioned above, the observations of Honda et al. [33] are given (dash dotted lines), except for the first transition as they did not consider the droplet-column mode. For the second and fourth transition the lower and upper limits of their observations are plotted. Although classification difficulties for the flow of R-134a on this tube existed, the observed transitions are approximately in agreement with the predictions of the flow pattern map of Roques et al. [75] and Honda et al. [33]. Generally, the observed flow pattern transitions occur at higher film Reynolds number than the predictions except for transition between column and column-sheet mode. The transition to the sheet mode with increasing mass flow rate was about twice as high as the predictions. For this transition a large hysteresis was observed.



For the plain tube in the lower plots in figure 6.5, the predictions of the flow pattern map of Hu and Jacobi [73] are given additionally for comparison (dotted lines). These transitions are close to the values of flow pattern map of Roques et al. [75]. However, all observed transitions are above the predictions, especially for the transition to/from the sheet mode. As mentioned above, this difference is explained by the fact, that the flows observed on the plain tube for R-134a are very unstable and do not correspond to ideal flow modes.

The mean values of the transition film Reynolds numbers neglecting the effect of hysteresis for all types of tubes are listed in table 6.2.

Tube	Tube pitch	D $\leftrightarrow$ DC	DC $\leftrightarrow$ C	C $\leftrightarrow$ CS	CS $\leftrightarrow$ S
Turbo-CSL	<i>25.5mm</i>	85	178	463	898
	<i>28.6mm</i>	103	200	490	856
	<i>44.5mm</i>	101	197	447	931
Gewa-C	<i>25.5mm</i>	92	188	436	888
	<i>28.6mm</i>	109	223	444	992
	<i>44.5mm</i>	129	252	491	1072
Turbo-Chil	<i>25.5mm</i>	156	234	442	1190
	<i>28.6mm</i>	165	270	440	1264
	<i>44.5mm</i>	164	261	482	1323
Plain	<i>25.5mm</i>	199	336	567	1323
	<i>28.6mm</i>	152	315	519	1348
	<i>44.5mm</i>	205	321	504	1508

Table 6.2: Transitions film Reynolds numbers for refrigerant R-134a measured at room temperature ( $Ga^{1/4} \approx 453$ ).

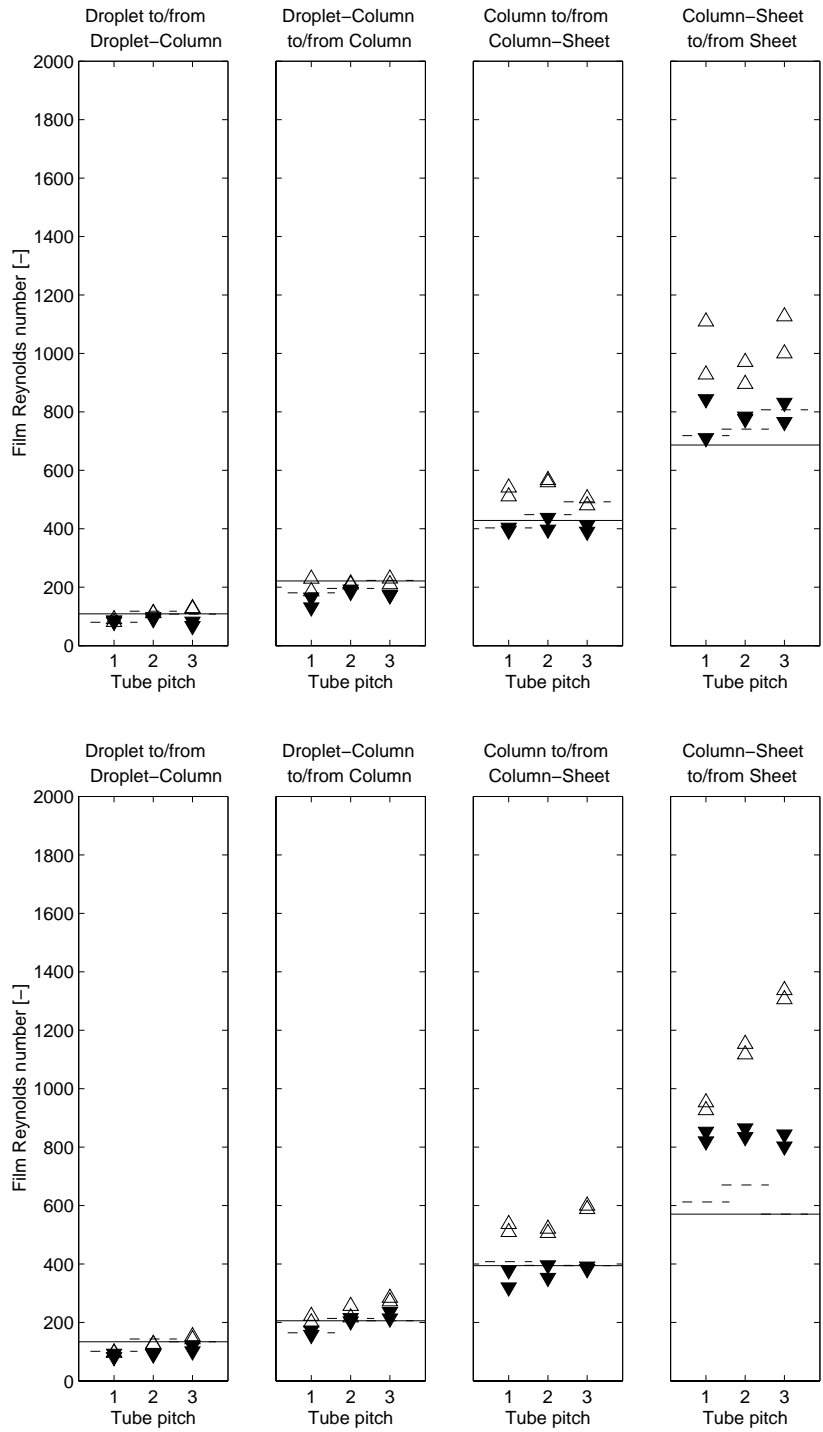


Figure 6.4: Observed transition film Reynolds numbers on Turbo-CSL (top) and Gewa-C tubes (bottom) for tube pitch  $25.5\text{mm}$  (1),  $28.6\text{mm}$  (2), and  $44.5\text{mm}$  (3) with increasing mass flow rate ( $\Delta$ ) and decreasing mass flow rate ( $\blacktriangledown$ ).

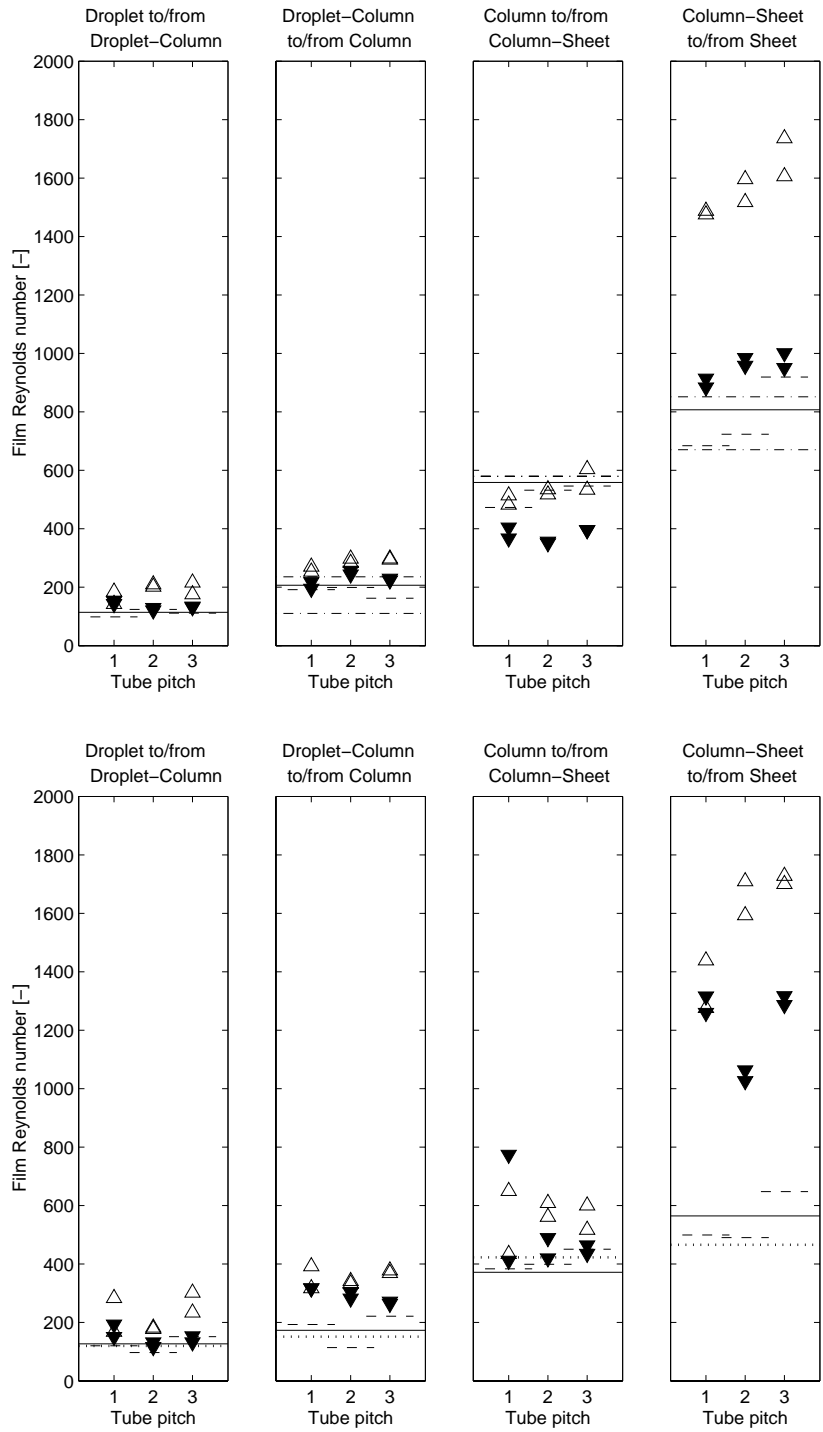


Figure 6.5: Observed transition film Reynolds numbers on Turbo-Chil (top) and plain tubes tubes (bottom) for tube pitch  $25.5mm$  (1),  $28.6mm$  (2), and  $44.5mm$  (3) with increasing mass flow rate ( $\Delta$ ) and decreasing mass flow rate ( $\blacktriangledown$ ).

## 6.4 Flow pattern observations with heat transfer

During the measurements of the heat transfer coefficient, the flow modes of the liquid flowing on the array of tubes were noted. At the smallest tube pitch of  $25.5\text{mm}$ , eight out of the ten tubes could be seen through the windows, for the tube pitch of  $28.6\text{mm}$  seven out of nine, and for the tube pitch of  $44.5\text{mm}$  four out of six, respectively. A high speed camera was installed in order to take short sequences of the flow patterns. The field of view was for all tube pitches centered on the second tube in the array, such that the flow falling on this tube and the tube below, the third tube, could be seen. The camera was positioned in front of the middle window and the flow was backlighted. Short sequences of  $5\text{s}$  duration were taken (30 frames per second, shutter speed of  $1/60$  to  $1/250\text{s}$ ) during the heat transfer measurements. Additionally, at the medium tube pitch of  $28.6\text{mm}$  high speed sequences of 250 images at 250 frames per second were acquired. First, the flow observations during measurements without liquid overfeed are discussed and then followed by the flow visualization during the measurements with liquid overfeed by the pump.

### 6.4.1 Without liquid overfeed

In figure 6.6 the condensate flows on the Turbo-CSL tube (left), on Gewa-C tube (middle), and on the Turbo-Chil tube (right) are depicted. These pictures were taken without liquid overfeed at a nominal row heat flux of  $20\text{kW/m}^2$  (upper pictures),  $40\text{kW/m}^2$  (middle), and  $60\text{kW/m}^2$  (lower pictures). The local film Reynolds numbers of the liquid leaving at the bottom of the tube determined from an energy balance are given in the pictures. At the lowest nominal heat flux below the top tube ( $Re \approx 50$ ) the flow pattern observed is droplet-column mode for the Turbo-CSL tube and droplet mode for the other two tubes. For these two tubes the droplets form liquid columns when they fall down, but as soon as they touch the tube below, these "columns" break down immediately. For the Turbo-CSL tube at the same conditions, breakdown of the "column" is observed for most of the falling sites, but at some locations thin columns are formed that do not break down over a long time period ( $4\text{s}$ ). Below the second tube at the same nominal heat flux ( $Re \approx 150$ ), basically the same behavior as below the top tube is observed. For the Turbo-CSL tube the number of sites with stable columns increases and they do not break down during the whole observation period. Sometimes two neighboring columns move towards each other and coalesce. For the Gewa-C, no stable columns are formed below the second tubes. The number of falling sites increases and also the durations of the "intermediate columns" increases, but they do not stay longer than  $1/3\text{s}$ . On the Turbo-Chil tube the flow off the bottom of the second tube at the lowest heat flux is even less regular than on the Gewa-C tube.

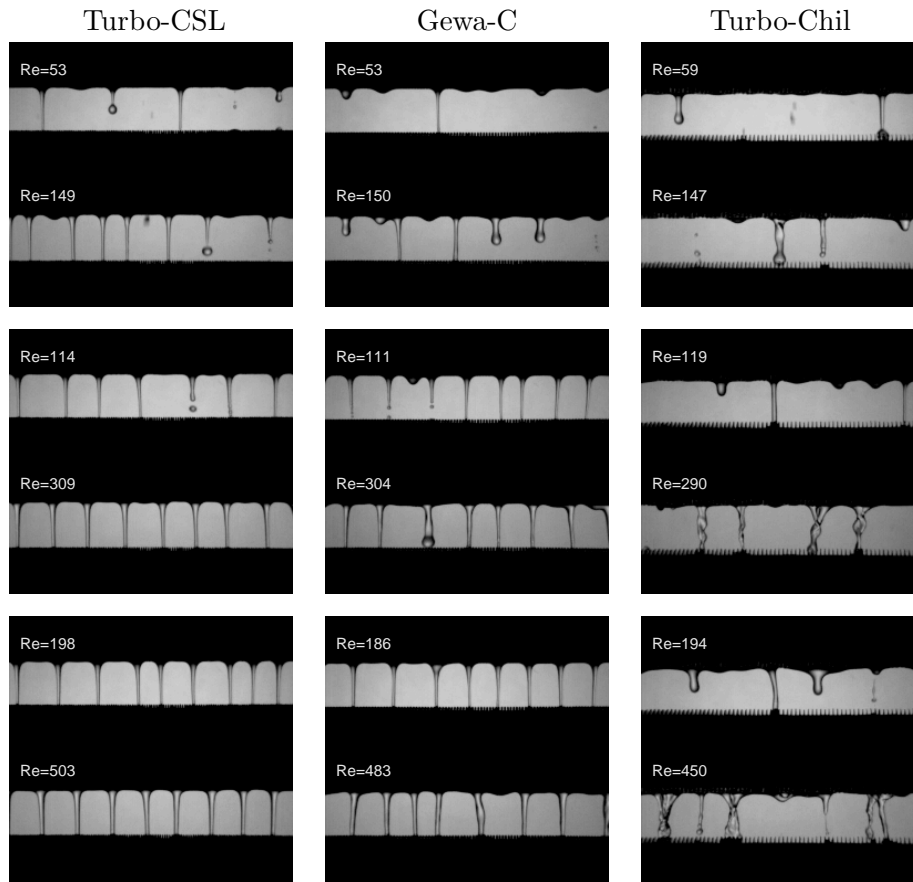


Figure 6.6: Intertube flow patterns observed on the second tube in the array (without overfeed) at a tube pitch of  $28.6\text{mm}$  for R-134a condensing at a nominal heat flux of  $20\text{kW/m}^2$  (top),  $40\text{kW/m}^2$  (middle), and  $60\text{kW/m}^2$  (bottom): Turbo-CSL (left), Gewa-C (middle), and Turbo-Chil (right).

The intermediate "columns" are not cylindrical and exist only during a short period of approximately  $1/10\text{s}$ .

At the nominal heat flux of  $40\text{kW/m}^2$  (middle row of pictures), for the Turbo-CSL tube and Gewa-C tubes, stable columns are formed at the bottom of the first tube, where the film Reynolds number is only about 110. For the Gewa-C, this observation is in contradiction with observations above, if one assumes that the flow patterns depend only on the film Reynolds number, as no stable columns were observed on the Gewa-C tube at  $Re = 150$  leaving the second tube. This indicates that the flow pattern leaving a tube depends also on the flow pattern of the liquid falling onto the tube. On the second tube at the nominal heat flux of  $40\text{kW/m}^2$ , the liquid arrives in the form of droplets at distinct locations on the top. As the enhancement

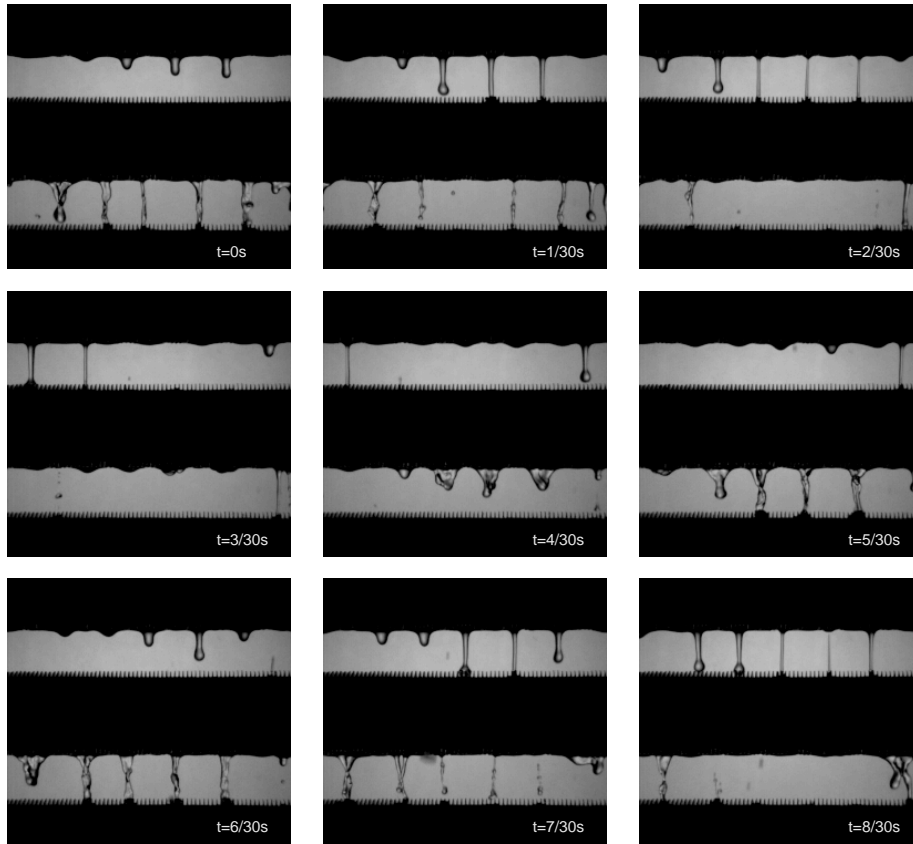


Figure 6.7: Condensate flow on the second tube in the array of low finned tubes (without overfeed) at a tube pitch of  $28.6\text{mm}$  for R-134a condensing at a nominal heat flux of  $40\text{kW}/\text{m}^2$ .

makes the axial spreading of the liquid difficult, it flows around the tube and leaves it approximately at the same axial location where the droplet hit the top of the tube. On the other hand, on the top tube the condensate is formed uniformly, which favors the formation of stable columns. Thus, on the Gewa-C tube at the nominal heat flux of  $40\text{kW}/\text{m}^2$ , stable columns are formed at the bottom of the first tube, at lower film Reynolds numbers compared to second tube at  $20\text{kW}/\text{m}^2$ , due to the uniform distribution of the liquid. For the Turbo-Chil tube at a nominal heat flux of  $40\text{kW}/\text{m}^2$ , neither below the top tube nor below the second tube stable columns are formed. The "intermediate columns" below the top tube are cylindrical, while the ones below the second tube are helically twisted. These twisted columns seem to be two columns being so close to each other that they touch and probably due to a small difference in momentum and departure angle, they spin around each other. This kind of flow pattern has only be observed

on the low finned Turbo-Chil tube. Both types of "intermediate columns" exist typically for  $1/10s$ .

At the highest nominal heat flux of  $60kW/m^2$ , the columns observed on the 3D enhanced tubes are stable. Below the top tube two neighboring columns coalesce and afterwards a new column is formed beside the coalesced column from time to time. This happens also rarely, below the second tube for the Gewa-C tube, while the columns below the second tube for the Turbo-CSL tube are very stable. It can be seen that the number of columns stays approximately the same, only the diameter increases, as the mass flow of refrigerant is doubled. For the Turbo-Chil tube, even at the highest heat flux, no stable columns are formed. The "intermediate columns" only become larger and occur during a little longer period up to  $1/3s$ .

In order to illustrate the fluctuation in the flow on the low finned tube, figure 6.7 shows a time sequence taken during condensation without liquid overfeed at a nominal heat flux of  $40kW/m^2$ . First, three "intermediate" columns are formed below the top tube. When they impinge on the second tube, liquid does not spread axially along the tube as it is channelled by the fins. Then the diameter of the columns decreases and they break down. The liquid that impinged on the second tube flows around the tubes and leaves at the bottom at the same axial positions. The three columns formed below the second tube are twisted and exist for about the same period as the "intermediate" columns formed below the first tube.

Figure 6.8 depicts the flow patterns observed on the enhanced tubes at a nominal heat flux of  $60kW/m^2$  for the three different tube spacings without liquid overfeed. For these conditions, no effect of tube spacing is observable. Stable columns are observed on the 3D enhanced tubes independent of the tube pitch. The average distances between the columns measured on these video images are  $7.3mm$  for the flow on the Turbo-CSL tube and  $7.9mm$  for the Gewa-C tube. These measured intercolumn distances are close to the most likely to appear Taylor wavelength for a thin film (according to Yung et al. [79] and Honda et al. [33] [30]) given by

$$\lambda_{thin\,film} = 2\pi\sqrt{\frac{2\sigma}{\rho_L g}} \quad (6.9)$$

which is  $7.0mm$  for R134-a at the current saturation temperature of  $304K$ . Instead, the critical wavelength is  $\lambda_c = 2\pi\sqrt{\sigma/(\rho_L - \rho_V)g}$  and the most dangerous wavelength is  $\lambda_D = \sqrt{3}\lambda_c$  (Carey [80]), which give values of  $5.0mm$  and  $8.6mm$ , respectively. Optical measurements of distances between the columns for water and glycol in a semester project in the LTCM laboratory (Schmitz [81]) found that the spacings varied from about 0.76 to 0.99 of the value given by equation 6.9, which thus gives values most similar to the critical wavelength.

On the Turbo-Chil tube, the flow pattern described above with the cylindrical and twisted "intermediate columns" is observed for all three tube

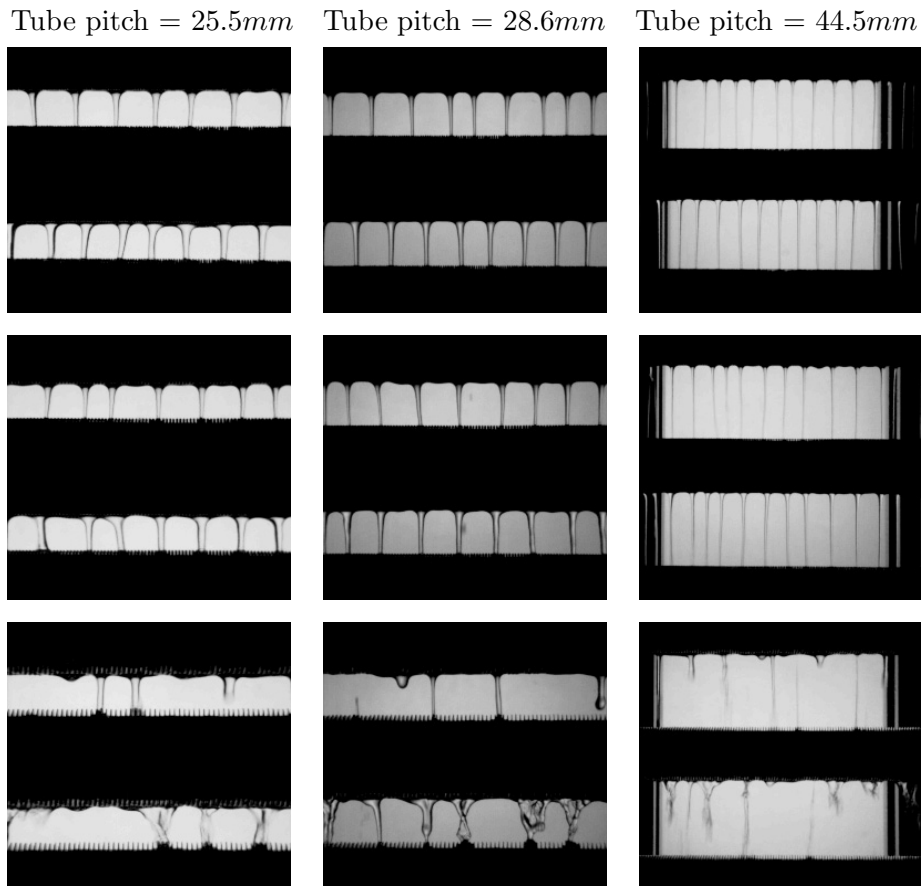


Figure 6.8: Intertube flow patterns observed on the second tube in the array (without overfeed) for R-134a condensing at a nominal heat flux of  $60kW/m^2$ : Turbo-CSL (top row), Gewa-C (middle row), and Turbo-Chil (bottom row).

pitches. The distances between the columns were not measured for this tube as the flow was not stable.

The effect of the liquid flow on the tubes on the heat transfer has been investigated for all types of tubes and is discussed first for both 3D enhanced tubes, as the liquid flow of R-134 can be classified in the normal five distinct flow patterns for these tubes. In figure 6.9 the heat transfer coefficient is given as function of the film Reynolds number of the liquid falling onto the tubes ( $Re_{top}$ ) for the measurements without overfeed at a tube pitch of  $28.6mm$ . In these measurements the nominal heat flux was varied from 20 to  $60kW/m^2$  in 5 steps. The flow pattern observed above each of the top seven tubes, which could be seen through the windows at this tube pitch, are illustrated by different symbols. Additionally, the four transitions observed



under adiabatic conditions are plotted as the vertical dashed lines (according to table 6.2). Note that the heat flux on a particular tube has an effect but is not differentiated in the graphs.

For the Turbo-CSL tube, during the heat transfer measurements, no droplet mode was observed. Even at the lowest nominal heat flux of  $20\text{kW}/\text{m}^2$  some stable columns were observed below the top tube as shown above at film Reynolds numbers as low as 50, while during the adiabatic tests the transition between droplet and droplet-column mode occurred around a film Reynolds number of 100. This difference might come from the fact that during adiabatic tests the liquid fell in droplets on the tubes, while with heat transfer the liquid flow is continuous below the top tube, showing again that the flow mode below one tube does not only depend on the liquid mass flow rate, but also how the liquid arrives onto the top of the tube. For the Turbo-CSL tube, the transition between droplet-column mode and column mode are in good agreement in the adiabatic and diabatic tests, occurring in both cases at a film Reynolds number of 200. In adiabatic tests, the mean value of the transition between column mode and column-sheet mode was at a film Reynolds numbers of about 500, while with heat transfer it was observed up to a film Reynolds number of 600, a little higher than the maximum value of this transition for adiabatic observations. A difference can be seen in the formation of the sheet mode during the adiabatic test and the heat transfer measurements. In the adiabatic tests, a zone with the column-sheet mode was observed while this zone is overlapping with the sheet mode during the heat transfer measurements. It was observed for the Turbo-CSL tube that flow mode changes from column mode directly to sheet mode without passing through the column-sheet mode. For example, at the highest heat flux (see figure 6.6), the flow pattern below the third tube (not seen on the image) is sheet mode at a film Reynolds number of only 700. The uniform axial distribution in column mode favors the formation of a uniform sheet.

For the Gewa-C (lower plot in figure 6.9), the droplet mode is only observed above the second tube at low heat flux. The range of film Reynolds numbers where the droplet-column mode occurs with heat transfer is larger than in the adiabatic tests. The same was found for the column mode, which was observed for the Gewa-C tube up to film Reynolds number of 600 in the diabatic tests. In contrast to the Turbo-CSL tube, for the Gewa-C tube the column-sheet mode was observed over a wide range of film Reynolds numbers. Above some film Reynolds numbers, the Gewa-C tube tended to form small sheets. Subsequently, the axial distribution was less uniform, which was unfavorable for the formation of the complete sheet mode. For the Gewa-C tube no complete sheet was observed during the measurements without overfeed at this spacing with film Reynolds numbers up to 1600 below the sixth tube in the array.

Regarding the effect on the heat transfer coefficient in figure 6.9, it can be seen that the heat transfer coefficient is highest for both types of tubes in

the droplet-column mode. With increasing inundation, in the column mode, column-sheet mode and sheet mode the heat transfer coefficient decreases. However, no strong effect on the heat transfer coefficient due to the change in flow modes can be seen. The variation in the heat transfer coefficient at a certain film Reynolds number is smaller in the column-sheet or sheet mode compared to the droplet-column and column mode. Above a film Reynolds number of 600, the heat transfer coefficient decreases approximately linearly with increasing film Reynolds number. This decrease is less pronounced for the Gewa-C tube. This difference might be explained by the difference in the observed flow pattern. In the column-sheet mode, as observed on the Gewa-C tube, there are small zones on the tube that are not inundated with liquid from the tube above, which is beneficial for the heat transfer.

Figure 6.10 depicts the corresponding two graphs for the Turbo-Chil tube and the plain tube. The heat transfer coefficients measured during the tests without overfeed are given together with the observed flow modes. As mentioned above, the classification of the observed flow pattern on these types of tubes was problematic. Apart from these classification difficulties, the observations with heat transfer and under adiabatic conditions (vertical dashed lines) are in fairly good agreement for the finned tube and the plain tube. As for the 3D enhanced tubes, no clear effect on heat transfer due a change in the flow mode was observed for the finned tube and the plain tube. This result is not surprising as the transitions were not distinctive for these two types of tubes.

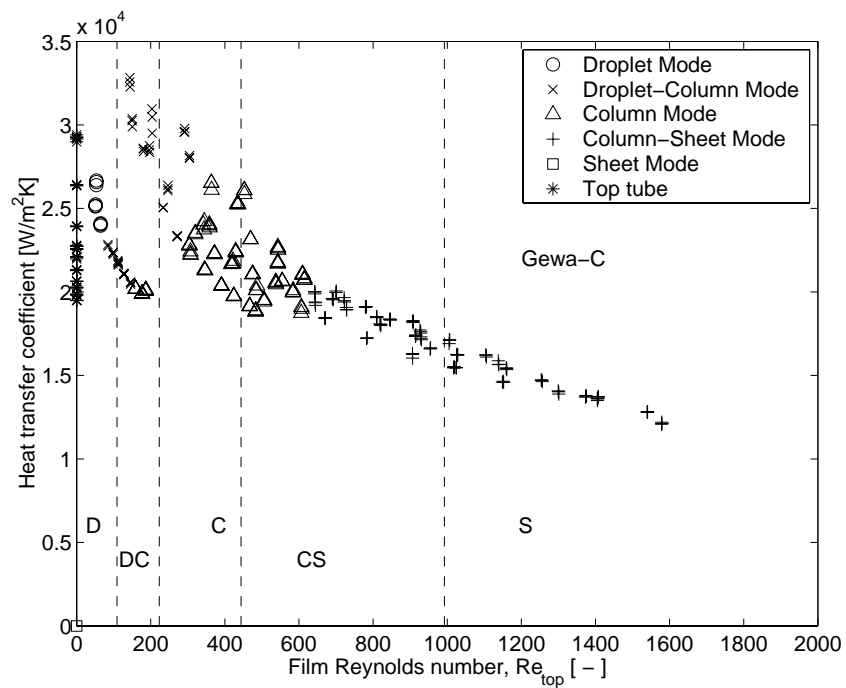
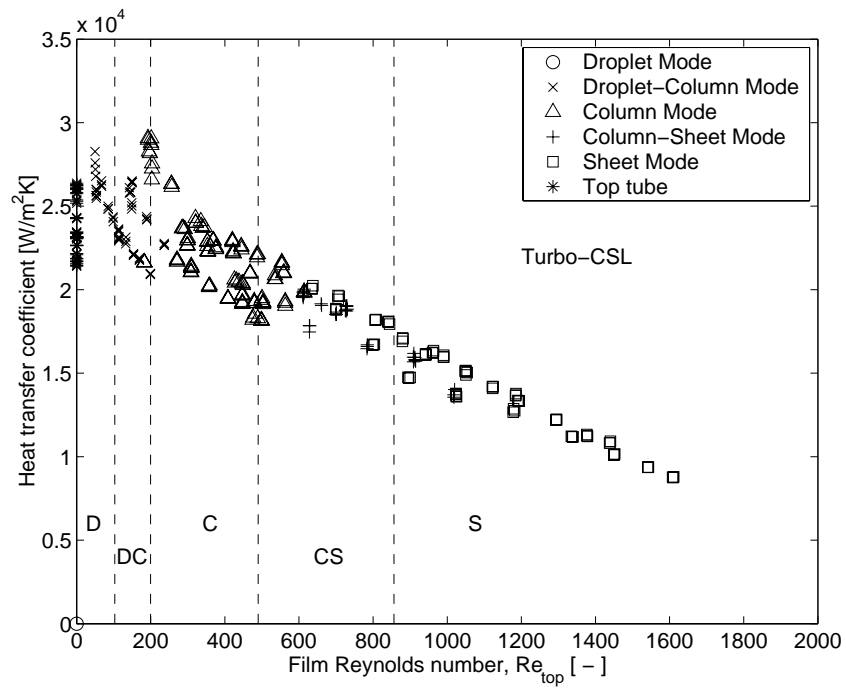


Figure 6.9: Heat transfer and flow pattern observations during the measurements without overfeed at a tube pitch of  $28.6\text{mm}$ : Turbo-CSL (top) and Gewa-C (bottom).

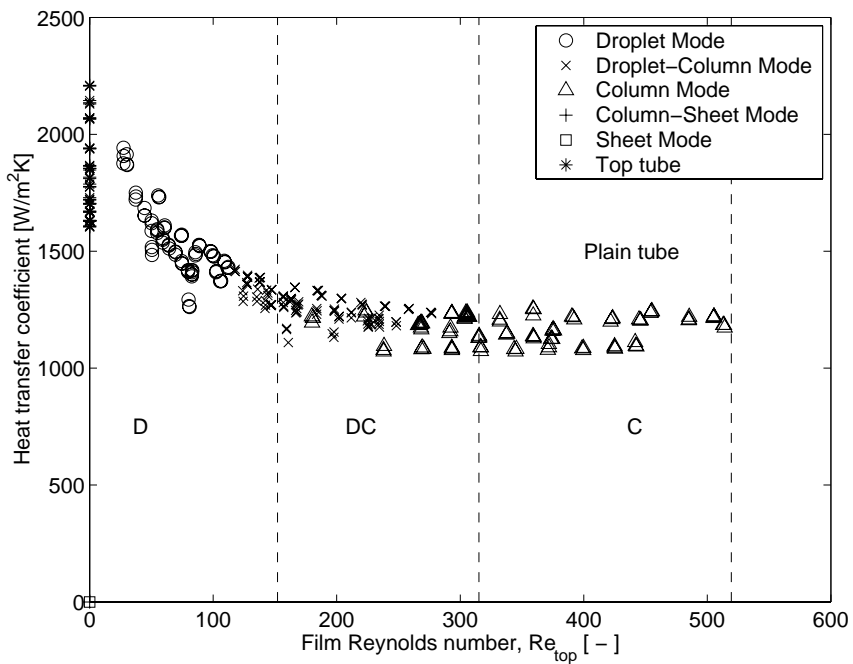
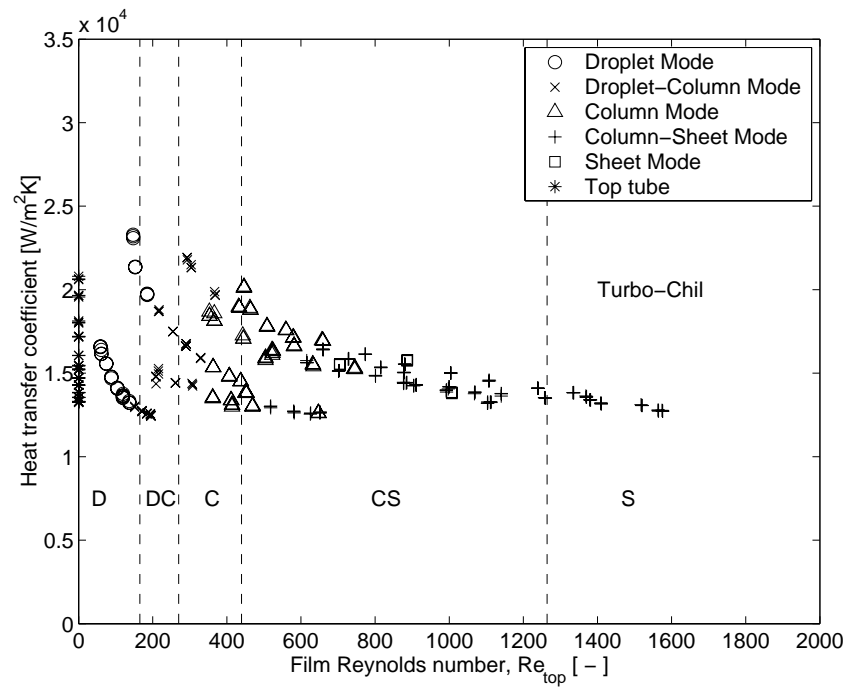


Figure 6.10: Heat transfer and flow pattern observations during the measurements without overfeed at a tube pitch of  $28.6mm$ : Turbo-Chil (top) and plain tube (bottom).

### 6.4.2 With liquid overfeed

In the previous section it was shown that in the column mode there is little effect of the tube spacing in the flow pattern. A similar behavior can also be observed for higher film Reynolds number achieved with liquid overfeed. Figure 6.11 depicts the observed flow patterns on the second and third tube in the array for the three enhanced types of tubes at two different tube pitches. During these observations liquid was fed onto the top tube in the array with a mass flow rate corresponding to a film Reynolds number of approximately 500. At the lower tube pitch on both 3D enhanced tubes column-sheet mode is observed. It can be seen that the Gewa-C tube tends to form small sheets compared to the Turbo-CSL tubes as mentioned above. Increasing tube pitch seems not to affect the flow pattern leaving the bottom and the same kind of sheets are formed. However, at the larger tube pitch, the sheets have more time to contract, resulting in a smaller axial width of the sheets. For the Gewa-C tube, the sheets contract completely at this flow rate so that the tube below receives a flow similar to the column-mode, which is beneficial for heat transfer since only a fraction of the tube length is inundated.

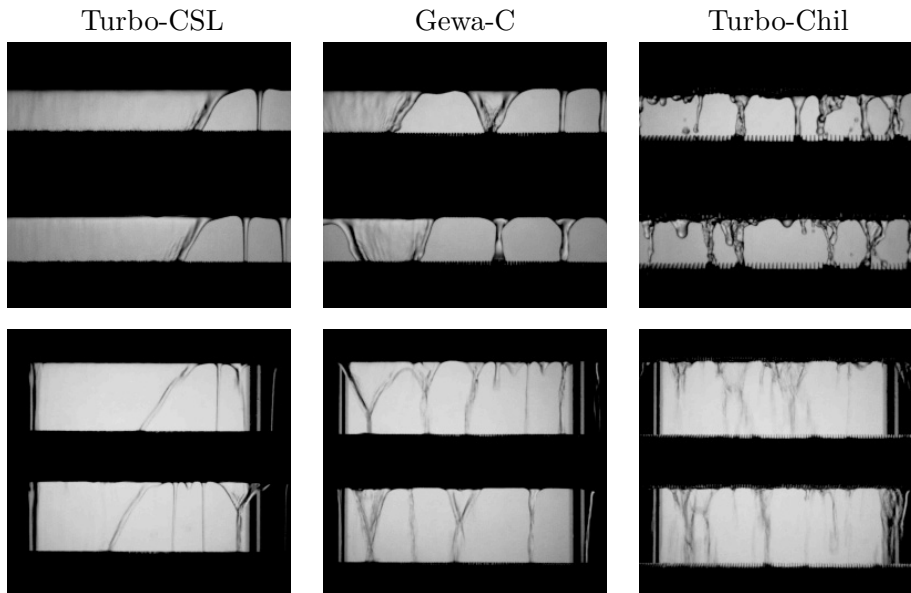


Figure 6.11: Intertube flow patterns observed on the second tube in the array for R-134a condensing at a nominal heat flux of  $20kW/m^2$  with liquid overfeed ( $Re \approx 500$ ): Tube pitch  $28.6mm$  (top), Tube pitch  $44.5mm$  (bottom).

A series of pictures covering the whole range of liquid overfeed rates tested in the present investigation are depicted in figures 6.12 and 6.13.

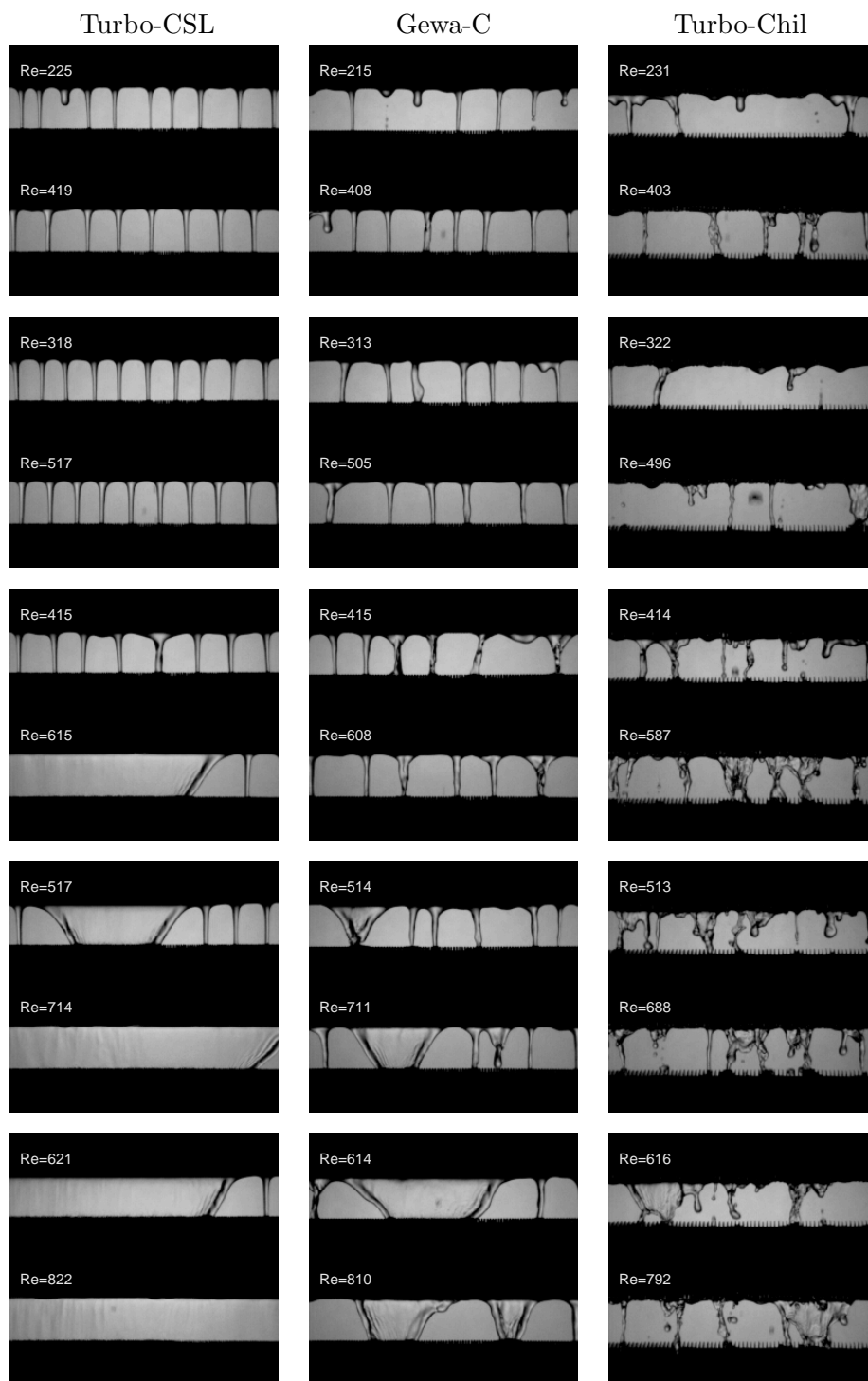


Figure 6.12: Intertube flow patterns observed on the second tube in the array (with overfeed) at a tube pitch of  $28.6\text{mm}$  for R-134a condensing at a nominal heat flux of  $40\text{kW/m}^2$ : Turbo-CSL (left), Gewa-C (middle), and Turbo-Chil (right).

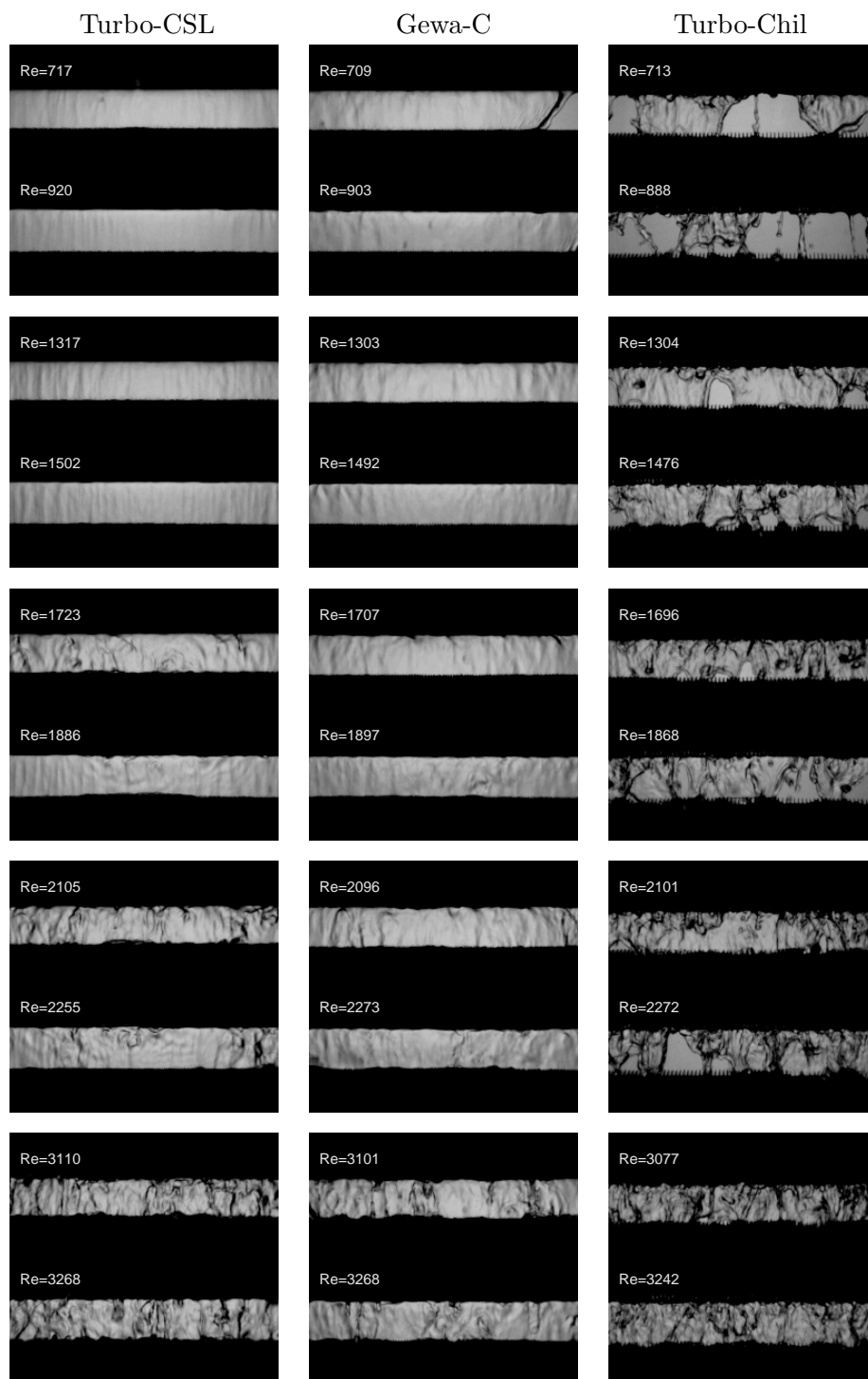


Figure 6.13: Intertube flow patterns observed on the second tube in the array (with overfeed) at a tube pitch of  $28.6\text{mm}$  for R-134a condensing at a nominal heat flux of  $40\text{kW/m}^2$ : Turbo-CSL (left), Gewa-C (middle), and Turbo-Chil (right).

These pictures were taken at a nominal heat flux of  $40kW/m^2$  at the tube pitch of  $28.6mm$ . At the lowest overfeed rate, droplet-column mode is observed for both types of 3D enhanced tubes at film Reynolds numbers of about 220. There are more stable columns on the Turbo-CSL tube than on the Gewa-C tube. With increasing overfeed rate columns are formed (second picture row), which are very regular on the Turbo-CSL tube opposed to the Gewa-C tube. For the Turbo-CSL tube, below the second tube in the second picture, the flow pattern is column mode at a film Reynolds number of 517. Interestingly, the same film Reynolds number is obtained below the first tube on the fourth picture but there a small sheet is formed. This difference is most likely due the difference in flow mode on the top of the tube, as in the latter case the liquid is fed directly from the distributor onto the tube. The width of the sheet increases on the Turbo-CSL with increasing film Reynolds number and at  $Re = 717$  a complete sheet is formed. For the Gewa-C tube, the formation of sheets starts approximately at the same film Reynolds number as for the Turbo-CSL tube ( $Re = 514$ ). The sheets formed on the Gewa-C tube are small compared to the ones formed on the Turbo-CSL tube and up to a film Reynolds number of about 800 no complete sheet is formed on the Gewa-C tubes. Comparing the last picture of the Gewa-C tube in figure 6.12 and the first one in figure 6.13, it can be that the flow pattern obtained below a tube is affected by the distribution onto the top of it. In the former case, small sheets are formed below the second tube at a film Reynolds number of about 800, while in the latter case almost a complete sheet is formed below the first tube at a film Reynolds number of 700. At higher film Reynolds numbers, the complete sheet formed on the 3D enhanced tubes becomes less stable with increasing film Reynolds number.

In the sheet mode, oscillations of the liquid sheet back and forth (front and back) were observed. These oscillations occurred for low overfeed rates in the lower part of the tube array. With increasing overfeed rate the oscillations increased in amplitude and were also observed below the top tube. For the Turbo-CSL tube at a film Reynolds number of about 1700, the oscillations below the top tube were so large that some of the liquid left the array of tubes sideways. For the Gewa-C tube the same was observed, but at higher film Reynolds numbers.

The flow on the low finned Turbo-Chil tube was very unstable compared to the flow on the 3D enhanced tubes as illustrated in figures 6.12 and 6.13. Even without overfeed, liquid left the array of tubes for the depicted conditions (nominal heat flux  $40kW/m^2$ , tube pitch  $28.6mm$ ), as the "columns" formed between the Turbo-Chil tubes moved back, forth, and sideways. The liquid left the finned tube sideways below the top tube of the array for film Reynolds numbers above approximately 500.



Figure 6.14 depicts a series of measurements with overfeed for the plain at a nominal heat flux of  $6kW/m^2$ . The liquid flow of R-134a on the plain tubes was observed to be very unstable like the flow on the low finned tube. Neither stable columns nor the formation of stable sheets could be seen. With increasing film Reynolds numbers the flow patterns changed gradually and no distinct transitions occurred. Little liquid left the array sideways below the top tube for film Reynolds numbers above 300 and a considerable amount left for film Reynolds numbers above 800.

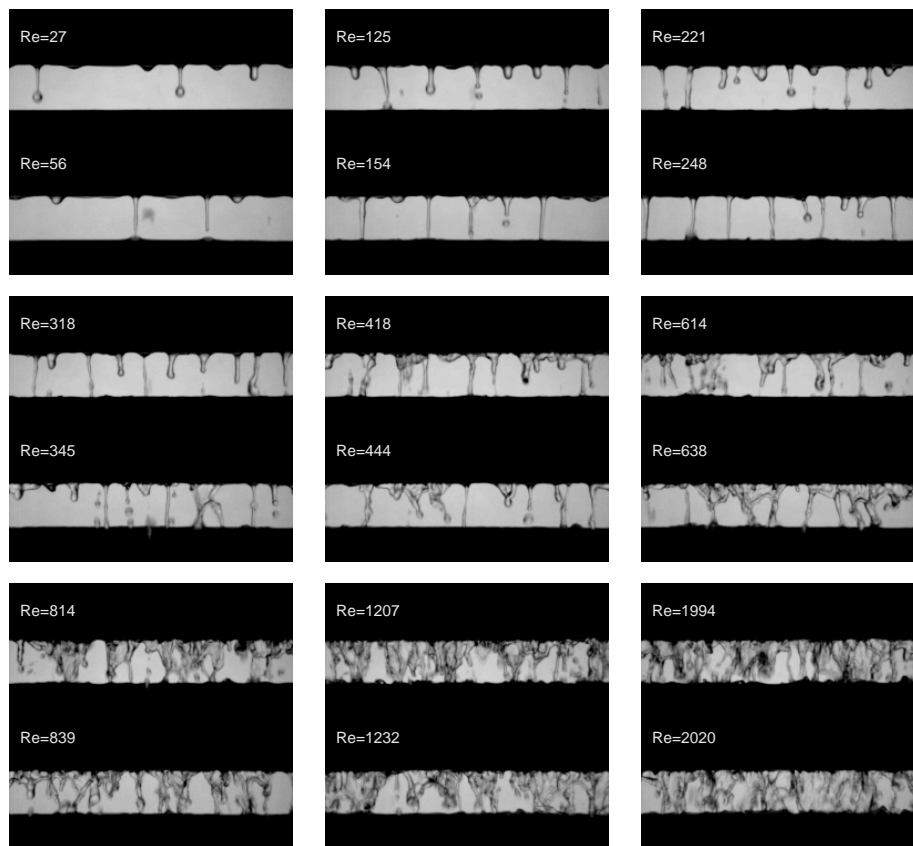


Figure 6.14: Intertube flow patterns observed for the plain tube on the second tube in the array (with overfeed) at a tube pitch of  $28.6mm$  for R-134a condensing at a nominal heat flux of  $6kW/m^2$ .

Figure 6.15 depicts the heat transfer coefficient measured on the second and third tube in the array for the Turbo-CSL tube and Gewa-C tube (shown in figures 6.12 and 6.13). The heat transfer coefficient is plotted as function of the film Reynolds number on the top of the tube and the observed flow modes above the tubes are given by the different symbols. The flow mode transitions determined under adiabatic conditions are given as verti-

cal dashed lines. With increasing film Reynolds number the heat transfer coefficient decreases for both types of tubes. Above a certain film Reynolds number the it decreases much slower. However, for both types of tubes this principal changes in heat transfer behavior occurred in the sheet mode and are most likely linked to the observed oscillations mentioned above and the liquid leaving. At the transitions between column mode and sheet mode no significant change in heat transfer performance is observed for both types of 3D enhanced tubes. At very low film Reynolds numbers (droplet-column mode), the heat transfer coefficient seems to decrease less with increasing film Reynolds numbers or to be almost constant. However, as only little data is available for these film Reynolds number no general conclusions can be drawn and further investigation is needed.

Figure 6.16 depicts the heat transfer coefficient measured on the second and third tube in the array for the Turbo-Chil tube and plain tube (shown in figures 6.12 to 6.14). For the low finned tube no effect on heat transfer due to a change in flow pattern can be seen. For the plain tube an increase in heat transfer coefficient with increasing film Reynolds number is observed in the sheet mode. However, this increase is most likely due to the observed sideways leaving of liquid.

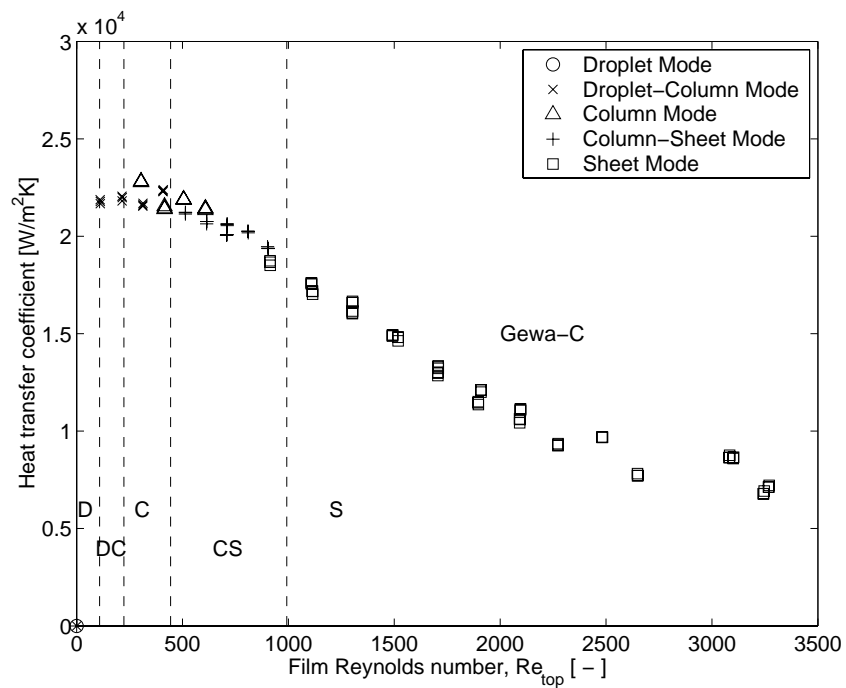
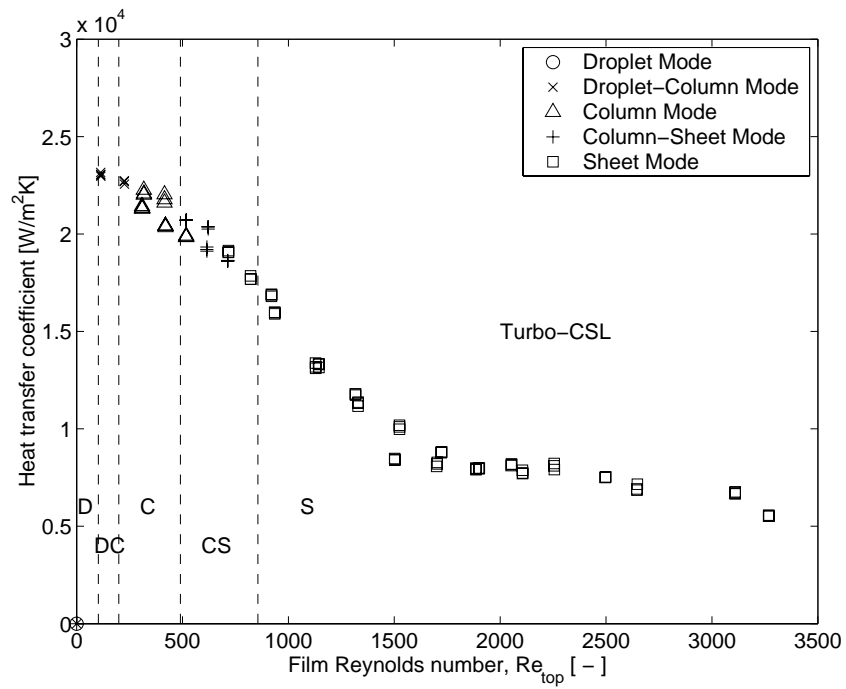


Figure 6.15: Heat transfer and flow pattern observations during the measurements with overfeed at a tube pitch of  $28.6\text{mm}$  at a nominal heat flux of  $40\text{kW/m}^2$ : Turbo-CSL (top) and Gewa-C (bottom).

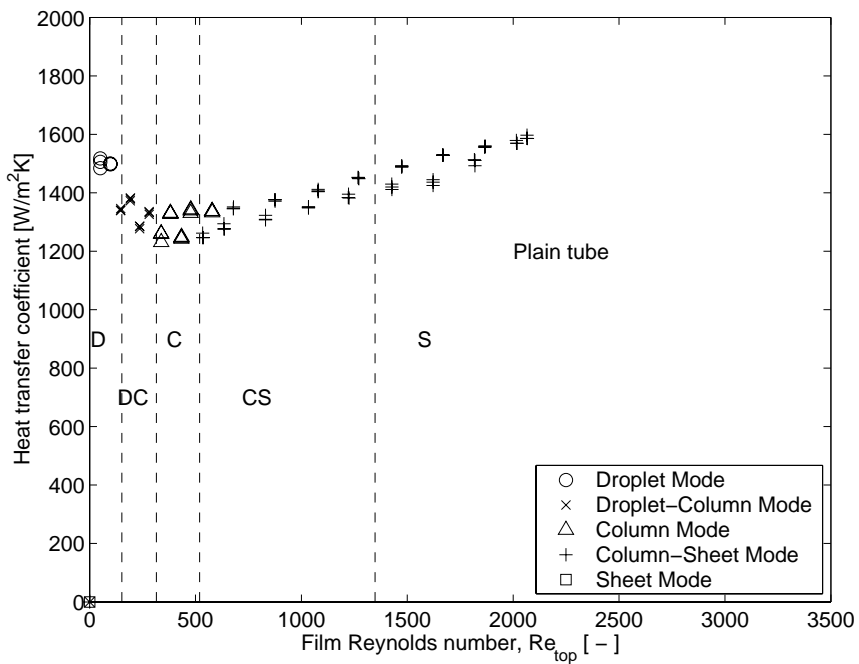
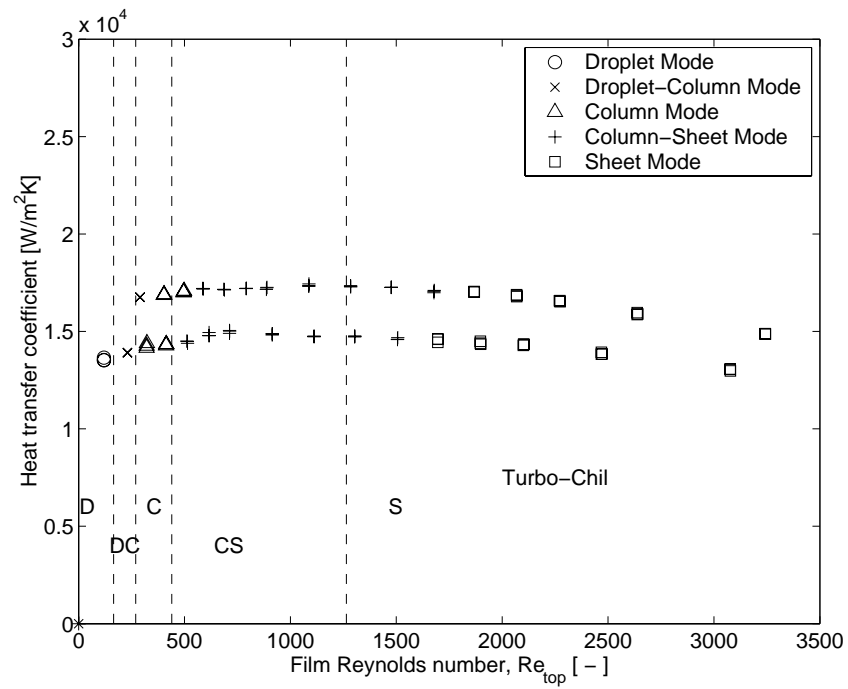


Figure 6.16: Heat transfer and flow pattern observations during the measurements with overfeed at a tube pitch of  $28.6mm$ : Turbo-Chil (top) and plain tube (bottom) at a nominal heat flux of  $40kW/m^2$  and  $6kW/m^2$ , respectively.

## 6.5 Conclusion

An integral part of the current investigation was dedicated to flow visualization of liquid flowing on the array of horizontal tubes. A short overview of flow pattern research was given and the five ideal flow modes were defined. With increasing mass flow rate (film Reynolds number) of refrigerant, the observed flow modes in this study were: droplet mode, droplet-column mode, column mode, column-sheet mode and sheet mode. The flow patterns of refrigerant were studied under adiabatic conditions using the pump only to feed liquid onto the top of the array at room temperature. A distinct difference between the flow patterns on the 3D enhanced tubes and those finned tube and the plain tube was observed for refrigerant R-134a. The ideal flow modes could strictly only be observed on the 3D enhanced tubes. The intertube liquid flow was very unstable on the low finned tube and on the plain tube. However, an attempt was made to determine the four transitions between the five flow modes for all four types of tubes and to compare them to other investigations. For the 3D enhanced tubes reasonable good agreement was found, apart from the transition to/from sheet mode which occurred at higher values in the present investigation. For the low finned tube and the plain tube, the agreement was found to be poorer, especially for the transition to/from sheet mode. The influence of tube spacing was found to be of minor importance on the observed flow pattern.

During the heat transfer measurements, the flow patterns were observed systematically on the array of tubes and video sequences were recorded showing the flow patterns between the first and third tubes in the array. It was found that the flow pattern of the liquid leaving the bottom of a tube does not only depend on the film Reynolds number, but also on the flow pattern falling onto the top of this tube. The flow patterns observed with heat transfer were in general agreement with the flow patterns observed without heat transfer.

For the 3D enhanced tubes, a difference in the formation of the liquid sheets was observed. The Gewa-C tube tended to form small sheets, while on the Turbo-CSL a complete sheet was formed at lower film Reynolds numbers. This might explain less pronounced degradation in heat transfer for the Gewa-C tube with increasing film Reynolds number.

For all four types of tubes, it was observed that liquid left the array of tubes sideways. Significantly, the larger amount was leaving the array of tubes sideways for the low finned tube and the plain tube as the flow on these tubes was always very unstable. For the 3D enhanced tubes, the behavior was different as the flow was stable at low film Reynolds numbers. With increasing film Reynolds numbers at the transition to the sheet mode or in the sheet mode, the liquid left the array sideways from time to time. The liquid sheets formed on the 3D tubes were observed to move forward and backward in a regular cyclic motion. For a further increase in film Reynolds

number, these oscillations were amplified up to a point where a part of the liquid did not always fall on the tube below. For the 3D enhanced tubes the effect on heat transfer of the flow modes was smaller than this effect of the liquid leaving the tubes sideways.

For the low finned tube and the plain tube, the classification of the flow patterns caused considerable difficulties and no clear transitions were observed due to the unstable liquid flow. Apart from these classification difficulties, for the finned tube no effect on heat transfer due to the flow pattern was observed. For the plain tube at low film Reynolds numbers, no effect on heat transfer by the droplet and column modes was found. In sheet mode, the heat transfer coefficient increased with increasing film Reynolds number, but this is also most likely linked to the fact that liquid was leaving the tubes sideways.

## Chapter 7

# Heat Transfer Models

In this chapter, the objective is to characterize the condensation heat transfer performance of four types of tubes, based on heat transfer measurements and on visual observations of the condensate flow. Comparisons were first made with existing models, next existing models were modified to achieve better agreement, and finally new models are proposed. First, the two 3D enhanced tube are treated, followed by the plain tube and the low finned tube.

### 7.1 3D enhanced tubes

As shown before, the heat transfer coefficients as a function of the film Reynolds numbers for the 3D enhanced tubes are basically characterized by two distinct zones. In the first zone the heat transfer coefficient decreases with increasing film Reynolds number. Above a certain film Reynolds number, the heat transfer coefficient then decreases much slower or achieves a constant value. Most likely this second behavior is linked to the fact that liquid leaves the array of tubes sideways (liquid "slinging") and reduces the inundation rate below that expected. This liquid "slinging" effect has also been noted and described by Wei and Jacobi [82] for adiabatic flows on arrays. Visual observations showed that the film Reynolds number at which the heat transfer behavior changed corresponded approximately to the film Reynolds number where the liquid starts to leave the tube row sideways.

#### 7.1.1 Without liquid leaving sideways

As a first step in modelling the heat transfer behavior of the 3D enhanced tubes (the Turbo-CSL and Gewa-C tubes), only the measurements where no liquid is leaving the tubes sideways are considered first, which were illustrated in section 5.5 (the data before the plateau). For this condition, for a given film Reynolds number, the heat transfer coefficient is dependent

on the heat flux, i.e. increasing the heat flux decreases the heat transfer coefficient.

During laminar film condensation, the heat transfer coefficient is dependent on condensation temperature difference. The concept of using a heat transfer coefficient defined as the ratio of heat flux to condensation temperature difference (saturation temperature minus base wall temperature) is debatable in such a case as also mentioned by Rose [59]. In other words, for calculating the heat flux for a given temperature difference, the heat transfer coefficient is multiplied by the temperature difference. When the heat transfer coefficient itself depends on the temperature difference (as in the case here) nothing is gained by separating the correlation for calculating the heat flux into a heat transfer coefficient and a condensation temperature difference (i.e. the idea behind Newton's law of cooling is that the heat transfer coefficient in convection is *not* a function of temperature difference, which in two-phase processes is normally not true). However, the heat transfer community is used to working with heat transfer coefficients, and for this reason it makes sense to use it for comparison purposes.

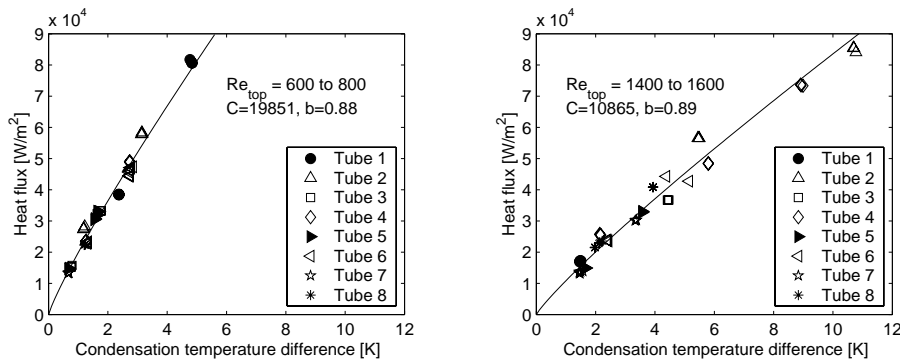


Figure 7.1: Limited heat flux range of measurements of the Turbo-CSL at the tube pitch  $25.5mm$ .

For fundamental understanding, it is helpful to look at the heat flux as a function of the condensation temperature difference as the dependent variable. During the measurements, the heat flux decreases with increasing liquid inundation for the same condensation temperature difference. For illustration purposes, the heat flux as a function of the condensation temperature difference for the Turbo-CSL tube at a pitch of  $25.5mm$  is given in figure 7.1. As the heat flux varies with liquid inundation, only data points in distinct ranges of inundation are plotted. On the left figure, data are limited to the points where the film Reynolds number of the liquid falling onto the top of the tube,  $Re_{top}$ , are in the range of 600 to 800, which is equivalent to a range of liquid mass flow as the physical properties were evaluated at the



saturation condition. On the right figure, data with film Reynolds numbers at the top of the tube in the range of 1400 to 1600 are shown. The data are from three measured heat fluxes at the smallest tube pitch on the top eight tubes. The ninth and the tenth could not be seen through the windows, and as it is not known if liquid is leaving sideways on these tubes, they were not considered in this analysis. As seen in figure 7.1, the data measured on eight different tubes at three different nominal heat fluxes ( $\approx 50$  data points) can be correlated by an equation of the following form

$$q_o = C \cdot \Delta T^b \quad (7.1)$$

The coefficients determined by a linear regression are given on the figures. The exponent  $b$  is approximately equal for these two cases, while the multiplicative constant  $C$  at the higher film Reynolds number is about half the value at the lower film Reynolds number. The same analysis was performed starting at film Reynolds numbers equal to 0 up to 2000 where the liquid starts to leave sideways. Little variation was found in the value of the exponent  $b$ , while the value of  $C$  decreased approximately linearly with increasing film Reynolds number. A similar behavior was also observed for the Gewa-C tube up to a film Reynolds number of 2500. For this reason, an equation as follows is suggested for the 3D enhanced tubes:

$$q_o = (a + c Re_{top}) \Delta T^b \quad (7.2)$$

A least squares optimization scheme was used with all measurements for each of the 3D enhanced tubes with inundation and no liquid leaving sideways in order to determine the values of the three constants in equation 7.2. The values of  $a$ ,  $b$  and  $c$  for the Turbo-CSL and Gewa-C tube are listed in table 7.1. The values of  $a$  and  $b$  are nearly identical and the difference in thermal performance comes from the value of  $c$ .

Tube	a [W/m <sup>2</sup> ]	b [-]	c [W/m <sup>2</sup> ]
Turbo-CSL	25500	0.91	-9.7
Gewa-C	25200	0.87	-6.5

Table 7.1: Coefficients in equation 7.2 for condensation on the tube array with a tube pitch of 25.5mm with no liquid leaving sideways.

For comparison purposes, a prediction of the heat transfer coefficient as function of the condensation temperature difference,  $\Delta T$ , and the liquid inundation,  $Re_{top}$ , can be calculated using equation 7.2 and  $\alpha_o = q_o/\Delta T$ . Comparisons of the measured and the predicted heat transfer coefficients for the Turbo-CSL and the Gewa-C tubes are depicted in figure 7.4. For both tubes, the predicted values are centered within the measured data points.

The heat transfer coefficients are about the same at low film Reynolds number for both types of tubes (coefficient  $a$ ). With increasing film Reynolds number, the heat transfer coefficients of the Turbo-CSL tube decrease faster than those of the Gewa-C tube, characterized by the coefficient  $c$ . The spread of the predicted values for the Turbo-CSL compared to Gewa-C is smaller due to the difference in the exponent  $b$ .

In order to make a quantitative comparison between the experimental results and the predictions, three statistical values are used. The relative error between measurement and prediction for each data point is defined by:

$$\epsilon_i = \frac{\text{pred}_i - \text{meas}_i}{\text{meas}_i} \quad (7.3)$$

The mean relative error is:

$$\epsilon = \frac{1}{N} \sum_{i=1}^N \epsilon_i \quad (7.4)$$

The mean absolute error is:

$$|\epsilon| = \frac{1}{N} \sum_{i=1}^N |\epsilon_i| \quad (7.5)$$

The standard deviation is:

$$\sigma = \left( \frac{1}{N-1} \sum_{i=1}^N (\epsilon_i - \epsilon)^2 \right)^{1/2} \quad (7.6)$$

The standard deviation is a measure of how the relative errors are distributed around the mean relative error. With a Gaussian distribution of relative errors, 68% are within  $\pm\sigma$  and 95% within  $\pm 2\sigma$ .

The relative errors for each data point are given in figure 7.2. The mean relative error for the Turbo-CSL tube is -1% with a standard deviation of 9.2%. For the Gewa-C tube, the mean relative error is -0.3% with a standard deviation of 7.2%.

The values of the coefficients  $a$  and  $b$  for both types of tubes were found to be very similar. For this reason, an attempt was made to characterize the difference in the heat transfer performance of the two 3D enhanced tubes only by the coefficient  $c$ . The values of the coefficients  $a$ ,  $b$  are set to the mean values obtained for both tubes, and then values of  $c$  were determined for both types of tubes. The results of this second prediction method and the comparison with the measurements are shown in figures 7.5 and 7.3.

With the second method the value of  $c$ , which characterizes the deterioration of the the heat transfer coefficient with increasing inundation, are  $-9.4W/m^2$  and  $-6.8W/m^2$  for the Turbo-Chil and the Gewa-C tube, respectively. These values and also the mean relative errors and the standard

deviations are very close to the first "tube specific" method. As these two 3D enhanced condensing tubes have rather similar geometries, this result is hence not so surprising. Since only one fluid, R-134a at  $31^{\circ}\text{C}$ , has been tested here, no attempt has been made to non-dimensionalize equation 7.2; it does have a form convenient to fitting data for other 3D tube/fluid combinations, however.

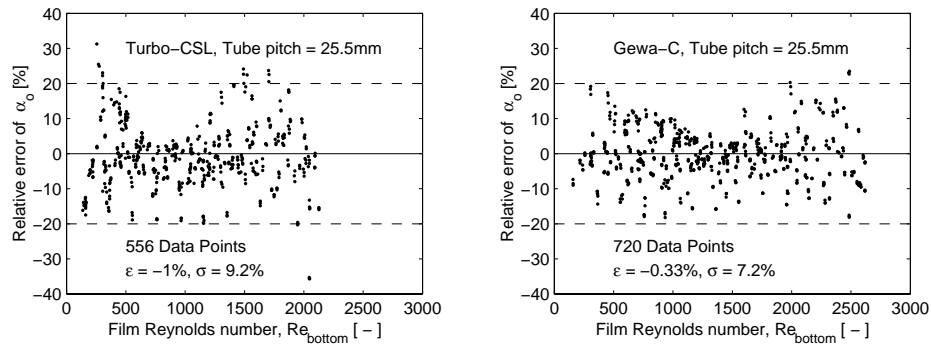


Figure 7.2: Prediction relative error of data at the tube pitch  $25.5\text{mm}$  (first method).

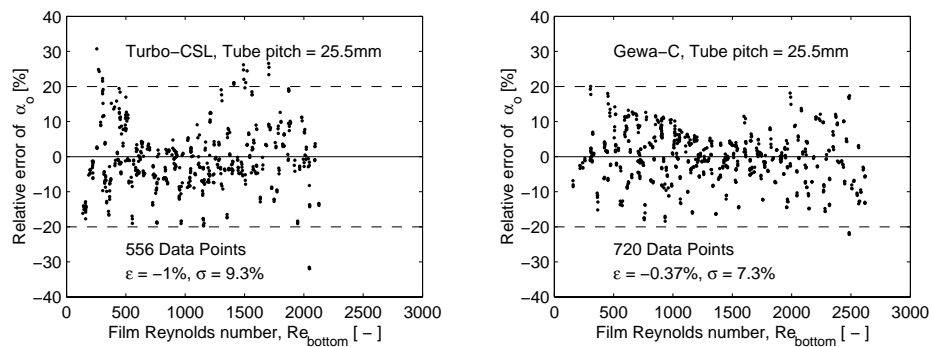


Figure 7.3: Prediction relative error of data at the tube pitch  $25.5\text{mm}$  (second method).

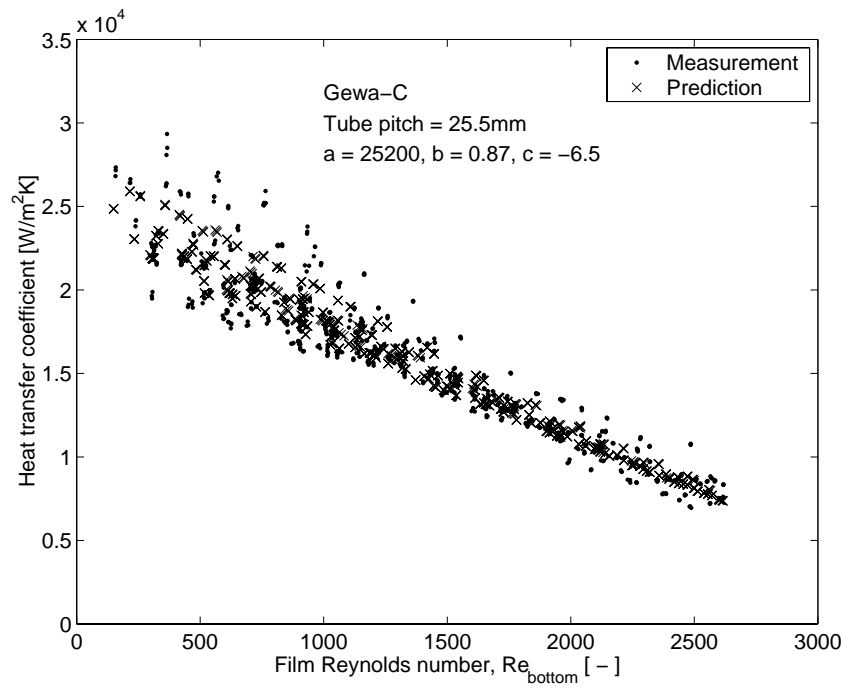
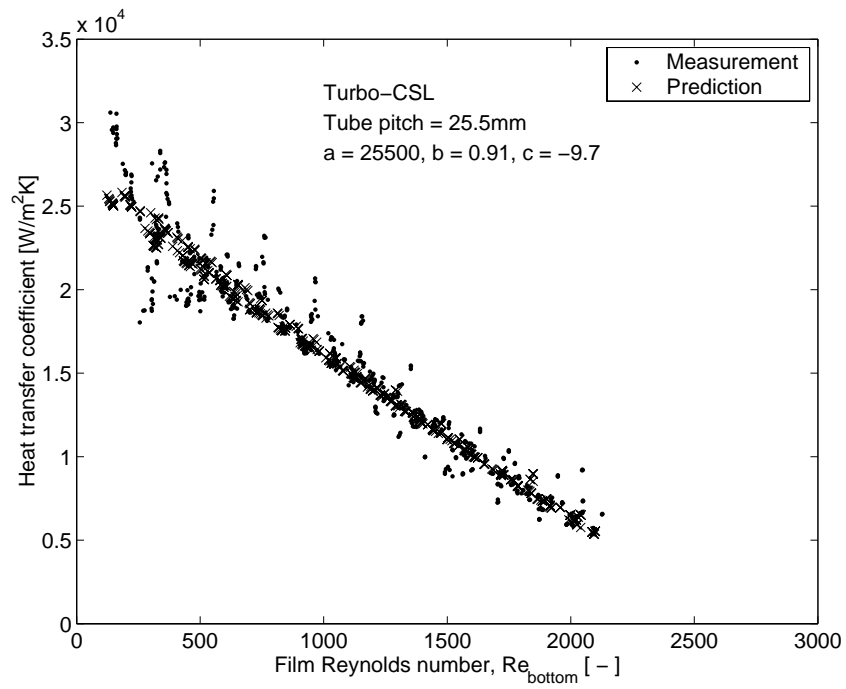


Figure 7.4: Prediction of heat transfer coefficient of the 3D enhanced tubes at a tube pitch of 25.5mm (first method).

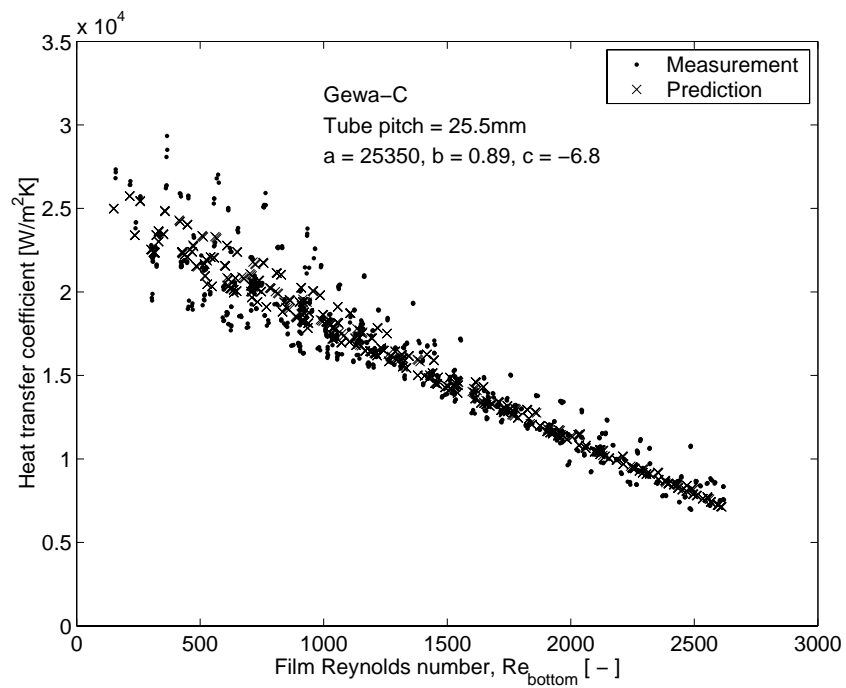
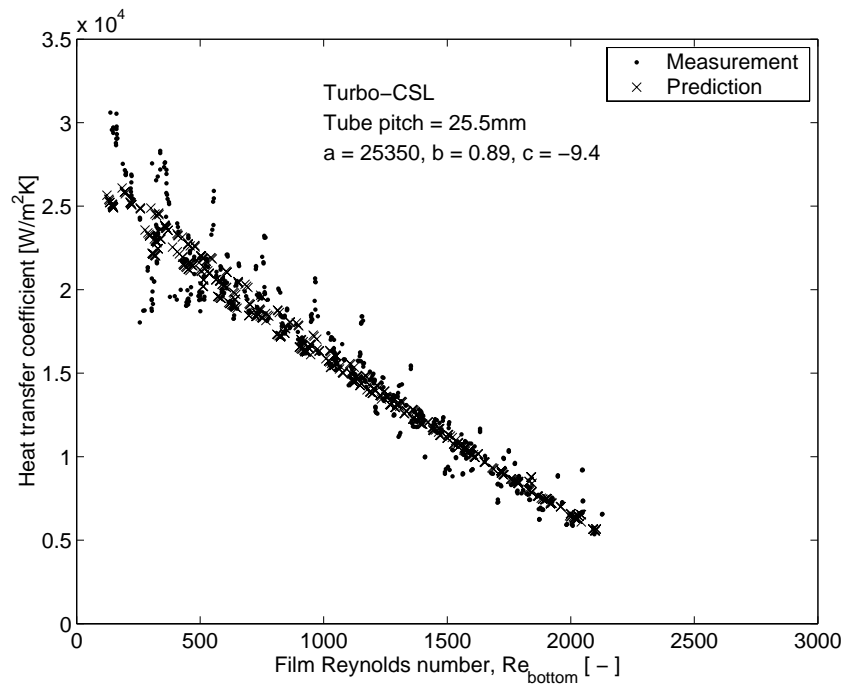


Figure 7.5: Prediction of heat transfer coefficient of the 3D enhanced tubes at a tube pitch of 25.5mm (second method).

### 7.1.2 With liquid leaving sideways

During the measurements, it was observed that because of unstabilities in the intertube flow, that some liquid leaves the tubes sideways and does not contact the lower tubes. For the 3D enhanced tubes this occurred at the transition to the sheet mode or in the sheet mode. At the transition, a continuous sheet is temporarily formed. When it breaks down, some liquid leaves the array of tubes sideways. Increasing the film Reynolds number, this break down phenomenon happens less. However, the continuous sheet is always unstable, moving a little forward and backward. For a further increase in film Reynolds number, this unstable movement is amplified and regular oscillations with frequencies of about  $1.5Hz$  are observed. At high film Reynolds numbers, the amplitude becomes so large that the liquid leaves the tubes sideways. As seen before, heat transfer deteriorates with increasing inundation. When some of the liquid leaves the array of tubes sideways, the tubes below receive less liquid on their top than otherwise expected, which has a beneficial effect on the heat transfer.

For this reason, a heat transfer model based on the present visual observations is proposed to account for the fraction of liquid leaving sideways. In an ideal situation, the liquid flows in a continuous sheet from the bottom of one tube onto the top of the tube below. The actual liquid does not however fall vertically in a stable sheet, but instead, it oscillates back and forth (front and back). With increasing mass flow rate, the amplitude of oscillation increases. This behavior is modelled as follows. The liquid is assumed to leave the bottom of the tube with a certain angle relative to the vertical, as illustrated in figure 7.6. This angle varies in time. The maximal angle of deflection of the liquid is nominated  $\theta$ . It is assumed that the angle  $\theta$  is a function of the film Reynolds number:

$$\theta = f(Re) \quad (7.7)$$

As long as  $\theta < \theta_{crit}$ , the liquid sheet oscillates on the top of the lower tube, but all the liquid stays on the tube. When  $\theta > \theta_{crit}$ , a fraction of the liquid misses the lower tube. The critical angle  $\theta_{crit}$  depends on the geometry of the tube array as follows:

$$\theta_{crit} = \arcsin\left(\frac{r_o}{p - r_o}\right) \quad (7.8)$$

where  $r_o$  is the tube radius and  $p$  is the tube pitch. The portion of liquid that leaves the tube is assumed to be proportional to the ratio of  $(\theta - \theta_{crit})/\theta$ . This means that the film Reynolds number on the top of the  $n$ th tube in the array can be expressed as

$$Re_{top,n} = \frac{\theta_{crit}}{\theta} Re_{bottom,n-1} \quad (7.9)$$

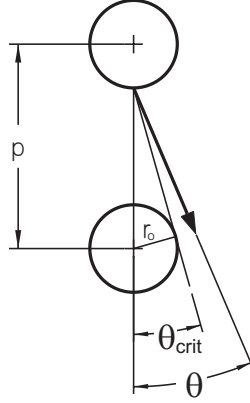


Figure 7.6: Schematic of liquid leaving the tube sideways.

Once the actual amount of liquid that falls on the top of the tube is known, equation 7.2 can be used to determine the heat flux on the tube. Thus, the heat flux of the  $n$ th tube becomes

$$q_{o,n} = \left( a + c \frac{\theta_{crit}}{\theta} Re_{bottom,n-1} \right) \Delta T^b \quad (7.10)$$

For application of this model, the calculation is started on the top tube of the array. As long as no liquid leaves ( $\theta < \theta_{crit}$ ), equation 7.2 is used to determine the heat flux on the tube and then by an energy balance gives the amount of liquid leaving the bottom of the tube. All the liquid flowing off the bottom of the tube is assumed to fall on the top of the tube below ( $Re_{top,n} = Re_{bottom,n-1}$ ). In this way the heat transfer can be determined on one tube after another stepping downwards in the array. As soon as the liquid starts to leave (when  $\theta > \theta_{crit}$ ), equation 7.9 is used to determine the amount of liquid that arrives on the tube below and subsequently equation 7.10 to determine the heat flux on the tube.

With these assumptions, the only unknown in the problem is the relationship between the angle  $\theta$  and the film Reynolds number (equation 7.7). To simplify matters, a linear function is assumed:

$$\theta = d Re + e \quad (7.11)$$

The present model using all the measured data for one type of tube were used to determine the coefficients  $d$  and  $e$  in equation 7.11 by a least square method. The results for the Turbo-CSL and the Gewa-C tube are listed

in table 7.2. A comparison of the measured and predicted heat transfer coefficients for all measurements for the 3D enhanced tubes are depicted in figure 7.7. The predicted heat transfer coefficient flattens out at three levels corresponding to the three tube pitches (and hence three different values of  $\theta_{crit}$ ). For these points, the amount of liquid condensed on the tube is nearly equal to the amount of liquid that leaves sideways and thus the heat transfer coefficient of the tube below does not decrease. The values of  $\theta_{crit}$  for the three tube pitches tested here are  $36^\circ$ ,  $30^\circ$  and  $16^\circ$ .

Each level of the plateaus corresponds to a certain percentage of liquid leaving the array of tubes sideways. The plateau observed at the smallest tube pitch of  $25.5mm$  corresponds approximately to 3% of the liquid leaving the array sideways. At the largest tube pitch of  $44.5mm$  approximately 10% of the liquid does not fall on the tube below and leaves the array of tubes sideways.

	d	e
Turbo-CSL	0.00027	0.08
Gewa-C	0.00018	0.14

Table 7.2: Coefficients in equation 7.11.

The relative errors of the present model are shown in figure 7.8 for both types of tubes. The distribution of the relative errors is given in figure 7.9. For instance, about 80% of the whole database for the two 3D enhanced tubes are predicted within the range of  $\pm 15\%$  error.

The relation for the maximum angle of deflection of the liquid leaving at the bottom of the tube was assumed to be linear (equation 7.11). According to the coefficients listed in table 7.2, which were determined using the whole data base, the liquid sheet is already deflected at small film Reynolds numbers ( $Re \approx 0$ ), as the values of the coefficient  $e$  are positive for both types of tubes. Apart from the fact that sheets are only formed at higher film Reynolds number, this does not correspond to the observations. In an evaluation using small subsets of data, the values of  $e$  were found to be negative for both types of tubes. In this case it was assumed that there was no deflection as long as the angle calculated with equation 7.11 was negative. This assumption, that the liquid starts to oscillate above a certain threshold value in the Reynolds number ( $\theta > 0$ ), is closer to the actual situation than the correlations given above ( $e > 0$ ). However, in a next step the relationship between the angle  $\theta$  and the film Reynolds number was forced to pass through the origin ( $e = 0$ ). The results of a new optimization of the value  $d$  are listed in table 7.3 as the second method in comparison with the values mentioned above for both types of tubes (1st method shown on table 7.2). Approximately the same standard deviation of the relative error compared to the whole database is obtained, while the mean relative error is about 1%



Tube	Method	a [ $W/m^2$ ]	b [-]	c [ $W/m^2$ ]	d [-]	e [-]	$\epsilon$ [%]	$\sigma$ [%]
Turbo-CSL	1st	25500	0.91	-9.7	0.00027	0.08	-2.4	12.9
	2nd	25500	0.91	-9.7	0.00031	0	-3.4	12.9
	3rd	25350	0.89	-9.4	0.00031	0	-3.2	12.8
	4th	25350	0.89	-9.4	0.00028	0	-8.8	13.3
Gewa-C	1st	25200	0.87	-6.5	0.00018	0.14	-1.9	10.1
	2nd	25200	0.87	-6.5	0.00024	0	-2.7	10.5
	3rd	25350	0.89	-6.8	0.00024	0	-3.1	10.6
	4th	25350	0.89	-6.8	0.00028	0	2.1	14.4

Table 7.3: Coefficients in equations 7.10 and 7.11 and relative errors of the prediction methods.

larger for the second method ( $e = 0$ ).

In the previous section, it was shown for the measurements without liquid leaving sideways, that the values of the coefficients  $a$  and  $b$  are similar for both types of tubes and the prediction error increases little if the same mean values are used for both tubes. An optimization using these mean values of  $a$  and  $b$  lead to equal values of  $d$  for both types of tubes as shown by the 3rd method. The relative mean error and standard deviation of this third method is also listen in table 7.3. The relative mean error is a little smaller for the Turbo-CSL tube while it increases only by 0.4% for the Gewa-C tube. The standard deviations are very close to those of the second method.

A further attempt to simplify the proposed model is to assume that the relationship between the angle  $\theta$  and the film Reynolds number can be approximated to be the same for both types of tubes used in the present investigation. Using a value of  $d = 0.00028$  as the best compromise of the values determined above, the values of the mean relative increase significantly as seen for the fourth method in table 7.3 for each type of tube. For this reason, this last approximation is not recommended.

The results are promising, proving that the observed behavior in heat transfer and liquid "slinging" can be described by the new method proposed above. While the method is empirical, it uses a minimum of empirical constants and includes some geometric characteristics in the liquid "slinging" process.

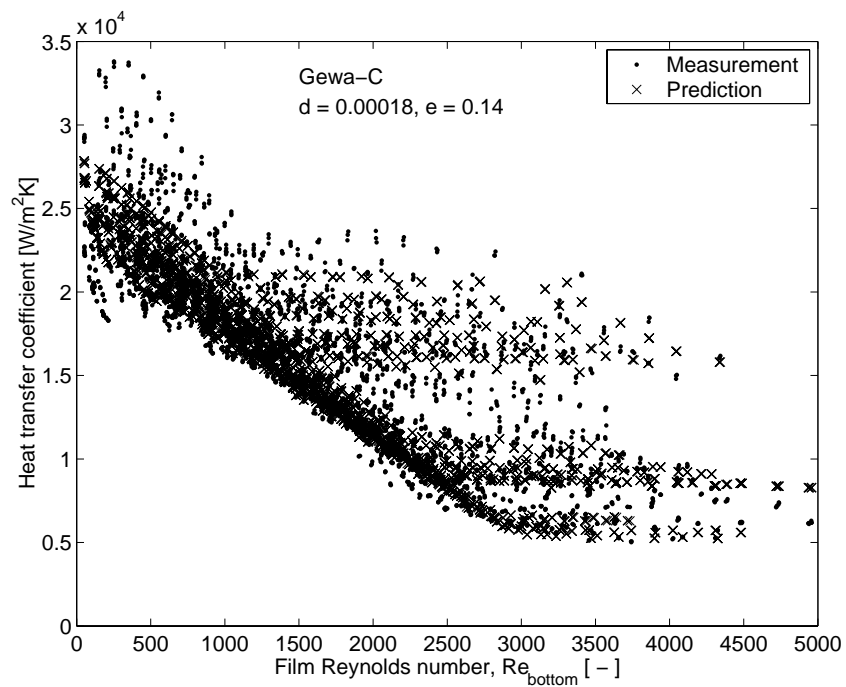
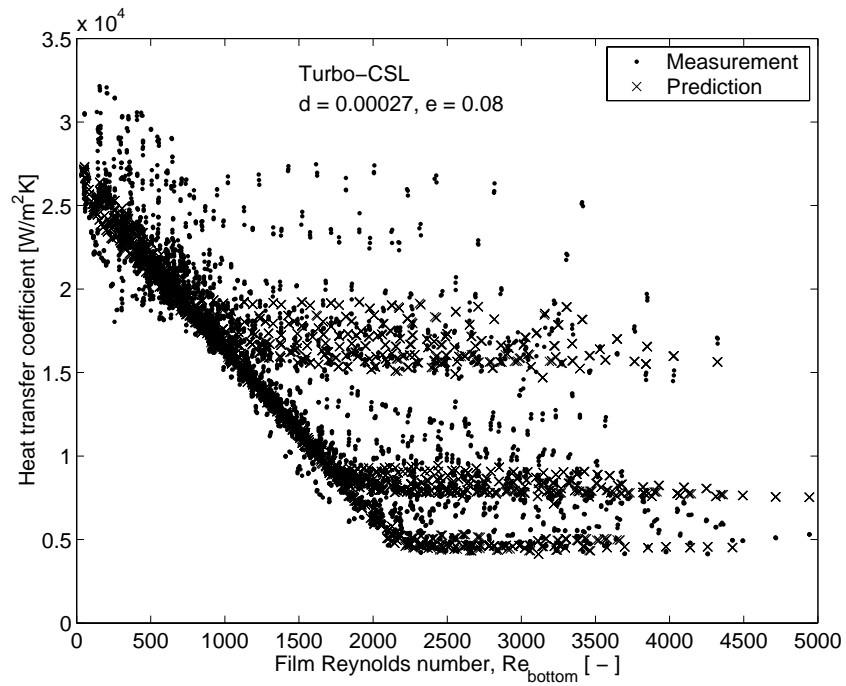


Figure 7.7: Prediction of heat transfer coefficients of the 3D enhanced tubes.

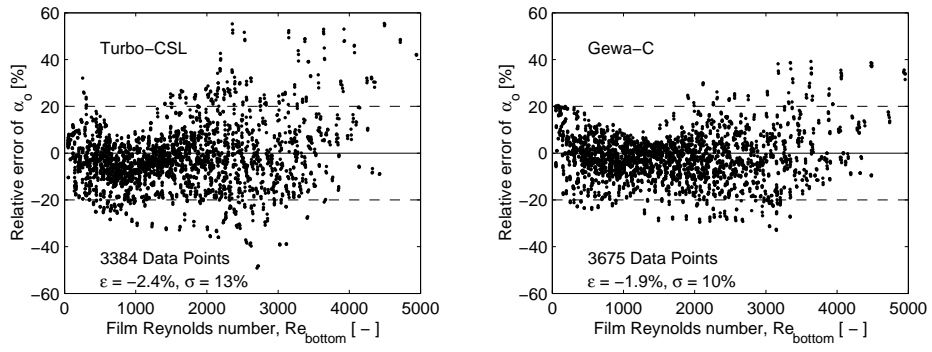


Figure 7.8: Relative errors of predictions.

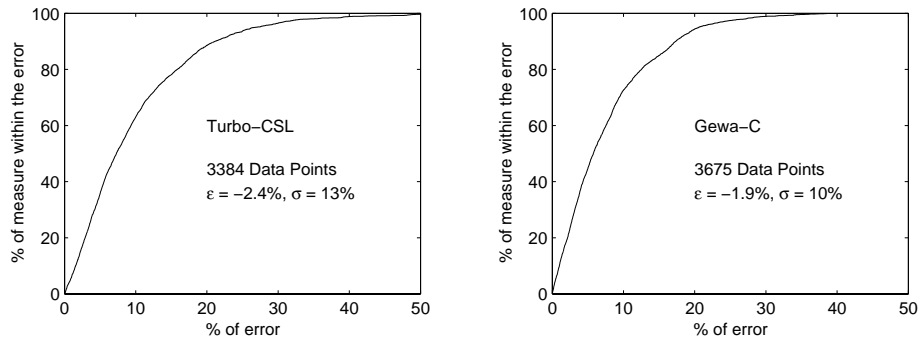


Figure 7.9: Distribution of the relative errors.

## 7.2 Plain tube

### 7.2.1 Comparison with Nusselt's theory

The heat transfer on a single plain tube can be well described using Nusselt's equation for laminar film condensation as shown in section 5.4.3. In this theory, the condensation number is a function of the film Reynolds number leaving the bottom of the tube:

$$\frac{\alpha_o}{\lambda_L} \left[ \frac{\mu_L^2}{\rho_L(\rho_L - \rho_V)g} \right]^{1/3} = 1.208 Re_{bottom}^{-1/3} \quad (7.12)$$

In textbooks, the Nusselt theory is often extended to an array of isothermal tubes. In the present investigation, the wall temperatures of the odd tubes in the array are higher as those of the even tubes due to the two-pass setup of the water circuit. A general form of equation 7.12 for the mean condensation number on a tube as a function of the condensation temperature and liquid inundation has been derived (see Appendix A.2).

$$\frac{\alpha_o}{\lambda_L} \left[ \frac{\mu_L^2}{\rho_L(\rho_L - \rho_V)g} \right]^{1/3} = 1.208 \left[ \frac{4}{\mu_L} \left( \frac{\Gamma_{bottom} - \Gamma_{top}}{\Gamma_{bottom}^{4/3} - \Gamma_{top}^{4/3}} \right)^{-3} \right]^{-1/3} \quad (7.13)$$

where

$$\Gamma_{bottom} = 1.923 \left[ \frac{r_o \lambda_L (T_{sat} - T_w)}{h_{LV}} \left[ \frac{\rho_L(\rho_L - \rho_V)g}{\mu_L} \right]^{1/3} + \Gamma_{top}^{4/3} \right]^{3/4} \quad (7.14)$$

The term in brackets on the right side of equation 7.13 corresponds to a film Reynolds number. Without inundation ( $\Gamma_{top} = 0$ ), equation 7.13 reduces to equation 7.12. With help of these equations, the experimental results of each tube in the array can be compared to Nusselt's theory. For illustration, figure 7.10 depicts a comparison for some measurements without overfeed. On the left, only data for the top two tubes are plotted. The data for the top tube are very close to the equation for condensation on a single tube (solid line) while data for the second tube are underpredicted by 22% by equation 7.13 (triangles). On the right figure, the data for the third tube are added. The data for the third tube are underpredicted by 28%. The measured data for the third tube follow the trend of the second tube and a similar behavior was found for the remaining tubes. On average, the second to the eighth tubes are underestimated by 27% by the Nusselt inundation theory at a tube pitch of 28.6mm. For the other tube pitches of 25.5mm and 44.5mm, the underpredictions are 27% (looking at first 7 tubes) and 28% (looking at first 3 tubes), respectively. This means

that the observed tube row effect for condensation on the array of tubes is less than predicted by Nusselt theory and is similar for all three measured tube pitches. A comparison of the predicted heat transfer coefficient based on Nusselt's inundation equation 7.14 with all experimental data from the measurements without liquid overfeed where no liquid was leaving the tubes sideways is depicted in 7.11. Thus, using equation 7.14 there is a significant tendency to underpredict the data.

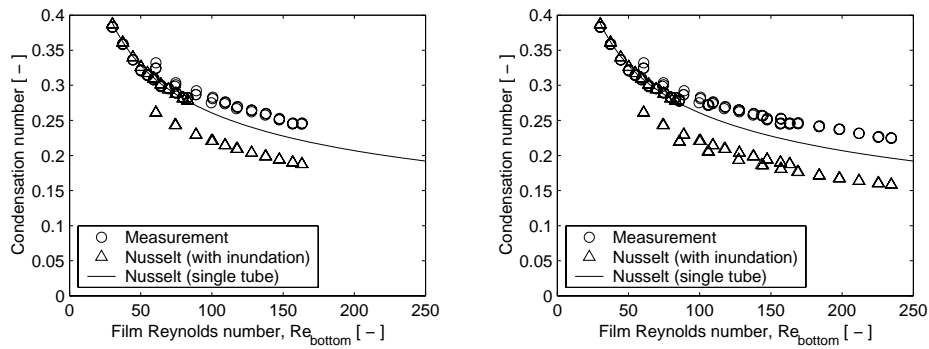


Figure 7.10: Comparison with Nusselt Theory for top two tubes (left) and top three tubes (right) with a tube pitch of  $28.6\text{mm}$ .

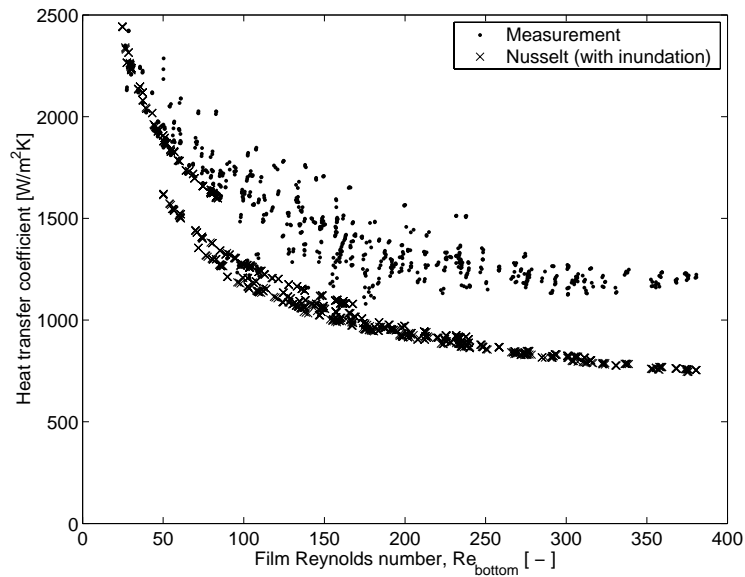


Figure 7.11: Measurements without liquid overfeed on the plain tube.

### 7.2.2 Tube row effect

In the literature, the inundation of condensate from tube row to tube row is often referred to as the tube row effect. The condensate from the above tubes drains onto the tubes below, increasing the amount of condensate flowing on each tube in addition to the new condensate formed on that particular tube. With increasing row number, starting from the top, the heat transfer performance of the tubes decreases and as such the mean heat transfer coefficient of the entire array. The performance of the entire array, or an individual tube, is often compared to the performance of the top tube. For high accuracy calculations this approach is not useful, as generally in a bundle, not only the inundation varies but also the surface temperature and the flow pattern. However, for comparison with other studies, the experimental results of the measurements without liquid overfeed will be presented as a function of position in the tube array.

The Nusselt theory for a single tube may be extended to a vertical array of horizontal tubes. Starting with the top tube without inundation, the analysis is applied to each individual tube utilizing the summation of the condensate flowing from the above tubes onto the top of the  $N$ th tube, counting from the top row towards the bottom. For uniform tube surface temperature, the Nusselt theory leads to

$$\frac{\bar{\alpha}_N}{\alpha_1} = N^{-1/4} \quad (7.15)$$

where  $\bar{\alpha}_N$  is the mean heat transfer coefficient on the entire array of  $N$  tubes and  $\alpha_1$  the mean heat transfer coefficient on the top tube in the array. Kern [3] modified this expression to reduce the row effect based on practical experience with actual condensers, changing the exponent to arrive at the following expression

$$\frac{\bar{\alpha}_N}{\alpha_1} = N^{-1/6} \quad (7.16)$$

In the present investigation the surface temperature of the tubes in the array was far from being uniform, mainly due the experimental setup with a two-pass water flow inside the tubes. Thus, the surface temperature of the tubes in the even row numbers was lower than on the odd tubes just above. An attempt is made to account for this non-uniformity of surface temperature. In analogy to equation 7.15, a similar expression with a correction for the non-uniformity of the surface temperature can be derived (see appendix A.3.1).

$$\frac{\bar{\alpha}_N}{\alpha_1} = N^{-1/4} \left( \frac{\overline{\Delta T}_N}{\Delta T_1} \right)^{-1/4} \quad (7.17)$$

where  $\Delta T_1$  is the condensation temperature difference on the top tube and  $\overline{\Delta T}_N = (\Delta T_1 + \Delta T_2 + \dots + \Delta T_N)/N$  is the mean condensation temperature difference on the entire tube array.

For this calculation, the mean heat transfer coefficient of the entire array of tubes was defined as the mean heat flux divided by the mean temperature difference:

$$\bar{\alpha}_N = \frac{\bar{q}_N}{\overline{\Delta T}_N} = \frac{\alpha_1 \Delta T_1 + \alpha_2 \Delta T_2 + \dots + \alpha_N \Delta T_N}{\Delta T_1 + \Delta T_2 + \dots + \Delta T_N} \quad (7.18)$$

Figure 7.12 depicts mean heat transfer performance of the entire array as a function the tube row. The mean heat transfer transfer coefficients divided by the heat transfer coefficient of the top tube for measurements at nominal heat fluxes of  $6kW/m^2$  (left) and  $20kW/m^2$  (right) are given. For comparison, the predictions, according to Nusselt and Kern for uniform surface temperature and both expressions with the correction for non-uniform surface temperature are also given. At the lower heat flux, the measurements are in agreement with the expression of Kern with the correction for non-uniform surface temperature. During the measurements, the surface temperature on the top tube is higher than on the other tubes because its performance is highest. For this reason, assuming a uniform surface temperature leads to a weaker tube row effect compared to the tube row effect taking into account the non uniformity of surface temperature. At the higher heat flux, the condensation temperature differences are larger than for the low heat flux, so the difference between the mean temperature and the temperature of the top tube are smaller and thus the temperature correction is smaller. At the heat flux of  $20kW/m^2$ , the observed data are higher than predicted by Kern's expression.

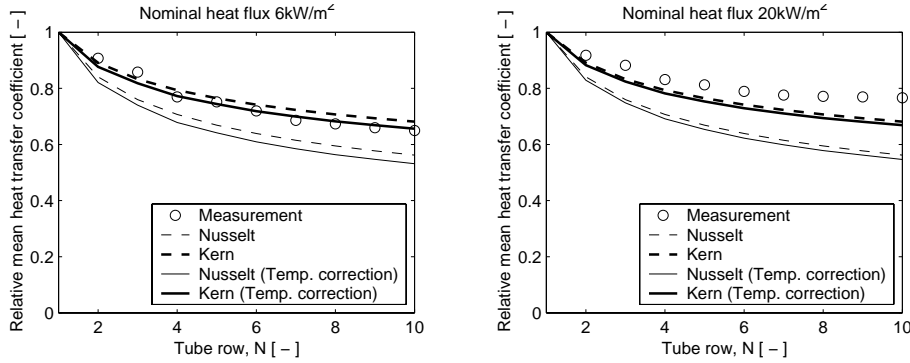


Figure 7.12: Tube row effect for the plain tube at a tube pitch of  $25.5mm$  at a nominal heat flux of  $6kW/m^2$  (left) and  $20kW/m^2$  (right).

Using the data and equations 7.15 and 7.17 to find the optimal exponents

Tube pitch	Nominal heat flux		
	$6kW/m^2$	$12kW/m^2$	$20kW/m^2$
25.5mm	-0.18 (-0.17)	-0.15 (-0.14)	-0.13 (-0.13)
28.6mm	-0.16 (-0.15)	-0.15 (-0.15)	-0.11 (-0.11)
44.5mm	-0.21	-0.13	-0.10

Table 7.4: Tube row effect for the plain tube without surface temperature correction (exponents in equation 7.15) for all tubes in the array and on the first six tubes (values in brackets).

Tube pitch	Nominal heat flux		
	$6kW/m^2$	$12kW/m^2$	$20kW/m^2$
25.5mm	-0.16 (-0.15)	-0.14 (-0.13)	-0.12 (-0.12)
28.6mm	-0.15 (-0.13)	-0.14 (-0.14)	-0.11 (-0.11)
44.5mm	-0.18	-0.12	-0.09

Table 7.5: Tube row effect for the plain tube with surface temperature correction (exponents in equation 7.17) for all tubes in the array and on the first six tubes (values in brackets).

in place of  $-1/4$ , tables 7.4 and 7.5 list the values of these exponents in the tube row expressions determined for the three tube pitches and for the three nominal heat fluxes. The values in brackets were determined using only the top six tubes at every tube pitch. Neglecting the effect of wall temperature non-uniformity leads to a weaker tube row effect. The differences for the different tube spacings are small. Generally, the tube row effect is stronger for lower heat fluxes. On average, tables 7.4 and 7.5 suggest an exponent of  $-1/7$  as opposed to  $-1/4$  of Nusselt and  $-1/6$  of Kern.

### 7.2.3 Waves and turbulent film condensation

It is known that the Nusselt theory has a limited range of applicability, as purely laminar condensate flow is only encountered at very low film Reynolds numbers. Little is known for condensation on horizontal tubes, but it has been intensively studied for condensation on a vertical plate. For this reason, a comparison of observations in literature for condensation on vertical plates (or tubes) are mentioned below. Observations of film condensation on vertical plates indicate that the interface becomes unstable and forms ripples or waves. These waves increase heat transfer by enlarging the interfacial area and reducing the mean thickness of the film.

According to Butterworth [83], the film Reynolds number for the onset of interfacial waves on a vertical plate occurs at about a film Reynolds number of 30. Another criterion for the onset of waves is related to the Archimedes number  $Ar_L$ , which is defined as



$$Ar_L = \frac{\rho_L^2 \sigma_L^{3/2}}{\mu_L^2 g^{1/2} (\rho_L - \rho_g)^{3/2}} \quad (7.19)$$

The laminar falling film condensation heat transfer on vertical plates is enhanced when

$$Re > 9.3 Ar_L^{1/5} \quad (7.20)$$

For refrigerant R-134a with an Archimedes number of 1.6 at the present test conditions, waves should occur according to this criterion for film Reynolds numbers above 10.

In the present investigation the film Reynolds number at the bottom of the top tube ranged from 20 to 80. As shown before, the heat transfer coefficient measured on the top tube was in very good agreement with Nusselt's theory for laminar film condensation. However, the coefficients measured on the second and the following tube are underpredicted by almost 30%. This observation is explained by the difference in flow pattern (as a continuous sheet was never observed) and by the occurrence of interfacial waves in analogy to condensation on a vertical plate.

To account for the effect of waves on heat transfer, Kutateladze [84] suggested an empirical correction of  $0.8(Re/4)^{0.11}$  for condensation on a vertical plate as mentioned by Thome [70]. Kutateladze and Gogonin [85] used an empirical correction term (referring to Labuntsov [86]) in the Nusselt equation for the enhancement of heat transfer on a vertical surface by the waves of  $(Re/2)^{0.04}$  over the range of film Reynolds number of  $10 < Re < 200$ .

During the present heat transfer measurements, the condensate flow on the plain array was very unstable as noted previously and due to the occurrence of liquid "slinging" some liquid left the tubes sideways. For clearness, and to reduce the effect of liquid "slinging" to a minimum, only the results of the top three tubes are considered in the following analysis.

Figure 7.13 depicts the measured data on the top three tubes at all tube pitches and heat fluxes. On the upper graph the data below the film Reynolds number of 400 are shown. The prediction by the Nusselt theory and predictions using an empirical multiplier to account for the waves are also plotted. At low film Reynolds numbers the lower limit of the measured data is well described by the Nusselt theory. These points are the measured values on the top tube without liquid inundation as seen before. On the top tube the measured data are very close to Nusselt theory up to film Reynolds numbers of about 80. For higher film Reynolds numbers the measured heat transfer coefficients are underestimated by Nusselt theory. Both empirical corrections for the waviness of the film lie within the measured data, showing that these corrections determined for condensation on vertical surface applied to the horizontal tube theory work well for condensation on horizontal tubes. The correction of Kutateladze [84] seems to be closest to the

measured data. The tendency of the Kutateladze [84] and Kutateladze and Gogonin [85] methods to underpredict the data at the high film Reynolds numbers is thought to be because of liquid slinging.

At high film Reynolds numbers the condensate flow may become turbulent. The transition threshold for the bundle is adapted from a vertical plate turbulent transition criterion of 1600 (but also values of 1200, 1800, and 2000 have been proposed as remarked by Thome [70]).

Colburn [87] set the transition at a film Reynolds number of 2000 when comparing his experimental data to the Nusselt theory. Applying an analogy to turbulent liquid flow in pipes, Colburn proposed the following correlation for the local condensing coefficient on a vertical plate:

$$\frac{\alpha}{\lambda_L} \left[ \frac{\mu_L^2}{\rho_L(\rho_L - \rho_V)g} \right]^{1/3} = 0.056Re^{0.2}Pr_L^{1/3} \quad (7.21)$$

Butterworth [83] recommends adapting the Labuntsov expression [86] for turbulent film condensation on a vertical plate to horizontal tubes for predicting local turbulent film condensation on the  $n$ th tube row in horizontal tube bundles:

$$\frac{\alpha_o}{\lambda_L} \left[ \frac{\mu_L^2}{\rho_L(\rho_L - \rho_V)g} \right]^{1/3} = 0.023Re^{0.25}Pr_L^{0.5} \quad (7.22)$$

On the lower plot in figure 7.13, the data over the entire measured range is given and the two correlations for condensation in the turbulent flow regime are added. For film Reynolds numbers above 1000, the prediction by the correlation of Labuntsov is within the scatter of the experimental data, while the correlation of Colburn clearly overpredicts the measured data.

Honda et al. [29] used an asymptotic correlation for condensation of stagnant R-113 vapor on a vertical column of horizontal tubes as follows:

$$\frac{\alpha_o}{\lambda_L} \left[ \frac{\mu_L^2}{\rho_L(\rho_L - \rho_V)g} \right]^{1/3} = [(1.2Re^{-0.3})^4 + (0.072Re^{0.2})^4]^{1/4} \quad (7.23)$$

They referred to [85] and [28] who developed this equation based on R-12 and R-21 data. The first term in equation 7.23 is the Nusselt solution with the enhancement factor for the waves from Kutateladze and Gogonin [85]. The second term is a correlation for turbulent condensation, similar to the expression of Colburn. However, as dependency of the Prandtl number is not clear (i.e.  $Pr_L$  has disappeared in equation 7.23), this equation does not capture the different value of  $Pr_L$  for R-134a in the comparison shown in figure 7.13. It can be seen, at low film Reynolds numbers, that equation 7.23 is asymptotic to the correlation of Kutateladze and Gogonin, and at high film Reynolds numbers it lies between the correlations of Colburn and

of Labuntsov, overpredicting most of the experimental data at high film Reynolds numbers.

In analogy to the correlation of Honda et al., the following equation was used to obtain a correlation fitting the present R-134a data on the top three tubes. The multiplier of the expression for the turbulent flow regime was found to be  $C = 0.060$ :

$$\frac{\alpha_o}{\lambda_L} \left[ \frac{\mu_L^2}{\rho_L(\rho_L - \rho_V)g} \right]^{1/3} = [(1.2Re^{-0.3})^4 + (C Re^{0.2})^4]^{1/4} \quad (7.24)$$

Honda et al. [29] found good agreement of their equation 7.23 with their experimental data for R-113 condensing at  $0.12MPa$  ( $Pr = 7.10$ ) on an in-line tube bundle at low vapor velocity. Applying a Prandtl number correction for R-134a ( $Pr = 3.38$ ) on their value analogous to the expression of Colburn, a similar value of  $C$  is obtained  $(0.072(3.38/7.10)^{1/3} = 0.056)$ . Hence including the Prandtl number in equation 7.23, the Honda et al. method predicts the present data for R-134a quite well, i.e. the second term inside the braces becomes  $0.037Re^{0.2}Pr_L^{1/3}$ .

A comparison of this proposed correlation with the experimental data is depicted in figure 7.14 (top). The predictions lie well centered within the experimental data and follow the trends of the data. However, this correlation, neglecting the effect of the tube pitch, fails to predict the scatter in the measurements, which is partly due to the different tube spacings in the data set. The distribution of the relative error of this correlation is given in 7.15 (left). The mean relative error is -1.2% with an standard deviation of 7.9%. Approximately, 80% of the measurements are within  $\pm 10\%$  error.

The observed behavior of heat transfer on an array of horizontal plain tubes can be described by a model combining a zone where the heat transfer is increased compared to the Nusselt theory by the occurrence of interfacial waves and a zone for turbulent condensation, where the heat transfer increases with increasing film Reynolds number. However, this behavior was especially observed for the top three tubes in the array. For the lower tubes the heat transfer coefficient was almost constant for film Reynolds numbers above 300.

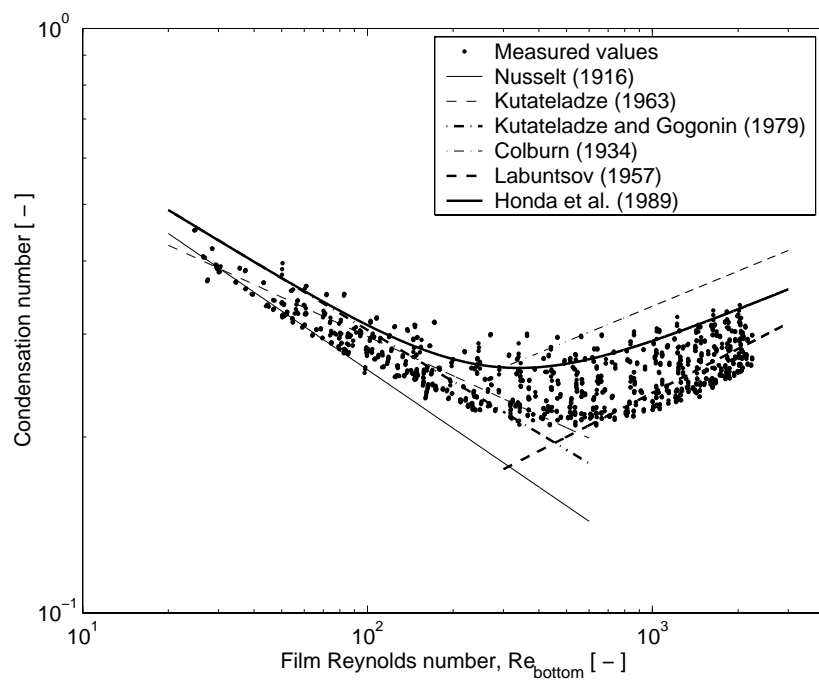
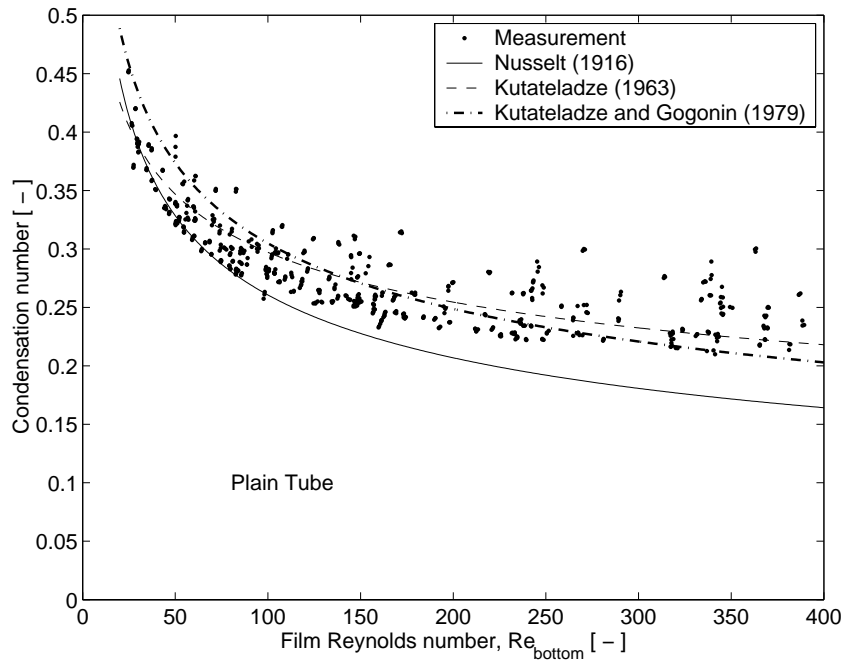


Figure 7.13: Local heat transfer coefficients on the top three plain tubes in the array. Comparison with correlations for the wavy and turbulent flow regimes on a vertical plate.

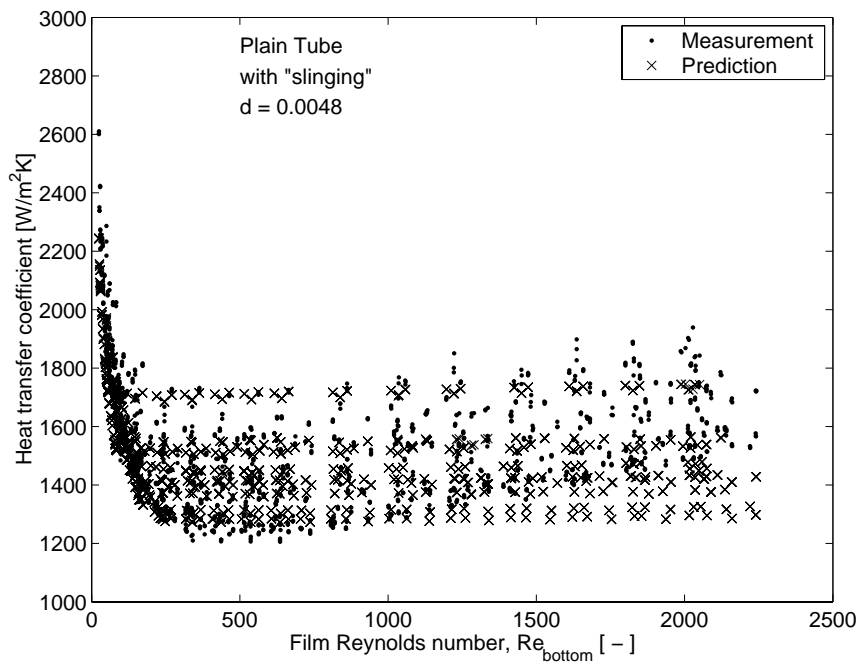
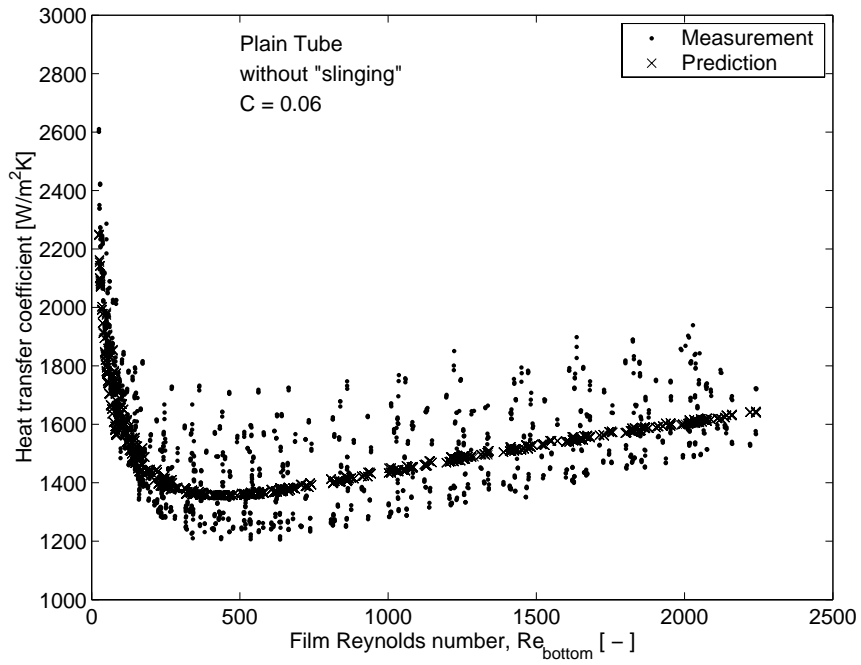


Figure 7.14: Prediction of heat transfer coefficients of the plain tubes (note that the vertical axis has been truncated to begin at 1000).

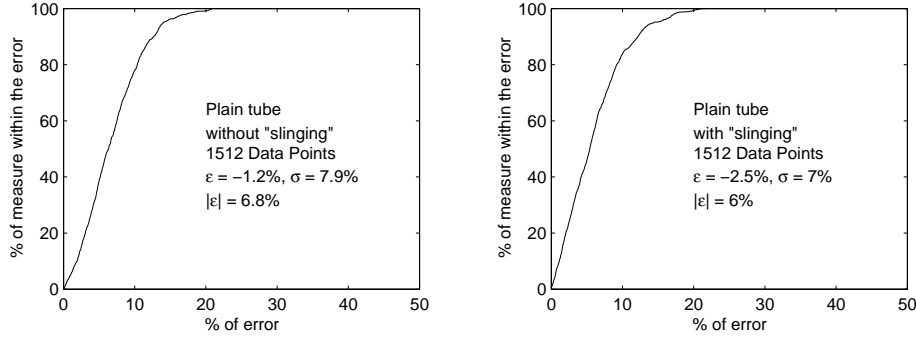


Figure 7.15: Distribution of the relative errors.

#### 7.2.4 With liquid leaving sideways

As mentioned before, during the measurements on the plain tubes, a considerable amount of liquid left the array of tubes sideways. For this reason, the importance of modelling the observed heat transfer behavior by taking into account the fact that some liquid leaves the tubes is also evident.

In analogy to the heat transfer model for the 3D enhanced tubes proposed above, the heat transfer on the array of plain tubes is modelled as follows. The liquid leaving at the bottom of the tubes does not fall vertically, but instead the liquid oscillates forward and backward below the tube (figure 7.6). The maximum angle of deflection,  $\theta$ , increases with increasing film Reynolds numbers. When this angle exceeds the critical angle (equation 7.8), the liquid leaves the array of tubes sideways. For  $\theta > \theta_{crit}$ , the fraction of liquid falling on the tube below is assumed to correspond to the ratio  $\theta_{crit}/\theta$ . The maximum angle of deflection is assumed to be proportional to the film Reynolds number:

$$\theta = d Re \quad (7.25)$$

For evaluation of this model, the calculation is started on the top tube in the array. When liquid is leaving sideways, the actual film Reynolds number on the top of the tubes below is determined by equation 7.9. The heat transfer on every tube is calculated based on the Nusselt theory taking waviness into account by the empirical correction used by Kuteladze and Gogonin [85] as in Honda et al. equation 7.23

$$\frac{\alpha_o}{\lambda_L} \left[ \frac{\mu_L^2}{\rho_L(\rho_L - \rho_V)g} \right]^{1/3} = 1.2 Re_{bottom}^{-0.3} \quad (7.26)$$

As the film Reynolds number leaving at the bottom of the tube is not

known in advance, an iterative calculation is necessary. The value of the coefficient  $d = 0.048$  was determined using all data of the measurements on the top three tubes for all three tube pitches. The value  $d$  is much larger than the ones determined on the 3D enhanced tubes, meaning the maximum angle of deflection increases faster with increasing film Reynolds number. Subsequently, the liquid leaves the array of tubes at lower film Reynolds numbers, which corresponds to the visual observations. The increased slinging effect of the plain tube compared to the 3D tubes can be explained by the capillary forces acting on the film of the 3D enhanced tubes. A comparison of predicted heat transfer coefficients and the measurements is depicted in figure 7.14 (bottom). At low film Reynolds numbers, the predicted heat transfer coefficient decreases according to equation 7.26. With increasing overfeed rates, the amount of liquid that leaves the array of tubes increases, resulting approximately in a constant inundation on the tubes and subsequently a constant heat transfer coefficient. The distribution of the relative errors of this model is given in figure 7.15 (right). The mean relative error is -2.5% with a standard deviation of 7%. Approximately 80% of the measurements are predicted within an error of  $\pm 9\%$ .

This simple model fails to predict the trend of the slight increase in heat transfer with increasing film Reynolds number, which was assumed to be due to turbulent heat transfer in the first model suggested above. However, the second model, based on the assumption some liquid is leaving the array, includes the effect of tube spacing, which leads to approximately the same scatter as that observed during the measurements. This effect of the tube spacing was completely ignored in all other previous models.

The two correlations proposed above have been developed using only the data of the top three tubes. In a comparison with data for all the tubes in the array, the first model, ignoring the effect of slinging, overpredicts the experimental data with a mean relative error of 10% and a standard deviation 12%, while the second model taking into account the effect of slinging gives an overprediction of 7.4% with a standard deviation of 13%. This means that for the second model, including the slinging effect is more suitable to describe the measured data in the present case. This is not surprising, as during the measurements, liquid was always seen leaving the array of plain tubes at high overfeed rates.

However, an optimization of the two models using all the data of the ten tubes (4245 datapoints) leads to  $C = 0.052$  and  $d = 0.0027$  for the first and second models, respectively. With these coefficients the mean relative error of the first model is 0.6% with a standard deviation of 10% and the mean error of the second model is -1.3% with a standard deviation of 12%. Both methods give similar results, but the second one that includes liquid slinging and tube pitch may be the better of the two. A new third model that includes the liquid slinging effect into the Honda model could be developed. In a tube bundle, the "slinging liquid" will deposit on nearby tubes and

could be thus incorporated into a complete bundle model.

### 7.3 Low finned tube

In the literature, the tube row effect on low finned tubes is often described using the equation derived by Nusselt's theory for plain tubes and adapting the value of the exponent. For comparison purposes, the following equation was used to quantify the tube row effect on the low finned tubes in the same way as for the plain tube in section 7.2.2:

$$\frac{\bar{\alpha}_N}{\alpha_1} = N^m \quad (7.27)$$

Table 7.6 lists the values of the exponent  $m$  in the tube row expression for the three tube pitches and for the three nominal heat fluxes. In order to determine the exponent  $m$  for the data without overfeed, all ten tubes were used for the smallest tube pitch. For the middle and the large tube pitches, all nine and all six tubes were used, respectively. The values determined using only the top six tubes for all tube pitches are very close to the ones listed in table 7.6. The observed tube row effect is very small for the finned tube ranging from  $m = -0.01$  effect to  $m = -0.07$ . There is little difference for the different tube pitches and the average values of  $m$  are also shown, which suggest exponents ranging from  $-1/16$  to  $-1/100$ . Generally, the tube row effect is stronger for lower heat fluxes. The very weak tube row effect is explained by the observed differences in condensate flow pattern. On the finned tube, the condensate flows very unsteady and does not form complete sheets as shown in the previous chapter. In addition, the fins prevent the axial spreading of the liquid of such that large portions of the tube are not affected by inundation from the tube above (as also can be observed in the images for the low finned tube in chapter 6).

Tube pitch	Nominal heat flux		
	$6kW/m^2$	$12kW/m^2$	$20kW/m^2$
25.5mm	-0.06	-0.03	-0.02
28.6mm	-0.07	-0.02	-0.01
44.5mm	-0.05	-0.03	-0.02
average	-0.06	-0.03	-0.02

Table 7.6: Tube row effect for the low finned tube (exponent  $m$  in equation 7.27) for all tubes in the array.

As the tube row effect on the low finned tube was found to be very small, a comparison with existing single tube correlations is made neglecting the tube row effect. Figure 7.16 depicts all the experimental data obtained



during the measurements without overfeed on all tubes. As for the comparison to single tube data in figure 5.6, the model of Sreepathi et al. [24] is closest to the experimental data, neglecting the tube row effect. As the data here are only for one fluid/one fin density combination no general conclusion can be made about the "best" overall method here.

The relative error and the distribution of the relative errors of the experimental data compared to the model of Sreepathi et al. are given in figure 7.17. Interestingly, the relative errors are smaller at high film Reynolds numbers. These film Reynolds numbers correspond to the lower tubes in the array in the bundle, where the tube row effect is expected to be highest.

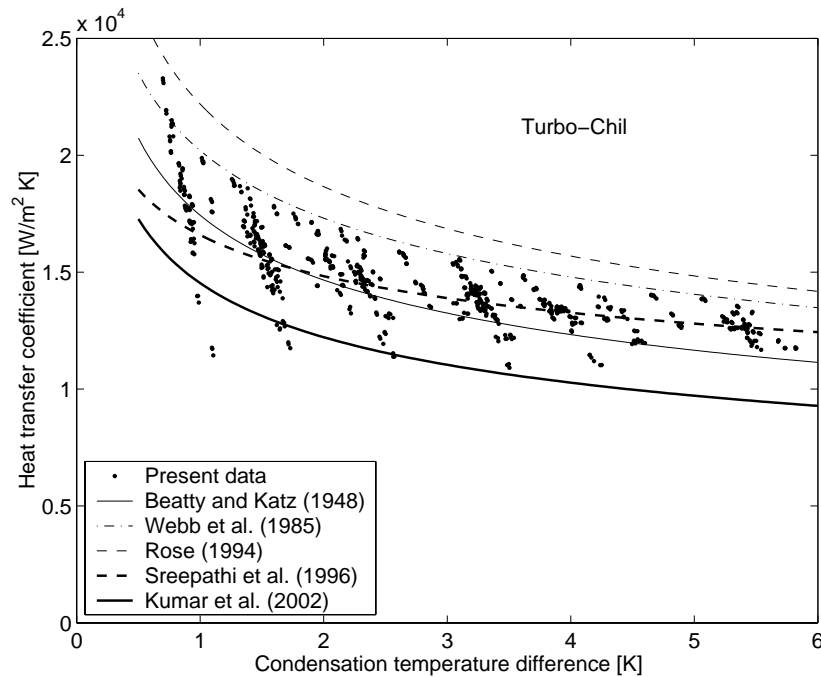


Figure 7.16: Comparison of all data of the measurements without overfeed with a selection of existing models for the low finned tube.

For design purposes, often the tube row effect in the following form is recommended for use:

$$\frac{\alpha_N}{\alpha_1} = N^{m+1} - (N - 1)^{m+1} \quad (7.28)$$

where  $\alpha_N$  is the local heat transfer coefficient on the  $N$ th tube. Based on the mean value of  $m = -0.03$  determined above, a exponent of 0.97 is obtained in equation 7.28. However, even this weak tube row effect applied to the whole data base of measurements without overfeed leads to underestimation

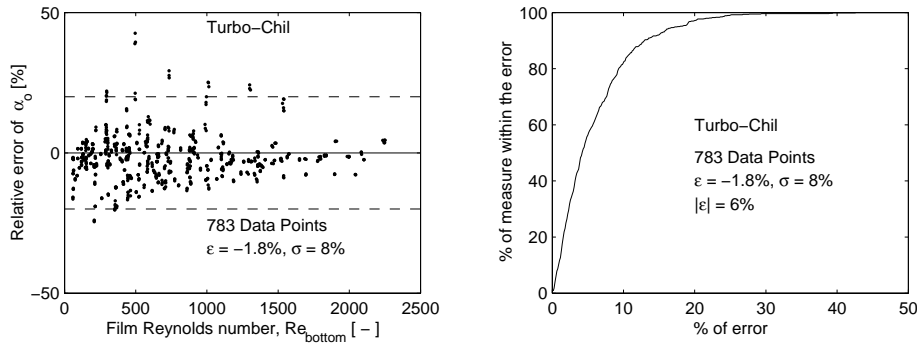


Figure 7.17: Relative errors compared to the model of Sreepahti (1996) for the measurements without overfeed.

of the heat transfer coefficient on the lower tubes in the array, thus the mean relative error becomes 5.3% with a standard deviation of 7.8%.

Figure 7.18 depicts the heat flux versus the condensation temperature for all measurements without overfeed. The data on all tubes in the array for all tube pitches can alternatively be correlated by a simple correlation of the following form:

$$q_o = a \cdot \Delta T^b \quad (7.29)$$

For the measurements without overfeed, the coefficients were found to be  $a = 17700 \text{ W/m}^2$  and  $b = 0.79$ . The relative error and the distribution of the error of the measurements compared to this curve fit are given in figure 7.19. The accuracy of this very simple correlation is about the same as the the model of Sreepathi et al.

Extending the analysis to the whole database including the measurements with liquid overfeed (3921 data points), the same behavior as described above for the measurements without overfeed are obtained. Even when the film Reynolds number is increased up to 4500, the model of Sreepathi et al., neglecting the effect of tube rows predicts the experimental data best. The mean relative error increases to -3.2% with a standard deviation of 7.9%. The heat transfer performance can also be correlated by equation 7.29, with the coefficients  $a = 18000 \text{ W/m}^2$  and  $b = 0.78$  (mean relative error 0.3%, standard deviation 7.7% ). No new general model for condensation on tube arrays of low finned is proposed here since, even though approximately 4000 data points were taken, only one fluid and one fin density are represented for very wide range of test conditions.

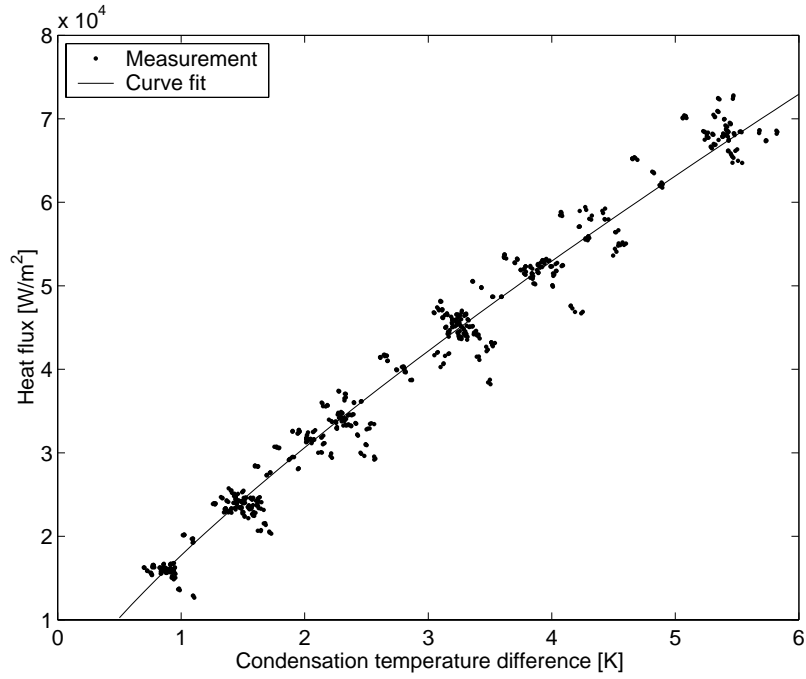


Figure 7.18: All data of the measurements without overfeed for the Turbo-Chil tube.

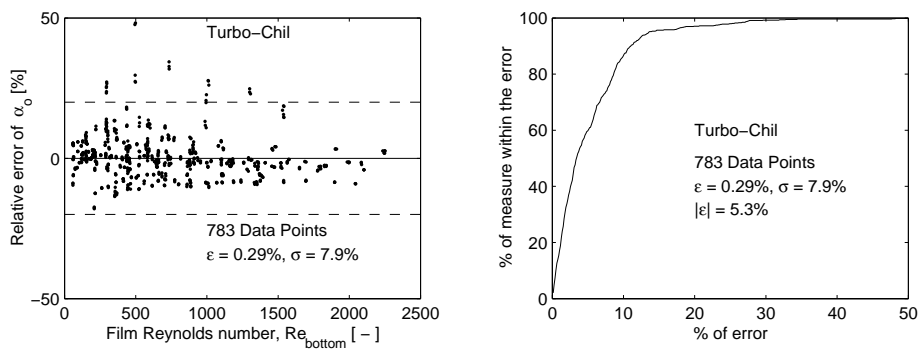


Figure 7.19: Relative errors of the curve fit for the measurements without overfeed.

## 7.4 Conclusion

The heat transfer performance of all four types of tubes was described. For 3D enhanced tubes, the heat transfer coefficient as function of the film Reynolds number was characterized by two distinct zones. At low film Reynolds numbers, the heat transfer coefficient decreased almost linearly and above a certain film Reynolds number the heat transfer coefficient decreases much slower or achieves a constant value. For both types of 3D enhanced tubes, the Turbo-CSL and the Gewa-C, the local heat flux on a tube in the array was correlated as function of condensation temperature difference and the liquid inundation in the form of the film Reynolds number falling on the tube. The coefficients in the correlation were found to be close for both tubes apart from the coefficient which corresponds to slope in the deterioration in heat transfer performance with increasing film Reynolds number. The heat transfer coefficient of the Gewa-C tube decreases less with increasing film Reynolds number. Visual observations revealed that liquid left the array of tubes sideways and hence a new model was proposed to account for this. This simple model is able to describe the observed heat transfer behavior with a minimum of empirical constants. All measurements at the three different tube pitches of both 3D enhanced tubes were underestimated by the model by a mean error of 3% with standard deviations less than 13%.

For the plain tube, the measured heat transfer coefficients on tubes without liquid inundation were found to be in good agreement with Nusselt's theory even for film Reynolds numbers leaving the bottom of the tube corresponding to the wavy (ripple) flow regime on a vertical plate. The heat transfer coefficient with condensate inundation were underestimated by 28% by application of Nusselt's theory on an array of tubes with non-uniform surface temperature. For the measurements without liquid overfeed, the tube row effect was expressed like in Nusselt's expression as the ratio of the mean heat transfer coefficient of the array to the heat transfer coefficient of the top tube. The mean value of the exponent in the expression was found to be  $m = -0.15$  (i.e.  $-1/7$ ) as opposed to the theoretical value of  $-1/4$ . A new modified tube row expression taking into account the non-uniform surface temperatures of the tubes in the array lead to a similar value of  $m = -0.14$  (i.e. again  $-1/7$ ), indicating that the effect of differences in the surface temperature on the tubes in the array were small in the present case.

It was shown that the measured data on the plain tubes can be described by an asymptotic model based on an equation for the wavy flow regime and an equation for the turbulent flow regime. Alternatively, it was shown that the data could also be described by a model that is based on the visual observations that a fraction of the condensate liquid leaves the array of tubes, in analogy to the model proposed for the 3D enhanced tubes.

For the low finned tube in analogy to the plain tube, an exponent in the

tube row expression of  $m = -0.03$  (i.e.  $-1/33$ ) was determined for the effect of liquid inundation. Neglecting the effect of inundation completely, all data measured on the low finned were underpredicted by the model of Sreepathi [24] by only -3% mean error with a standard deviation of 8%. A similar prediction accuracy could also be made by an simple empirical correlation.



## Chapter 8

# Conclusions

The aim of the present investigation was to study the effect of condensate inundation on plain and enhanced tubes. In the literature, the effect of condensate inundation has mainly been investigated experimentally. Large differences in the effect of inundation were found for different types of tubes and test conditions in the literature. Very often these differences were attributed to different flow patterns of the condensate on the array of tubes, but in most studies there was little or no visual access to observe the condensation process to verify these suppositions.

The experimental approach in the present study was split into two parts: measurement of the heat transfer coefficients and visualization of the condensate flow on the tubes. A test facility has been constructed specifically for the current investigation. The test facility consists basically of a natural circulation loop for refrigerant R-134a and a forced convection loop for the cooling water. The test section is equipped with an elaborated distribution system of liquid refrigerant onto the top of the array of tested tubes to study the effect of condensate inundation. The test facility is thus capable of simulating various operating conditions in a large condenser inside the test section.

Heat transfer measurements were performed on a vertical array of horizontal tubes installed in the test section. A novel measurement approach was applied in order to get local heat transfer coefficients at the mid point of every tube in the array of tubes as opposed to tube length averaged values measured in previous studies. In order to observe the condensation process on external surface of the tubes, the test section was equipped with large windows. The tubes tested were  $554\text{mm}$  in length and  $19.05\text{mm}$  ( $3/4$  in.) in diameter. Four types of tubes, a plain tube, a 26 fpi / 1024 fpm low finned tube (Turbo-Chil), and two tubes with 3D enhanced surface structures (Turbo-CSL and Gewa-C), were tested at the tube pitches of 25.5, 28.6 and  $44.5\text{mm}$ . Depending on the tube pitch, 6 to 10 tubes were installed in the test section in the array at one time.

The water side heat transfer coefficients were determined experimentally for all tubes using a modified Wilson plot technique. The Wilson plot procedure was implemented using nucleate pool boiling on the outside of a tube for each type of tubes. A known water side coefficient allowed the determination of the external heat transfer coefficient during condensation based on measurement of the water temperature inside the tube and its profile to get the local heat flux.

Measurements with liquid overfeed onto the top of the array were performed for each type of tube at three different heat flux levels. Additionally, measurements without liquid overfeed were made by varying the heat flux. In summary, a new accurate, local heat transfer database has been obtained that includes approximately 15000 data points covering a wide range of liquid film Reynolds numbers (up to  $\sim 5000$ ), tube pitches (25.5 to 44.5mm) and heat fluxes (5 to  $100kW/m^2$ ) for four types of tubes for R-134a condensing at a saturation temperature of  $31^\circ C$ .

The measured heat transfer coefficients on the plain tube without liquid inundation were in good agreement with the Nusselt theory. For the low finned tube without liquid inundation, good agreements with the prediction methods of Sreepathi et al. [24] and Beatty and Katz [9] were found.

For small inundation rates, the heat transfer coefficients for the 3D enhanced tubes were high compared to the finned tube. Increasing the inundation rates deteriorated the performance the 3D enhanced tubes. The heat transfer coefficient flattened out at a certain film Reynolds number for the 3D enhanced tubes. The heat transfer coefficients of the Turbo-CSL were slightly higher than those of the Gewa-C for small inundations, but the decrease with increasing inundation rate was less pronounced for the Gewa-C compared to the Turbo-CSL. The heat transfer coefficient of the finned tube varied little with the inundation rate. The heat transfer performance of the plain tube decreased first sharply and then increased again slowly with increasing inundation rates.

For low inundation rates, the heat transfer coefficients were similar for the three tube pitches. For the 3D enhanced tubes, the heat transfer coefficient achieved a constant level at a lower film Reynolds number for the larger tube pitch. This level was higher for the larger tube pitch. The heat transfer coefficient of the finned tube varied little with the tube pitch. For the plain tube, an increase in heat transfer coefficient is observed for the largest tube pitch. The heat transfer coefficients decreased with increasing heat flux for the four type of tubes. This decrease was less pronounced for increasing inundation rates, apart from the plain tube.

The liquid flow was studied as well under adiabatic conditions as during condensation. In both cases a distinct difference between the flow patterns on the 3D enhanced tubes and those on the finned tube and the plain tube was observed for refrigerant R-134a. The ideal flow modes (droplet, column, and sheet mode) together with the intermediate ones could strictly only be



observed on the 3D enhanced tubes. On the low finned tube and on the plain tube the intertube liquid flow was very unstable.

However, an attempt was made to determine the four transitions between the five ideal flow modes under adiabatic conditions for all four types of tubes and to compare them to other investigations. During the heat transfer measurements the flow patterns were observed systematically on the array of tubes and video sequences were recorded. It was found that the flow pattern of the liquid leaving off the bottom of a tube did not only depend on film Reynolds number, but also on the flow pattern falling onto this tube. The flow patterns observed with heat transfer were in agreement with the flow patterns observed without heat transfer.

For the 3D enhanced tubes, a difference in the formation of the liquid sheets was observed. The Gewa-C tube tended to form small sheets, while on the Turbo-CSL a complete sheet was formed at lower film Reynolds numbers. This might explain the less pronounced degradation in heat transfer for the Gewa-C tube with increasing film Reynolds number since a smaller fraction of the Gewa-C tube is inundated.

For all four types of tubes, it was observed that liquid left the array of tubes sideways. Significantly, larger amounts left the array of tubes sideways for the low finned tube and the plain tube as the flow on these tubes was always very unstable. For the 3D enhanced tubes the behavior was different as the flow was stable at low film Reynolds numbers. With increasing film Reynolds numbers at the transition to the sheet mode or in the sheet mode, the liquid left the array sideways from time to time. The liquid sheets formed on the 3D tubes were observed to move forward and backward in a regular cyclic motion. For a further increase in film Reynolds number, these oscillations were amplified up to a point where a part of the liquid did not always fall on the tube below. For the 3D enhanced tubes, this effect of leaving liquid was more important than the effect of the flow modes on heat transfer.

For the low finned tube and the plain tube, the classification of the flow patterns caused considerable difficulties and no clear transitions were observed due to the unstable liquid flow. Apart from these classification difficulties, for the finned tube no effect on heat transfer due to the flow pattern was observed. For the plain tube at low film Reynolds numbers, no effect on heat transfer by the droplet and column modes was found. In sheet mode, the heat transfer coefficient increased with increasing film Reynolds number, but this was also most likely linked to the fact that liquid left the tubes sideways.

The heat transfer performance of all four types of tubes was characterized. For both types of 3D enhanced tubes, the Turbo-CSL and the Gewa-C, the local heat flux on a tube in the array was correlated as function of condensation temperature difference and the liquid inundation in the form of the film Reynolds number falling on the tube. The coefficients in the corre-

lation were found to be close for both tubes apart from the coefficient which corresponds to the slope in the deterioration in heat transfer performance with increasing film Reynolds number. This difference originates most likely in the difference of the sheet formation. Visual observations revealed that liquid left the array of tubes sideways and hence a new model was proposed to account for this. This simple model was able to describe the observed heat transfer behavior with a minimum of empirical constants. All measurements at the three different tube pitches of both 3D enhanced tubes were underestimated by the model by a mean error of 3% with standard deviation less than 13%.

It was shown that the measured heat transfer data of the plain tube can be described by an asymptotic model based on an equation for the wavy flow regime and an equation for the turbulent flow regime. Alternatively, it was shown that the data could also be described by a model that is based on the visual observations that a fraction of the condensate leaves the array of tubes, in analogy to the model proposed for the 3D enhanced tubes.

For the low finned tube, the effect of inundation was found to be very small; thus neglecting it completely, all data measured on the low finned tube were underpredicted by the model of Sreepathi [24] by -3% mean error with a standard deviation of 8%. A similar prediction accuracy could also be made by a simple empirical correlation.

This investigation proved the importance in making simultaneous flow observations during heat transfer measurements during condensation on an array of tubes. The original aim of this work was to determine the effect of the flow modes on heat transfer. It was found that these ideal modes were not distinctive for the plain tube and the low finned tube, while also liquid left the array sideways due to the unstable nature of the flow. Even for the 3D enhanced tubes, where the flow modes were distinguishable, their effect on heat transfer was dominated by liquid leaving the tube sideways at high film Reynolds numbers. For the 3D enhanced tubes, further attention should be directed to study the effect of the flow pattern on heat transfer at low film Reynolds numbers, as the presented model describes the whole range of measurements and might be less accurate at low film Reynolds numbers. The presented models can be extrapolated to determine the performance of tube bundles, as in a staggered or in-line arrangement of horizontal tubes, but the liquid that leaves one column of tubes sideways will necessarily hit another tube located beside in a bundle and hence bundle tests are required to quantify these effects. Probably, the amount of liquid that leaves a column of tubes sideways is approximately the same as it receives from the tubes in the neighboring column. In the present investigation, a vertical array of tubes was studied and the model can strictly only be applied for such a configuration. However, this work is a step forward in the development of a general heat transfer model for tube bundles for plain, low fin and 3D enhanced tubes.

Future tests including vapor shear and other refrigerants should be run to attain more comprehensive understanding of the condensation process on horizontal tubes. Additionally, measuring the amount of liquid that leaves the tubes sideways and bundle tests will be helpful.



## Appendix A

# Integral Analysis of Nusselt

In this chapter, first Nusselt's analysis for condensation on a plate is given according to Thome [70] followed by the analysis for laminar film condensation on horizontal tube with inundation. The last section is the derivation of a tube row expression for non-uniform wall temperature in analogy to Nusselt's tube row expression.

### A.1 Laminar film condensation on a vertical plate

Laminar film condensation of a pure single-component saturated vapor was among the first heat transfer problems to be successfully analyzed from a fundamental point of view. The definitive work is by Nusselt [1] in two papers published one week apart in 1916 that has been widely described in numerous books since. The original analysis applies specifically to laminar flow of a condensing film on a vertical surface. However, it is possible to generalize this approach to a number of other geometric cases and for this reason it is worthwhile to examine his analysis in some detail here. The Nusselt falling film analysis closely represents experimental results on vertical plates if no ripples or noncondensing gases are present and the film flow is laminar.

First of all, figure A.1 depicts the process of laminar film condensation on a vertical plate from a quiescent vapor. The film of condensate begins at the top and flows downward under the force of gravity, adding additional new condensate as it flows. The flow is laminar and the thermal profile in the liquid film is assumed to be fully developed from the leading edge. Thus, the temperature profile across the film is linear and heat transfer is by one-dimensional heat conduction across the film to the wall. Other assumptions in the Nusselt analysis are as follows:

- The vapor temperature is uniform and is at its saturation temperature;

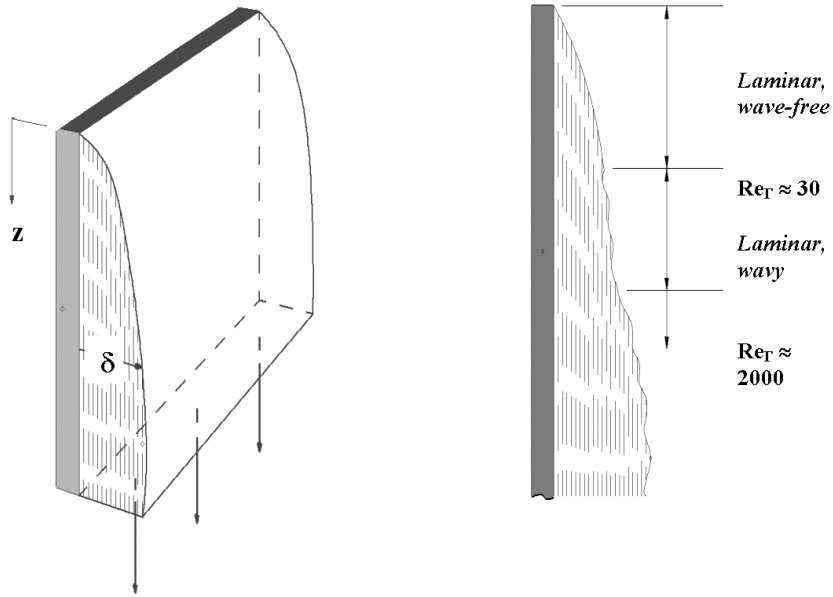


Figure A.1: Film condensation on a vertical plate.

- Gravity is the only external force acting on the film (momentum is neglected so there is a static force balance);
- The adjoining vapor is stagnant and does not exert drag on the film;
- Fluid properties are constant;
- The sensible cooling of the film is negligible with respect to the latent heat;
- The curvature of the interface is negligible so the saturation temperature of the interface is that of a planar interface determinable from the vapor pressure curve of the fluid.

The integral analysis of the process on a vertical plate is represented in figure A.2. At a distance  $z$  from the top, the thickness of the film is  $\delta$ . Ignoring inertia effects, i.e. no acceleration of the flow, a force balance on the liquid element gives

$$(\delta - y)dz(\rho_L - \rho_V)g = \mu_L \left( \frac{du_y}{dy} \right) dz \quad (\text{A.1})$$

In this expression gravity acts as a body force on the element of volume  $(\delta - y)(dz)(1)$  where a unit width of the plate is assumed. The viscous force is for the shear on the film at distance  $y$  from the wall over the length  $dz$ .

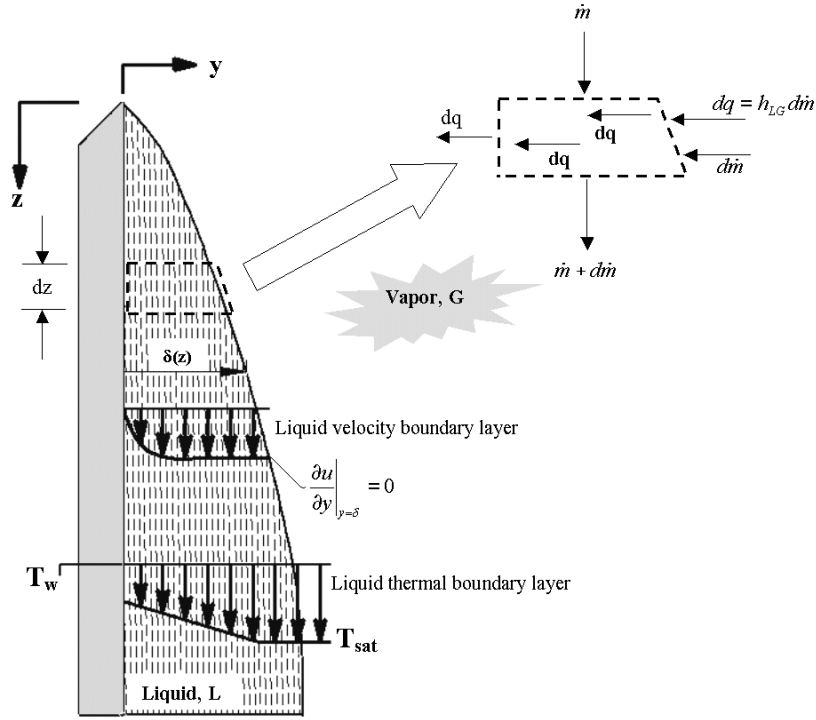


Figure A.2: Integral representation of falling laminar film condensation on a vertical plate.

While this expression is for a vertical plate, it is applicable to an inclined plate as long as the angle of inclination is sufficient for drainage of the condensate. For an inclined plate, the force of gravity  $g$  on the film in the above expression is replaced with  $g \sin(\beta)$ , where  $\beta$  is the angle of the plate relative to horizontal. Now, rearranging and integrating this expression from the initial boundary condition of  $u_y = 0$  at  $y = 0$ , then the velocity profile at any location  $y$  in the film is obtained to be:

$$u_y = \frac{(\rho_L - \rho_V)g}{\mu_L} \left[ y\delta - \frac{y^2}{2} \right] \quad (\text{A.2})$$

Integrating this velocity profile across the film, the mass flow rate of condensate per unit width of the plate  $\Gamma$  is

$$\Gamma = \rho_L \int_0^\delta u_y dy = \frac{\rho_L(\rho_L - \rho_V)g\delta^3}{3\mu_L} \quad (\text{A.3})$$

$\Gamma$  has the dimensions of  $kg/ms$ , which represents the flow rate in  $kg/s$  per unit width of the plate. Differentiating this expression with respect to

$\delta$ , where  $\delta = 0$  at  $z = 0$ , the rate of increase of the film flow rate with film thickness is

$$\frac{d\Gamma}{d\delta} = \frac{\rho_L(\rho_L - \rho_V)g\delta^2}{\mu_L} \quad (\text{A.4})$$

Taking the film surface temperature as  $T_{sat}$  and the wall temperature as  $T_w$ , the heat conducted across the liquid film element of length  $dz$  with a thermal conductivity of  $\lambda_L$  is

$$dq = \frac{\lambda_L}{\delta}(T_{sat} - T_w)dz \quad (\text{A.5})$$

Applying an energy balance, this rate of heat transfer by conduction is equal to the rate of latent heat removed from the vapor at the interface, which means  $dq = h_{LV}d\Gamma$ . The rate of condensation on this element ( $d\Gamma$ ) is thus

$$d\Gamma = \frac{\lambda_L}{\delta h_{LV}}(T_{sat} - T_w)dz \quad (\text{A.6})$$

Substituting A.6 into A.4, separating variables and then integrating from  $\delta = 0$  at  $z = 0$  gives

$$\mu_L \lambda_L (T_{sat} - T_w) z = \rho_L (\rho_L - \rho_V) g h_{LV} \left( \frac{\delta^4}{4} \right) \quad (\text{A.7})$$

Rearranging this expression for the local film thickness, it is

$$\delta = \left[ \frac{4\mu_L \lambda_L z (T_{sat} - T_w)}{\rho_L (\rho_L - \rho_V) g h_{LV}} \right]^{1/4} \quad (\text{A.8})$$

The physical significance of the film thickness is that of the conduction length through a solid of the same thickness, seeing that in laminar film condensation the thermal resistance is only conduction from the interface to the wall. The film thickness is shown by the above expression to be directly proportional to the temperature difference ( $T_{sat} - T_w$ ), such that a larger temperature difference results in a higher condensation rate.

From the thermal conductive resistance across the film, the local condensation heat transfer coefficient  $\alpha_f(z)$  at any point  $z$  from the top of the plate is

$$\alpha_f(z) = \frac{\lambda_L}{\delta} = \left[ \frac{\rho_L (\rho_L - \rho_V) g h_{LV} \lambda_L^3}{D_o \mu_L (T_{sat} - T_w)} \right]^{1/4} \quad (\text{A.9})$$

Integrating A.9 from  $z = 0$  to  $z$ , the mean heat transfer coefficient for the plate up to point  $z$  is



$$\alpha_f = \frac{1}{z} \int_0^z \alpha_f(z) dz = 0.943 \left[ \frac{\rho_L(\rho_L - \rho_V)gh_{LV}\lambda_L^3}{\mu_L z(T_{sat} - T_w)} \right]^{1/4} \quad (\text{A.10})$$

Comparing the above expressions, it is seen that the mean coefficient  $\alpha_f$  on the plate from 0 to  $z$  is 4/3 times the value of the local coefficient  $\alpha_f(z)$  at  $z$ . The mean heat transfer coefficient can also be obtained from

$$\alpha_f = \frac{\Gamma(z)h_{LV}}{z(T_{sat} - T_w)} \quad (\text{A.11})$$

where  $\Gamma(z)$  is the condensate flow rate per unit width at a distance  $z$  from the top of the plate. Combining A.11 with A.6 to eliminate  $(T_{sat} - T_w)$ , another expression for the thickness of the condensate at point  $z$  from the top is

$$\delta = \frac{\lambda_L \Gamma(z) dz}{\alpha_f z d\Gamma} \quad (\text{A.12})$$

Eliminating  $\delta$  by combining A.12 with A.3 yields the differential expression

$$\lambda_L \left[ \frac{\rho_L(\rho_L - \rho_V)g}{3\mu_L} \right]^{1/3} \frac{dz}{z} = \frac{\alpha_f \Gamma^{1/3} d\Gamma}{\Gamma(z)} \quad (\text{A.13})$$

Integrating over  $z$  gives the mean heat transfer coefficient as

$$\alpha_f = 0.925 \left[ \frac{\rho_L(\rho_L - \rho_V)g\lambda_L^3}{\mu_L \Gamma(z)} \right]^{1/3} \quad (\text{A.14})$$

It is inconvenient to utilize an expression for the condensing heat transfer coefficient in terms of  $(T_{sat} - T_w)$  as in A.10 since the wall temperature is unknown beforehand in heat exchanger design and results in an iterative solution procedure. For the present situation the heat transfer coefficient can also be expressed in terms of the local film Reynolds number, which at a distance  $z$  below the top of the plate is defined as

$$Re = \frac{4\Gamma(z)}{\mu_L} \quad (\text{A.15})$$

Substituting A.15 into A.14 and rearranging, the mean heat transfer coefficient up to point  $z$  is

$$\frac{\alpha_f}{\lambda_L} \left[ \frac{\mu_L^2}{\rho_L(\rho_L - \rho_V)g} \right]^{1/3} = 1.47 Re^{-1/3} \quad (\text{A.16})$$

where the bracketed term to the left of the equal sign together with its exponent is the characteristic length. The local condensing heat transfer coefficient in terms of film Reynolds number is

$$\frac{\alpha_f(z)}{\lambda_L} \left[ \frac{\mu_L^2}{\rho_L(\rho_L - \rho_V)g} \right]^{1/3} = 1.1Re^{-1/3} \quad (\text{A.17})$$

The condensing heat transfer coefficient for a laminar film is thus seen to be inversely proportional to the film Reynolds number to the 1/3 power. This can be compared, for instance, to fully developed laminar flow inside a tube in which the laminar heat transfer coefficient is independent of the Reynolds number.

Bromley [88] extended the Nusselt theory to include subcooling of the condensate in the heat balance. Following in this line, Rohsenow [67] showed that empirically adding a sensible heat term to the latent heat of vaporization gave reasonable results, defining an effective latent heat of evaporation as:

$$h'_{LV} = h_{LV} \left[ 1 + 0.68 \left( \frac{c_{p,L}(T_{sat} - T_w)}{h_{LV}} \right) \right] \quad (\text{A.18})$$

The subcooling correction is typically negligible with respect to the latent heat since condensing temperature differences tend to be small.

Regarding other physical properties, Drew [68] proposed that they be evaluated at an effective film temperature, which he gave as  $[T_w + 0.25(T_{sat} - T_w)]$ . For small temperature differences, it is sufficiently accurate to calculate the properties at the saturation temperature. The above analysis can also be applied to the outside or inside of a vertical tube, as long as the tube diameter is much larger than  $\delta$  and the effect of vapor shear remains small.

## A.2 Laminar film condensation on a horizontal tube

Applying the Nusselt integral approach for laminar film condensation on a vertical isothermal plate, the similar process on the outside of a single, horizontal tube can be analyzed. Gravitation ( $g \sin \beta$ ) is applied around the circumference of the tube, where  $\beta$  is the angle around the perimeter from the top.

An energy balance between the one dimensional heat conduction across the liquid film thickness  $\delta$  and the latent heat absorbed by the liquid from the condensing vapor at the interface gives

$$h_{LV}d\Gamma = \frac{\lambda_L}{\delta}(T_{sat} - T_w)r_o d\beta \quad (\text{A.19})$$

where  $r_o$  is the radius of the tube and  $\beta$  the angle around the perimeter from the top. The film thickness derived for a inclined plate is

$$\delta = \left[ \frac{3\mu_L\Gamma}{\rho_L(\rho_L - \rho_V)g \sin \beta} \right]^{1/3} \quad (\text{A.20})$$

where  $\beta$  is the angle of the plate relative to horizontal. Substitution of equation A.20 in equation A.19 gives

$$\Gamma^{1/3} d\Gamma = \frac{r_o \lambda_L (T_{sat} - T_w)}{h_{LV}} \left[ \frac{\rho_L (\rho_L - \rho_V) g}{3\mu_L} \right]^{1/3} \sin^{1/3} \beta d\beta \quad (\text{A.21})$$

Integrating from the top of the tube where  $\Gamma = \Gamma_{top}$  at  $\beta = 0$  to the bottom where  $\Gamma = \Gamma_{bottom}$  at  $\beta = \pi$  yields

$$\frac{3}{4} \Gamma_{bottom}^{4/3} - \frac{3}{4} \Gamma_{top}^{4/3} = \frac{r_o \lambda_L (T_{sat} - T_w)}{h_{LV}} \left[ \frac{\rho_L (\rho_L - \rho_V) g}{3\mu_L} \right]^{1/3} A \quad (\text{A.22})$$

where  $A = \int_0^\pi \sin^{1/3} \beta d\beta = 2.587$ . Rearranging gives the condensate flow rate leaving the tube on one side of the tube per unit axial length of tube:

$$\Gamma_{bottom} = \left[ \frac{4A}{3} \frac{r_o \lambda_L (T_{sat} - T_w)}{h_{LV}} \left[ \frac{\rho_L (\rho_L - \rho_V) g}{3\mu_L} \right]^{1/3} + \Gamma_{top}^{4/3} \right]^{3/4} \quad (\text{A.23})$$

An energy balance on the circumference of the tube gives the mean heat transfer coefficient for the perimeter of the tube as

$$h_{LV} (\Gamma_{bottom} - \Gamma_{top}) = \pi r_o \alpha_o (T_{sat} - T_w) \quad (\text{A.24})$$

The heat transfer coefficient may also be written in terms of condensate flow rates as

$$\frac{\alpha_o}{\lambda_L} \left[ \frac{\mu_L^2}{\rho_L (\rho_L - \rho_V) g} \right]^{1/3} = \frac{A}{\pi} \left( \frac{4}{3} \right)^{4/3} \left[ \left( \frac{\mu}{4} \right)^{-1/3} \frac{\Gamma_{bottom} - \Gamma_{top}}{\Gamma_{bottom}^{4/3} - \Gamma_{top}^{4/3}} \right] \quad (\text{A.25})$$

## A.3 Condensation on horizontal tube bundles

### A.3.1 Tube row effect for non-uniform surface temperature

The Nusselt theory for a single tube may be extended to a vertical array of horizontal tubes. The condensate formed the above tubes drains onto the tube below, increasing the amount of condensate flowing on each tube in addition to the new condensate formed on that particular tube. Starting with the top tube without inundation, the analysis is applied to each individual tube utilizing the summation of the condensate flowing from the above tubes onto the top of the  $N$ th tube, counting from the top row towards the bottom. Applying an energy balance to the entire surface of the array of tubes yields

$$(\alpha_1 \Delta T_1 + \alpha_2 \Delta T_2 + \dots + \alpha_N \Delta T_N) 2\pi r = 2h_{LV} \Gamma_{bottom,N} \quad (\text{A.26})$$

According to equation A.23, the mass flow rate per unit width on one side of the tube at the bottom of the  $N$ th tube can be written as

$$\Gamma_{bottom,N} = \left[ C \Delta T_N + \Gamma_{bottom,N-1}^{4/3} \right]^{3/4} \quad (\text{A.27})$$

where

$$\Delta T_N = (T_{sat} - T_{w,N}) \quad (\text{A.28})$$

and

$$C = 3.449 \frac{r_o \lambda_L}{h_{LV}} \left[ \frac{\rho_L (\rho_L - \rho_V) g}{3\mu_L} \right]^{1/3} \quad (\text{A.29})$$

where the value 3.449 comes from  $4/3(2.587)$ . For an array of  $N$  tubes without overfeed onto the top first tube, the mass flow rate per unit width on one side of the tubes becomes

$$\Gamma_{bottom,N} = [C (\Delta T_1 + \Delta T_2 + \dots + \Delta T_N)]^{3/4} \quad (\text{A.30})$$

Substitution into A.27 yields

$$(\alpha_1 \Delta T_1 + \alpha_2 \Delta T_2 + \dots + \alpha_N \Delta T_N) \pi r = h_{LV} C^{3/4} (\Delta T_1 + \Delta T_2 + \dots + \Delta T_N)^{3/4} \quad (\text{A.31})$$

Defining the mean condensation temperature difference as

$$\overline{\Delta T}_N = \frac{1}{N} (\Delta T_1 + \Delta T_2 + \dots + \Delta T_N) \quad (\text{A.32})$$

and the mean heat transfer coefficient as

$$\bar{\alpha}_N = \frac{\bar{q}_N}{\bar{\Delta T}_N} = \frac{\alpha_1 \Delta T_1 + \alpha_2 \Delta T_2 + \dots + \alpha_N \Delta T_N}{N \bar{\Delta T}_N} \quad (\text{A.33})$$

equation A.31 can be written as

$$\bar{\alpha}_N N \bar{\Delta T}_N \pi r = h_{LV} C^{3/4} (N \bar{\Delta T}_N)^{3/4} \quad (\text{A.34})$$

The mean heat transfer coefficient on the entire array of  $N$  tubes is

$$\bar{\alpha}_N = \frac{h_{LV}}{\pi r} C^{3/4} (N \bar{\Delta T}_N)^{-1/4} \quad (\text{A.35})$$

Dividing by the heat transfer coefficient of the top tube, this yields the general form of this expression:

$$\frac{\bar{\alpha}_N}{\alpha_1} = N^{-1/4} \left( \frac{\bar{\Delta T}_N}{\Delta T_1} \right)^{-1/4} \quad (\text{A.36})$$

By an energy balance the ratio the local heat transfer coefficient of the  $N$ th tube to the heat transfer coefficient on the top tube is obtained.

$$\frac{\alpha_N}{\alpha_1} = \left[ N^{3/4} \left( \frac{\bar{\Delta T}_N}{\Delta T_1} \right)^{3/4} - (N-1)^{3/4} \left( \frac{\bar{\Delta T}_{N-1}}{\Delta T_1} \right)^{3/4} \right] \frac{\Delta T_1}{\Delta T_N} \quad (\text{A.37})$$

Notably, these two expressions reduce to that of Nusselt for uniform wall temperature on all tubes.



# Bibliography

- [1] W. Nusselt. Die Oberflächenkondensation des Wasserdampfes. *Zeitschrift des Vereins deutscher Ingenieure*, 60(27 and 28):541–546 and 569–575, 1916.
- [2] R. Gregorig. Film condensation on finely rippled surface with consideration of surface tension. *Zeitschrift für angewandte Mathematik und Physik*, 5:36–49, 1954.
- [3] D.Q. Kern. Mathematical development of tube loading in horizontal condensers. *AIChE Journal*, 4(2):157–160, 1958.
- [4] P.J Marto. Recent progress in enhancing film condensation heat transfer on horizontal tubes. *Heat Transfer Engineering*, 7(3-4):53–63, 1986.
- [5] P.J Marto. An evaluation of film condensation on horizontal integral-fin tubes. *Journal of Heat Transfer*, 110:1287–1305, 1988.
- [6] R.L. Webb. Vapor space condensation. *Principles of Enhanced Heat Transfer*, Chapter 12, John Wiley & Sons, Inc., New York:373–431, 1994.
- [7] J.R. Thome. Condensation of fluorocarbon and other refrigerants: A state-of-the-art review. Technical report, Prepared for Air-Condition and Refrigeration Institute (ARI), Arlington, Virginia, 1998.
- [8] R.K. Shah, S.Q. Zhou, and K.A. Tagavi. The role of surface tension in film condensation in extended surface passages. *Enhanced Heat Transfer*, 6:179–216, 1999.
- [9] K.O. Beatty and D.L. Katz. Condensation off vapors on outside of finned tubes. *Chemical Engineering Progress*, 44(1):55–70, 1948.
- [10] D.L. Katz and J.M. Geist. Condensation on six finned tubes in a vertical row. *Trans. ASME*, 70:907–914, 1948.
- [11] R.L. Webb and C.G. Murawski. Row effect for R-11 condensation on enhanced tubes. *Journal of Heat Transfer*, 112:768–776, 1990.

- [12] C. Zener and A. Lavi. Drainage systems for condensation. *Journal of Engineering for Power*, 96(3):209–215, 1974.
- [13] T.A. Adamek. Bestimmung der Kondensationsgrößen auf feingewellten Oberflächen zur Auslegung optimaler Wandprofile. *Wärme und Stoffübertragung*, 15:255–270, 1981.
- [14] V.A. Karkhu and V.P. Borovkov. Film condensation of vapor at finely-finned horizontal tubes. *Heat Transfer – Soviet Research*, 3(2):183–191, 1971.
- [15] T.M. Rudy. An analytical model to predict condensate retention on horizontal integral-fin tubes. *ASME-JSME Thermal Engineering Joint Conference*, 1:373–378, 1983.
- [16] T.M. Rudy and R.L. Webb. An analytical model to predict condensate retention on horizontal integral-fin tubes. *Journal of Heat Transfer*, 107:361–368, 1985.
- [17] H. Honda, S. Nozu, and K. Mitsumori. Augmentation of condensation of horizontal finned tubes by attaching a porous drainage plate. *Proceedings of the ASME-JSME Thermal Engineering Joint Conference*, 3:289–295, 1983.
- [18] H. Masuda and J.W. Rose. Static configuration of liquid films on horizontal tubes with low radial fins: implications for condensation heat transfer. *Proc. R. Soc. London A*, 410:125–139, 1987.
- [19] R.L. Webb, T.M. Rudy, and M.A. Kedzierski. Prediction of the condensation coefficient on horizontal integral-fin tubes. *Journal of Heat Transfer*, 107:369–376, 1985.
- [20] H. Honda and S. Nozu. A prediction method for heat transfer during film condensation on horizontal low integral-fin tubes. *Journal of Heat Transfer*, 109:218–225, 1987.
- [21] H. Honda and S. Nozu. A generalized prediction method for heat transfer during film condensation on a horizontal low-finned tube. *JSME International Journal, Series II*, 31(4):709–717, 1988.
- [22] J.W. Rose. An approximate equation for the vapour-side heat transfer coefficient for condensation on low-finned tubes. *International Journal of Heat Mass Transfer*, 37(5):865–875, 1994.
- [23] A. Briggs and J.W. Rose. Effect of fin efficiency on a model for condensation heat transfer on a horizontal, integral-fin tube. *International Journal of Heat Mass Transfer*, 37(Suppl. 1):457–463, 1994.



- [24] L.K. Sreepathi, S.L. Bapat, and S.P. Sukhatme. Heat transfer during film condensation of r-123 vapour on horizontal integral-fin tubes. *Journal of Enhanced Heat Transfer*, 3(2):147–164, 1996.
- [25] M. Belghazi, A. Bontemps, and Marvillet C. Filmwise condensation of a pure fluid and binary mixture in a bundle of enhanced surface tubes. *International Journal of Thermal Sciences*, 41:631–638, 2002.
- [26] G.F. Smirnov and I.I. Lukanov. Study of heat transfer from freon-11 condensing on a bundle of finned tubes. *Heat Transfer – Soviet Research*, 4(3):51–56, 1972.
- [27] I.I. Gogonin, D.A. Kabov, and V.I. Sosunov. Heat transfer in condensation of R-12 vapor on bundles of finned tubes. *Kholodil'naya Tekhnika*, 1:26–29, 1983.
- [28] S.S. Kutateladze, I.I. Gogonin, and V.I. Sosunov. The influence of condensate flow rate on heat transfer in film condensation of stationary vapour on horizontal tube banks. *International Journal of Heat Mass Transfer*, 28(5):1011–1018, 1985.
- [29] H. Honda, B. Uchima, S. Nozu, H. Nakata, and T. Fujii. Condensation of downward flowing R-113 vapor on bundles of horizontal smooth tubes. *Heat Transfer – Japanese Research*, 18(6):31–52, 1989.
- [30] H. Honda, S. Nozu, and Y. Takeda. A theoretical model of film condensation in a bundle of horizontal low finned tubes. *Journal of Heat Transfer*, 111:525–532, 1989.
- [31] H. Honda, B. Uchima, S. Nozu, H. Nakata, and E Torigoe. Film condensation of R-113 on in-line bundles of horizontal finned tubes. *Journal of Heat Transfer*, 113:479–486, 1991.
- [32] H. Honda and S. Nozu. Effects of bundle depth and working fluid on the optimized fin geometry of a horizontal low finned condenser tube. *2nd Int. Symp. Condensers and Condensation, HTFS*, pages 407–416, 1990.
- [33] H. Honda, S. Nozu, and Y. Takeda. Flow characteristics of condensate on a vertical column of horizontal low finned tubes. *Proceedings of the ASME-JSME Thermal Engineering Joint Conference*, 1:517–524, 1987.
- [34] H. Honda, B. Uchima, S. Nozu, E Torigoe, and S. Imai. Film condensation of R-113 on staggered bundles of horizontal finned tubes. *Journal of Heat Transfer*, 114:442–449, 1992.
- [35] H. Honda, H. Takamtsu, and K. Kim. Condensation of CFC-11 and HCFC-123 in in-line bundles of horizontal finned tubes: Effect of fin geometry. *Journal of Enhanced Heat Transfer*, 1(2):197–209, 1994.

- [36] H. Honda and K. Kim. Effect of fin geometry on the condensation heat transfer performance of a bundle of horizontal low-finned tubes. *Journal of Enhanced Heat Transfer*, 2(1-2):139–147, 1995.
- [37] H. Honda, H. Takamatsu, N. Takada, and T. Yamasaki. Design method for shell and tube condensers in refrigeration units. *Heat Transfer in Condensation, Eurotherm Seminar 47, Paris, Oct. 4–5*, pages 110–115, 1995.
- [38] H. Honda, H. Takamatsu, N. Takada, O. Makishi, and H. Sejimo. Condensation of HCFC-123 in staggered bundles of horizontal finned tubes. *Proceedings of the 4th ASME-JSME Thermal Engineering Joint Conference*, 2:415–422, 1995.
- [39] H. Honda, H. Takamatsu, and N. Takada. Condensation of HCFC-123 in bundles of horizontal finned tubes: Effects of fin geometry and tube arrangement. *International Journal of Refrigeration*, 19(1):1–9, 1996.
- [40] H. Honda, N. Takata, H. Takamatsu, J.S. Kim, and K. Usami. Condensation of downward-flowing HFC-134a in a staggered bundle of horizontal finned tubes: Effect of fin geometry. *International Journal of Refrigeration*, 25:3–10, 2002.
- [41] S.B. Memory, R.W. Mazzone, and P.J. Marto. Enhanced laminar film condensation of R-113 using wire-wrap on a horizontal roped tube bundle. *Heat Transfer: 3rd UK National Heat Transfer Conf., University of Birmingham, England, Institution of Chemical Engineers Symposium Series*, 129(1):249–262, 1992.
- [42] D.M. Eissenberg. *An investigation of the variables affecting steam condensation on the outside of a horizontal tube bundle*. PhD thesis, University of Tennessee, 1972.
- [43] C.M. Chu and J.M. McNaught. Condensation on bundles of plain and low-finned tubes – Effect of vapour shear and condensate inundation. *Heat Transfer: 3rd UK National Heat Transfer Conf., University of Birmingham, England, Institution of Chemical Engineers Symposium Series*, 129(1):225–232, 1992.
- [44] J.M. McNaught and C.M. Chu. Heat transfer measurements in condensation on bundles of low-finned tubes: Effects of fin frequency. *Eng. Foundation Conf., Condensation and Condenser Design, St. Augustine, Florida, USA*, pages 367–376, 1993.
- [45] C.M. Chu and J.M. McNaught. Tube bundle effects in crossflow condensation on low-finned tubes. *Proc. 10th International Heat Transfer Conf., Brighton, Institution of Chemical Engineers Symposium Series*, 135(3):293–298, 1994.

- [46] J.B. Huber, L.E. Rewerts, and M.B. Pate. Shell-side condensation heat transfer of R-134a – Part I : Finned-tube performance. *ASHRAE Transactions*, 100(Part 2):239–247, 1994.
- [47] J.B. Huber, L.E. Rewerts, and M.B. Pate. Shell-side condensation heat transfer of R-134a – Part II : Enhanced tube performance. *ASHRAE Transactions*, 100(Part 2):248–256, 1994.
- [48] J.B. Huber, L.E. Rewerts, and M.B. Pate. Shell-side condensation heat transfer of R-134a – Part III : Comparison with R-12. *ASHRAE Transactions*, 100(Part 2):257–264, 1994.
- [49] L.E. Rewerts, J.B. Huber, and M.B. Pate. The effect of R-134a inundation on enhanced tube geometries. *ASHRAE Transactions*, 102(Part 2):285–296, 1996.
- [50] L.E. Rewerts, J.B. Huber, and M.B. Pate. The effect of R-123 condensate inundation and vapor shear on enhanced tube geometries. *ASHRAE Transactions*, 102(Part 2):273–284, 1996.
- [51] L.E. Rewerts, J.B. Huber, and M.B. Pate. The effect of noncondensable gas on the condensation of R-123 on enhanced tube geometries. *ASHRAE Transactions*, 103(Part 1):149–163, 1997.
- [52] T.-N. Nguyen and P.E. Orozco. Condensation of R-113 on enhanced surfaces. *ASHRAE Transactions*, 100(Part 1):736–743, 1994.
- [53] W.Y. Cheng and C.C. Wang. Condensation of R-134a on enhanced tubes. *ASHRAE Transactions*, 100(Part 2):809–817, 1994.
- [54] F. Kulis, A. Compingt, P. Mercier, and P. Rivier. Design method for shell and tube condensers in refrigeration units. *Heat Transfer in Condensation, Eurotherm Seminar 47, Paris*, pages 133–138, 1995.
- [55] J.-F. Roques. *Falling Film Evaporation on a Single Tube and on a Tube Bundle*. PhD thesis, Swiss Federal Institute of Technology, Lausanne, 2004.
- [56] E.E. Wilson. A basis for rational design of heat transfer apparatus. *ASME Transactions*, 37:47–82, 1915.
- [57] D.E. Briggs and E.H. Young. Modified Wilson plot techniques for obtaining heat transfer correlations for shell and tube heat exchangers. *Chemical Engineering Progress Symposium Series*, 65(92):35–45, 1969.
- [58] R. Kumar, H.K. Varma, K.N. Agrawal, and B. Mohanty. A comprehensive study of modified Wilson plot technique to determine the heat transfer coefficient during condensation of steam and R-134a over single

- horizontal plain and finned tubes. *Heat Transfer Engineering*, 22(2):3–12, 2001.
- [59] J.W. Rose. Heat-transfer coefficients, Wilson plots and accuracy of thermal measurements. *Experimental Thermal Fluid Science*, 28:77–86, 2004.
- [60] F.P. Incropera and D.P. DeWitt. *Fundamentals of Heat and Mass Transfer*, chapter 8, page 445. John Wiley & Sons, New York, 4th edition, 1996.
- [61] V. Gnielinski. New equations for heat and mass transfer in turbulent pipe and channel flow. *International Chemical Engineering*, 16(2):359–368, 1976.
- [62] F.P. Incropera and D.P. DeWitt. *Fundamentals of Heat and Mass Transfer*, chapter 8, page 424. John Wiley & Sons, New York, 4th edition, 1996.
- [63] M. Belghazi, A. Bontemps, Signe J.C., and Marvillet C. Condensation heat transfer of a pure fluid and binary mixture outside a bundle of smooth horizontal tubes. comparison of experimental results and a classical model. *International Journal of Refrigeration*, 24:841–855, 2001.
- [64] R. Kumar, H.K. Varma, B. Mohanty, and K.N. Agrawal. Condensation of R-134a vapor over single horizontal circular integral-fin tubes with trapezoidal fins. *Heat Transfer Engineering*, 21(2):29–39, 2000.
- [65] Y.J. Chang, C.T. Hsu, and C.C. Wang. Single-tube performance of condensation of R-134a on horizontal enhanced tubes. *ASHRAE Transactions*, 102(Part 1):821–829, 1996.
- [66] M. Belghazi, A. Bontemps, and Marvillet C. Condensation heat transfer on enhanced surface tubes: Experimental results and predictive theory. *Journal of Heat Transfer*, 124:754–761, 2002.
- [67] W.M. Rohsenow. Heat transfer and temperature distribution in laminar film condensation. *Trans. ASME*, 79:1645–1648, 1956.
- [68] W.H. McAdams. *Heat Transmission*. McGraw-Hill, New York, 3rd edition, 1954.
- [69] T.M. Rudy and R.L. Webb. Theoretical model for condensation on horizontal integral-fin tubes. *AIChE Symposium Series*, 79(225):11–18, 1983.
- [70] J.R. Thome. Condensation on external surfaces. *Engineering Databook III*, Chapter 7, <http://www.wolverine.com>, 2004.

- [71] R. Kumar, H.K. Varma, B. Mohanty, and K.N. Agrawal. Prediction of heat transfer coefficient during condensation of water and R-134a on single horizontal integral-fin tubes. *International Journal of Refrigeration*, 25:111–126, 2002.
- [72] J. Mitrovic. Influence of tube spacing and flow rate on heat transfer from a horizontal tube to a falling liquid film. *Proc. 8th International Heat Transfer Conf., San Francisco*, 4:1949–1956, 1986.
- [73] X. Hu and A.M. Jacobi. The intertube falling film part 1-flow characteristics, mode transitions and hysteresis. *ASME J. Heat Transfer*, 118:616–625, 1996.
- [74] X. Hu and A.M. Jacobi. Departure-site spacing for liquid droplets and jets falling between horizontal circular tubes. *Exp. Therm. Fluid Sci.*, 16:322–331, 1998.
- [75] Roques J.-F., Dupont V., and Thome J.R. Falling film transitions on plain and enhanced tubes. *Journal of Heat Transfer*, 124:491–499, 2002.
- [76] Roques J.-F. and Thome J.R. Flow patterns and phenomena for falling films on plain and enhanced tube arrays. *Proc. Third International Conference on Compact Heat Exchangers and Enhancement Technology for the Process Industries, Davos, Switzerland, 1-6 July*, pages 391–398, 2001.
- [77] Roques J.-F. and Thome J.R. Falling film transitions between droplets, column and sheet flow modes on a vertical array of horizontal 19 fpi and 40 fpi low finned tubes. *Proc. 1st International Conference on Heat Transfer, Fluid Mechanics and Thermodynamics, HEFAT2002, 8-10 April, Kruger Park, South Africa*, pages 523–528, 2002.
- [78] Roques J.-F. and Thome J.R. Falling film transitions between droplet, column and sheet modes on a vertical array of horizontal 19 fpi and 40 fpi low finned tubes. *Heat Transfer Engineering*, 24:40–45, 2003.
- [79] D. Yung, J.J. Lorenz, and E.N. Ganic. Vapor/liquid interaction and entrainment in falling film evaporators. *Journal of Heat Transfer*, 102:20–25, 1980.
- [80] V. P. Carey. *Liquid–Vapor Phase-Change Phenomena: an introduction to the thermophysics of vaporization and condensation process in heat transfer equipment*, pages 96–97. Taylor & Francis, 1992.
- [81] J Schmitz. Utilisation et amélioration d’un programme de traitement d’images: Application aux écoulements sur un arrangement vertical de tubes horizontaux. Semester project, LTCM, EPFL, 2003.

- [82] Y.-H. Wei and A.M. Jacobi. Vapor-shear, geometric, and bundle-depth effects on intertube falling-film modes. *Proc. 1st International Conference on Heat Transfer, Fluid Mechanics and Thermodynamics, HEFAT2002, 8-10 April, Kruger Park, South Africa*, pages 40–46, 2002.
- [83] D. Butterworth. Film condensation of pure vapor. *Hemisphere Handbook of Heat Exchanger Design*, Chapter 2.6.2, Hemisphere, New York, 1990.
- [84] S.S Kutateladze. *Fundamentals of Heat Transfer*. Academic Press, New York, 1963.
- [85] S.S. Kutateladze and I.I. Gogonin. Heat transfer in film condensation of slowly moving vapor. *International Journal of Heat Mass Transfer*, 22:1593–1599, 1979.
- [86] D.A. Labuntsov. Heat transfer in film condensation of pure vapours on vertical surfaces and horizontal tubes. *Teploenergetika*, 7:72–80, 1957.
- [87] A.P. Colburn. Notes on the calculation of condensation where a portion of the condensate layer is in turbulent motion. *Trans. AIChE*, 30:187–193, 1934.
- [88] L.A. Bromley. Effect of heat capacity of condensate. *Ind. Eng. Chem*, 44:2966, 1952.

# Curriculum Vitae

Daniel Gstöhl  
Date of birth: 29th of December 1974  
Nationality: Liechtenstein

## Education:

- 1995 Graduation exam (latin), Gymnasium Vaduz, Liechtenstein
- 2000 Master's degree in Mechanical Engineering, specializations:  
Internal combustion engines and material sciences  
Swiss Federal Institute of Technology Zürich (ETH), Switzerland
- 2004 PhD at the Laboratory of Heat and Mass Transfer  
Swiss Federal Institute of Technology Lausanne (EPFL), Switzerland

## Professional Experience:

- 1998 N.R. Industries, Bangkok, Thailand  
Programming of pharmaceutical machines, Internship
- 1999 ABB Alstom Power, Baden-Dättwil, Switzerland  
Thermoacoustic characterization of a premix-burner, Internship